



**HAL**  
open science

# Photo-responsive systems in aqueous solution: from model polyelectrolytes to polyelectrolyte-surfactant complexes

Yazhao Liu

► **To cite this version:**

Yazhao Liu. Photo-responsive systems in aqueous solution: from model polyelectrolytes to polyelectrolyte-surfactant complexes. Theoretical and/or physical chemistry. Université de Strasbourg, 2021. English. NNT: 2021STRAE007 . tel-04095619

**HAL Id: tel-04095619**

**<https://theses.hal.science/tel-04095619>**

Submitted on 12 May 2023

**HAL** is a multi-disciplinary open access archive for the deposit and dissemination of scientific research documents, whether they are published or not. The documents may come from teaching and research institutions in France or abroad, or from public or private research centers.

L'archive ouverte pluridisciplinaire **HAL**, est destinée au dépôt et à la diffusion de documents scientifiques de niveau recherche, publiés ou non, émanant des établissements d'enseignement et de recherche français ou étrangers, des laboratoires publics ou privés.

*ÉCOLE DOCTORALE de Physique et de Chimie-Physique*

Institut Charles Sadron

## THÈSE

 présentée par :

**Yazhao LIU**

soutenue le : 29 Janvier 2021

pour obtenir le grade de : **Docteur de l'université de Strasbourg**

Discipline/ Spécialité : Chimie Physique

**Systèmes photo-stimulables en solution : polyélectrolytes modèles et complexes polyélectrolytes-tensioactifs**

**THÈSE dirigée par :**

**M. COMBET Jérôme**

Maître de conférences, Université de Strasbourg

**RAPPORTEURS :**

**M. CHASSENIEUX Christophe**

Professeur, Le Mans Université

**M. COUSIN Fabrice**

Ingénieur-Chercheur CEA, Université Paris-Saclay

---

**AUTRES MEMBRES DU JURY :**

**Mme MALIKOVA Natalie**

Chargée de recherche CNRS, Sorbonne Université

**Mme FERLAY Sylvie**

Professeur, Université de Strasbourg

**M. MÉSINI Philippe**

Directeur de Recherche CNRS, Université de Strasbourg



# Acknowledgement

This thesis, performed at the Institut Charles Sadron (ICS, CNRS UPR 22) in the University of Strasbourg, was supervised by Dr. Jérôme Combet.

First and foremost, I would like to express my deepest gratitude to my supervisor, Jérôme Combet for believing in me and providing me this opportunity to learn, progress and to contribute to this research project. I'm thankful for his time and effort for the manuscript. I have greatly appreciated all his patient guidance and valuable advices not only for the scientific research but also for quotidian life, who supported me to accomplish this work throughout the three years.

Second, I wish to thank the jury members, Pr. Christophe CHASSENIEUX, Dr. Fabrice COUSIN, Dr. Natalie MALIKOVA, Pr. Sylvie FERLAY and Pr. Philippe MÉSINI for taking their time to review my thesis.

Third, I'm also thankful to Pr. Philippe Mésini for his kind guidance and professional advices for the synthesis part of my thesis and for the time he spent to the correction of my manuscript. I have learned a lot about organic synthesis, polymerization, and analysis technics.

Then, my sincere thanks go to my colleagues at ICS for their contribution, support, training or aid on different instruments. I would like to thank M. Jean-Philippe Lamps for his training and advices for all the synthesis experiments and for the synthesis of poly(styrenesulfonate). I would like to thank Guillaume Fleith for his training and support for SAXS measurements, his help for SANS experiments at LLB and for lending me LEGO bricks. I want to thank Mélanie Legros and Catherine Foussat for all the SEC measurements; Leandro Jacomine and Wiebke Drenckhan for the training on the tensiometer and advices about surface tension measurements; Marc Schutz for the Cryo-TEM investigations; Delphine Chan-Seng for her advice on RAFT polymerization, Laurent Herrmann for the electronics of the irradiation devices, and Francois Courtier for the design of the SAXS sample holder. I would like to thank Michel Rawiso for his advices,

his encouraging words and sharing his knowledge about everything.

My gratitude also goes to all the collaborators. I would like to thank Alexis Chennevière, Arnaud Helary, Fabrice Cousin and other colleagues at LLB for their help during SANS experiments and Mériem Er-Rafik at DTU (Denmark) for the CryoTEM measurements.

To my friends and colleagues at ICS, especially my coffee pals for their accompany and inspiration. I would like to thank especially my best friends Zheng LIU, Lu YU and Tongtong YANG since junior high school for their supporting and accompany. To finish, I express my sincere gratitude and appreciation for my parents who offer me this opportunity to study in France and my husband Da SHI, who has supported, encouraged and accompanied me to accomplish this thesis.

# Résumé de thèse

## Chapter I. Introduction

Les matériaux "intelligents" sont des matériaux dont les propriétés peuvent être modifiées de manière significative par un stimulus externe (comme un stress mécanique, un champ électrique ou magnétique, la lumière, la température, le pH, *etc.*). Le développement de systèmes "intelligents" en solution aqueuse a suscité un grand enthousiasme pour leurs applications industrielles et académiques. Parmi les stimuli, la lumière présente un intérêt particulier car c'est une source propre et facile à manipuler. Une grande variété de chromophores a été incorporée dans des molécules hydrosolubles conduisant à différents systèmes photosensibles pour lesquels les changements de morphologie, de propriétés interfaciales ou de propriétés en solution ont été largement étudiés.

Dans ce projet, nous nous intéressons aux solutions aqueuses de systèmes photo-stimulables modèles formés à partir de polymères chargés (polyélectrolytes, PEs) et de tensioactifs.

Les PEs sont des polymères qui possèdent des groupements ionisables. Dans un solvant polaire tel que l'eau, ces groupements se dissocient conduisant à l'apparition de polyions chargés et de contre-ions libres en solution. Les solutions de PEs combinent des propriétés caractéristiques des solutions de polymères et des électrolytes. Elles font l'objet d'études intensives tant au niveau fondamental qu'au niveau industriel. Elles présentent des propriétés physico-chimiques intéressantes, telles qu'une viscosité élevée, une capacité à l'auto-assemblage et la capacité d'interagir avec différentes (macro)molécules (tensioactif, protéine, ADN, PE). La combinaison de chromophores photoréactifs et de systèmes macromoléculaires à base de PEs conduit à de nouvelles organisations structurales en solution aqueuse dont les propriétés sont modifiables par simple irradiation.

Le chromophore azobenzène (Azo) est utilisé dans notre étude (Figure 1). Le groupement Azo présente une isomérisation *trans* → *cis* sous irradiation UV. Cette transition s'accompagne d'une diminution significative de la distance entre deux phényles, et de l'augmentation du moment dipolaire (de  $\approx 0$  à 3 D pour un groupement Azo sans substituant). Au-delà du simple aspect conformationnel, cette transition modifie également la balance hydrophile/hydrophobe dans nos systèmes. La transformation inverse (*cis* → *trans*) peut se produire par simple relaxation thermique dans l'obscurité, ou par photoisomérisation en utilisant une lumière bleue.

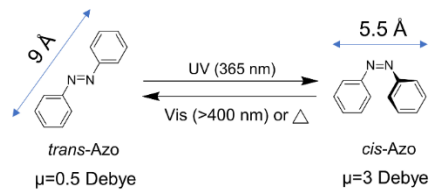


Figure 1 Structure des isomères azobenzene *trans* et *cis*

L'objectif de cette thèse est de concevoir, synthétiser et caractériser des systèmes photosensibles modèles à base de PEs en solution aqueuse ainsi que d'étudier leur transformation structurale sous irradiation (diffusion des rayons X et des neutrons aux petits angles, SAXS et SANS). Le groupement Azo a été incorporé de différentes façons dans nos systèmes.

Le premier système étudié concerne des chaînes de polyacrylate de sodium contenant des groupements Azo. Le chromophore est ici greffé sur des chaînes latérales du squelette macromoléculaire des polyions.

Le deuxième système est composé de tensioactifs contenant des groupements Azo (Azo-tensioactif) et de PEs « classiques » de charge opposée. Ce sujet est étroitement lié à la complexation tensioactif/PE, thématique que l'on retrouve de nombreuses formulations industrielles.

Enfin, les Azo-tensioactifs purs présentent également des propriétés d'auto-assemblage extrêmement intéressantes. En présence de co-tensioactifs, de nouvelles organisations structurales peuvent se former. Le troisième système étudié est constitué de mélanges d'Azo-tensioactifs de co-tensioactifs et montre une variation réversible importante de la viscosité sous irradiation.

D'un point de vue fondamental, ces systèmes peuvent également apporter un regard nouveau sur les solutions de PEs (transition hydrophile/hydrophobe, rôle des contre-ions, PEs associatifs...).

## Chapter II. Polyélectrolytes Azo-modifiés

Les polymères hydrophobes et amphiphiles sont capables d'adopter une conformation particulière, mais aussi de s'auto-assembler pour former des particules colloïdales, des vésicules... La balance hydrophile/ hydrophobe est un paramètre clé pour expliquer la formation de ces structures. L'ajout d'un groupement Azo sur le PE (groupement latéral) offre la possibilité de modifier l'hydrophobie du système et de provoquer une réorganisation structurale par simple irradiation lumineuse.

## II.1 Azo-polyacrylates (PAA-Azo<sub>y</sub>)<sub>n</sub>

Nous avons synthétisé quatre Azo-polyacrylates (Schéma 1) de masses molaires distinctes (chaînes longues et chaînes courtes) contenant différentes fractions molaires en Azo ( $\tau_{azo}$ ). Ils sont nommés (PAA-Azo<sub>y</sub>)<sub>n</sub>, où  $y$  est la fraction molaire en unités Azo (ou encore, fraction en monomères modifiés) et  $n$  est le degré de polymérisation. (PAA-Azo<sub>0.11</sub>)<sub>42Sigma</sub> et (PAA-Azo<sub>0.15</sub>)<sub>39Sigma</sub> sont obtenus à partir d'un acide polyacrylique commercial. (PAA-Azo<sub>0.15</sub>)<sub>54RAFT</sub> et (PAA-Azo<sub>0.11</sub>)<sub>738RAFT</sub> sont obtenus à partir d'un acide polyacrylique bien défini (synthétisé par polymérisation RAFT). Les caractéristiques des Azo-polyacrylates utilisés sont résumées dans le Tableau 1.

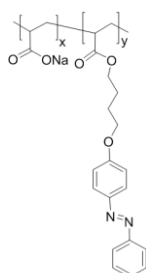


Schéma 1 Structure chimique des Azo-polyacrylates de sodium (PAA-Azo<sub>y</sub>)<sub>n</sub>.

	$M_w$ (g·mol <sup>-1</sup> )	$M_n$ (g·mol <sup>-1</sup> )	$I_p$	$DP_n$ par SEC	$DP_n$ par NMR	$\tau_{azo}$ (%)
(PAA-Azo <sub>0.11</sub> ) <sub>42Sigma</sub>	5800	4400	1.33	42	/	10.7
(PAA-Azo <sub>0.15</sub> ) <sub>39Sigma</sub>	5700	4500	1.26	39	/	15.1
(PAA-Azo <sub>0.15</sub> ) <sub>54RAFT</sub>	7700	6900	1.13	56	54	15.0
(PAA-Azo <sub>0.11</sub> ) <sub>738RAFT</sub>	76100	60600	1.26	595	738	11.4

Tableau 1 Caractéristiques des Azo-polyacrylates de sodium

## II.2 Photoisomérisation

La photoconversion des (PAA-Azo<sub>y</sub>)<sub>n</sub> en solution aqueuse a été étudiée par spectroscopie d'absorption UV-Visible.

### II.2.1 Rapport trans/cis

Le rapport *trans/cis* est un paramètre important qui influence l'organisation finale des systèmes photosensibles. La fraction molaire en isomères *trans* ( $x_{trans}$ ) peut être déterminée par des mesures d'absorption UV-Visible.

La Figure 2a montre la variation des spectres UV-Vis d'une solution très diluée de (PAA-Azo<sub>0.11</sub>)<sub>42Sigma</sub> sous irradiation UV. L'isomère *trans* (courbe bleue, dark) présente une bande d'absorption forte à 338 nm correspondant à une transition  $\pi$ - $\pi^*$  et une bande faible à 440 nm attribuée à une transition  $n$ - $\pi^*$ . Sous irradiation UV, la bande d'absorption à 338

nm diminue tandis que sa position est déplacée à 319 nm. En outre, le pic d'absorption centré à 440 nm devient plus important. Deux points isosbestiques sont observés à 300 et 405 nm. Ceci est la signature de la coexistence des deux isomères *trans* et *cis* en solution (système à deux états) : tous les spectres UV-Vis peuvent être décomposés comme une combinaison linéaire du spectre *trans* pur et du spectre *cis* pur pondérés par leurs fractions molaires respectives. L'état pur *trans* peut être obtenu en laissant reposer l'échantillon deux jours dans le noir (« Dark »).

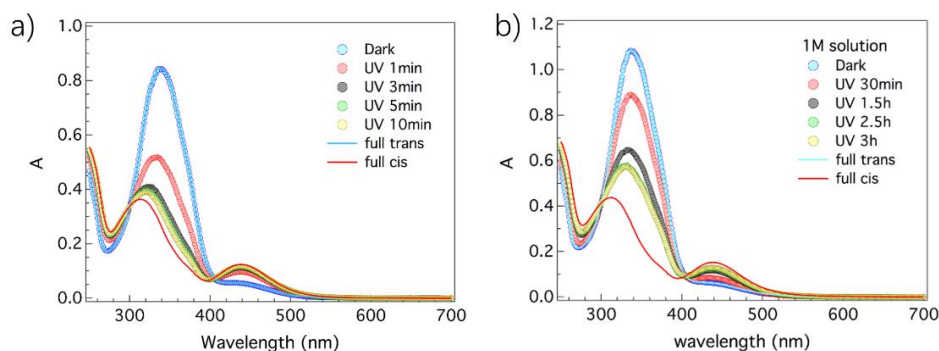


Figure 2 Variation des spectres UV-Vis de (PAA-Azo<sub>0.11</sub>)<sub>42Sigma</sub> sous UV a) solution diluée (0.05 mM en Azo) ; b) solution concentrée (0.1 M en Azo après dilution rapide).

Il est donc possible d'extraire la fraction *trans*  $x_{trans}$  à n'importe quel temps d'irradiation (ou de relaxation) si les spectres d'absorption associés aux formes *trans*  $A_{trans}(\lambda)$  et *cis* purs  $A_{cis}(\lambda)$  sont connus, en utilisant la relation :

$$A(\lambda) = x_{trans}A_{trans}(\lambda) + (1 - x_{trans})A_{cis}(\lambda)$$

L'analyse par absorption UV-vis nécessite des concentrations extrêmement faibles en chromophores. Dans les études structurales réalisées par diffusion des rayons X et des neutrons aux petits angles, les concentrations sont beaucoup trop élevées pour être mesurées directement par UV-vis (0.06 M à 1 M en monomères, soit  $\approx$  6 mM à 100 mM en Azo). Pour quantifier  $x_{trans}$  à l'état stationnaire ( $x_{trans}^{eq}$ ) dans ces échantillons "concentrés", une dilution rapide (facteur 1000 ou 2000) est nécessaire avant la mesure d'absorption. On considère implicitement que la dilution ne perturbe pas le rapport trans/cis initial, et ce, même si elle modifie l'organisation structurale. Un exemple réalisé à 1 M ( $\approx$  0.1 M en Azo) est donné sur la Figure 2b.

La cinétique de la photoconversion sous irradiation UV a été étudiée plus en détail dans le cas de (PAA-Azo<sub>0.11</sub>)<sub>42Sigma</sub> pour chacune des concentrations mesurées par diffusion aux petits angles. L'évolution de  $x_{trans}$  en fonction du temps d'irradiation est présentée sur la Figure 3. Le temps pour atteindre l'état stationnaire est d'autant plus long que la concentration est importante. D'autre part, la fraction  $x_{trans}$  à l'équilibre dépend

également de la concentration initiale des solutions. Elle est d'environ 32 % pour une solution à 1 M alors qu'elle est proche de 10% pour une solution plus diluée (0.0625 M).

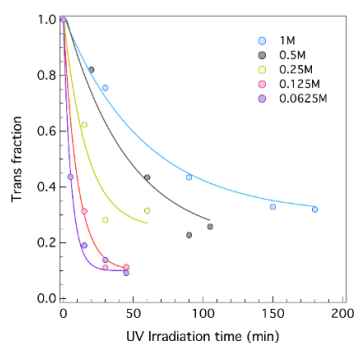


Figure 3 Variation de la fraction  $x_{trans}$  en fonction du temps d'irradiation pour (PAA-Azo<sub>0.11</sub>)<sub>42Sigma</sub>, concentrations 0.0625 M – 1 M en monomères.

## II.2.2 Réversibilité

Plusieurs cycles d'irradiation UV-Blue ont été appliqués sur des solutions d'Azo-polymères afin de tester la réversibilité de la photoconversion. La variation de  $x_{trans}$  a été suivie par absorption UV-vis. Une bonne réversibilité après 3 cycles d'irradiation est observée.

## II.2.3 Comparaison des spectres UV-Vis des Azo-polymères

La position de la bande d'absorption (« dark » state) est très sensible à l'environnement local des groupements Azo. Un décalage vers les plus petites longueurs d'ondes (blue-shift) est attendu lorsque l'Azo est sous forme agrégée. On dispose ainsi d'un indicateur pour sonder l'organisation des chromophores en solution. Pour la même fraction en Azo ( $\tau_{azo} = 0.11$ ), la chaîne longue (PAA-Azo<sub>0.11</sub>)<sub>738RAFT</sub> présente un décalage vers le bleu par rapport à la chaîne courte (PAA-Azo<sub>0.11</sub>)<sub>42Sigma</sub> (Figure 4a). Cela indique que l'organisation structurale locale est différente, et que les groupements Azo ne sont pas directement au contact de l'eau avec les chaînes longues (des agrégats contenant les chromophores sont présents même aux faibles concentrations mesurées). Les bandes d'absorption des deux Azo-polymères courts de plus forte composition en Azo ( $\tau_{azo} = 0.15$ ) sont quasiment à la même position : la structure locale est très similaire aux très faibles concentrations (Figure 4b). Elle est sans doute assez proche de celle rencontrée pour les chaînes courtes à  $\tau_{azo} = 0.11$ .

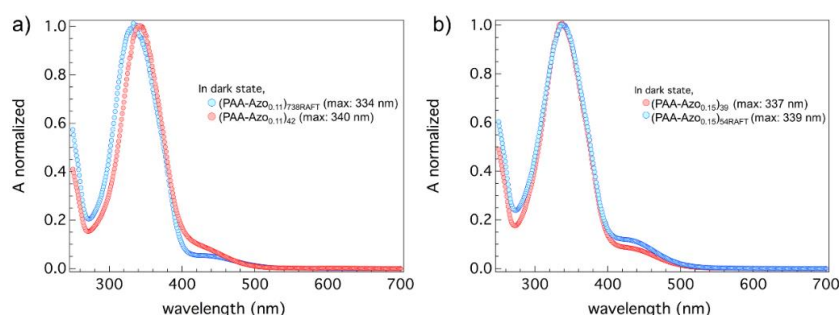


Figure 4 Spectres d'absorption normalisés de : a) Azo-polymères longs et courts,  $\tau_{\text{azo}} = 0.11$  ; b) Azo-polymères courts,  $\tau_{\text{azo}} = 0.15$ . Tous les spectres ont été mesurés à une concentration en Azo d'environ 0.05 mM.

## II.3 Organisation structurale

Nous avons étudié l'organisation structurale des quatre Azo-polymères en solution par diffusion des rayons X aux petits angles (SAXS). Le poly(acrylate de sodium) NaPAA non modifié a également été étudié comme système de référence.

### II.3.1 Organisation structurale des solutions de (PAA-Azo<sub>0.11</sub>)<sub>738RAFT</sub> : chaînes longues, $\tau_{\text{azo}} = 0.11$

De façon générale, les courbes de diffusion montrent un pic de corrélation à une position  $q^*$  caractéristique des répulsions électrostatiques et de l'organisation des chaînes en solution.  $q^*$  varie comme une loi de puissance avec la concentration,  $c^\alpha$ , où l'exposant  $\alpha$  dépend de l'état de dispersion des polyions, ou plus généralement, des objets en solution. Pour NaPAA<sub>738RAFT</sub> (sans groupement Azo),  $q^*$  varie comme  $c^{1/2}$  (Figure 5c, courbe noire) : on est en régime semi-dilué (régime caractéristique d'un PE hydrophile en bon solvant). La position du maximum est liée à la maille du réseau enchevêtré (longueur de corrélation).

Les courbes de diffusion de (PAA-Azo<sub>0.11</sub>)<sub>738RAFT</sub> à différentes concentrations sont présentées sur la Figure 5 (dark : a, UV : b). La position du pic varie selon une loi de puissance avec la concentration ( $q^* \propto c^\alpha$ ) mais l'exposant  $\alpha$  est maintenant égal à 0.3 ( $\alpha \approx 1/3$ ) dans l'obscurité (dark) et à 0.26 sous irradiation UV. Ce comportement est très différent de celui observé dans le cas du simple NaPAA ( $\alpha \approx 1/2$ ) : nous ne sommes plus en régime semi-dilué comme observé précédemment. La forme des courbes de diffusion est également modifiée par rapport aux solutions de NaPAA. Elles sont maintenant caractéristiques de particules chargées en solution. En présence de groupements Azo le long du squelette, les polyions ont donc tendance à s'effondrer et à former des agrégats denses. Le régime en  $c^{1/3}$  observé dans l'obscurité est alors caractéristique d'une simple loi de dilution des agrégats. La variation en  $c^{0.26}$  observée sous UV préfigure un changement du nombre d'agrégation des particules sous irradiation.

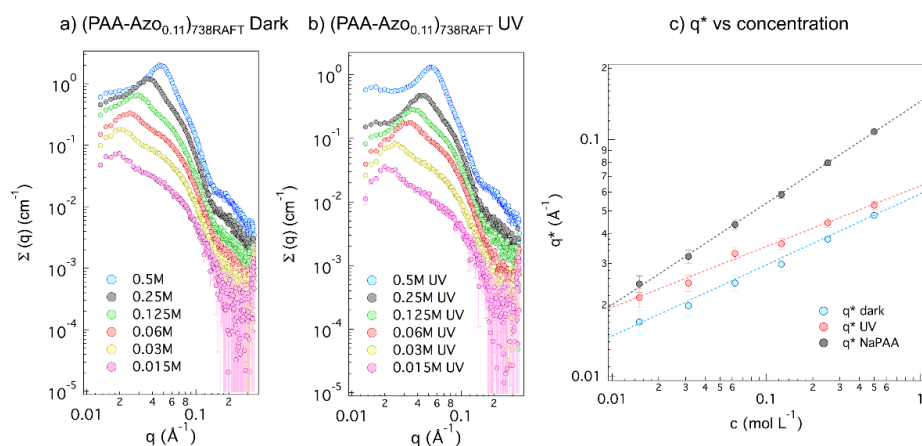


Figure 5 Résultats SAXS pour  $(\text{PAA-Azo}_{0.11})_{738\text{RAFT}}$ . a) mesures dans l'obscurité (dark) ; b) mesures sous UV ; c) variation de  $q^*$  en fonction de la concentration.

Des mesures de microscopie électronique (Cryo-TEM) dans l'obscurité (dark) ont été effectuées à  $0.03 \text{ mol L}^{-1}$ . Bien que cette technique ait une résolution limitée ( $\approx 2 \text{ nm}$ ), elle fournit des informations essentielles (taille, forme, répartition des objets) qui complètent parfaitement l'analyse SAXS (Figure 6). Les images montrent des objets sphériques distincts, répartis de façon homogène dans le film. Des petites particules (diamètre moyen  $5 - 6 \text{ nm}$ ) coexistent avec quelques rares objets allongés (flèches longues). Ces résultats valident définitivement notre description colloïdale des polymères modifiés en solution. D'après ces observations, nous avons utilisé un modèle des particules chargées sphériques polydisperses pour analyser les mesures de diffusion.

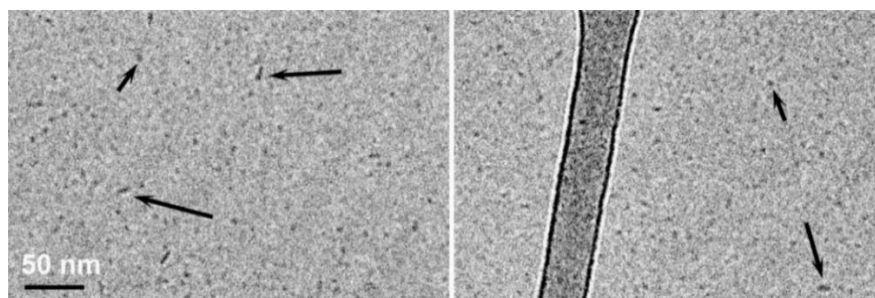


Figure 6 Images CryoTEM pour  $(\text{PAA-Azo}_{0.11})_{738\text{RAFT}}$  à  $0.03 \text{ mol L}^{-1}$  (dark). Petites flèches : petits objets sphériques. Longues flèches : objets allongés.

Une diminution inattendue de l'intensité en  $q^{-2}$  est observée autour de  $0.2 \text{ \AA}^{-1}$ . Cette valeur est proche de la diffusion observée dans les solutions de NaPAA pur. Elle indique clairement la présence de segments de PAA chargés dans le système. En d'autres termes, les particules denses n'incorporent pas tous les monomères de PAA : certaines parties des polyions restent en solution. Ce type de comportement se retrouve souvent avec des particules décorées de polymères ou avec des polymères ramifiés en étoile. Dans ces

systèmes, des chaînes sont attachées à un cœur (core) et forment une couche plus ou moins dense en périphérie (shell). Ce phénomène est concevable avec nos PEs modifiés car ils sont fortement amphiphiles : certaines parties de chaînes (contenant les groupements Azo) peuvent se regrouper en un cœur hydrophobe tandis que des segments chargés restent en solution. Une couche (shell) formée d'un réseau de polyions (bouts de chaînes, boucles...) se forme alors autour d'un cœur (core) contenant les groupements photosensibles.

D'un point de vue diffusion, ce système peut être traité comme une particule « homogène » core-shell tant que les fluctuations de concentration du réseau de polymère (à l'intérieur du shell) sont négligeables (ce qui n'est généralement pas le cas à grand  $q$ ). En première approximation, ces fluctuations de concentration peuvent être prises en compte en rajoutant une contribution spécifique à l'intensité théorique prévue par un simple modèle core-shell.<sup>1</sup> En pratique, toutes les données ont été corrigées de cette contribution spécifique avant d'être analysées.

Nous avons analysé les courbes de diffusion (0.015 M – 0.5 M) avec un modèle classique core-shell homogène (facteur de forme) combiné à un facteur de structure  $S(q)$  développé pour les colloïdes chargés dans un potentiel de Coulomb répulsif.<sup>2,3</sup> Nous pouvons anticiper que la densité de longueur de diffusion moyenne (SLD) de la couche sera proche de celle du solvant puisqu'elle est assimilable à une solution de PE semi-diluée. Un exemple d'affinement est présenté dans la Figure 7 (dark, UV,  $c = 0.5 \text{ mol L}^{-1}$ ).

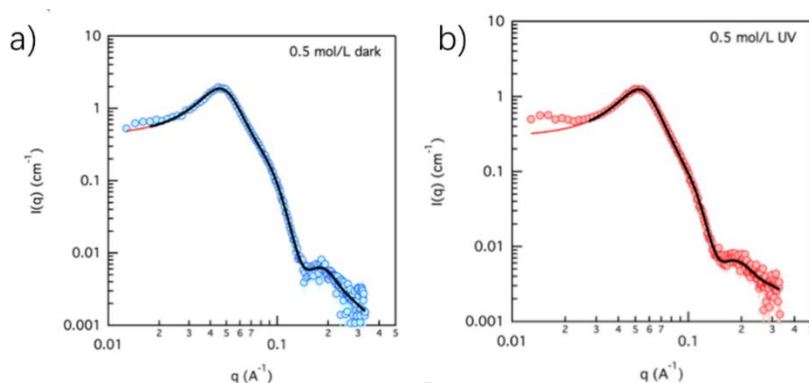


Figure 7 Courbes SAXS et fits en absence de lumière (dark) et sous UV pour (PAA-Azo<sub>0.11</sub>)<sub>738</sub>RAFT pour une concentration de 0.5 mol L<sup>-1</sup>.

Nous pouvons maintenant donner une description schématique de la structure des particules (Figure 8). En absence de lumière (état dark), elles présentent un cœur hydrophobe dense de rayon environ 29 Å (contenant principalement les groupements Azo) entouré d'une couche (shell) formée par des segments de PAA chargés (solution semidiluée). La taille du cœur ne change pas avec la concentration (sauf pour la plus faible, 0.015 mol L<sup>-1</sup>, où la statistique des courbes n'est plus très bonne). Ceci est cohérent avec

les mesures Cryo-TEM qui montrent des particules d'un diamètre de l'ordre de 6 nm (le shell n'est pas visible par Cryo-TEM pour des raisons de contraste). Ce résultat important est en accord avec la variation de  $q^*$  avec la concentration  $c$  observée précédemment. En effet, l'exposant de la loi de puissance ( $q^* \propto c^\alpha$ )  $\alpha \approx 1/3$  est caractéristique d'une simple loi de dilution, c'est-à-dire sans variation du nombre d'agrégation (i.e., du nombre de chaînes formant les agrégats : le volume du cœur des particules est constant).

La couche externe des particules (shell) contient des segments de polyions (bouts de chaînes et boucles à la surface du cœur). L'épaisseur de cette couche varie entre 23 Å à 63 Å suivant la concentration. L'organisation structurale de cette couche est néanmoins plus complexe que celle d'une solution de polymère neutre classique considérée pour corriger les données (fluctuations de concentration). Cet aspect pourrait être amélioré.

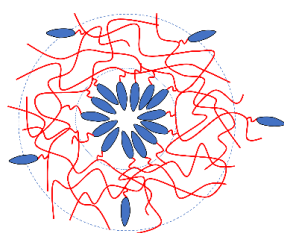


Figure 8 Représentation schématique des agrégats de (PAA-AZO<sub>0.11</sub>)<sub>738</sub>RAFT

Sous UV,  $q^*$  est plus élevé tandis que l'exposant  $\alpha$  est réduit ( $\alpha = 0.26$ ). En outre l'intensité du pic est réduite d'un facteur important (proche de 2). Ceci indique une concentration en particules plus importante et donc, une diminution du nombre d'agrégation. Ce phénomène, plus marqué aux faibles concentrations, est compatible avec la réduction de la taille du cœur observée sous UV (de 28 à 21 Å lorsque  $c$  varie de 0.5 à 0.015 mol L<sup>-1</sup>, correspondant à une réduction du volume d'un facteur 2).

Il est donc possible par simple stimuli lumineux de contrôler la taille des particules en modifiant leur nombre d'agrégation (nombre de chaînes par particule). Ce nombre est toutefois assez limité et n'excède pas quelques unités (< 4).

### **II.3.2 Organisation structurale des solutions de PAA-Azo : chaînes courtes, $\tau_{azo} = 0.11$**

Pour les solutions de NaPAA non modifiés (NaPAA<sub>23sigma</sub> et NaPAA<sub>54RAFT</sub>),  $q^*$  varie en  $c^{1/3}$  : on est en régime dilué sur toute la gamme de concentrations. Les chaînes de NaPAA sont solubles à l'échelle moléculaire,  $q^*$  est relié à la distance moyenne inter-chaînes.

Les courbes de diffusion et la variation de  $q^*$  avec la concentration pour les PAA-Azo sont présentées sur la Figure 9. Contrairement aux chaînes longues, différents régimes en concentration (i.e. différent exposants  $\alpha$ ) apparaissent. Comme les solutions de NaPAA non modifiés sont en régime dilué sur toute la gamme de concentrations, on peut

raisonnablement supposer que c'est également le cas pour  $(\text{PAA-Azo}_{0.11})_{42\text{Sigma}}$ . L'écart par rapport à une simple loi de dilution  $c^{1/3}$  peut donc révéler une association (ou agrégation) entre polymères.

Pour les faibles concentrations ( $\alpha = 1/3$ , régime I), les positions des pics de diffusion du PAA-Azo sont identiques à celles des PAA non modifiés (sans Azo). On observe la loi de dilution associée au régime dilué, les chaînes sont solubles à l'échelle moléculaire.

Pour les concentrations entre 0.03 et 0.1 mol L<sup>-1</sup> (régime II), les positions  $q^*$  de NaPAA sont superposables à celles de PAA-Azo sous UV : les chaînes modifiées sont toujours solubilisées à l'échelle moléculaire. En absence de lumière (dark), ce n'est plus le cas. Les valeurs de  $q^*$  sont désormais plus faibles tandis que  $\alpha < 1/3$  : les chaînes commencent à s'agréger, on sonde des objets chargés de plus en plus distants. Ce régime est assez intéressant car un simple stimuli lumineux permet de « casser » les agrégats (irradiation UV) ou au contraire, de les créer (lumière bleue) de façon complètement réversible.

Pour les concentrations encore plus élevées (régime III),  $q^*$  ne varie plus avec  $c$ . Nous sommes dans un régime où la distance inter-objets reste constante lorsque la concentration augmente : les polyions ajoutés contribuent à faire grossir les agrégats existants. Le profil de diffusion suggère une organisation étoilée (dark) partiellement modifiée sous UV.

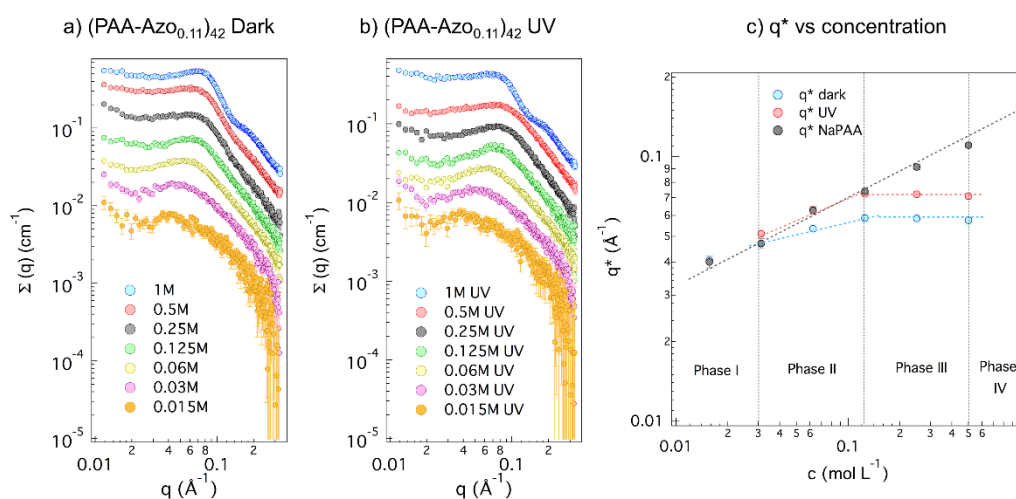


Figure 9 Résultats SAXS pour  $(\text{PAA-Azo}_{0.11})_{42\text{Sigma}}$ . a) mesures dans l'obscurité (dark) ; b) mesures sous UV ; c) variation de  $q^*$  en fonction de la concentration.

### II.3.3 Organisation structurale des solutions de PAA-Azo : chaînes courtes, $\tau_{\text{azo}} = 0.15$

Lorsque nous augmentons le taux de greffage en Azo des chaînes courtes ((PAA-Azo<sub>0.15</sub>)<sub>39Sigma</sub> et (PAA-Azo<sub>0.15</sub>)<sub>54RAFT</sub>), le comportement général observé par diffusion des rayons X est assez similaire. Néanmoins, seuls les régimes I (sous UV) et II (dark, UV)

sont conservés.

Pour les PEs en absence de lumière (dark), la variation de  $q^*$  peut se décrire par une loi de puissance ( $q^* \propto c^\alpha$ ) avec un seul exposant  $\alpha$  sur toute la gamme de concentrations ( $\alpha = 0.25$  et  $0.23$  pour (PAA-Azo<sub>0.15</sub>)<sub>39Sigma</sub> et (PAA-Azo<sub>0.15</sub>)<sub>54RAFT</sub> respectivement). Ce comportement correspond au régime II précédent, les chaînes sont agrégées.

Sous UV, deux régimes apparaissent. En dessous de  $0.03 \text{ mol L}^{-1}$  (comme pour (PAA-Azo<sub>0.11</sub>)<sub>42Sigma</sub>, Figure 9c),  $q^*$  atteint les valeurs du NaPAA pur (régime I). Dans cette gamme de concentrations les agrégats peuvent être désassemblés de façon réversible par simple irradiation UV. Ce comportement est assez similaire à celui observé pour (PAA-Azo<sub>0.11</sub>)<sub>42Sigma</sub>, mais la gamme de concentrations est désormais beaucoup plus faible. Ceci est une conséquence directe de la teneur plus élevée en Azo.

Au-delà de  $0.03 \text{ mol L}^{-1}$ ,  $q^*$  suit toujours une loi de puissance avec des exposants de  $0.12$  ((PAA-Azo<sub>0.15</sub>)<sub>39Sigma</sub>) et  $0.16$  ((PAA-Azo<sub>0.15</sub>)<sub>54RAFT</sub>). Le maximum s'affine tandis qu'un épaulement bien défini apparaît autour de  $0.15 \text{ \AA}^{-1}$ . Nous sommes en présence d'objets de type core-shell constitués d'un cœur formé par les groupements Azo et une couche constituée de segments de PAA en régime semi-dilué.

## Chapter III. Complexes de Azo-tensioactifs et polyélectrolytes de charge opposée

Les complexes tensioactif/PE sont utilisés dans de très nombreux domaines tels que les peintures, la conservation des aliments, le contrôle rhéologique...

Les Azo-tensioactifs présentent des propriétés modulables sous irradiation. La combinaison des PEs et des Azo-tensioactifs offre de nouvelles possibilités pour contrôler l'organisation structurale des complexes à l'aide d'un simple stimulus lumineux.

### III.1 Azo-tensioactifs

Les Azo-tensioactifs sont composés d'une tête polaire, d'un espaceur  $OR_2$ , d'un groupement Azo et d'une queue alkyle  $R_1$  (Figure 10). Pour simplifier les notations, ils sont appelés  $x\text{Azo}y\text{TAB}$ , où  $x$  est le nombre de carbones de la queue alkyle  $R_1$  et  $y$  est le nombre de carbones de l'espaceur  $R_2$ . La position du groupement Azo au sein du tensioactif varie suivant la combinaison ( $R_1$ ,  $R_2$ ). Dans ce travail, nous avons synthétisé deux Azo-tensioactifs : 4Azo2TAB et 8Azo2TAB.

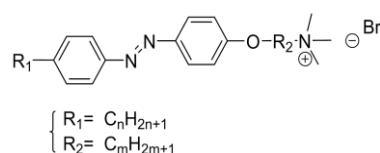


Figure 10 Structure d'un Azo-tensioactif

La concentration micellaire critique (CMC) est définie comme la concentration au-dessus de laquelle des micelles commencent à se former. Les CMC des Azo-tensioactifs ont été déterminées par tensiométrie (tensiomètre Kibron) à 21°C dans l'obscurité et sous irradiation UV. La CMC est estimée à 2.6 mM pour la forme *trans*-4Azo2TAB (dark) et à 8.2 mM pour la forme *cis*-4Azo2TAB (sous UV). Le 8Azo2TAB est plus hydrophobe, la CMC de la forme *trans* est de 0.29 mM tandis que celle de la forme *cis* est de 0.82 mM.

### III.1.1 Photoisomérisation

La photoisomérisation des Azo-tensioactifs a été étudiée par absorption UV-Vis. Les isomères *trans* présentent une bande d'adsorption maximale à 350 nm, tandis que les isomères *cis* sont caractérisés par deux bandes à 312 nm et 435 nm. Deux points isobestiques sont présents à 302 nm et à 426 nm. Les isomères *cis* peuvent rapidement revenir dans un état *trans* par irradiation avec de la lumière bleue. Ce processus est parfaitement réversible. La relaxation thermique a été également étudiée. Un temps caractéristique de l'ordre de 85 h pour 4Azo2TAB et de 195 h pour 8Azo2TAB ont été déterminés.

La fraction molaire en isomères *trans* ( $x_{trans}$ ) a été estimée par RMN pour les deux Azo-tensioactifs à 50 mM.  $x_{trans}$  est de 15 % dans l'état stationnaire sous irradiation UV et de 82 % sous irradiation par une lumière bleue.

### III.1.2 Étude de l'organisation structurale

L'organisation des solutions micellaires a été étudiée par SAXS et SANS (Figure 11). L'analyse des données a été réalisée en combinant le facteur de forme d'un ellipsoïde de révolution et le facteur de structure de colloïdes chargés dans un potentiel Coulombien. Le groupement Azo ayant une densité de longueur de diffusion (SLD) très différente de celle des groupements alkyles, une organisation « hétérogène » de type core-shell (avec deux SLD distinctes  $\rho_{shell}$  et  $\rho_{core}$ ) a également été testé pour décrire les agrégats micellaires.

Les isomères *trans*-4Azo2TAB forment des micelles ellipsoïdales oblates d'axes (majeur  $R_a$  et mineur  $R_b$ ) 35 Å et 20 Å. Sous irradiation UV (forme *cis*), le changement d'hydrophobie des chromophores et du paramètre d'empilement conduisent à un shift de la CMC et une réorganisation structurale importante :  $R_a = 23$  Å et  $R_b = 17$  Å. L'affinement à l'aide d'un modèle core-shell conduit à un rayon mineur du cœur proche de la longueur de la chaîne alkyle étendue. Cette observation tend à valider une description plutôt hétérogène des particules.

Les isomères *trans*-8Azo2TAB (chaîne alkyle deux fois plus plus longue), s'auto-assemblent en agrégats plus volumineux ( $R_a = 66$  Å,  $R_b = 24 - 28$  Å). La taille des agrégats diminue de 70% sous UV :  $R_a = 31$  Å,  $R_b = 22$  Å.

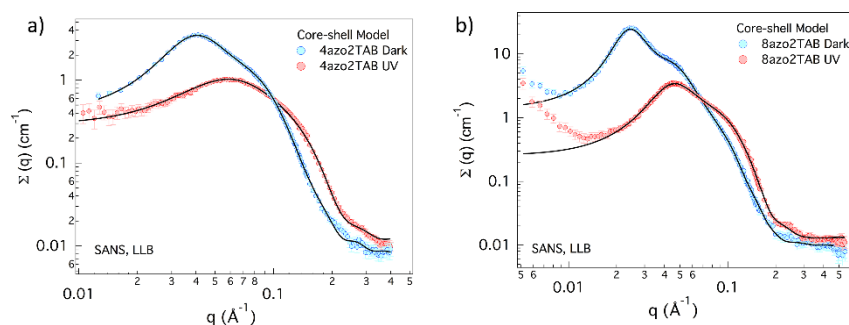


Figure 11 Courbes SANS. Fits avec un modèle core-shell pour a) 4Azo2TAB 50 mM ; b) 8Azo2TAB 50 mM

En conclusion, 4Azo2TAB et 8Azo2TAB s'auto-assemblent et forment des agrégats ellipsoïdaux oblates au-dessus de la CMC. Un modèle de type core-shell permet de mieux rendre compte de l'intensité aux grands  $q$  (notamment pour 8Azo2TAB) : le core est composé de queues alkyle hydrophobes, et le shell (toujours plus ou moins hydrophobe) contient le reste de la molécule (Schéma 2).

Avec une queue alkyle plus longue, le volume des micelles de *trans*-8Azo2TAB est 4.5 fois plus grand que celui de *trans*-4Azo2TAB. Sous irradiation UV, les micelles de 8Azo2TAB et 4Azo2TAB subissent une transition structurale radicale : si leur forme reste toujours ellipsoïdale, leurs volumes sont réduits d'un facteur 3 à 6.

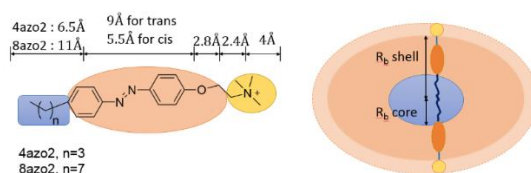


Schéma 2 Représentation schématique des agrégats micellaires sous forme core-shell.

### III.2 Complexes Azo-tensioactif/PE

Différents mélanges d'Azo-tensioactifs et de PEs de charge opposée ont été étudiés. Le poly(styrène sulfonate) (PSS), a été choisi comme PE modèle.

Le choix du système de référence Azo-tensioactif/PSS a été guidé par des mesures SAXS sur une série d'échantillons de rapports molaires  $r$  ( $r = [\text{Azo-tensioactif}]/[\text{PSS}] = 0.15 - 1.0$ ) et de concentrations  $c_{\text{PSS}}$  ( $c_{\text{PSS}} = 50 - 300$  mM) différents. Les complexes de 4Azo2TAB/PSS sont solubles tant que  $r < 0.6$  ( $r < 0.8$  pour 8Azo2TAB/PSS). Plus  $r$  est grand, plus les variations structurales sont importantes sous UV. Une concentration trop élevée peut ralentir la diffusion des particules et l'homogénéisation de la solution (plus grande viscosité). Le mélange **Azo-surfactant/PSS 50 mM/100 mM ( $r = 0.5$ )** est le meilleur compromis (diffusion rapide, absorption acceptable) et a constitué notre système de référence.

### III.2.1 Photoisomérisation

Deux types d'échantillons ont été étudiés : le système de référence de concentration C (4Azo2TAB/PSS, 50 mM/100 mM), et une solution très diluée (C/1000, 0.05 mM/0.1 mM). La cinétique de photoisomérisation a été étudiée par spectroscopie d'absorption.

Pour la solution très diluée (C/1000), l'état photo-stationnaire sous UV est atteint après environ 5 min d'irradiation et contient seulement 8% d'isomères *trans* (figure 12 a et c).

Pour le système de référence "concentré" C, l'état stationnaire est atteint après plus de 2 h d'irradiation et contient encore 39% d'isomère *trans* (figure 12 b et c). La différence entre la Figure 12a et la Figure 12b montre que la concentration est un facteur important qui impacte directement l'efficacité de l'irradiation et la cinétique d'isomérisation.

Sous irradiation bleue, l'isomérisation inverse *cis* → *trans* se produit, conduisant à un état stable composé de 89 % d'isomères *trans* et 11 % d'isomères *cis* pour le système de référence C.

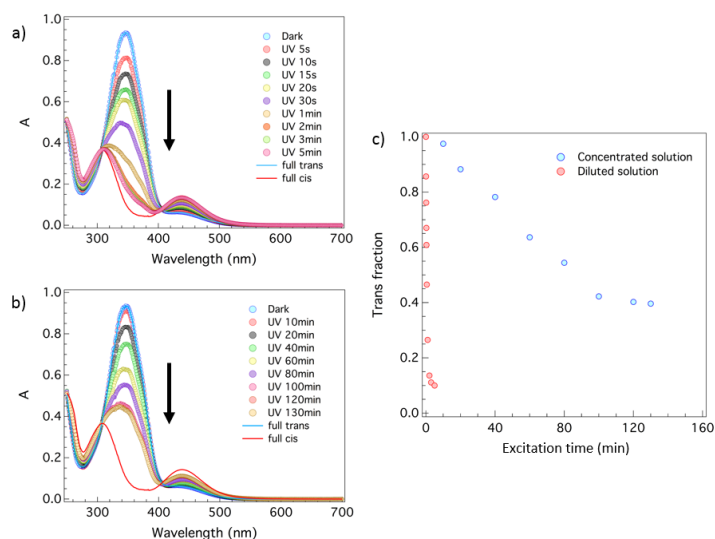


Figure 12 Variation du spectre UV-Vis pour 4Azo2TAB/PSS a) C/1000 ; 0.05 mM/0.1 mM ; b) C, 50 mM/100 mM, les mesures sont réalisées après prélèvement et dilution d'une partie de la solution irradiée. c) variation de  $X_{trans}$  en fonction du temps d'irradiation.

Plusieurs cycles d'irradiation UV ↔ bleu ont été réalisés pour les mélanges à C/1000 et montrent une parfaite réversibilité.

La photoisomérisation des complexes 8Azo2TAB/PSS n'a pas été étudiée de façon aussi poussée. Leur comportement reste néanmoins extrêmement similaire.

### III.2.2 Étude par RMN

La RMN a été utilisée pour confirmer l'association entre les Azo-tensioactifs et les chaînes de PSS (Figure 13a). Pour le mélange 4Azo2TAB/PSS-H, les pics des protons aliphatiques sont plus larges et légèrement décalés. Les pics aromatiques (6 - 8 ppm) se

superposent et sont difficiles à distinguer. Pour révéler uniquement la contribution de 4Azo2TAB, nous avons utilisé du PSS deutéré (PSS-D). Le spectre semble quasiment identique mais les larges pics à 7.41 ppm et 6.10 ppm disparaissent désormais (Figure 13b). Les quatre pics entre 6 ppm et 8 ppm (correspondant principalement aux protons aromatiques du 4Azo2TAB) sont très différents de ceux du 4Azo2TAB pur, ce qui indique que le tensioactif interagit fortement avec les polyions dans le mélange.

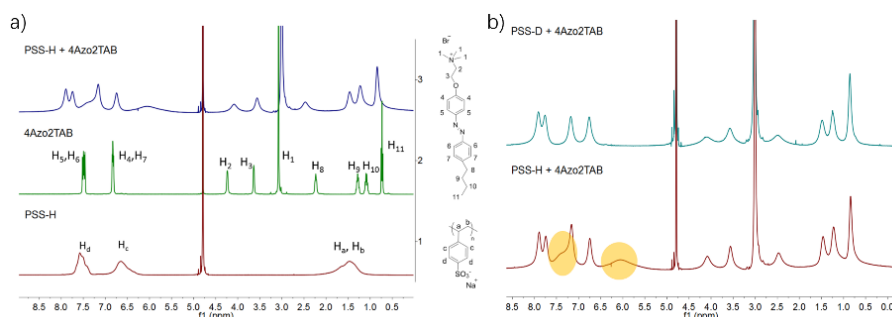


Figure 13  $^1\text{H}$  spectres RMN dans  $\text{D}_2\text{O}$  de complexes 4Azo2TAB/PSS.

La localisation probable du PSS dans les agrégats peut être déterminée en comparant le spectre de 4Azo2TAB pur à celui des mélanges 4Azo2TAB/PSS-D. La variation du déplacement chimique  $\Delta\delta$  ( $\Delta\delta = \bar{\delta}_{\text{complexes}} - \bar{\delta}_{\text{pure}}$ ) dépend de l'environnement local des protons dans les complexes, et donc, de l'organisation des agrégats.

La présence du cycle aromatique (styrène) induit généralement un blindage ( $\Delta\delta$  négatif). Les protons de la tête polaire  $\text{H}_1$  et de l'espaceur ( $\text{H}_2$ ,  $\text{H}_3$ ) sont légèrement blindés ( $\Delta\delta$  négatif), ce qui confirme une interaction importante entre le PSS et la zone polaire du tensioactif. La plus grande variation des déplacements  $\Delta\delta$  est observée dans la région aromatique. On peut ainsi supposer que les cycles benzéniques du PSS se trouvent à l'intérieur des agrégats micellaires à proximité des groupement Azo. Ceci est cohérent avec d'autres études sur des systèmes tensioactifs / PEs sans Azo.<sup>4,5</sup>

### III.2.3 Étude structurale par SANS

Les mesures SANS (dark, UV) ont été effectuées à une seule concentration  $C$  et dans différentes conditions de contraste. Ces expériences visent à déterminer les organisations respectives des différentes espèces (polyions et tensioactifs). Nous avons utilisé du PSS deutéré ( $\text{PSS}_\text{D}^-$ ) et des Azo-tensioactifs hydrogénés qui possèdent des SLD extrêmement différentes ( $8\text{Azo}2\text{TA}^+ : \rho_{8\text{Azo}2\text{TA}^+} = 1.00 \cdot 10^{10} \text{ cm}^{-2}$ ,  $4\text{Azo}2\text{TA}^+ : \rho_{4\text{Azo}2\text{TA}^+} = 1.30 \cdot 10^{10} \text{ cm}^{-2}$ ,  $\text{PSS}_\text{D}^- : \rho_{\text{PSS}_\text{D}^-} = 6.35 \cdot 10^{10} \text{ cm}^{-2}$ ). Il est ainsi possible de trouver un mélange  $\text{H}_2\text{O}/\text{D}_2\text{O}$  dont la SLD est identique à celle de l'Azo-tensioactif ( $\rho_{\text{solvant}} = \rho_{\text{azosurf}}$ ) afin de révéler la fonction de structure partielle des polyions ou de trouver un mélange  $\text{H}_2\text{O}/\text{D}_2\text{O}$  tel que  $\rho_{\text{solvant}} = \rho_{\text{PSS}}$  pour masquer la contribution des polyions (méthode de l'effacement de contraste).

Les mesures SANS dans différents mélanges  $\text{H}_2\text{O}/\text{D}_2\text{O}$  sont présentées sur la Figure 14. Dans  $\text{D}_2\text{O}$  ( $\phi_{\text{D}_2\text{O}} = 1$ ,  $\rho_{\text{D}_2\text{O}} = 6.38 \cdot 10^{10} \text{ cm}^{-2}$ ) seuls les tensioactifs sont visibles. Au

contraire, dans un mélange H<sub>2</sub>O/D<sub>2</sub>O avec  $\phi_{D_2O} = 0.267$  ( $\rho_{\text{solvant}} = 1.30 \cdot 10^{10} \text{ cm}^{-2}$ ), seuls les polyions sont visibles (ce mélange H<sub>2</sub>O/D<sub>2</sub>O ne correspond pas parfaitement à la SLD de 8Azo2TA<sup>-</sup>, *i.e.*  $1.00 \cdot 10^{10} \text{ cm}^{-2}$ , il n'y aura cependant aucune influence sur la modélisation des données). Une condition de contraste intermédiaire avec  $\phi_{D_2O} = 0.475$  ( $\rho_{\text{solvant}} = 2.74 \cdot 10^{10} \text{ cm}^{-2}$ ) a également été utilisée. Dans cette situation, chaque fonction de structure partielle contribue à l'intensité diffusée.

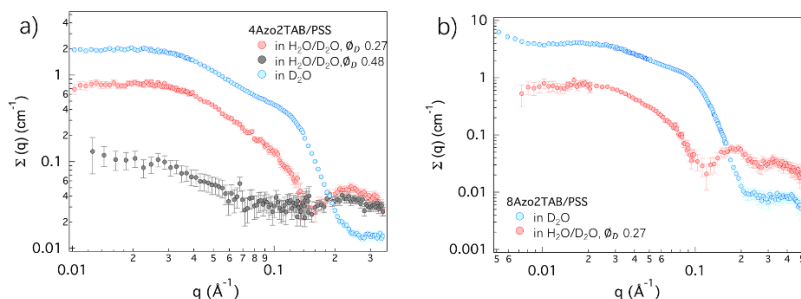


Figure 14 Mesures SANS dans différents mélanges H<sub>2</sub>O/D<sub>2</sub>O pour a) 4Azo2TAB/PSS; b) 8Azo2TAB/PSS.

Pour  $q \leq 0.03 \text{ \AA}^{-1}$ , les courbes de diffusion montrent toutes un plateau similaire. Dans cette plage de vecteurs de diffusion, nous sommes sensibles aux corrélations intermoléculaires à longues distances. Pour  $q > 0.03 \text{ \AA}^{-1}$ , on est plus sensible au facteur de formes des objets en solution. Les profils de diffusion varient avec le contraste révélant une organisation structurale hétérogène à l'échelle locale. La présence d'une oscillation bien définie autour de  $0.25 \text{ \AA}^{-1}$  (dans H<sub>2</sub>O/D<sub>2</sub>O,  $\phi_{D_2O} = 0.267$  où l'on sonde la structure des chaînes) indique une réorganisation globale des polyions et la formation d'agrégats nanométrique relativement bien définis. Les solutions de NaPSS « pur » ne présentent jamais ce comportement.

La fonction de structure partielle de 4Azo2TAB (dans D<sub>2</sub>O) est assez proche de ce que l'on observe aux grands angles sur des simples solutions micellaires. Elle est caractéristique de particules globulaires. Une autre particularité importante est la présence d'un épaulement entre  $0.03$  et  $0.1 \text{ \AA}^{-1}$ . Cette signature originale est liée aux corrélations à courte portée entre les particules. Celles-ci ne sont donc pas uniformément réparties dans la solution (comme de simples micelles isolées) et ont tendance à s'assembler pour former des objets de plus grandes taille (agrégats d'agrégats).

Toutes ces remarques suggèrent une image où les polyions s'enroulent autour d'agrégats globulaires et les relient les uns aux autres. Les complexes semblent donc s'organiser en collier de perles. Plus précisément, les polyions et les tensioactifs forment les petits objets globulaires, les tensioactifs sont au cœur de l'agrégat tandis que les polyions se trouvent plutôt en surface. Comme suggéré par les mesures RMN, une partie de la chaîne peut également pénétrer dans l'agrégat et interagir fortement avec les groupements Azo.

Pour l'analyse des données, nous supposons que l'intensité diffusée est dominée par le facteur de forme du collier de perles  $P(q)$  ( $S(q) = 1$ ) aux grands  $q$  ( $q > q_{\min}$  avec  $q_{\min} = 0.05 \text{ \AA}^{-1}$  pour 4Azo2TAB/PSS et  $0.04 \text{ \AA}^{-1}$  pour 8Azo2TAB/PSS). Le facteur de forme d'une telle organisation a été décrit dans le cadre des PEs hydrophobes.<sup>6</sup> Dans notre situation, nous utilisons une version simplifiée et négligeons la contribution des segments de polyions qui relient les perles (Schéma 3). Les perles sont quant à elles modélisées par un assemblage core-shell ellipsoïdal.

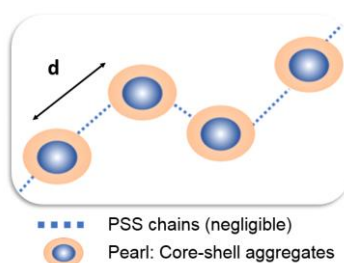


Schéma 3 Représentation schématique du modèle collier de perles.

Les fits reproduisent parfaitement les données pour les deux conditions de contraste (Figure 15), en absence de lumière (dark) et sous irradiation UV. Le rayon mineur du cœur est systématiquement proche de la longueur étirée des chaînes alkyles des tensioactifs : comme les simples solutions micellaires, les groupements alkyles forment le cœur des agrégats. Pour les complexes 4Azo2TAB/PSS, les rayons du shell (majeur, mineur) sont de 26 et 18 Å. Les complexes 8Azo2TAB/PSS forment des agrégats plus volumineux avec des rayons de 34 et 20 Å.

L'épaulement observé dans les fonctions de structure des tensioactifs (entre 0.03 et 0.1 Å<sup>-1</sup>, Figure 15a et Figure 15c) et lié aux corrélations inter-perles est parfaitement reproduit. Il nous permet de déterminer une valeur précise de la distance moyenne entre perles. Cette distance est quasiment le double du rayon du shell (majeur) : les perles sont très proches les unes des autres.

Le modèle permet également de reproduire l'oscillation observée autour de 0.2 – 0.3 Å<sup>-1</sup> sur la fonction de structure des polyions. Celle-ci provient finalement de l'organisation des chaînes de PSS dans la couche (shell) autour du cœur micellaire (Figure 15b et Figure 15d),.

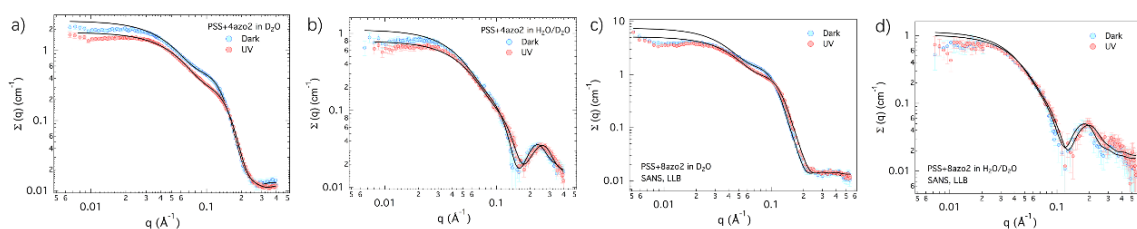


Figure 15 Mesures SANS pour 4Azo2TAB/PSS a) dans D<sub>2</sub>O et b) dans H<sub>2</sub>O/D<sub>2</sub>O,  $\phi_{D_2O} = 0.267$ ; Mesures SANS pour 8Azo2TAB/PSS c) dans D<sub>2</sub>O et d) dans H<sub>2</sub>O/D<sub>2</sub>O,  $\phi_{D_2O} = 0.267$ .

Les paramètres géométriques déterminés pour les deux conditions de contraste sont très similaires. Les polyions ne décorent pas seulement les micelles préexistantes, mais sont intimement mixés avec les groupements Azo au niveau du shell (co-micellisation). La taille globale de l'agrégat est plus petite que celle des micelles de tensioactifs purs (à concentration égale) malgré l'incorporation des polyions.

Sous irradiation UV, l'oscillation caractéristique dans la fonction de structure des polyions est déplacée vers les grands  $q$  : la taille de l'agrégat est réduite (Figure 15b et Figure 15d). Ce phénomène est également visible sur la fonction de structure des tensioactifs (D<sub>2</sub>O) et plus spécifiquement, sur l'épaule associée aux corrélations inter-perles. Le déplacement aux grands  $q$  sous UV indique une diminution de la distance inter-perles.

Le volume des perles sous UV est réduit de 29%. Cette variation est cependant beaucoup plus faible que celle observée pour les micelles pures (69% pour les micelles 4Azo2TAB et 83% pour les micelles 8Azo2TAB).

### III.2.4 Étude structurale par SAXS

L'analyse SAXS est similaire à celle réalisée par SANS. Le modèle reproduit relativement bien les données (Figure 16). Les rayons du shell sont toutefois plus importants que ceux déterminés par SANS (de quelques Å : rayons majeur et mineur 31 Å - 22 Å pour 4Azo2TAB/PSS et 35 Å - 24 Å pour 8Azo2TAB/PSS). Cet effet pourrait être dû à la présence d'une couche de contre-ions condensée toujours plus visible par diffusion des rayons-X que par diffusion de neutrons.

Sous UV, des modifications importantes sont observées aux grands  $q$  indiquant un réarrangement structural et une réduction de la taille des perles (24 % pour 4Azo2TAB/PSS et 26% pour 8Azo2TAB/PSS). Cette variation est comparable à celle observée par diffusion de neutron et est parfaitement réversible par simple irradiation de lumière bleue.

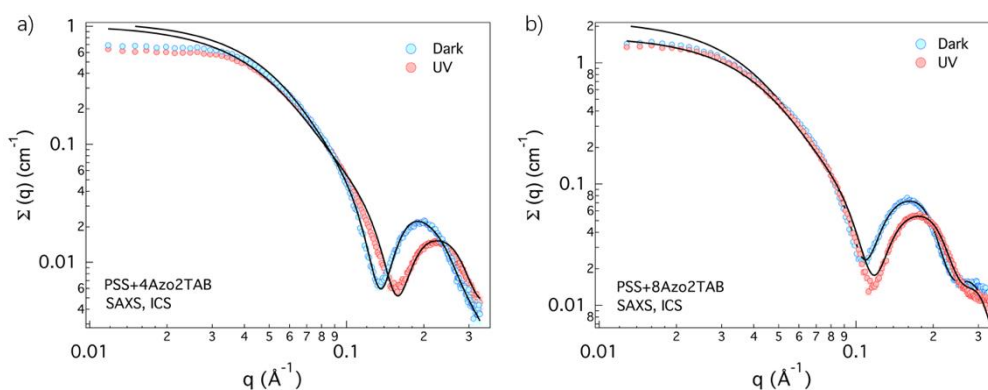


Figure 16 Mesures SAXS pour a) 4Azo2TAB/PSS ; b) 8Azo2TAB/PSS.

### III.2.5 Étude par microscopie électronique (Cryo-TEM)

Des mesures de Cryo-TEM ont été effectuées sur les complexes Azo-surfactant/PSS (en absence de lumière) à une concentration de C/10 (Figure 17). Dans ces expériences seuls les rayons externes des perles (rayons du shell) sont potentiellement observables. La structure interne des agrégats n'est pas accessible.

Pour 4Azo2TAB/PSS (Figure 17a), les objets sont très difficiles à observer. Tout au plus, on peut remarquer la présence de petits agrégats qui ne sont pas répartis de manière homogène dans le film et ont tendance à s'assembler entre eux (cercle de la Figure 17a).

Pour 8Azo2TAB/PSS (Figure 17b), des petites particules apparaissent clairement. Elles ne sont pas réparties de façon homogène et forment des assemblages en colliers de perles. Cette observation valide définitivement notre approche. La taille des perles ( $\approx 7$  nm) coïncide également avec les mesures par diffusion de rayonnement. Le nombre exact de perles est plus compliqué à déterminer et peut également varier d'un collier à l'autre. Cet exemple met en évidence la complémentarité entre la microscopie électronique et la diffusion pour révéler l'organisation structurale dans les systèmes complexes.

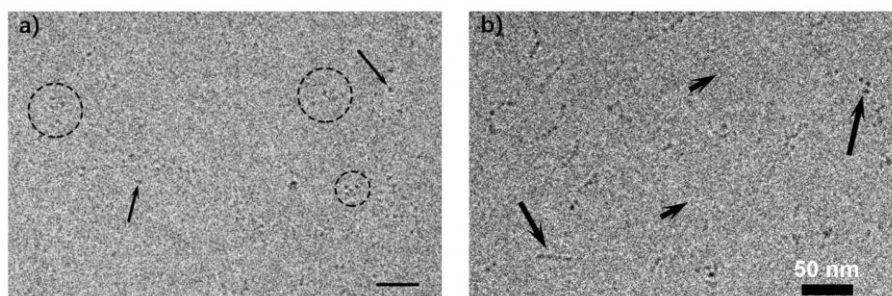


Figure 17 Images de Cryo-TEM mesurées à C/10 pour a) 4Azo2TAB/PSS, Flèche : particule isolée. Cercles : petits agrégats de particules (agrégat d'agrégats) ; b) 8Azo2TAB/PSS, Flèche courte : région sans agrégat micellaire. Flèche longue : région où on observe une densité élevée d'agrégats. Les micelles ne sont pas réparties de manière homogène dans le film. L'organisation en collier de perles est clairement visible.

## Chapter IV. Auto-assemblage d'Azo-tensioactifs et co-tensioactifs

Cette dernière partie concerne des systèmes auto-assemblés photostimulables formés à partir d'Azo-tensioactifs photosensibles et de co-tensioactifs. Nous nous sommes inspirés d'un travail issu de la littérature sur les mélanges de bromure de cetyltriméthylammonium (CTAB) et de salicylate de sodium (NaSal, co-micellisation) conduisant à la formation micelles allongées (« wormlike micelles ») et à l'apparition d'un gel. Nous avons constaté que 8Azo2TAB (de taille similaire à CTAB) formait des gels en présence de NaSal ou de benzenesulfonate de sodium (NaBenSulf) (Schéma 4). Le

mélange Azo-tensioactif/co-tensioactif de composition 75 mM/62.5 mM (noté C) a été choisi comme système de référence.

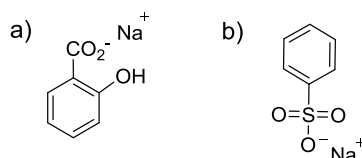


Schéma 4 a) structure chimique de salicylate de sodium (NaSal); b) structure chimique de benzenesulfonate de sodium (NaBenSulf)

## IV.1 Auto-assemblage du 8Azo2TAB/salicylate de sodium (NaSal)

Sous irradiation UV, la viscosité de ces systèmes diminue fortement (solution fluide, Figure 18). Nous avons cherché l'origine de ce phénomène en sondant leur organisation structurale.

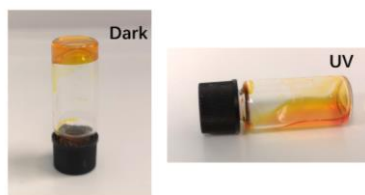


Figure 18 Photos du mélange 8Azo2TAB/NaSal (C, 75 mM/62.5 mM) dans l'obscurité (dark, gel) et et sous irradiation UV (fluide).

### IV.1.1 Photoisomérisation

#### IV.1.1.1 Absorption UV-Vis

Le mélange *trans*-8Azo2TAB/NaSal (concentration C/2000) présente une bande d'absorption à 351 nm et une bande plus faible à environ 440 nm associées à la molécule de 8Azo2TAB. L'épaulement à 305 nm correspond à une bande d'absorption de NaSal. Sous irradiation UV, la bande d'absorption à 440 nm (caractéristique de la molécule *cis*-8Azo2TAB) augmente tandis que la bande d'absorption forte à 351 nm est décalée vers les petites longueurs d'ondes et se superpose à celle du NaSal (vers 300 nm). La photoconversion est totalement réversible lors de cycles d'irradiation UV/bleue.

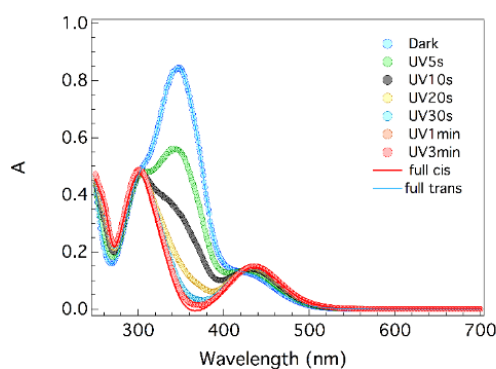


Figure 19 Variation du spectre d'absorption UV-Vis du mélange 8Azo2TAB/NaSal sous UV pour différents temps d'irradiation.

#### IV.1.1.2 RMN

Comme le montre la Figure 20a, la solution de NaSal présente des pics étroits bien définis. La solution de 8Azo2TAB (dont la concentration est supérieure à la CMC) présente des pics plus larges en raison de la formation de micelles. Les pics du mélange 8Azo2TAB/NaSal (C, 75 mM/62.5 mM) montre également des pics assez larges (courbe bleue sur la Figure 20a). Les pics  $H_2$ ,  $H_3$  de l'espaceur  $R_2$  de 8Azo2TAB (4.23 ppm et 3.60 ppm disparaissent) indiquant la formation d'agrégats de taille beaucoup plus importante. En général, les cycles aromatiques entraînent un blindage pour les molécules adjacentes. Le pic intense à 3.1 ppm (associé à  $H_1$ ) est déplacé à 2.9 ppm indiquant que les molécules de NaSal sont proches de la tête polaire de 8Azo2TAB. Au contraire, les pics associés à la queue hydrophobe (environ 0.8 - 1.5 ppm) ne sont pas altérés : leur environnement n'est pas influencé par l'ajout de NaSal. Toutes ces observations suggèrent que les molécules de NaSal sont plutôt localisées dans la région hydrophile des agrégats de 8Azo2TAB.

Un échantillon moins concentré (C/4, 18.75 mM/15.62 mM) a également été étudié (Figure 20b). La courbe sous irradiation UV (Figure 20b, courbe verte) montre la séparation de certains pics liée à la coexistence des isomères *trans* et *cis*. En particulier, le pic intense associé à  $H_1$  (situé initialement à 2.82 ppm) se scinde en deux contributions (3.01 ppm pour les isomères *trans* et 2.93 ppm pour les isomères *cis*) permettant la détermination du rapport *trans/cis* dans la solution. À l'équilibre sous UV, le rapport *trans/cis* est estimé à 26:74. Sous irradiation de lumière bleue, le rapport *trans/cis* revient à 81:19.

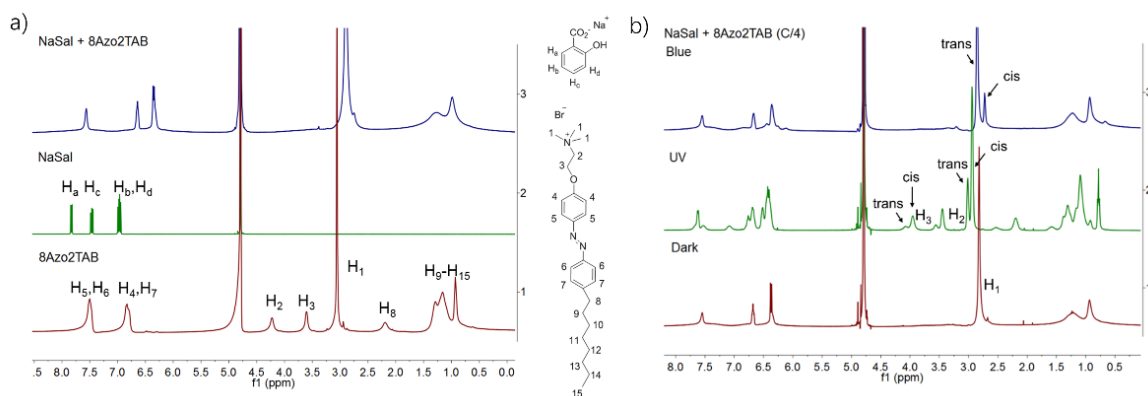


Figure 20  $^1\text{H}$  spectres RMN dans  $\text{D}_2\text{O}$  pour a) 8Azo2TAB, NaSal et 8Azo2TAB/NaSal (C).  
 b) 8Azo2TAB/NaSal (C/4), dark, irradiation UV, irradiation bleue.

### IV.1.2 Études structurales

Les propriétés rhéologiques macroscopiques dépendent de la microstructure du système. La diffusion du rayonnement ainsi que la microscopie électronique sont des techniques complémentaires qui permettent de sonder l'organisation structurale à différentes échelles spatiales.

### IV.1.3 Mesures Cryo-TEM

Des mesures de Cryo-TEM ont été effectuées sur 8Azo2TAB/NaSal C/4 (Figure 21, Dark et UV). Les images montrent clairement deux organisations distinctes. En absence de lumière (dark) nous observons des particules allongées de diamètre 5 - 7 nm et de plusieurs micromètres de longueur. Après 4 heures d'irradiation UV, on observe majoritairement des petits objets globulaires de diamètre environ 4 nm ainsi que des particules allongées (diamètre environ 4 nm, longueurs comprises entre 10 et 30 nm). Cette transition morphologique explique la variation des propriétés rhéologiques (gel  $\rightarrow$  fluide). Afin d'obtenir une meilleure description de l'organisation structurale, ces observations ont été combinées avec des mesures de diffusion aux petits angles.

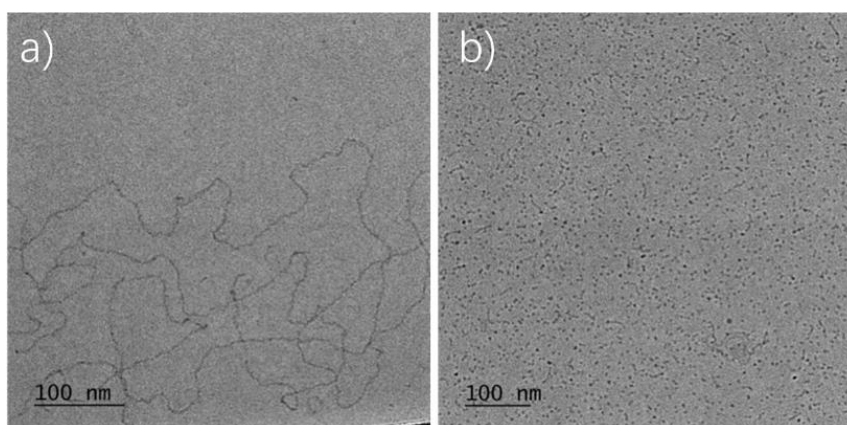


Figure 21 Image Cryo-TEM de 8Azo2TAB/NaSal (C/4) a) Dark et b) UV.

#### IV.1.4 SANS

Sur la Figure 22, nous présentons les mesures SANS réalisées à la concentration C/4. En absence de lumière (dark), la longueur de persistance des micelles allongées (évaluée sur les images de Cryo-TEM) est supérieure aux distances caractéristiques observables par diffusion de neutrons : on sonde uniquement la structure des « segments » et leur terme de section. Aux faibles vecteurs de diffusion, l'intensité varie quasiment en  $q^{-1}$ . Ce comportement est caractéristique de particules en bâtonnet et est cohérent avec les observations de Cryo-TEM. On note cependant une petite contribution du facteur de structure dans cette région angulaire. Dans le domaine  $q > 0.03 \text{ \AA}^{-1}$ , nous sommes sensibles à la section des particules. L'absence d'oscillation caractéristique (ou de minimum) peut être liée à un problème de polydispersité ou à la présence d'une section elliptique. Un modèle cylindrique de section elliptique nous a semblé plus approprié et a été utilisé pour affiner les données.

Sous irradiation UV, nous constatons une forte diminution de l'intensité aux petits  $q$  indiquant une modification importante de la forme des particules. Curieusement, nous ne trouvons pas de régime de Guinier (plateau) aux petits *angles*. Ceci est lié à la forte polydispersité des objets suggérée par Cryo-TEM. La modélisation est donc assez compliquée. Les petits objets globulaires étant plus abondants, nous avons utilisé un modèle d'ellipsoïde de révolution homogène et restreint le domaine en  $q$  affiné. Le rayon majeur (suivant l'axe de révolution) a été fixé de façon arbitraire.

Les SLD des particules sont quasiment identiques aux valeurs théoriques attendues. Comme la fraction volumique a été fixée à sa valeur nominale, nous concluons que les deux composants (surfactants et co-surfactants) sont intégrés dans les agrégats micellaires. Les rayons majeur et mineur de la section (dark) sont de 33 Å et 20 Å. Sous UV, le rayon mineur de l'agrégat ellipsoïdal est de 21 Å. Les rayons mineurs des agrégats sont systématiquement plus faibles que la longueur étendue de la molécule de 8Azo2TAB ( $\approx 30 \text{ \AA}$ ) mais aussi, que ceux observés à 50 mM dans les solutions micellaires. La présence du NaSal modifie donc profondément l'organisation locale du tensioactif par rapport à une micelle classique.

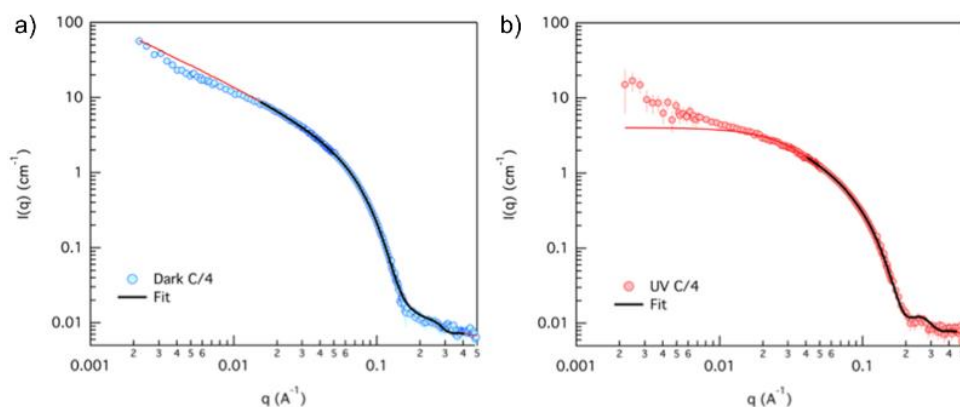


Figure 22 Mesures SANS et fits. Solutions de 8azo2TAB/NaSal (C/4) a) dark (modèle core-shell cylindre avec section ellipsoïdale) et b) UV (ellipsoïde prolatae).

#### IV.1.5 SAXS

Nous avons complété cette étude par des mesures SAXS (Figure 23). L'analyse est similaire à celle effectuée par diffusion de neutrons. La seule différence est l'introduction d'une organisation de type core-shell. En absence de lumière (dark) la section des agrégats cylindriques est identique à celle déterminée par SANS. Sous UV, une réorganisation de l'autoassemblage est observée. Les micelles de 8Azo2TAB/NaSal sous UV peuvent être modélisées par un ellipsoïde prolata d'axe mineur 25 Å.

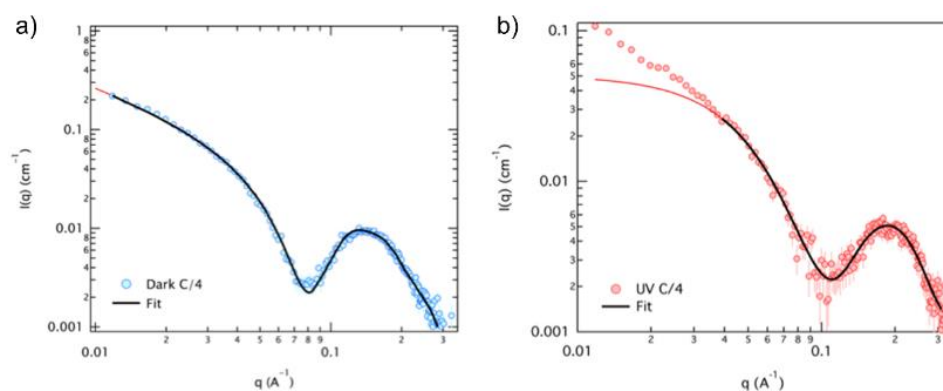


Figure 23 Mesures SAXS et fit. Solutions de 8azo2TAB/NaSal C/4 a) dark (modèle cylindrique core-shell avec section ellipsoïdale) et b) UV (ellipsoïde prolatae).

## IV.2 Auto-assemblage de 8Azo2TAB/sodium benzenesulfonate (NaBenSulf)

La structure chimique de NaBenSulf est très proche de celle des monomères PSS utilisés dans les complexes tensioactif/PE. Il conduit néanmoins à un comportement différent lorsqu'il est mélangé avec des Azo-tensioactifs. Le système 8Azo2TAB/NaBenSulf (C, 75 mM/62.5 mM) forme par exemple un gel en absence de lumière (Figure 24). Comme

avec NaSal, on peut supposer que la présence de micelles allongées est à l'origine de ce phénomène. Les différences chimiques entre NaSal et NaBenSulf peuvent néanmoins entraîner une morphologie micellaire différente que nous avons essayé d'étudier.



Figure 24 Photos du mélange 8Azo2TAB/NaBenSulf (C, 75 mM/62.5 mM) dark (gel) et sous UV (fluide).

#### IV.2.1 Photoisomérisation par RMN

Le mélange 8Azo2TAB/NaBenSulf C/4 (18.75 mM/15.62 mM) a été analysé par  $^1\text{H}$  RMN (Figure 25a). Le mélange présente des pics plus larges que ceux observés dans les spectres des composants individuels. On observe clairement que les protons de la région hydrophile de 8Azo2TAB ( $\text{H}_1$ ,  $\text{H}_2$ ,  $\text{H}_3$ ) sont blindés. En revanche, les protons de la région hydrophobe ( $\text{H}_8$  -  $\text{H}_{15}$ ) ne sont pas influencés par l'ajout de NaBenSulf. On peut donc une fois de plus supposer que les molécules de NaBenSulf sont intercalées entre les têtes hydrophiles et participent à la formation des micelles. Ceci sera également prouvé par diffusion aux petits angles.

Pour l'espaceur  $\text{C}_2\text{H}_4$  ( $\text{H}_2$ ,  $\text{H}_3$ ), les pics attribués aux espèces *trans* et *cis* sous irradiation UV permettent de déterminer un rapport *trans/cis* de 13:87 dans l'état stationnaire. Inversement, sous irradiation par de la lumière bleue (isomérisation de *cis*  $\rightarrow$  *trans*) le mélange retrouve sa viscosité initiale, le rapport *trans/cis* passe à 84:16.

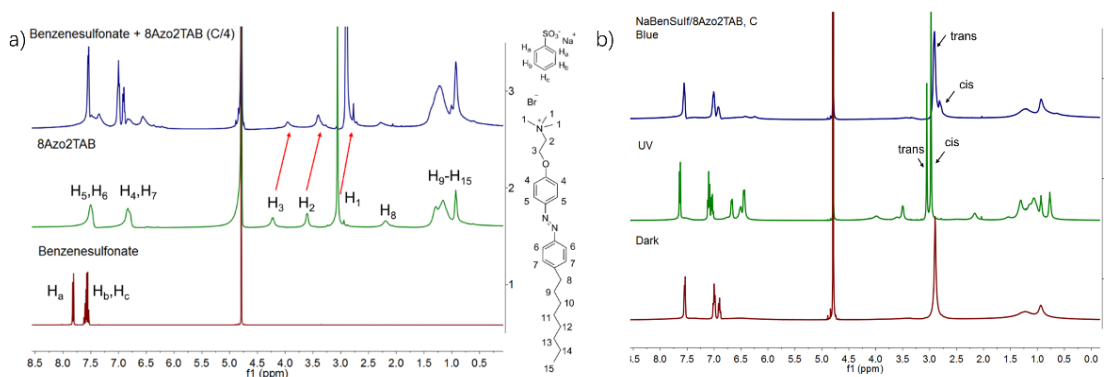


Figure 25 Spectres  $^1\text{H}$  RMN dans  $\text{D}_2\text{O}$  pour a) NaBenSulf, 8Azo2TAB, 8Azo2TAB/NaBenSulf C/4 (18.75 mM/15.62 mM) ; b) 8Azo2TAB/ NaBenSulf (C), dark, irradiation UV, irradiation bleue

#### IV.2.2 Études structurales par SANS et SAXS

Seule la concentration C/4 a été mesurée par SANS (Figure 26) et SAXS (Figure 27).

Dans l'obscurité, l'intensité varie quasiment en  $q^{-1}$  aux plus faibles valeurs de  $q$ . Sous irradiation UV, on distingue désormais un régime de Guinier (la polydispersité observée avec 8Azo2TAB/NaSal semble avoir disparu). La présence d'un facteur de structure reste toujours un peu visible en dessous de  $q = 0.03 \text{ \AA}^{-1}$ .

Nous avons modélisé l'intensité avec un cylindre infini de section elliptique pour les mesures en absence de lumière (dark) et un ellipsoïde prolate pour les mesures sous UV (Figure 26). Nous avons considéré des particules homogènes pour la diffusion de neutrons et une organisation core-shell pour la diffusion de rayons-X (Figure 27).

À l'état dark (micelles allongées), les mesures SANS et SAXS conduisent à des valeurs très similaires pour le terme de section (rayons majeur et mineur du shell par SANS : 33 et 20 Å ; rayons majeur et mineur du shell par SAXS : 37 et 23 Å). La différence de 3 - 4 Å pourrait provenir de la présence d'une couche de contre-ions plus visible par SAXS. Sous UV (micelles globulaires), les mesures SANS et SAXS donnent des tailles comparables (rayons majeur et mineur de l'ellipsoïde par SANS : 40 et 21 Å ; rayon majeur et mineur de l'ellipsoïde par SAXS : 39 et 24 Å). La différence est négligeable. Le cœur des agrégats est constitué des chaînes alkyles du 8Azo2TAB. La couche (shell) est quant à elle constituée des groupements Azo et des groupements hydrophyles de l'Azo-tensioactifs mais aussi, des molécules de NaBenSulf comme suggéré par la RMN.

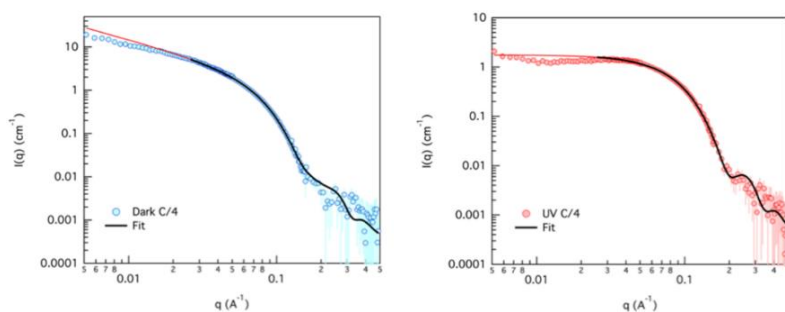


Figure 26 Mesures SANS et fits (dark et UV). Solutions de 8Azo2TAB/NaBenSulf C/4 (18.75 mM/15.62 mM)

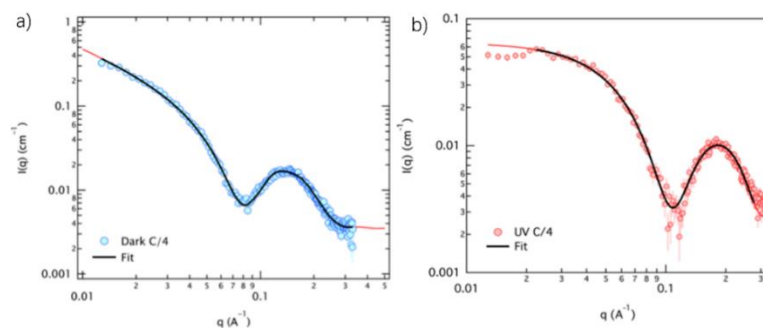


Figure 27 Mesures SAXS et fits (dark et UV). Solution de 8Azo2TAB/NaBenSulf C/4 (18.75 mM/15.62 mM)

## Chapter V. Conclusion

Cette thèse vise à étudier des systèmes photostimulables modèles en solution aqueuse à base de PEs et de tensioactifs. Cette photosensibilité est liée à la présence d'un chromophore azobenzène qui subit une isomérisation *trans* → *cis* sous irradiation UV. Nous nous intéressons plus particulièrement au processus de photoconversion de ces systèmes, à leur organisation structurale et aux transformations induites sous irradiation. Trois systèmes ont été étudiés par spectroscopie d'absorption UV-Visible, RMN, diffusion aux petits angles et Cryo-TEM.

### ➤ **Polyacrylates de sodium modifiés par des groupements Azo**

Le greffage de groupements Azo sur les chaînes latérales des polyacrylates de sodium augmente l'hydrophobicité des PEs et conduit à la formation d'agrégats photosensibles. La structure de ces agrégats dépend de la longueur du polymère, de la fraction en Azo ainsi que de la concentration.

Nous constatons que des agrégats compacts de type core-shell sont formés pour les longues chaînes ((PAA-Azo<sub>0.11</sub>)<sub>738</sub>RAFT). Le cœur dense est constitué des groupements Azo tandis que le shell est composée de segments de polyions. Un nombre très limité de chaînes composent les agrégats. Sous irradiation UV, ces agrégats sont partiellement désassemblés et forment des particules plus petites. Il pourrait être intéressant de diminuer la teneur en Azo sur les longues chaînes : en modifiant la répulsion électrostatique entre les segments de polyions, on pourrait imaginer pouvoir casser complètement le cœur hydrophobe sous UV.

Pour les chaînes courtes contenant 11 % d'Azo, l'organisation structurale (et l'association macromoléculaire) varie désormais avec la concentration. Les chaînes courtes contenant 15 % d'Azo présentent une organisation similaire, mais le cœur est plus compact. Dans ces systèmes, il est possible de trouver une plage de concentrations dans laquelle des agrégats peuvent s'assembler et se désassembler par simple stimulus lumineux. Ce régime pourrait être intéressant pour certaines applications telles que le transport de composés actifs. Le cœur hydrophobe pouvant encapsuler des molécules et les libérer sous irradiation UV.

### ➤ **Complexes Azo-tensioactif/PSS**

Les Azo-tensioactifs 8Azo2TAB et 4Azo2TAB purs forment des micelles photosensibles en solutions aqueuses. Ces agrégats peuvent être décrits par un assemblage core-shell ellipsoïdal dans laquelle le cœur contient les queues alkyles

hydrophobes et le shell est composé des groupements Azo et des têtes polaires. Sous irradiation, la photoconversion *trans* → *cis* du groupement Azo modifie le paramètre d'empilement critique et l'hydrophobie du tensioactif : une diminution significative de la taille des micelles est observée.

Ces Azo-tensioactifs interagissent fortement avec des PEs de charge opposée comme le PSS. Les mesures RMN confirment la forte interaction entre les cycles aromatiques du polyion et le shell des micelles (tête polaire, unité Azo) : les polyions participent à la micellisation. L'organisation structurale des Azo-tensioactifs et du PSS dans les complexes peut être étudiée séparément par SANS. Nous montrons l'existence d'agrégats globulaires (perles) composés à la fois de tensioactifs et de polyions. Ces agrégats ont une organisation core-shell : le core contient les chaînes alkyles des tensioactifs tandis que le shell est composée des groupements Azo, des têtes polaires ainsi que des segments de polyions. Ces agrégats ne sont pas uniformément repartis dans la solution et s'organisent en collier de perles. Cette structure est confirmée par les images de Cryo-TEM. Sous irradiation, les modifications structurales sont modestes. La taille des perles n'est réduite (de manière réversible) que d'environ 30%.

Dans cette étude, nous démontrons définitivement l'existence d'une organisation en collier de perles dans les complexes Azo-tensioactifs/PSS et plus généralement, dans les complexes tensioactifs/PEs.

#### ➤ **Mélanges Azo-tensioactifs/co-tensioactifs**

L'ajout de NaSal ou de NaBenSulf aux Azo-tensioactifs conduit à la formation de micelles allongées et à la création d'un gel. Une transition réversible gel ↔ fluide est observée sous irradiation alternative UV/bleu.

Les études RMN montrent que les anions aromatiques sont intercalés dans la couche hydrophile des micelles. Cette hypothèse est validée par l'étude SANS et SAXS. Les micelles ont été modélisées par un cylindre de section elliptique (micelles allongées) en absence de lumière et par un ellipsoïde prolata sous UV. Une organisation de type core-shell est mise en évidence. Le core est constitué des queue alkyles (C<sub>8</sub>H<sub>17</sub>) tandis que le shell contient principalement les groupements Azo, l'espaceur (C<sub>2</sub>H<sub>4</sub>) et la tête hydrophile du tensioactif, mais aussi les anions aromatiques du co-tensioactif. L'irradiation UV déstabilise les micelles allongées et conduit à la formation de micelles ellipsoïdales. La diffusion aux petits angles donnent une image précise des modifications structurales à l'échelle locale. La transformation *trans* ↔ *cis* des isomères au niveau moléculaire se propage à l'échelle nanométrique (micelles allongées ↔ micelles ellipsoïdales) jusqu'à l'échelle macroscopique pour aboutir à une transition réversible gel ↔ fluide. Nous avons ici un bon exemple de propriété macroscopique qui peut être modifiée par une simple

irradiation UV. Des études rhéologiques sur ces systèmes pourraient certainement révéler des effets intéressants, notamment en ce qui concerne la concentration et la nature du co-surfactant.

## Références

- (1) Dingenouts, N.; Seelenmeyer, S.; Deike, I.; Rosenfeldt, S.; Ballauff, M.; Lindner, P.; Narayanan, T. Analysis of Thermosensitive Core-Shell Colloids by Small-Angle Neutron Scattering Including Contrast Variation. *Phys. Chem. Chem. Phys. - PHYS CHEM CHEM PHYS* **2001**, *3*, 1169–1174.
- (2) Hayter, J. B.; Penfold, J. Self-Consistent Structural and Dynamic Study of Concentrated Micelle Solutions. *J. Chem. Soc. Faraday Trans. 1 Phys. Chem. Condens. Phases* **1981**, *77* (8), 1851–1863.
- (3) Hansen, J.-P.; Hayter, J. B. A Rescaled MSA Structure Factor for Dilute Charged Colloidal Dispersions. *Mol. Phys.* **1982**, *46* (3), 651–656.
- (4) Gao, Z.; Kwak, J. C. T.; Wasylshen, R. E. An NMR Study of the Binding between Polyelectrolytes and Surfactants in Aqueous Solution. *J. Colloid Interface Sci.* **1988**, *126* (1), 371–376.
- (5) Effing, J. J.; McLennan, I. J.; van Os, N. M.; Kwak, J. C. T. <sup>1</sup>H NMR Investigations of the Interactions between Anionic Surfactants and Hydrophobically Modified Poly(Acrylamide)s. *J. Phys. Chem.* **1994**, *98* (47), 12397–12402.
- (6) Schweins, R.; Huber, K. Particle Scattering Factor of Pearl Necklace Chains. *Macromol. Symp.* **2004**, *211* (1), 25–42.



## Summary

General Introduction .....	I
Chapter I. Polyelectrolytes in aqueous solution .....	1
I.1 Basics of polyelectrolytes .....	2
I.1.1 Classification of polyelectrolytes .....	2
I.1.2 Basic energy and length scales .....	3
I.1.3 Electric screening: influence of the ionic strength .....	4
I.1.4 Persistence length.....	5
I.2 Structural organization of hydrophilic polyelectrolytes in aqueous solution.....	5
I.2.1 Isolated polyelectrolytes chains .....	5
I.2.2 Chains in semidilute regime.....	8
I.3 Hydrophobic Polyelectrolytes.....	9
I.3.1 Definition and examples.....	9
I.3.2 Conformation of hydrophobic polyelectrolyte .....	11
I.4 Surfactant/Polyelectrolytes complexes .....	13
I.4.1 Formation of complexes.....	14
I.4.2 Structural organization of the complexes .....	16
Chapter II. The state of the art of “smart” photosensitive systems in aqueous solution .....	23
II.1 Azobenzene.....	23
II.1.1 Overview of azobenzene properties .....	23
II.1.2 Isomerization mechanism .....	25
II.1.3 Effect of the substitution on azobenzene isomerization.....	25
II.1.4 Photostationary state .....	26
II.2 The state of the art of azobenzene based materials .....	28
II.2.1 Amphiphilic photoresponsive polymers .....	28
II.2.2 Self-assembly of photoresponsive surfactants in aqueous solution ...	33
II.2.3 Oppositely charged Polymer/Azo-surfactant complexes .....	39
Chapter III. Synthesis, characterizations and sample preparation .....	47
III.1 Polyelectrolytes .....	47
III.1.1 Target compounds and synthetic scheme.....	47
III.1.2 Controlled radical polymerization RAFT .....	48
III.1.3 Synthesis of the PAA chains.....	51
III.1.1 Modification of the PAA by the azobenzene bearing groups .....	57
III.1.2 Conclusion.....	62
III.1.3 Experimental procedures for the polyelectrolyte syntheses. ....	62
III.2 Azo-containing surfactants.....	67
III.2.1 4Azo2TAB .....	68
III.2.2 8Azo2TAB .....	70
III.3 Sample preparations .....	72
III.3.1 Polyelectrolyte aqueous solutions .....	72
III.3.2 Polyelectrolyte/Surfactant complexes solutions .....	72
III.3.3 Azo-surfactant/Aromatic salt solutions .....	72

Chapter IV. Analysis techniques.....	75
IV.1 UV and Blue light irradiation .....	75
IV.1.1 Light sources .....	75
IV.1.2 Comparison between UV tube and UV LEDs irradiation .....	76
IV.2 Small-Angle X-ray and Neutron Scattering .....	80
IV.2.1 Generalities.....	80
IV.2.2 Form factor.....	82
IV.2.3 Scattering length densities (SLD).....	82
IV.2.4 SAXS experimental conditions and illumination protocol .....	90
IV.2.5 SANS experimental conditions and Illumination protocol .....	94
IV.3 NMR .....	95
IV.4 Size Exclusion Chromatography (SEC) .....	96
IV.5 UV-Vis absorption spectroscopy .....	96
IV.6 Surface tension measurement.....	98
IV.7 Thermogravimetric analysis (TGA).....	98
IV.8 Transmission electron microscopy (Cryo-TEM) .....	99
Chapter V. Azo-functionalized polyelectrolytes.....	103
V.1 Azo-containing polyelectrolytes .....	103
V.2 Photoisomerization behaviours.....	104
V.2.1 <i>Trans/Cis</i> ratio .....	104
V.2.2 Reversibility.....	108
V.2.3 Comparison of Azo-polymers UV-Vis spectra.....	109
V.3 Structural organization study .....	110
V.3.1 Reference systems: poly(sodium acrylate) (NaPAA).....	110
V.3.2 Azo polymers: general observations .....	112
V.3.3 Structural reversibility upon irradiation and thermal relaxation.....	115
V.3.4 Structural organization in long chain PAA-Azo solutions ( $\tau_{\text{azo}} = 0.11$ ) .....	117
V.3.5 Structural organisation in short chain PAA-Azo solutions ( $\tau_{\text{azo}} = 0.11$ ) .....	126
V.3.6 Structural organization in short chain PAA-Azo solutions ( $\tau_{\text{azo}} = 0.15$ ) .....	133
V.3.7 Conclusion .....	137
Chapter VI. Complexes of polyelectrolytes and oppositely charged Azo-surfactants .....	141
VI.1 Azo-surfactants .....	142
VI.2 Characterization of micelles.....	143
VI.2.1 Surface tension and critical micellar concentration (CMC).....	143
VI.2.2 Photoisomerization study .....	145
VI.2.3 Structural organization study.....	149
VI.2.4 Conclusion .....	163
VI.3 Azo-surfactant/Polyelectrolyte complexes.....	164
VI.3.1 Azo-Surfactant/Polyelectrolyte ratios and concentrations .....	164
VI.3.2 Photoisomerization study .....	168

VI.3.3 Structural study by NMR.....	171
VI.3.4 Structural study by SAXS and SANS .....	178
VI.3.5 Conclusion .....	193
Chapter VII. Self-assembly of azo surfactants with co-surfactants .....	197
VII.1 Self-assembly of 8Azo2/sodium salicylate (NaSal).....	197
VII.1.1 Azo-surfactant/NaSal: molar ratio and concentration .....	197
VII.1.2 Photoconversion study .....	198
VII.1.3 Structural study .....	202
VII.2 Self-assembly of 8Azo2TAB/sodium benzenesulfonate .....	211
VII.2.1 Study by NMR.....	212
VII.2.2 Structural study .....	214
VII.3 Comparison of wormlike micelles systems.....	220
General Conclusion and Perspectives .....	225
Appendix .....	229



# General Introduction

“Smart” materials are advanced materials with properties that can be changed significantly by an external stimulus (such as mechanical stress, electric or magnetic fields, light, temperature, pH *etc.*). The development of “smart” systems in aqueous solution, able to respond to external stimuli have attracted much enthusiasm for their potential industrial applications and academic research. Compared to other stimuli, light is of particular interest since it is a clean source, and it is easy to handle temporally and spatially. A large variety of chromophores have been incorporated into water soluble molecules forming diverse photo-responsive systems. Photo-induced changes in morphology, surface or bulk properties have been widely studied.

In this work, we focus on light-responsive systems and more exactly polyelectrolytes-based “smart” systems.

Polyelectrolytes (PEs) are charged polymers in solutions. They present interesting physicochemical properties in aqueous solution such as high viscosity, the capacity to self-assemble and to interact with diverse (macro)molecules (surfactant, protein, DNA, PEs) in aqueous solution. The combination of photo-responsive chromophores and PEs systems leads to a large variety of new structural organization in aqueous solution that can possibly be modified by simple irradiation. These light induced modifications at the molecular scale can sometimes propagate to the macroscopic scale and hence, modify certain properties of the solutions. The knowledge of the structural organization is a key point to elucidate the origin of this phenomenon. From a fundamental point of view, these photo-sensitive systems can also bring a new perspective on the physics of PEs. That concerns for instance the hydrophilic-hydrophobic transition in hydrophobic PEs, the role of the valence of counterions but also, associative PEs.

The objective of this thesis is to design, synthesize and characterize model photo-responsive PEs systems and then, to investigate their structural organization under irradiation. The azobenzene chromophore (Azo) is used in our study. It exhibits a *trans/cis* isomerization leading to a modification of its dipole moment. Azo group not only brings a ‘photo-tunable’ local reorganization, but also modifies the hydrophilic/hydrophobic balance in our PE systems.

Azo group has been incorporated in PEs systems in different ways. The first system is Azo-containing sodium polyacrylates. The Azo group is grafted on the

side chain of PEs macromolecular backbone. The main questions are related to the structural organisation of these hydrophobically modified PEs in solution. Do we have extended or collapsed polyions? Can we control their conformation by simple light stimuli?

The second system is composed of Azo-containing surfactants (Azo-surfactant) and oppositely charged PEs. Azo units are incorporated in the surfactants molecules and not grafted on PEs. This topic is closely related to that of surfactant/PE complexation which is often found in industrial formulations.

Pure Azo-surfactants also present interesting self-assembly properties. In the presence of co-surfactants, different organizations may be formed. The third photo-responsive system investigated in this work is made of Azo-surfactant/co-surfactant mixtures. Their solutions show particular rheological properties and an interesting reversible gel to fluid transition under light irradiation.

This thesis contains seven chapters. The first chapter introduces general concepts about polyelectrolytes.

The second chapter presents general characteristics of azobenzene and summarize works of azo-containing aqueous solution systems.

In the third chapter, we describe the synthesis and the characterization of different Azo-containing compounds as well as the samples preparation. The synthesis of azobenzene, Azo-surfactants and Azo-containing polymers are presented.

The fourth chapter discusses the problem of light sources, the photo-stationary state and all analytical technics.

In the next three chapters, we present the results on our three studied systems: Azo-containing sodium polyacrylates, Azo-surfactant/PE complexes and Azo-surfactant/co-surfactant systems. We aim at figuring out the structural organization of these systems, their photo-behaviors and the structural variation under light stimulus. Small-angle scattering technics (SAXS and SANS), NMR and UV-Vis spectroscopy will be our main experimental techniques.

Nomenclature		
$a$	Monomer length	Å
$A$	Absorbance	
$c^*$	Critical overlap concentration	mol L <sup>-1</sup>
$c_p$	Monomer concentration	mol L <sup>-1</sup>
$d$	Distance	m
$D$	Size of the subunit blob	Å
$DP_n$	Degree of polymerization	
$e$	Electronic charge	C
$E(R)$	Free energy	J
$f$	Chemical charge fraction	
$I$	Ionic strength	mol L <sup>-1</sup>
$I_p$	Polydispersity index	
$g$	Number of monomers in a subunit blob	
$k_B$	Boltzmann constant	J K <sup>-1</sup>
$\kappa_D^{-1}$	Debye length	Å
$l$	Distance between two consecutive charges along the polyion	Å
$l_B$	Bjerrum length	Å
$l_p$	Persistence length	Å
$l_{pe}$	Electrostatic persistence length	Å
$M_n$	Number-average molar mass	g mol <sup>-1</sup>
$M_w$	Weight-average molar mass	g mol <sup>-1</sup>
$p$	Conversion rate	
$R$	End-to-end distance of a polymer chain	Å
$T$	Temperature	K
$U_{ij}$	Electrostatic interaction energy	J
$x_{trans}$	Molar fraction of <i>trans</i> -isomer	
$z$	Valency of ions	
$\gamma$	Surface tension	N m <sup>-1</sup>
$\Theta$	Theta temperature	K
$\epsilon$	Dielectric constant	
$\tau_{azo}$	Molar fraction of azo unit	
$\xi$	Correlation length	Å

---

Abbreviation	
AIBN	2,2'-Azobisisobutyronitrile
AMAMPS	Poly(acrylamide-co-sodium-2-acrylamido-2-methylpropane sulfonate)
ATRP	Atomic transfer radical polymerization
Azo	Azobenzene
CAC	Critical aggregation concentration
CMC	Critical micelle concentration
CNC	Charge neutralization concentration
CPP	Critical packing parameter
CTAB	Cetyltrimethylammonium bromide
DMF	Dimethylformamide
DMSO	Dimethyl sulfoxide
LCST	Lower critical solution temperature
NaPAA	Sodium polyacrylate
PSS	Polystyrene sulfonate
PAA	Polyacrylic acid
PDADMAC	Poly(diallyl-dimethylammonium chloride)
PE	Polyelectrolyte
PEG	Poly(ethylene glycol)
RAFT	Reversible addition-fragmentation transfer polymerisation
SANS	Small-angle neutron scattering
SAXS	Small-angle X-ray scattering
SEC	Size exclusion chromatography
SLD	Scattering length density
TGA	Thermogravimetric analysis
THF	Tetrahydrofuran
UV	Ultraviolet

---

# Chapter I. Polyelectrolytes in aqueous solution

Polyelectrolytes (PEs) are polymers that own ionizable functional groups. In a polar solvent such as water, PEs can dissociate into charged polyions and counterions. PEs exhibit both polymeric and electrolyte properties, at the origin of useful and unique applications. As an important element in soft matter, PEs have been the focus of intensive studies both at fundamental and industrial levels. Their applications are mostly related to flow modification and stability properties of aqueous solutions and gels (flocculation agents, thickeners, conditioners and emulsifiers). They are commonly found in shampoos, soaps, and cosmetic products. Due to their water solubility, they are also investigated for biochemical and medical applications. Furthermore, some PEs can be added to food products as food coatings and release agents.

The presence of electrostatic charges along the chain is at the origin of the water solubility and the stability of the solution. Many efforts have been done in the field of theoretical studies, simulations and experiments to describe PE systems. This is however challenging since many variables are involved and highly correlated. Theoretical approaches have been carried out starting from works of Katchalsky and Kuhn<sup>1,2</sup>, in which PE chains were described as rod-like charged entities. Scaling models were later introduced by de Gennes *et al.*<sup>3</sup> where PEs were modeled as an extended array of electrostatic blobs. For PE in poor solvent condition, Dobrynin *et al.*<sup>4</sup> proposed a necklace-like structure made of beads connected by narrow strings. Later, theoretical models were extended to more complicated situations such as PEs in semidilute regime, in the presence of multivalent ions or in addition of salts. Because of the particularity of each PE systems and the various parameters involved, the theories that describe the conformational and dynamic properties of charged polymer chains are quite diverse. They are well reviewed in an extensive literature<sup>5-9</sup>. Thanks to the scattering techniques, which are able to probe the structural organization, a lot of progress has been made<sup>10-17</sup> and a wealth of information on PEs organizations in dilute and semi-dilute solutions has been obtained. Other approaches by computer simulation have been developed to understand structural properties<sup>18,19</sup>, counterions distribution<sup>20-22</sup> and salt effect<sup>23,24</sup>. Some simulations has also helped to predict and support scattering experiments<sup>25</sup>.

Even if PEs are used in many fields, we still don't have a full comprehensive understanding of their solutions. The objective of this chapter is to give a general introduction on these systems. We will present briefly a classification for PEs, some basic definitions, and the usual models for the conformation of hydrophilic PEs. Then the hydrophobic PEs will be shortly described. The complexation of PEs and oppositely charged surfactants is an important subject of the thesis. The binding process and the structural organization will also be discussed.

## **I.1 Basics of polyelectrolytes**

### **I.1.1 Classification of polyelectrolytes**

PEs can be classified in different ways. Based on the sign of the charge along the backbone, we may have polyanions or polycations. According to the acid-base properties of the ionizable groups, we can distinguish between strong and weak PEs. In analogy to strong acids and bases, strong PEs are fully ionized in solution. The number of charges and their positions along the chain are fixed or "quenched" (pH-independent charge distribution). On the other side, weak polyacids or polybases can be partially ionized. Their ionisation degree varies with the pH and charges fluctuate along the chain ("annealed" PEs).

A PE is said to be hydrophilic when its backbone is in a good solvent condition in water. When the skeleton is in poor solvent, we usually talk about hydrophobic PEs. The hydrophilic/hydrophobic character of a PE can be gradually varied by introducing hydrophilic/hydrophobic monomers along the backbone (copolymer). The final structural organization will be highly dependent on the hydrophilic/hydrophobic balance in the systems. Partially sulfonated polystyrene (PSS) in which sulfonated styrene and neutral styrene are present is a good example for hydrophobic PE. NaPAA (sodium polyacrylate) is commonly referred as a hydrophilic PE. Ionene polymers represent a unique class of cationic polymers in which ionic sites are located on the skeletons and where the charge distribution is regular and can be carefully adjusted<sup>26</sup>.

The natural/synthetic origin also provides a way to classify PEs. Natural PEs include for instance polysaccharides (alginates, hyaluronic acid or hyaluronate, carrageenan, chitosan), polypeptides, DNA and proteins. The chemical structure of natural PEs is often very complex and often irregular (polydispersity, branching). Synthetic PE are usually much simpler. Classical examples are poly(acrylic acid),

poly(methacrylic acid), poly(acrylamide-2-methyl-propane sulfonate), poly(sodium styrene sulfonate) and polydiallyldimethylammonium chloride. Some PEs are given in Figure 1.

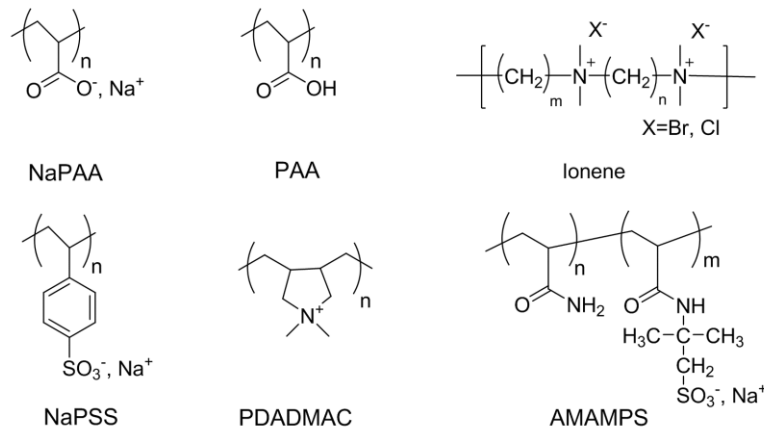


Figure 1 Chemical structure of sodium polyacrylate (NaPAA), polyacrylic acid (PAA), Ionene, sodium polystyrene sulfonate (NaPSS), Poly(diallyl-dimethylammonium chloride) (PDADMAC) and poly(acrylamide-co-sodium-2-acrylamido-2-methylpropane sulfonate) (AMAMPS).

Other classifications based on the stiffness (flexible, rigid), the architecture (linear, branched, crosslinked, pendant groups) and the composition (homopolymer, copolymer) can also be found in the literature.

In the present work, we are more especially interested in **highly charged, linear, flexible** synthetic polyelectrolytes (**NaPAA** and **NaPSS**).

### 1.1.2 Basic energy and length scales

PEs are composed of many repeating units. They can be obtained by polymerization of ionizable monomers or by post-functionalization of neutral polymers with ionizable groups. The size  $a$  of monomer is in the order of 2.5 Å for vinyl polymers. The average number of monomers in the chain (degree of polymerization) is referred to  $N$ . The concentration of PEs is generally defined in term of monomer concentration  $c$  ( $\text{mol L}^{-1}$ ). The average distance between two successive charges along the PE chain is denoted  $l$ . After ionization in polar solvent, polyions carry a chemical charge fraction  $f$  ( $f = a/l$ ) which is also determined by the ratio of ionized monomers to the total number of monomers. For highly charged PE, we may observe a counterion condensation phenomena leading to a reduction of the net charge along the chain. The chemical charge fraction is then replaced by an effective charge fraction  $f_{\text{eff}}$ .

Electrostatic interaction brings also a characteristic distance. Consider a pair of ions owning charges  $z_i e$  and  $z_j e$  separated by a distance  $d_{ij}$  in a solvent with uniform dielectric constant  $\epsilon$ , the electrostatic interaction energy  $U_{ij}$  is given by the Coulomb law as:

$$\frac{U_{ij}}{k_B T} = z_i z_j \frac{e^2}{4\pi\epsilon_0\epsilon k_B T} \frac{1}{d_{ij}} \quad (1)$$

where  $k_B$  is the Boltzmann constant,  $T$  the absolute temperature (in Kelvin),  $z_i$  and  $z_j$  the valency of the ions,  $e$  the electronic charge, and  $\epsilon_0$  is the vacuum permittivity.

We define the Bjerrum length  $l_B$  as the distance at which the electrostatic interaction energy between two elementary charges is comparable to the thermal agitation energy  $k_B T$ . In standard units,  $l_B$  is given by:

$$l_B \equiv \frac{e^2}{4\pi\epsilon_0\epsilon k_B T} \quad (2)$$

For oppositely charged ions separated by a distance shorter than  $l_B$ , the attraction between them is stronger than  $k_B T$  and the ions are more likely to be paired instead of completely dissociated. The surrounding solvent should be sufficiently polar to ionize PEs. For pure water at 25 °C,  $\epsilon \approx 78.4$  so that  $l_B \approx 7.14 \text{ \AA}$

### 1.1.3 Electric screening: influence of the ionic strength

The range of the electrostatic interaction between ions is given by the Debye length  $\kappa_D^{-1}$ , also known as the screening distance. To put it simply, at a distance smaller than  $\kappa_D^{-1}$ , charges interact via an unscreened Coulomb potential. At larger distances interaction vanishes.  $\kappa_D^{-1}$  can be written:

$$\kappa_D^{-1} = \left( \frac{1000 N_A e^2}{\epsilon_0 \epsilon k_B T} \sum_i z_i^2 c_i \right)^{-\frac{1}{2}} = (4\pi l_B I)^{-\frac{1}{2}} \quad (3)$$

Where  $c_i$  is the concentration of ions  $i$  in mol L<sup>-1</sup>. The term  $\sum z_i^2 c_i$  corresponds to the ionic strength  $I$ . The Debye length is inversely proportional to the ionic strength: when the concentration of ions is increased, the electrostatic interactions are shielded, and the Debye length is reduced.

For monovalent salts in water ( $\epsilon \approx 78.4$ , at 25 °C and  $l_B \approx 7.14 \text{ \AA}$ ), the Debye length  $\kappa_D^{-1}$  depends only on the salt concentration  $c_s$ :

$$\kappa_D^{-1} \approx \frac{0.304}{\sqrt{c_s}} \text{ nm} \quad (4)$$

For pure water (pH 7 without added salt), the self-dissociation leads to the

presence of  $H^+$  and  $OH^-$  ions, with a concentration of  $10^{-7}$  mol  $L^{-1}$ . Thus, even in this ideal situation, the electrostatic interaction will be screened (approximately over a distance of 700 nm). For significant salt concentrations (counterions or added salts), the Debye length varies from a few tens of nanometers to a few angstroms.

### I.1.4 Persistence length

The persistence length  $l_p$  quantifies the stiffness of a polymer. On length scales shorter than  $l_p$ , the polymer behaves like a rigid rod. For charged polymers in solution,  $l_p$  is increased due to repulsive interaction between monomers. It is often considered that it can be written as the sum of an intrinsic contribution  $l_{p0}$  (persistence length in absence of charge) and an electrostatic contribution  $l_{pe}$ .

$$l_p = l_{p0} + l_{pe} \quad (5)$$

The first calculation was proposed by Odijk<sup>27</sup>, Skolnick and Fixman<sup>28</sup>. On the condition that  $\kappa_D l_p \gg 1$  and for a highly charged rod-like chain, the electrostatic persistence length  $l_{pe}$  scales as  $\kappa_D^{-2}$ . Therefore, the electrostatic persistence length can be significantly large for salt-free conditions ( $\kappa_D^{-1} \rightarrow \infty$ ).

$$l_{pe} = \frac{1}{4\kappa_D^2 l_B} \quad (6)$$

This model considers the electrostatic interaction as a perturbation of the elastic free energy, it is therefore limited to semi-flexible or rigid PEs ( $l_{pe} \ll l_p$ ).

Theories developed for flexible PEs showed that in absence of added salt,  $l_p$  varied as the Debye length  $\kappa_D^{-1}$ .<sup>29,30</sup>

## I.2 Structural organization of hydrophilic polyelectrolytes in aqueous solution

### I.2.1 Isolated polyelectrolytes chains

We first consider a PE chain as a connected sequence of charged and neutral monomers in a salt-free solution at infinite dilution. This simplified model helps to introduce some important concepts relative to PEs.

### I.2.1.1 Strongly charged polyelectrolytes: Counterion condensation and effective charge

In the case of a highly charged PE ( $f \rightarrow 1$ ), counterions are supposed to be dissociated in aqueous solution. However, if the charge fraction is too high, the electrostatic potential around the chain is so large that part of these ions are trapped in the vicinity of the chains (Manning-Oosawa condensation<sup>31-33</sup>). The chemical charge fraction  $f$  has to be replaced by the effective charge  $f_{eff}$ . If the distance  $l$  between two chemical charges along the polyion is larger than  $zl_B$  ( $z$  is the valency of the ions), that is to say  $f$  is small, no condensation is observed: the final charge fraction  $f$  is equal to the chemical charge fraction. If the distance between two consecutive charges  $l$  along the polyion is lower than  $zl_B$ , the counterion condensation takes place until the effective charge  $f_{eff}$  is equal to:

$$f_{eff} = \frac{a}{zl_B} \quad (7)$$

The minimum distance between two effective charges along the macroion is then given by the Bjerrum length  $l_B$  for monovalent counterions, and  $zl_B$  for multivalent counterions. As given in Figure 2, once Manning's condensation threshold is reached ( $f=a/zl_B$ ), an the increase in chemical charge fraction does not longer modify the net charge of PEs.

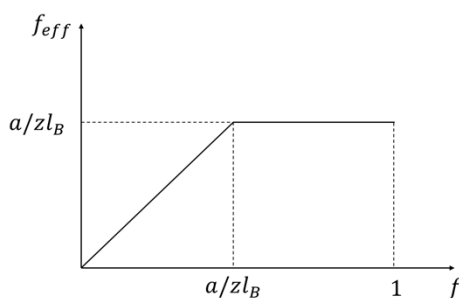


Figure 2 Evolution of the effective charge  $f_{eff}$  as a function of chemical charge fraction  $f$ .

### I.2.1.2 Weakly charged PEs: Electrostatic blobs

We consider a weakly charged flexible polyion in very dilute solution (counterions are neglected). The electrostatic interaction tends to swell the chain: we might expect a 'fully extended' conformation for PEs at very small concentration. However, since the swelling causes entropy loss, this is not favourable. Based on the Flory theory for neutral polymer chains, Katchalsky and coworkers<sup>2</sup> proposed the first model for charged polyions. A PE with  $N$  monomers

and a charge fraction  $f$  is described as a random coil with end-to-end distance  $R$ . The free energy  $E(R)$  contains two contributions: the conformational entropy (in the Gaussian approximation) and the electrostatic energy.

$$E(R) = k_B T \left( \frac{R^2}{Na^2} + \frac{(Nf)^2 l_B}{R} \right) \quad (8)$$

The minimization of the free energy leads to:

$$R \sim N f^{\frac{2}{3}} (l_B a^2)^{\frac{1}{3}} \quad (9)$$

The end-to-end distance  $R$  is proportional to  $N$  suggesting that a flexible PE chain without salt would adopt an 'extended' conformation. A more sophisticated model based on the electrostatic blob concept was later introduced by de Gennes *et al.*<sup>3</sup>. PE chain can be viewed as a linear string of 'blobs'. Each blob is composed of a flexible subchain containing several monomers  $g$ . The chain inside the blob is not perturbed by the electrostatic interactions. Due to the electrostatic repulsion between blobs, they tend to align: a PE chain is elongated and form an 1D array of blobs with an overall size  $R$  (Figure 3).

Assuming that the electrostatic energy of each blob is comparable to the thermal energy  $k_B T$ , the blob size  $D_e$  is given by:

$$\frac{l_B (fg)^2}{D_e} \sim 1 \quad (10)$$

Where  $f$  is the fraction of charged monomers and  $g$  is the number of monomers in a blob.

If the subchain in the blob can be considered as a Gaussian chain,  $D_e^2 \sim gl^2$ . Combining with eq (8), we have:

$$D_e \sim b \left( \frac{f^2 l_B}{a} \right)^{-\frac{1}{3}} \quad (11)$$

$$g \sim \left( \frac{f^2 l_B}{a} \right)^{-\frac{2}{3}} \quad (12)$$

The total length  $R$  of the PE chain is  $R \sim N f^\nu$ . The exponent  $\nu$  depends on the solvent quality ( $\nu = 2/3$  for  $\theta$  solvent and  $\nu = 4/7$  for good solvent).

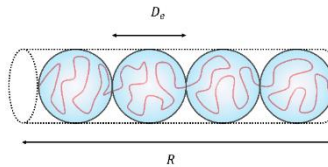


Figure 3 Schematic representation of a weakly charged, flexible chain in a very dilute solution. Inspired from Ref 8.

## I.2.2 Chains in semidilute regime

So far, we only considered the conformation of isolated PE chains in salt-free dilute solution. When the concentration increases, the distance between chains decreases. At a certain concentration  $c^*$ , chains start to overlap and form a network of mesh size  $\xi$ . This critical concentration  $c^*$  can be estimated from the degree of polymerization and the typical volume of the chain ( $\theta$  solvent):

$$c^* \approx a^{-3} N^{-2} \left( \frac{l_B}{a} \right)^{-1} f^{-2} \quad (13)$$

To be concrete, let us consider a highly charged vinyl polymer chain ( $a = 2.5$  Å) with an effective charge fraction of 0.35 in aqueous solution ( $l_B = 7.14$  Å). The calculated  $c^*$  values for different degree of polymerization  $N$  are listed in Table 1.

$N$	100	1000	10000
$c^*$ (mol L <sup>-1</sup> )	$3 \cdot 10^{-2}$	$3 \cdot 10^{-4}$	$3 \cdot 10^{-6}$

Table 1 Estimated critical overlap concentration  $c^*$  for chains of different lengths according to eq(13).

The critical concentration decreases strongly with the length of the PE chain. Hence, most of the experiments with long PE are usually performed in a concentration beyond the overlap concentration  $c^*$  (*i.e.*, in the semi-dilute regime). This semi-dilute regime has been described by de Gennes<sup>3</sup> and Dobrynin<sup>4</sup> as an isotropic entangled system as depicted in Figure 4. Such a system is characterized by a single correlation length  $\xi$ .  $\xi$  represents both the mesh size of the network and the screening length of the electrostatic interaction.

For length scales smaller than  $\xi$ , electrostatic interactions dominate, each polyion segment behaves like a single chain in dilute regime (extended conformation of electrostatic blobs of size  $D_e$ ). At distances larger than  $\xi$ , the interactions are screened out and the chain behaves like a random walk of correlation blobs of size  $\xi$ . The correlation length  $\xi$  in a good solvent can be written as:

$$\xi = (ac_p)^{-\frac{1}{2}} \left( \frac{l_B}{a} \right)^{-\frac{1}{7}} f^{-\frac{2}{7}} \quad (14)$$

Many experimental works agree with this scaling law<sup>11,15,17,34</sup> and therefore to the isotropic model. If the concentration increases even further, the network is more compact, and we reach the concentrated regime. This range is out of the

scope of our investigation and won't be presented here.

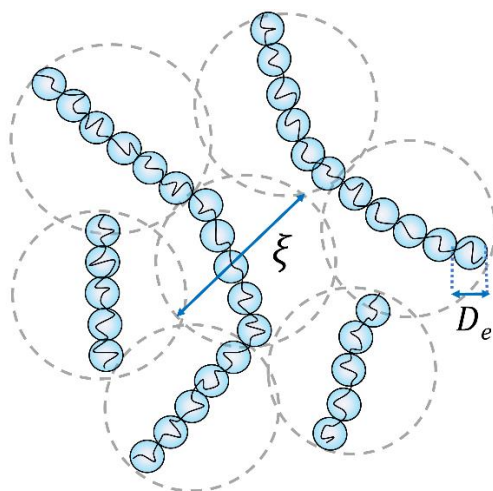


Figure 4 Schematic representation of a semi-dilute polyelectrolyte solution. Inspired from Ref 8.

In small-angle scattering measurements, PEs solutions present a broad peak at a scattering vector  $q^*$ . This maximum originates from the electrostatic interaction between polyions. It disappears when salt is added due to screening effects<sup>35</sup>. The position of the peak varies with the concentration according to different scaling laws  $q^* \propto c^\alpha$ . In dilute regime ( $c < c^*$ ),  $q^*$  varies as  $c^{1/3}$  and is related to the distance between the center of mass of the polyions ( $q^* = 2\pi/d$ ). In semidilute regime ( $c > c^*$ ), chains are entangled and form an overlapping network characterized by a mesh size  $\xi$ .  $q^*$  now varies as  $c^{1/2}$  and probes the mesh size  $\xi$  ( $q^* = 2\pi/\xi$ ).

## I.3 Hydrophobic Polyelectrolytes

### I.3.1 Definition and examples

PEs are called 'hydrophobic' when the backbone or parts of the monomers are in poor solvent condition. The water solubility and the structural organization of the chain result from the balance between the electrostatic repulsions (that tend to stretch the polyions and stabilize the solution) and the hydrophobic interactions (that leads to their collapse). Hydrophobic PEs can be classified according to their architecture (Figure 5). Ionic groups can be introduced as pendant groups onto hydrophobic monomers of the main chain. A classic example is the polystyrene sulfonate obtained by partial sulfonation of a polystyrene chain<sup>36</sup>. Water is a bad solvent for styrene but it is a good solvent for styrene sulfonate. In that case,

changing the sulfonation degree does not only modify the charge fraction (and the electrostatic interaction) but also the hydrophobicity of the sample. Similarly, based on an ionic backbone, a low fraction of hydrophobic groups can be added onto the sidechains or the two extremities (hydrophobically modified polyelectrolyte). The most studied family<sup>37,38</sup> is a derivative of poly(sodium acrylate), on which hydrophobic moieties can be readily grafted. If the fraction of hydrophobic groups is high, they are usually named ‘polysoap’. This situation will correspond to one of our model systems.

The notion of amphiphilic PEs often appears when we talk about hydrophobic PEs, due to the coexistence of hydrophilic and hydrophobic parts. We also hear about associative PEs referring to amphiphilic polymers that can form supramolecular assemblies (micelles, lamellar phases, gels). We should note that it may be sometimes difficult to find which category the hydrophobic PEs belong to since there are no sharp boundaries among the different classifications.

In this present work, one basic idea was to modulate the hydrophobicity of Azo-modified PE by light stimulus and to determine the induced structural modifications. Light-sensitive systems may provide an interesting way to follow the hydrophobic transition without having to use different PEs of distinct hydrophobic/hydrophilic properties.

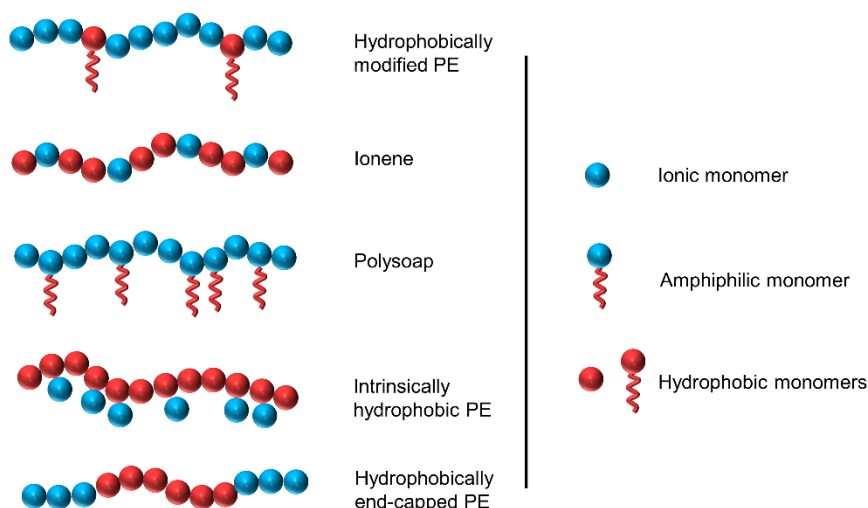


Figure 5 Schematic representation of various hydrophobic PEs. Reproduced from Ref 39.

## I.3.2 Conformation of hydrophobic polyelectrolyte

### I.3.2.1 Necklace conformation in dilute solutions

Hydrophobic PEs but also, the hydrophilic/hydrophobic transition in these systems are still very active field of study, both on a theoretical and experimental level. The hydrophobic interaction in hydrophobic PE favours the collapse of the chain into globule, while the electrostatic repulsion between charged groups tends to stretch the polyion and improves its solubility in water. The conformation of PE chains in poor solvent results from the balance between electrostatic and hydrophobic interactions. The reflection on the shape of hydrophobic PEs was inspired from the problem of charged droplet by Rayleigh<sup>40</sup>. A charged droplet is unstable beyond a critical charge ( $> e(\gamma R^3/kTl_B)^{1/2}$ , where  $\gamma$  is the surface tension) and breaks into smaller droplets, which are in equilibrium at a finite distance. The instability appears when the electrostatic energy is comparable to the surface tension energy. For PEs, we are in a very similar situation. We can imagine a neutral polymer in bad solvent condition which is therefore collapsed (droplet). The question is what happens when charges are added along the chain. It is impossible to tear apart the polyions due to the chemical bonds. But the chain can minimize its free energy by adopting a particular shape made of small globules connected by narrow strings: the necklace conformation. This model was first proposed by Kantor and Kardar<sup>41</sup> to describe polyampholytes chains (random sequences of positive and negatively charged monomers). Then it was applied to hydrophobic PE by Dobrynin and coworkers<sup>42,43</sup>.

Consider a hydrophobic polyelectrolyte chain with  $N$  monomers of size  $a$  and a charge fraction  $f$  in poor solvent of dielectric constant  $\epsilon$ . The reduced temperature is  $\tau = (\Theta - T)/\Theta$ , where  $\Theta$  is the theta temperature of the polymer-solvent system.

When the charge fraction  $f$  is higher than  $(\tau a/l_B N)^{1/2}$ , the chain turns into a necklace conformation of  $N_{bead}$  beads of size  $D_b$  and  $N_{bead} - 1$  strings as schematized in Figure 6.

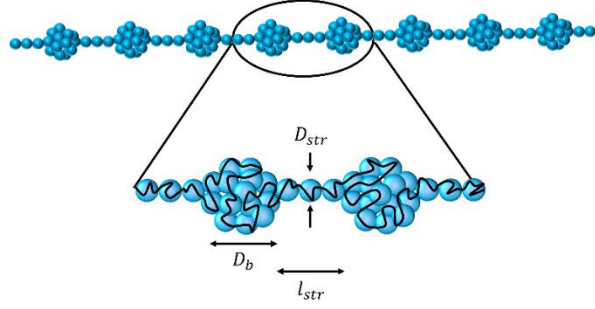


Figure 6 The necklace conformation of hydrophobic PE chain. Reproduced from Ref 40.

### 1.3.2.2 Necklace conformation in semi-dilute solutions

Similar to scaling laws for hydrophilic polyelectrolytes, Dobrynin and coworkers<sup>43</sup> developed a scaling model for hydrophobic PEs in semi-dilute solutions.

Just above the critical overlap concentration, an isotropic network is formed and described by a correlation length  $\xi$ .

$$\xi \approx ag_b^{\frac{1}{4}}(ca^3)^{-\frac{1}{2}} \quad (15)$$

For length scales smaller than  $\xi$ , the segment behaves like a single necklace chain in dilute solution. At a distance larger than  $\xi$ , chains adopt a random walk conformation. This concentration range corresponds to the string-controlled regime (Figure 7 a). The correlation length  $\xi$  decreases as  $c^{-1/2}$  until it is smaller than the string length  $l_{str}$ . A threshold concentration  $c_b$  is defined when these two lengths have the same order of magnitude ( $\xi \approx l_{str}$ ).

For concentrations  $c > c_b$ , the electric repulsion between beads is screened, only one bead is present per correlation volume  $\xi^3$ . We suppose that most of the polymer mass is located in the beads. The correlation length is then inversely proportional to  $c^{1/3}$ :

$$\xi \approx \left( \frac{a\tau}{l_B f^2} \right)^{\frac{1}{3}} c^{-\frac{1}{3}} \approx \left( \frac{g_b}{c} \right)^{\frac{1}{3}} \quad (16)$$

This regime is referred to the bead-controlled regime (Figure 7 b). This hydrophilic/hydrophobic transition therefore modifies both the chain conformation (the size of the bead is changing), but also the dispersion state of the polyions in semi-dilute regime (in the string-controlled regime  $\xi \propto c^{-1/2}$ ,  $\xi > l_{str}$  while in the bead-controlled regime  $\xi \propto c^{-1/3}$ ,  $\xi < l_{str}$ ).

The pearl-necklace configuration of this theoretical description is quite difficult

to evidence experimentally. Scattering experiments are well suited techniques to study the structural organization in these systems. Since the transition modifies the dispersion state, characteristic variations should be found for the variation  $q^* = f(c)$ . Since  $q^* = 2\pi/\xi$ , one should find  $q^* \propto c^{1/2}$  in the string-controlled regime and  $q^* \propto c^{1/3}$  in the bead-controlled regime.

Different concentration regimes were indeed found in partially sulfonated poly(styrenesulfonate)<sup>44–46</sup>. If  $q^*$  still varies as  $c^\alpha$ , now  $\alpha$  (in between 1/2 and 1/3) depends on the hydrophobicity of the sample. Form factor measurements can also be measured and compared to theoretical model<sup>47</sup>. These experiments evidenced the formation of string and globules. However, these kinds of investigation are very rare.

One idea behind this thesis was to trigger the transition by simple UV stimulus (that changes the hydrophilic/hydrophobic balance in the azo-containing PEs), without changing the chemistry of the polyions.

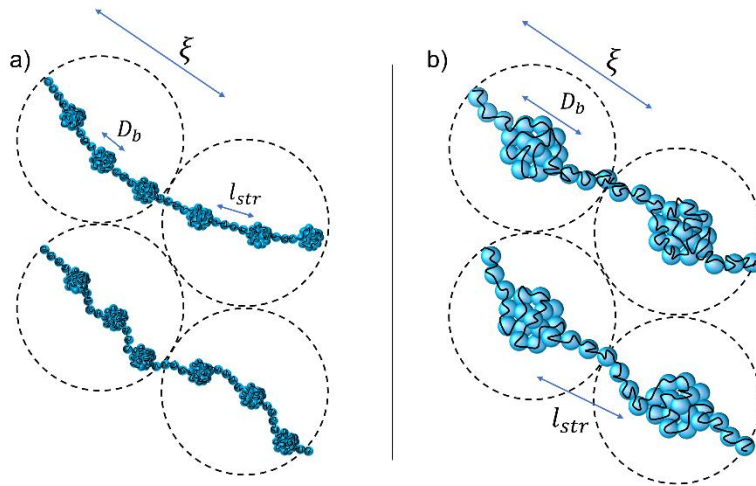


Figure 7 a) String-controlled regime ( $c^* < c < c_b$ ,  $\xi > l_{str}$ ); b) Bead-controlled regime ( $c \geq c_b$ ,  $\xi \leq l_{str}$ ).

Reproduced from Ref 8.

## I.4 Surfactant/Polyelectrolyte complexes

Complexes can be formed readily between polyelectrolytes (PEs) and oppositely charged surfactants. Surfactants are known to modify the surface tension, the phase behaviour and the rheology of a solution<sup>48,49</sup>. The addition of PEs has been proved to enhance further the bulk and interfacial properties leading to enormous potential applications. Various combinations of PEs and surfactants result in unique behaviours and structural arrangements due to the formation of

surfactant/PE complexes. We present here a brief summary on their formation and their structural organization in solution.

### 1.4.1 Formation of complexes

Binding of surfactants to PEs chains is the first step leading to the formation of the complexes. According to the surfactant concentration, two mechanisms can be observed. When a very low amount of surfactants is added in the PE solution, they bound to the polyions in a non-cooperative manner. When the concentration is increased, the adsorption process becomes cooperative (adjacent sites are more likely filled with surfactants) leading to the formation of small PE/surfactant aggregates. This cooperative binding occurs at a “critical aggregation concentration” (CAC) that can be several orders of magnitude lower than the “classical” critical micelle concentration (CMC). Binding isotherms measured by potentiometric and calorimetric titrations may provide information on the binding mechanism. It is usually a sigmoidal curve that depicts the fraction of surfactants bound per monomer (degree of binding  $\beta$ ) as a function of the surfactant concentration. The number of bound surfactants increases linearly with the surfactant concentration in the cooperative binding regime. The slope allows to determine the binding constant  $K_0$ , which is directly related to the strength of the interaction between surfactants and PEs.

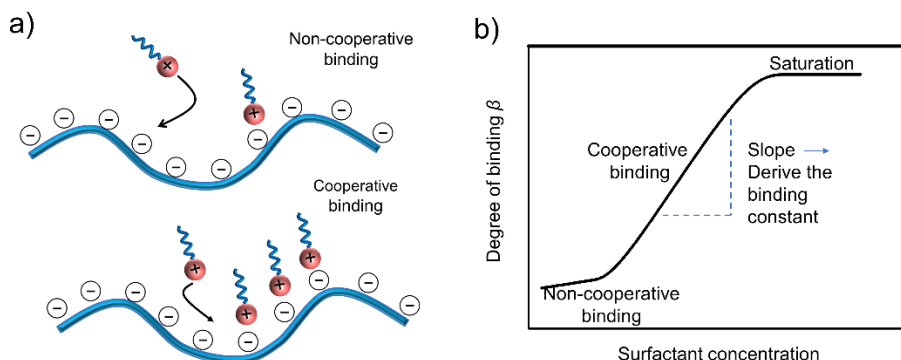


Figure 8 a) Binding process of surfactant to polyelectrolyte b) Illustration of the binding isotherm: degree of binding vs surfactant concentration. Reproduced from Ref 50.

For charged systems, the initial binding and adsorption of charged surfactants to PEs are mainly promoted by electrostatic interactions. But hydrophobic interactions are also responsible to the formation of aggregates through the interactions between nearby surfactant tails. A high charge density for PEs may increase the strength of the electrostatic interactions and thus increase the

contribution of electrostatic effects. On the other hand, with addition of salts, the Coulomb interactions are screened out and the complexation is more sensitive to the hydrophobic interactions. The hydrophobic interactions may also play dominant role in the case of hydrophobically modified PEs and oppositely charged surfactants systems.

From a thermodynamic point of view, the complexation between a polyion and an oppositely charged surfactant is entropically favoured<sup>51</sup>. The positive contribution to the entropy variation due to the release of counterions is more important than the negative contribution from the loss of configurational entropy of PEs. The enthalpy change can be positive or negative depending on the charge density of PEs and the salt concentration. The complexation process is generally endothermic for highly charged PEs and exothermic for weakly charged PEs<sup>52</sup>. The addition of salts weakens the electrostatic interactions and reduces the enthalpy of the binding process. Thus, the complexation may become endothermic at high ionic strength<sup>52,53</sup>.

The complexation process depends on the surfactant concentration as illustrated in Figure 9. In a salt-free solution, at low surfactant concentrations, the charged polar head of surfactant is attracted electrostatically by the PE chain. With increasing the surfactant concentration, the CAC is reached. It corresponds to the point where the PE associates with the surfactant to a measurable degree. In general, the CAC value is a few orders of magnitude lower than CMC of the pure surfactant solution. Above the CAC, PEs start to form aggregates with the surfactants. One PE chain may interact with many micellar aggregates or inversely one micelle may interact with many chains. When the molar ratio reaches 1:1, charges of the polyions are neutralized by that of surfactants. It corresponds to the charge neutralization concentration (CNC). The stoichiometric mixture of PEs and surfactants usually leads to phase separation forming precipitates or ordered structures. In some systems, increasing further the surfactant concentration may allow the re-solubilization of the complex and the formation of micelles if the concentration of free surfactants in solution is higher than CMC. PE/surfactant complexes display a rather complicated phase behaviour, which depends largely on the choice of PE and surfactant. The investigation of phase behaviour has been well reviewed in many articles<sup>51,54,55</sup>.

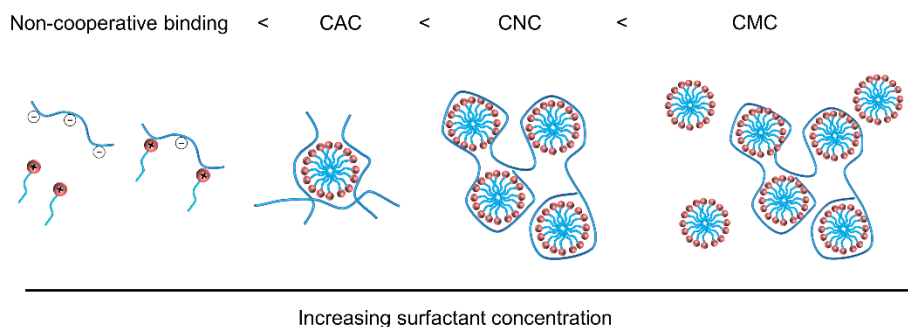


Figure 9 Complexes structure with increasing surfactant concentration. Reproduced from Ref 50.

### I.4.2 Structural organization of the complexes

The structure of surfactant/PE complexes and their phase behaviour result from the balance between electrostatic and hydrophobic interactions. It also depends on the intrinsic properties of PEs (stiffness of the polyion, charge density, degree of polymerization) and surfactants (length of the hydrophobic tail, critical packing parameter, number of charged groups)<sup>50,56,57</sup>. The complexes are also responsive to chemical environment such as the ionic strength, the pH of the solution (weak PE) or the addition of co-solvent<sup>58-60</sup>.

Several typical structures are illustrated in Figure 10. For weakly charged PEs, the system is mainly influenced by hydrophobic interactions, the behaviour is similar to the association of surfactants with neutral polymers. The hydrophobic tail of surfactant has a tendency to interact with PE backbone. We may observe a bottle-brush conformation. We can also find micelle-PE complexes associated in a pearl-necklace structure in which the polyions can penetrate inside the micellar aggregates. Depending on the charge density of PE, the micelles will be densely packed together or separately distributed along the polyion. For more hydrophobic PEs, spherical or worm-like micelles may be formed with the PEs incorporated in the hydrophobic core<sup>61</sup>. When the charge density is higher, the complexation process is dominated by electrostatic interactions. The necklace structure is formed on the condition that the PE chains decorate the micelles rather than penetrating into the core<sup>58</sup>. The stretch extent depends on the flexibility of PE chains. In the case of more rigid PEs or block copolymers, it's possible to obtain a bilayer like structure<sup>62</sup>.

Even if the necklace organization is a globally accepted structure, experiments proving its existence are rather rare. In this thesis, we intend to study the complexes with surfactant of variable hydrophobicity (and packing parameter)

by small-angle scattering. We plan to evidence the structural organization of both components separately and to follow the variations triggered by UV irradiation.

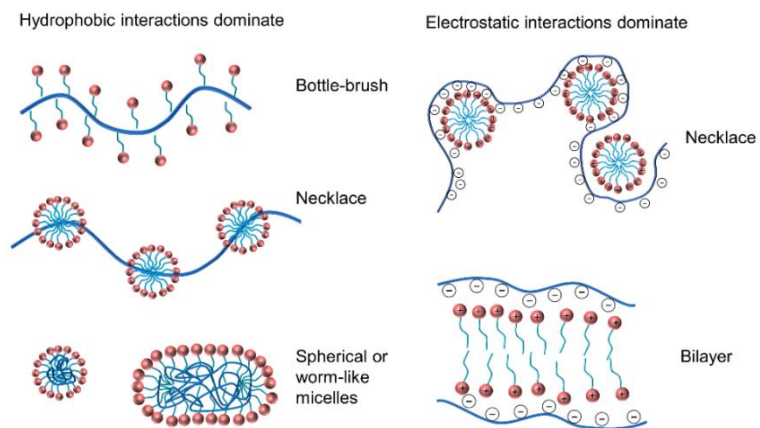


Figure 10 Typical micellar or micelle-like structures formed with PEs. Reproduced from Ref 50.

## References:

- (1) Katchalsky, A.; Künzle, O.; Kuhn, W. Behavior of Polyvalent Polymeric Ions in Solution. *J. Polym. Sci.* **1950**, *5* (3), 283–300.
- (2) Kuhn, W.; Künzle, O.; Katchalsky, A. Verhalten polyvalenter Fadenmolekelionen in Lösung. *Helv. Chim. Acta* **1948**, *31* (7), 1994–2037.
- (3) De Gennes, P. G.; Pincus, P.; Velasco, R. M.; Brochard, F. Remarks on Polyelectrolyte Conformation. *J. Phys.* **1976**, *37* (12), 1461–1473.
- (4) Dobrynin, A. V.; Colby, R. H.; Rubinstein, M. Scaling Theory of Polyelectrolyte Solutions. *Macromolecules* **1995**, *28* (6), 1859–1871.
- (5) Jannink, G.; Cloizeaux, J. des. Polymers in Solution. *J. Phys. Condens. Matter* **1990**, *2* (1), 1–24.
- (6) Muthukumar, M. *50th Anniversary Perspective: A Perspective on Polyelectrolyte Solutions*. *Macromolecules* **2017**, *50* (24), 9528–9560.
- (7) Barrat, J.-L.; Joanny, F. Theory of Polyelectrolyte Solutions. In *Advances in Chemical Physics*; John Wiley & Sons, Ltd, 1996; pp 1–66.
- (8) Dobrynin, A.; Rubinstein, M. Theory of Polyelectrolytes in Solutions and at Surfaces. *Prog. Polym. Sci.* **2005**, *30* (11), 1049–1118.
- (9) Eisenberg, H. Polyelectrolytes, Thirty Years Later. *Biophys. Chem.* **1977**, *7* (1), 3–13.
- (10) Nishida, K.; Kaji, K.; Kanaya, T. Charge Density Dependence of Correlation Length Due to Electrostatic Repulsion in Polyelectrolyte Solutions. *Macromolecules* **1995**, *28* (7), 2472–2475.
- (11) Nishida, K.; Kaji, K.; Kanaya, T. High Concentration Crossovers of Polyelectrolyte Solutions. *J. Chem. Phys.* **2001**, *114* (19), 8671–8677.
- (12) Nallet, F.; Jannink, G.; Hayter, J. B.; Oberthür, R.; Picot, C. Observation of the Dynamics of Polyelectrolyte Strong Solutions by Quasi-Elastic Neutron Scattering. *J. Phys.* **1983**, *44* (1), 87–99.
- (13) Prabhu, V. M.; Muthukumar, M.; Wignall, G. D.; Melnichenko, Y. B. Polyelectrolyte Chain Dimensions and Concentration Fluctuations near Phase Boundaries. *J. Chem. Phys.* **2003**, *119* (7), 4085–4098.
- (14) De la Cruz, M. O.; Belloni, L.; Delsanti, M.; Dalbiez, J. P.; Spalla, O.; Drifford, M. Precipitation of Highly Charged Polyelectrolyte Solutions in the Presence of Multivalent Salts. *J. Chem. Phys.* **1995**, *103* (13), 5781–5791.
- (15) Combet, J.; Isel, F.; Rawiso, M.; Boué, F. Scattering Functions of Flexible Polyelectrolytes in the Presence of Mixed Valence Counterions: Condensation and Scaling. *Macromolecules* **2005**, *38* (17), 7456–7469.
- (16) Krause, R.; Maier, E. E.; Deggelmann, M.; Hagenbüchle, M.; Schulz, S. F.; Weber, R. Static Light Scattering by Solutions of Salt-Free Polyelectrolytes. *Phys. Stat. Mech. Its Appl.* **1989**, *160* (2), 135–147.
- (17) Combet, J.; Rawiso, M.; Rochas, C.; Hoffmann, S.; Boué, F. Structure of Polyelectrolytes with Mixed Monovalent and Divalent Counterions: SAXS Measurements and Poisson–Boltzmann Analysis. *Macromolecules* **2011**, *44* (8), 3039–3052.

- (18) Micka, U.; Holm, C.; Kremer, K. Strongly Charged, Flexible Polyelectrolytes in Poor Solvents: Molecular Dynamics Simulations. *Langmuir* **1999**, *15* (12), 4033–4044.
- (19) Stevens, M. J.; Kremer, K. The Nature of Flexible Linear Polyelectrolytes in Salt Free Solution: A Molecular Dynamics Study. *J. Chem. Phys.* **1995**, *103* (4), 1669–1690.
- (20) Winkler, R. G.; Gold, M.; Reineker, P. Collapse of Polyelectrolyte Macromolecules by Counterion Condensation and Ion Pair Formation: A Molecular Dynamics Simulation Study. *Phys. Rev. Lett.* **1998**, *80* (17), 3731–3734.
- (21) Liu, S.; Muthukumar, M. Langevin Dynamics Simulation of Counterion Distribution around Isolated Flexible Polyelectrolyte Chains. *J. Chem. Phys.* **2002**, *116* (22), 9975–9982.
- (22) Liao, Q.; Dobrynin, A. V.; Rubinstein, M. Molecular Dynamics Simulations of Polyelectrolyte Solutions: Osmotic Coefficient and Counterion Condensation. *Macromolecules* **2003**, *36* (9), 3399–3410.
- (23) Liu, S.; Ghosh, K.; Muthukumar, M. Polyelectrolyte Solutions with Added Salt: A Simulation Study. *J. Chem. Phys.* **2003**, *119* (3), 1813–1823.
- (24) Zhang, R.; Duan, X.; Ding, M.; Shi, T. Molecular Dynamics Simulation of Salt Diffusion in Polyelectrolyte Assemblies. *J. Phys. Chem. B* **2018**, *122* (25), 6656–6665.
- (25) Carrillo, J.-M. Y.; Dobrynin, A. V. Polyelectrolytes in Salt Solutions: Molecular Dynamics Simulations. *Macromolecules* **2011**, *44* (14), 5798–5816.
- (26) Malikova, N.; Čebašek, S.; Glenisson, V.; Bhowmik, D.; Carrot, G.; Vlachy, V. Aqueous Solutions of Ionenes: Interactions and Counterion Specific Effects as Seen by Neutron Scattering. *Phys Chem Chem Phys* **2012**, *14* (37), 12898–12904.
- (27) Odijk, T. Polyelectrolytes near the Rod Limit. *J. Polym. Sci. Polym. Phys. Ed.* **1977**, *15* (3), 477–483.
- (28) Skolnick, J.; Fixman, M. Electrostatic Persistence Length of a Wormlike Polyelectrolyte. *Macromolecules* **1977**, *10* (5), 944–948.
- (29) Dobrynin, A. V. Electrostatic Persistence Length of Semiflexible and Flexible Polyelectrolytes. *Macromolecules* **2005**, *38* (22), 9304–9314.
- (30) Barrat, J.-L.; Joanny, J.-F. Persistence Length of Polyelectrolyte Chains. *Europhys. Lett. EPL* **1993**, *24* (5), 333–338.
- (31) Manning, G. S. Limiting Laws and Counterion Condensation in Polyelectrolyte Solutions I. Colligative Properties. *J. Chem. Phys.* **1969**, *51* (3), 924–933.
- (32) Manning, G. S. Counterion Condensation Theory Constructed from Different Models. *Phys. Stat. Mech. Its Appl.* **1996**, *231* (1–3), 236–253.
- (33) Manning, G. S.; Ray, J. Counterion Condensation Revisited. *J. Biomol. Struct. Dyn.* **1998**, *16* (2), 461–476.
- (34) Turquois, T.; Rochas, C.; Taravel, F.-R.; Doublier, J. L.; Axelos, M.-A.-V. Small-Angle X-Ray Scattering of  $\kappa$ -Carrageenan Based Systems: Sols, Gels, and Blends with Carob Galactomannan. *Biopolymers* **1995**, *36* (5), 559–567.

- (35) Nierlich, M.; Williams, C. E.; Boué, F.; Cotton, J. P.; Daoud, M.; Famoux, B.; Jannink, G.; Picot, C.; Moan, M.; Wolff, C.; Rinaudo, M.; de Gennes, P. G. Small Angle Neutron Scattering by Semi-Dilute Solutions of Polyelectrolyte. *J. Phys.* **1979**, *40* (7), 701–704.
- (36) Essafi, W.; Spiteri, M.-N.; Williams, C.; Boue, F. Hydrophobic Polyelectrolytes in Better Polar Solvent. Structure and Chain Conformation As Seen by SAXS and SANS. *Macromolecules* **2009**, *42* (24), 9568–9580.
- (37) Petit, F.; Iliopoulos, I.; Audebert, R.; Szönyi, S. Associating Polyelectrolytes with Perfluoroalkyl Side Chains: Aggregation in Aqueous Solution, Association with Surfactants, and Comparison with Hydrogenated Analogues. *Langmuir* **1997**, *13* (16), 4229–4233.
- (38) Rajagopalan, V.; Olsson, U.; Iliopoulos, I. Effect of Adsorbing Polyelectrolytes on a Balanced Nonionic Surfactant–Water–Oil System. *Langmuir* **1996**, *12* (18), 4378–4384.
- (39) Iliopoulos, I. Association between Hydrophobic Polyelectrolytes and Surfactants. *Curr. Opin. Colloid Interface Sci.* **1998**, *3* (5), 493–498.
- (40) Rayleigh, Lord. On the Equilibrium of Liquid Conducting Masses Charged with Electricity. *Lond. Edinb. Dublin Philos. Mag. J. Sci.* **1882**, *14* (87), 184–186.
- (41) Kantor, Y.; Kardar, M. Excess Charge in Polyampholytes. *Europhys. Lett. EPL* **1994**, *27* (9), 643–648.
- (42) Dobrynin, A. V.; Rubinstein, M.; Obukhov, S. P. Cascade of Transitions of Polyelectrolytes in Poor Solvents. *Macromolecules* **1996**, *29* (8), 2974–2979.
- (43) Dobrynin, A. V.; Rubinstein, M. Hydrophobic Polyelectrolytes. *Macromolecules* **1999**, *32* (3), 915–922.
- (44) Essafi, W. Structure Des Polyelectrolytes Fortement Charges. Thesis, Université Paris VI, 1996.
- (45) Spiteri, M. N. Conformation et Arrangement Des Polyelectrolytes En Solution Semi-Diluee. Etude Par Diffusion Des Neutrons Aux Petits Angles. Thesis, Université de Paris-Sud Orsay, 1997.
- (46) Baigl, D.; Ober, R.; Qu, D.; Fery, A.; Williams, C. E. Correlation Length of Hydrophobic Polyelectrolyte Solutions. *Eur. Lett* **2003**, *62* (4), 588–594.
- (47) Spiteri, M. N.; Williams, C. E.; Boué, F. Pearl-Necklace-Like Chain Conformation of Hydrophobic Polyelectrolyte: A SANS Study of Partially Sulfonated Polystyrene in Water <sup>†</sup>. *Macromolecules* **2007**, *40* (18), 6679–6691.
- (48) Zhou, S.; Chu, B. Assembled Materials: Polyelectrolyte–Surfactant Complexes. *Advanced Materials* **2000**, *12* (8), 545–556.
- (49) Uchman, M.; Gradzielski, M.; Angelov, B.; Tošner, Z.; Oh, J.; Chang, T.; Štěpánek, M.; Procházka, K. Thermodynamic and Kinetic Aspects of Coassembly of PEO–PMAA Block Copolymer and DPCI Surfactants into Ordered Nanoparticles in Aqueous Solutions Studied by ITC, NMR, and Time-Resolved SAXS Techniques. *Macromolecules* **2013**, *46* (6), 2172–2181.
- (50) Khan, N.; Brettmann, B. Intermolecular Interactions in Polyelectrolyte and Surfactant Complexes in Solution. *Polymers* **2018**, *11* (1), 51.

- (51) Lindman, B.; Antunes, F.; Aidarova, S.; Miguel, M.; Nylander, T. Polyelectrolyte-Surfactant Association—from Fundamentals to Applications. *Colloid J.* **2014**, *76* (5), 585–594.
- (52) Ou, Z.; Muthukumar, M. Entropy and Enthalpy of Polyelectrolyte Complexation: Langevin Dynamics Simulations. *J. Chem. Phys.* **2006**, *124* (15), 154902.
- (53) Nizri, G.; Lagerge, S.; Kamyshny, A.; Major, D. T.; Magdassi, S. Polymer–Surfactant Interactions: Binding Mechanism of Sodium Dodecyl Sulfate to Poly(Diallyldimethylammonium Chloride). *J. Colloid Interface Sci.* **2008**, *320* (1), 74–81.
- (54) Langevin, D. Complexation of Oppositely Charged Polyelectrolytes and Surfactants in Aqueous Solutions. A Review. *Adv. Colloid Interface Sci.* **2009**, *147–148*, 170–177.
- (55) Gradzielski, M.; Hoffmann, I. Polyelectrolyte-Surfactant Complexes (PESCs) Composed of Oppositely Charged Components. *Curr. Opin. Colloid Interface Sci.* **2018**, *35*, 124–141.
- (56) Kayitmazer, A. B.; Shaw, D.; Dubin, P. L. Role of Polyelectrolyte Persistence Length in the Binding of Oppositely Charged Micelles, Dendrimers, and Protein to Chitosan and Poly(Dimethyldiallylammonium Chloride). *Macromolecules* **2005**, *38* (12), 5198–5204.
- (57) Goswami, M.; Borreguero, J. M.; Pincus, P. A.; Sumpter, B. G. Surfactant-Mediated Polyelectrolyte Self-Assembly in a Polyelectrolyte–Surfactant Complex. *Macromolecules* **2015**, *48* (24), 9050–9059.
- (58) Lam, V. D.; Walker, L. M. A pH-Induced Transition of Surfactant–Polyelectrolyte Aggregates from Cylindrical to String-of-Pearls Structure. *Langmuir* **2010**, *26* (13), 10489–10496.
- (59) Wang, X.; Li, Y.; Li, J.; Wang, J.; Wang, Y.; Guo, Z.; Yan, H. Salt Effect on the Complex Formation between Polyelectrolyte and Oppositely Charged Surfactant in Aqueous Solution. *J. Phys. Chem. B* **2005**, *109* (21), 10807–10812.
- (60) Pojják, K.; Bertalanits, E.; Mészáros, R. Effect of Salt on the Equilibrium and Nonequilibrium Features of Polyelectrolyte/Surfactant Association. *Langmuir* **2011**, *27* (15), 9139–9147.
- (61) Plazzotta, B.; Fegyver, E.; Mészáros, R.; Pedersen, J. S. Anisometric Polyelectrolyte/Mixed Surfactant Nanoassemblies Formed by the Association of Poly(Diallyldimethylammonium Chloride) with Sodium Dodecyl Sulfate and Dodecyl Maltoside. *Langmuir* **2015**, *31* (26), 7242–7250.
- (62) Chiappisi, L.; Hoffmann, I.; Gradzielski, M. Complexes of Oppositely Charged Polyelectrolytes and Surfactants – Recent Developments in the Field of Biologically Derived Polyelectrolytes. *Soft Matter* **2013**, *9* (15), 3896.



# Chapter II. The state of the art of “smart” photosensitive systems in aqueous solution

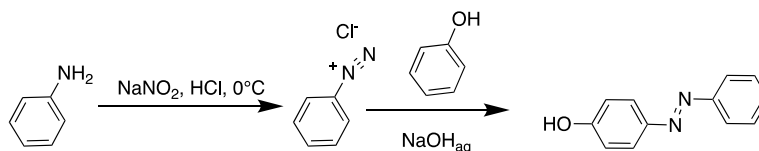
Chromophores are usually conjugated systems that absorb light. Under a suitable light source irradiation, photoactive molecules can undergo photoisomerization (*i.e.*, stilbene<sup>1,2</sup>, azobenzene<sup>3</sup>), photocleavage (*i.e.*, *o*-nitrobenzyl ester<sup>4,5</sup>, coumarin<sup>6</sup>) or ring opening/closing reaction (*i.e.*, dithienylethene<sup>7,8</sup>, spiropyran<sup>9–11</sup>) in a reversible or irreversible way.

In this chapter, we will focus on azobenzene derivatives. We will give a general presentation of the structural and physical properties, as well as their response to light irradiation. Remarkable works of these photo-tunable systems will be summarized.

## II.1 Azobenzene

### II.1.1 Overview of azobenzene properties

Azobenzene (Azo) is an extensively studied chromophore showing a very efficient photochemical isomerization. Azo family was firstly discovered as commercial synthetic colouring agents in 1800s and used in textile, printing and paper manufacturing<sup>12</sup>. In 1937, Hartley and coworkers observed for the first time the *trans*  $\rightleftharpoons$  *cis* photoisomerization of azobenzene and could successfully isolate the *cis* isomer<sup>13</sup>. Since then, the photochemistry of the Azo family has gained great attention and a large variety of azo-containing photoresponsive systems have been developed. The *trans/cis* photoconversion is a totally reversible process, triggered simply by a light stimulus within the large absorption band of the *trans* configuration. Azo, is a robust molecule, which shows a remarkable photostability even after prolonged irradiation. Azo compounds can be synthesized from the well-known azo-coupling reaction, including the first diazotization of primary aromatic amine to form its diazonium salt and then the coupling reaction between the diazonium salt and another aromatic compound (Scheme 1). Methods of Azo family synthesis and their functionalization have been well developed and described in a large literature<sup>14–16</sup>.



Scheme 1 Synthesis route of azobenzene.

The thermal stable *trans* conformation adopts a planar structure with a near-zero dipole moment (Figure 1a). Upon irradiation with UV light, Azo undergoes a transformation from a *trans* to a *cis* isomer. This photoinduced transition is accompanied by a significant decrease of distance between the two phenyls, and the increase of the dipole moment from near zero to 3 Debye (for Azo without substituents). The *cis*-Azo state has a bent conformation with the phenyl rings twisted  $55^\circ$  out of the plane from the initial Azo group. The reverse transformation (*cis*  $\rightarrow$  *trans*) can occur either by thermal relaxation in the dark or by irradiation with blue light (within the absorption band of the *cis* state).

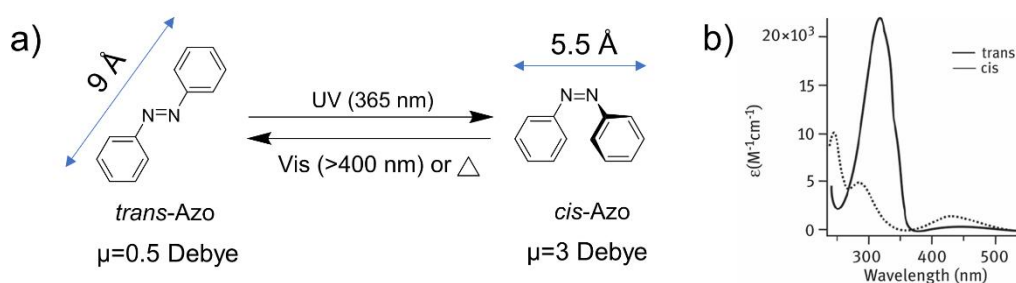


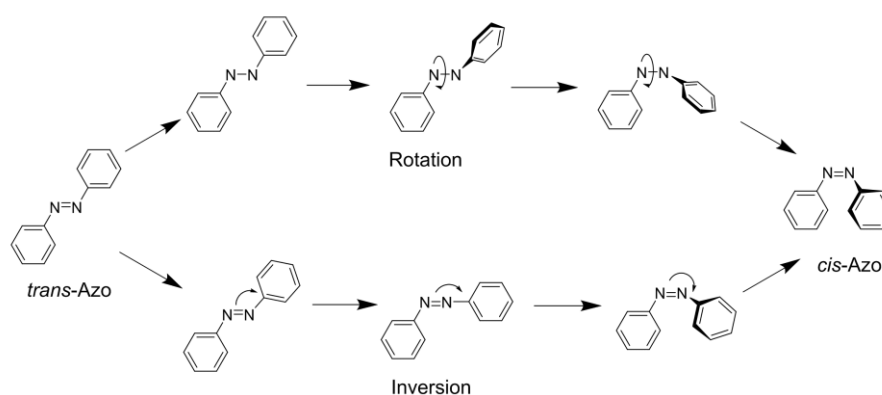
Figure 1 a) Structures of *trans* and *cis* isomers of azobenzene; b) Absorption spectra of *trans* and *cis* isomers of azobenzene dissolved in ethanol. Adapted from Ref 17.

As shown in Figure 1b, the conjugated  $\pi$  system of Azo results in a strong electronic absorption. For *trans* isomer, a strong absorption band is observed around 320 - 350 nm (depending on the nature of the substituent and the solvent) and arises from the  $\pi \rightarrow \pi^*$  transition. A weaker band appears in the visible region (around 440 nm) for the  $n \rightarrow \pi^*$  transition. Upon UV irradiation, the *trans*-form converts to the *cis* form leading to a decrease of the absorption band in the UV region and the increase of the band in the visible region. In the same time, the  $\pi \rightarrow \pi^*$  transition band of *cis* isomer is displaced to a shorter wavelength around 260 - 300 nm.

## II.1.2 Isomerization mechanism

The mechanism of photoisomerization has been a controversial subject<sup>18–21</sup>. Two main mechanisms –rotation and inversion- have been proposed (Scheme 2). The rotation pathway begins with the rupture of the N=N double bond allowing a free rotation around the N-N single bond. The C-N-N-C dihedral angle is changed by an out of plane torsion, whereas the N-N-C angle remains fixed at about 120°. Finally, the reformation of the double N=N bond leads to the *cis* isomer.<sup>19</sup>

For the inversion mechanism, the isomerization occurs via an in-plane inversion of the N=N-C angle between the Azo group and the adjacent carbon of the phenyl ring. The C-N-N-C dihedral angle is fixed at 0°. The N=N-C angle increases to 180° forming a transition state with one *sp* hybridized azo-nitrogen atom<sup>20,21</sup>.



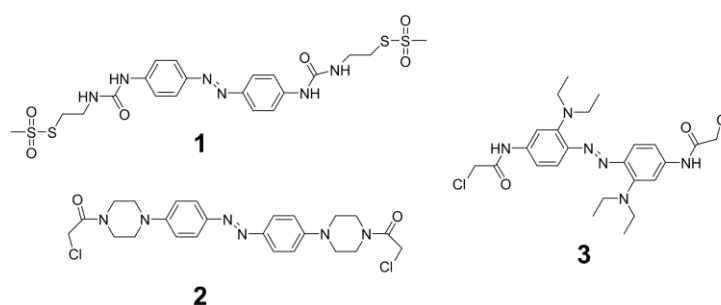
Scheme 2 Proposed mechanisms for azobenzene *trans* ↔ *cis* isomerization. Reproduced from Ref 21.

## II.1.3 Effect of the substitution on azobenzene isomerization

The absorption band (and therefore, the optimal wavelengths for photoisomerization) can be strongly influenced by the substituents on the phenyl rings. An electron donor group at the *ortho* or *para* positions of the benzene rings can lead to a red-shift (*i.e.*, longer wavelength) of the absorption spectra of *trans*-Azo<sup>22</sup>. This effect is highly desirable for photo-switch biological applications where long wavelengths are needed for the irradiation<sup>17,22–25</sup>. The red-shift can be even more important with an acceptor group at one *para* position and a donor group at the other *para* position (push-pull type Azo)<sup>26</sup>. Because of their polarized structure, the absorption properties of 'push-pull' Azo are also solvent dependent<sup>24</sup>.

The ring-substituents also affects the lifetime of the metastable *cis* isomer

(generally on the order of hours). Introducing electron-donor or ‘push-pull’ type groups can lower the thermal energy barrier of the *trans*  $\rightleftharpoons$  *cis* photoconversion and thus accelerate the rate of thermal isomerization. Fast thermal relaxation means that it is difficult to maintain a steady fraction of *cis* isomer for a long period of time. The Woolley group have designed a series of red-shifted Azo compounds<sup>22,27,28</sup>, presented in Figure 2. The *para*-substituted Azo compound (**1**) and (**2**) shifts the maximum absorbance to 382 nm and 450 nm respectively with a half-life on the order of seconds. The *para*- and *ortho*- substituted (**3**) is further red-shifted, but the lifetime of its *cis* isomer is much shortened.



Compound	$\lambda_{max}$ (trans)	$\tau_{1/2}$ (cis to trans)
1	382 nm	11 s
2	450 nm	2 s
3	530 nm	0.7 s

Figure 2 Structures of red-shifted Azo compounds Ref 22,27,28.

The incorporation of bulky substituent or more generally, the introduction of conformational strain on the macrocyclic compounds can increase the thermal energy barrier for the back-isomerization and hence, improve the stability of the *cis*-form. An azo derivative with *para*-substituted bulky groups created by Shirota et al.<sup>29</sup> has a lifetime of 60 days. Rau et al.<sup>30</sup> reported an azobenzenophanes with three-carbon bridges for which the *cis*-form is stable at room temperature with a lifetime of about a year.

#### II.1.4 Photostationary state

After a certain irradiation time, Azo containing systems (bulk or solution) reach a photostationary state. In this equilibrium state, the rates of the photo-induced *trans*-to-*cis* isomerization is identical to the rate of photo- and heat-induced *cis*-to-*trans* isomerization. The composition in *cis* and *trans* isomers

remains constant. The UV-Vis absorption spectroscopy and NMR are common technics to determine the *trans/cis* fraction in the stationary state.

The *trans*  $\rightleftharpoons$  *cis* isomerization is always a dynamic equilibrium. For most of Azo derivatives, the photoconversion under light irradiation will never lead to a final state containing 100% *cis*-Azo or 100% *trans*-Azo. The composition at the steady state depends on the excitation properties (wavelength and intensity) but also on the absorption spectra of the compound<sup>31,32</sup>. Light sources with a narrow wavelength distribution minimize the inverse conversion caused by undesired wavelengths, are used preferably. For classical Azo compounds, the stationary state contains predominantly the *cis* isomers under UV irradiation. For red-shifted Azo derivatives, the absorption spectra of *cis* and *trans* isomers overlap, the stationary state is a mixture that may contain more or less *cis* isomers. In some cases, a single wavelength can promote both the forward and the reverse photoreactions, leading to a continual interconversion between the two isomers.

Tabor et al.<sup>33</sup> reported that the concentration of Azo compounds also affects the *trans/cis* ratio at the stationary state. He found that the kinetic of *trans*  $\leftrightarrow$  *cis* conversion was not first order, suggesting a diffusion limited process. The penetration of irradiation light may be limited by the strong absorption of the solution, which results in a rapid isomerisation of uppermost Azo molecules, followed by a diffusion-limited mixing and photoconversion of the remaining Azo molecules. This situation is very important in this thesis, since we usually work on thick samples of large absorption. The typical time needed to reach the stationary state will highly depend on the diffusion coefficient of the Azo molecules (or Azo containing particles).

Since *trans* isomer is a thermally stable isomer, the fraction of *cis* isomers in the dark state is lower than most detection limits. Thus, without visible light irradiation, the thermal *cis*-to-*trans* relaxation can lead to an all-*trans* steady state. A sample kept in dark for long enough time can be considered as composed of 100% *trans* isomers.

## II.2 The state of the art of azobenzene based materials

Azo derivatives show a large flexibility and versatility in molecular design. Azo moiety can be inserted into a matrix, attached by covalent bond or mixed in a non-covalent way (electrostatic, hydrophobic or  $\pi$ - $\pi$  interactions). Many Azo derivatives have been used in different types of materials to provoke a photosensitive response: polymer systems<sup>34</sup>, liquid crystals<sup>35</sup>, colloidal assemblies<sup>36,37</sup>, layer-by-layer thin films. Notable achievements have been done in biological systems in which Azo compounds were used as light-triggered ligands or cross-linkers and allowed the control of the structure and the function of peptides, proteins, DNA *etc*<sup>17,38</sup>. In this work, we will exclusively focus on photo-responsive systems in aqueous solution, including Azo-containing macromolecules, Azo-containing surfactants and Azo-surfactant/Polyelectrolyte systems.

### II.2.1 Amphiphilic photoresponsive polymers

Amphiphilic polymers are bearing both hydrophilic and hydrophobic units. The hydrophilic substituent can be charged, ionisable or neutral. Typically, sulfonate, pyridyl, carboxyl, hydroxyl and amino groups are used as hydrophilic group. Water soluble poly(ethylene glycol) (PEG) can be used for the polymer design as well. A large variety of architectures can be obtained by varying the polymer architecture, the monomer structure, the type and ratio of hydrophobic substituent, the molecular weight of polymer. Owing to their amphiphilic properties, amphiphilic polymers are widely used both in daily living and industry as rheology modifiers, adhesives, stabilizers and suspending agents for drug delivery systems.

Azo-containing amphiphilic polymers (Azo-polymers) have gained an increasing attention for their excellent photo-responsive ability. The photoisomerization from *trans*-apolar isomer to *cis*-polar isomer may affect the polymer structure leading to large modifications such as phase transition, the swelling/shrinking of polymer, micelles deformation. We introduce hereafter some typical examples. The presentation of synthesis strategies for amphiphilic Azo-polymers can be found in Appendix d).

Amphiphilic Azo-polymers is widely used to prepare multilayer films through a layer-by-layer process. Highly light sensitive hollow capsules were prepared by multilayer films, using an alternative deposition of poly[1-[4-(3-carboxy-4-hydroxyphenylazo)benzenesulfonamido]-1,2-ethanediyl, sodium salt] (PAZO) and polydiallyldimethylammonium chloride (PDADMAC) on silicon dioxide templates<sup>39</sup>. After removing the template (using 0.2 M NH<sub>4</sub>F and HF buffer solution at pH = 4.5), the capsules were illuminated with UV radiation. The AZO moieties in the multilayers tend to self-organize in the form of J-aggregates. The re-orientation of Azo moieties within shell formations destroyed progressively the integrity of capsule until the final breakage (Figure 3). This UV induced capsule breakage offered a new way to modulate the release of encapsulated drugs.

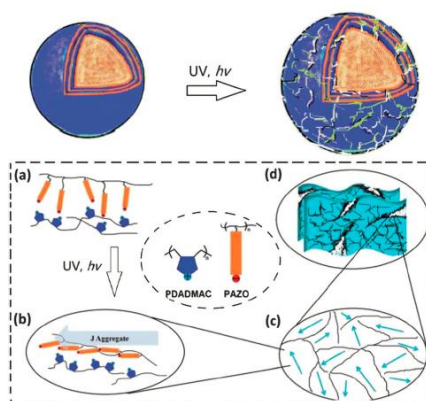


Figure 3 Schematic illustration of (PDADMAC/PAZO) microcapsule disruption induced by UV irradiation. Adapted from Ref <sup>39</sup>.

Colloidal particles can be constructed from random amphiphilic Azo-polymers in selective solvents. The general preparation process consists of dissolving the polymer in an organic solvent and adding gradually water in the polymer solution. By increasing the water content, the solubility of polymers in the mixed aqueous-organic dispersion media is decreased, which promotes its gradual aggregation<sup>40</sup>. For example, the random copolymer shown in Figure 4, can form micro-particles in aqueous media<sup>41</sup>. The formation of colloidal particles was provoked by gradual addition of different NaOH solutions of different concentrations to the THF copolymer solutions. They found that the particle size depends on the Azo molar fraction in the copolymers and the preparation conditions (such as the nature and the evaporation rate of the solvents). However, they did not investigate the structural modifications under UV irradiation.

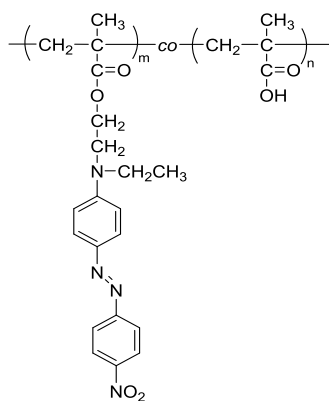


Figure 4 Structure of amphiphilic copolymer.

Li et al.<sup>42,43</sup> reported that uniform colloidal spheres could be formed from polyacrylic acid based random Azo-polymer (Figure 5, R = H) in THF/H<sub>2</sub>O mixed solution. Aggregates started to form above a critical water content (25%), and the colloids grew as the water content increased (Figure 6). The photoisomerization behavior and the morphology modification upon UV irradiation were investigated. Aggregates totally disrupted when the water content was below 37.5 vol%. For higher values (50-80 vol%), colloidal spheres could be partially disaggregated by UV light irradiation.

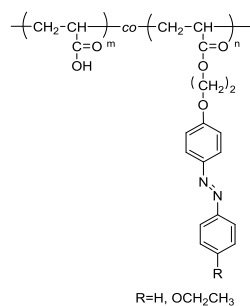


Figure 5 Scheme of poly(acrylic acid) based Azo-polyelectrolytes.

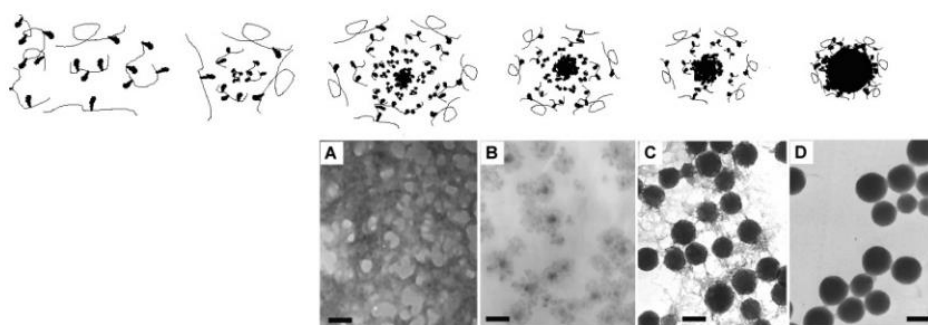


Figure 6 Schematic representation of the sphere formation process and the TEM images of samples obtained with different water contents. Water content (vol %): a) 20%, b) 30%, c) 40% and d) 50%. The scale bars in the figures are 100 nm. Adapted from Ref <sup>43</sup>.

A quite similar amphiphilic Azo-polymer shown in Figure 5 (with R = OCH<sub>2</sub>CH<sub>3</sub>), was found to form hollow spheres by mixing polymer aqueous solutions (in THF/water media (v:v = 1:1)), and slowly evaporating THF<sup>44</sup>. Factors such as the polymer initial concentration in THF, water addition rate, and diluent volume affected the size and shell thickness of the hollow spheres. “Vesicle-like” spheres underwent an obvious morphological transition when exposed to the UV light (Figure 7).

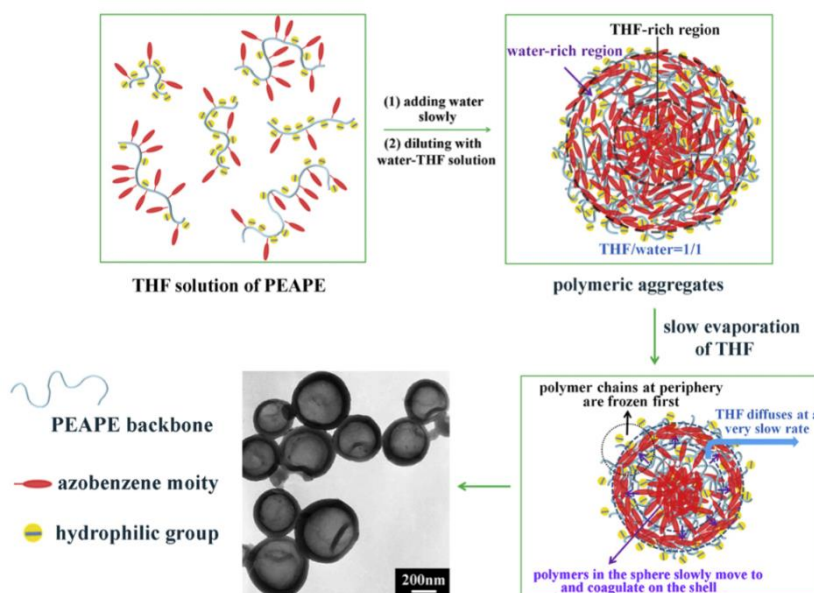


Figure 7 Schematic illustration of the formation of the hollow microspheres. Adapted from Ref <sup>44</sup>.

Diblock and triblock Azo-polymers have gained an increasing attention due to their well-controlled structure and the wide morphological possibilities. More precisely the size and the form of the self-assemblies can be varied by the nature and the length of the blocks as well as the nature of the solvent (and co-solvent). The preparation process is also an important factor that influences the final morphology of the system. As an example, diblock copolymer PAzoMA-*b*-PAA (Figure 8) can form micellar aggregates in H<sub>2</sub>O/dioxane solvent<sup>45</sup>. The morphology (vesicles or micelles) depends on the water fraction. The photoisomerization of Azo units can lead to the deformation and the fusion of the vesicles under UV light illumination (Figure 9).

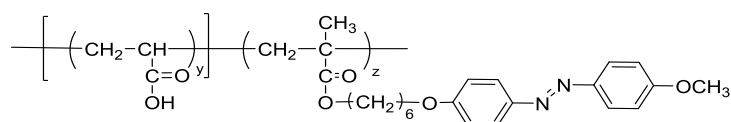


Figure 8 Synthesis route of diblock copolymer PAzoMA-*b*-PAA.

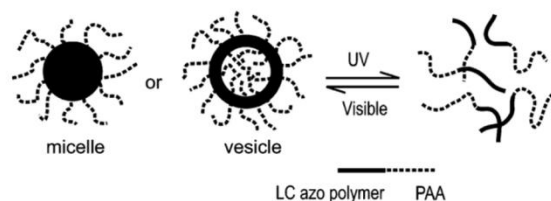


Figure 9 Schematic representation of the disruption and the reformation of vesicles upon UV and visible light irradiation. Adapted from Ref 45.

Finally, random amphiphilic Azo-polymers can also be used as a light-triggered modulator in complex systems with surfactants and proteins. When mixed with Bovine Serum Albumin (BSA), random amphiphilic Azo-polymers (Figure 10) form complexes with photoresponsive properties<sup>46</sup>. Reversible light triggered association is observed in water solution leading to large variations of the viscosity. The affinity of BSA for the polymer depends both the length of the hydrophobic spacer on the azobenzene and the presence of additional *n*-alkyl side groups.

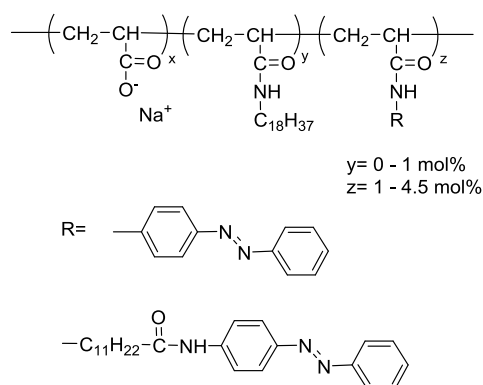


Figure 10 Structure of random Azo-modified poly(acrylic acid).

The light-responsive association/dissociation of complexes between neutral surfactant (TX100) and random Azo-modified polymers derived from polyacrylic acid was investigated (Figure 11)<sup>47</sup>. The binding isotherms of TX100 were determined by capillary electrophoresis. Micelle-like clusters were formed due to hydrophobic interactions between Azo-containing side groups and micelles of TX100 (above the CMC) as shown in Figure 12. It is proposed that some Azo groups may be anchored in the TX100 micelles. This process depends on the

distance between adjacent chromophores and is controlled by the free energy of created loop. Exposure to UV light decreases the free-energy of Azo association and thus Azo-anchors detach from TX100 micelles. The maximum response was obtained when the molar ratio of bound azobenzene to bound surfactant is low, most typically below 20:100.

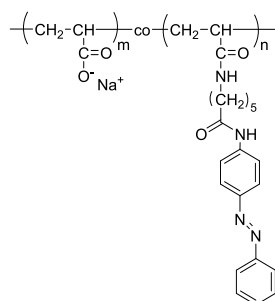


Figure 11 structure of Azo-modified poly(acrylic acid).

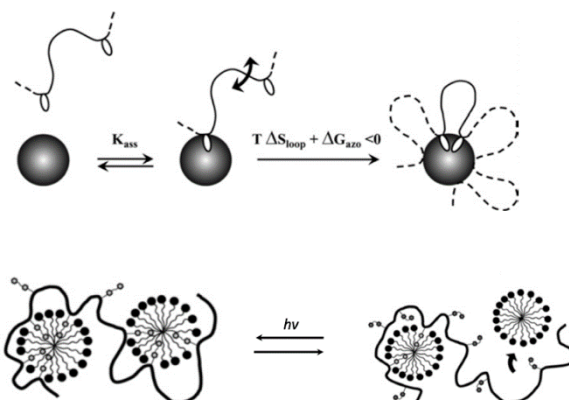


Figure 12 Illustration of AMP multiple association onto a hydrophobic cluster and the variation of the composition of complexes upon light irradiation. Adapted from Ref 47.

## II.2.2 Self-assembly of photoresponsive surfactants in aqueous solution

### II.2.2.1 Photoresponsive surfactants

Azo-containing surfactants (Azo-surfactant) are a widely investigated light-responsive amphiphile family. Azo-surfactant is composed of a hydrophilic polar head, an Azo group and a hydrophobic tail. A spacer is usually introduced between the polar head and the chromophore. The hydrophilic head can be cationic, anionic or neutral, the most commonly used being the trimethylammonium and di(ethyleneoxide) groups. Surfactants form micellar aggregates at a concentration above the critical micelle concentration (CMC). Light stimulus can trigger the polarity and the conformation of Azo moiety leading to a modification of the hydrophobicity and the critical packing parameter of the surfactant. Herein, UV

irradiation can change the CMC and the morphology of the micelles. A subtle selection of the tail and spacer lengths enables to amplify these photo-induced effects. Synthesis and structural characterisation of diverse Azo-surfactants have been reported. We only present here several Azo-surfactants, which show interesting response to light stimulus.

$C_m\text{Azo}C_n\text{TAB}$  is the most studied structure of Azo-surfactants (Figure 13). The relation between the total length of the hydrophobic segment ( $R_1 + R_2$ ) and the CMC value was investigated by Hayashita *et al.*<sup>48</sup> (moderate total length,  $4 \leq R_1+R_2 \leq 8$ ) and Blayo *et al.*<sup>36</sup> (from moderate to long total length,  $8 \leq R_1+R_2 \leq 14$ ). The driving force for the micellization is the presence of hydrophobic segment. Increasing the tail or the spacer length can decrease the CMC. Additionally, the tail length has a stronger influence on the CMC than the spacer. For a fixed total hydrophobic length, a longer tail leads to a lower CMC.

Under UV irradiation, most of the Azo adopt a *cis* conformation, the surfactants become more hydrophilic (while the CPP is changed). Consequently, the CMC of the *cis* conformation ( $\text{CMC}_{cis}$ ) is always higher than that of the *trans* state ( $\text{CMC}_{trans}$ ). The difference between the CMC of *trans* and *cis* isomers ( $\Delta\text{CMC}$ ) is maximum for a total hydrophobic length of 6 carbons ( $\Delta\text{CMC} = 5.9 \text{ mmol L}^{-1}$  for  $C_2\text{Azo}C_4\text{TAB}$ ).  $\Delta\text{CMC}$  represents the range of concentrations in which micelles are formed only for the *trans* isomers but also, where micelles are disassociated into single surfactant molecules under UV light exposure. A large  $\Delta\text{CMC}$  range may be especially interesting for the reversible release of drug or reversible encapsulation. The size and shape of various cationic azo-surfactants micelles above the CMC have been measured by SANS and reported on different systems<sup>36,49–51</sup>. Blayo *et al.*<sup>36</sup> found that azo-surfactants bearing hydrophobic segments from 8 to 14 carbons self-assemble into ellipsoidal or elliptical cylinder micelles. The aggregation number increases with the total length ( $R_1 + R_2$ ). The structural modification under UV illumination varies with the Azo position along the surfactant molecule. The *cis*-aggregates adopt sphere or ellipsoidal shapes with smaller size and smaller aggregation number.

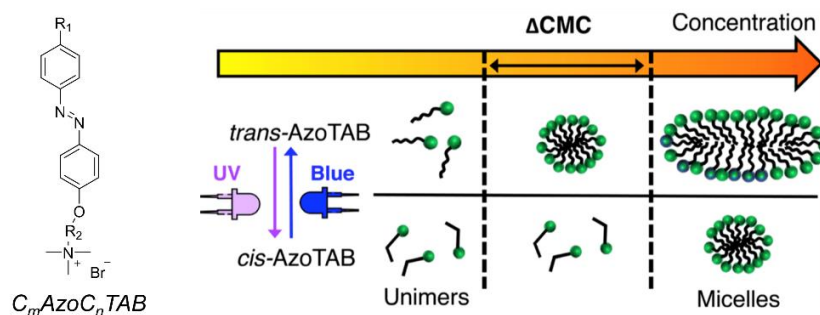


Figure 13 Schematic illustration of structural variation of Azo-surfactant micelles. Adapted from Ref 36.

Kozlecki et al.<sup>52</sup> have synthesized and studied two classes of anionic Azo-surfactants by surface tension and cyclic voltammetric techniques. Compared to the standard anionic surfactants (without Azo)  $C_nSO_3Na$  and  $C_nCO_2Na$  (Figure 14), the addition of Azo moiety to the hydrophobic tail improves both adsorption and micellization properties, and leads to a decrease of the CMC values. Kozlecki suggested that the Azo moiety is hydrophobically equivalent to 8.4 units of  $CH_2$  in the alkyl chain.

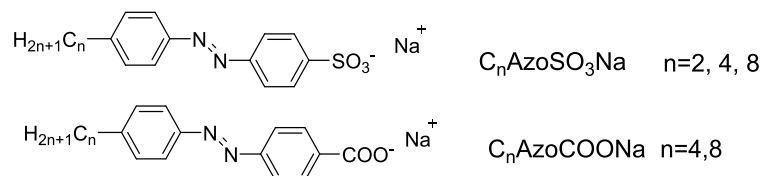


Figure 14 Structure of anionic Azo-surfactants  $C_nSO_3Na$  and  $C_nCO_2Na$ .

Shang et al.<sup>53</sup> investigated a class of nonionic photoresponsive surfactants composed of a polar di(ethyleneoxide) head and a spacer varying between 2 and 8 methylene groups ( $C_4AzoC_nE_2$ ) as given in Figure 15. For the *trans*-form, they found a linear decrease of the  $CMC_{trans}$  when increasing the spacer length from two to six methylene groups. The variation of the  $CMC_{cis}$  is not monotonic as in the case of charged Azo-surfactants. For the *cis*-form, the  $CMC_{cis}$  of  $C_4AzoC_2E_2$  is three times larger than that of  $C_4AzoC_4E_2$ . However, a further increase of spacer length to 6  $CH_2$  results in a decrease of the  $CMC_{cis}$  value.

For surfactants with 8  $CH_2$  spacers, the hydrophobic interaction predominates resulting in immediate aggregation and precipitation in the *trans*-form.

The maximum  $\Delta CMC$  was 21.1  $\mu M$  with  $C_4AzoC_4E_2$ . And the largest surface tension modification was found with four  $CH_2$  and six  $CH_2$ , approximately 10  $mM m^{-1}$ . The structure of the aggregates formed by  $C_4AzoC_4E_2$  and  $C_4AzoC_6E_2$  was further investigated. The *trans*- $C_4AzoC_4E_2$  and *trans*- $C_4AzoC_6E_2$  self-assemble

into bilamellar and unilamellar vesicles respectively, while both *cis* isomers form a bicontinuous phases under UV light<sup>37</sup>.

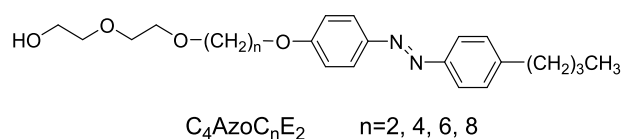


Figure 15 Structure of nonionic Azo-surfactant  $C_4AzoC_nE_2$ .

Tabor et al.<sup>33</sup> have designed three photoswitchable carbohydrate-based surfactants (Figure 16). Structural modifications under radiation were monitored *in situ* by time-resolved small-angle neutron scattering. The micelle morphology and the aggregation number depend on surfactant concentration. At a concentration near the  $CMC_{trans}$  value, UV irradiation causes a complete disaggregation of the micelles. At a concentration slightly higher than the  $CMC_{cis}$ , the rod-like micelles formed by *trans* isomers convert into smaller spherical micelles formed by *cis* isomers upon UV irradiation. For a concentration much higher than the  $CMC_{cis}$ , *trans/cis* isomerization only leads to a decrease of the diameter of rod-like micelles, whereas the length is unaffected.

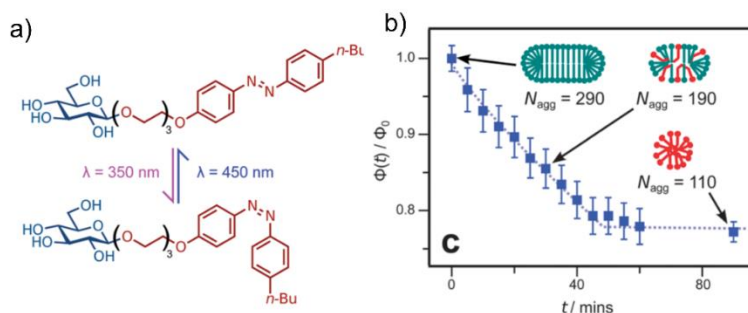


Figure 16 a) Structure of carbohydrate-based Azo-surfactants; b) Volume fraction of micelles in solution ( $\phi(t)$ ) as photoisomerization progresses (from fits of SANS data). Adapted from ref 33.

### II.2.2.2 Wormlike micelles

It is well known that certain cationic surfactants with long alkyl chain and aromatic salts (e.g., tosylate, cinnamate, salicylate) can form thread-like micelles in aqueous solution resulting in an entangled network with a pronounced viscoelasticity<sup>54</sup>. Typical systems are cetyltrimethylammonium bromide (CTAB) with sodium salicylate (NaSal)<sup>55</sup> or dichlorobenzoate<sup>56</sup> and

dodecyltrimethylammonium chloride (DTAC) with NaSal<sup>57</sup>.

The impact of additives on the micelles morphology can be rationalized on the basis of the critical packing parameter (CPP) (Figure 17). The CPP value is defined as  $CPP = V/al$ , where  $V$  is the volume of the hydrophobic part of the surfactant,  $a$  is the effective area of the headgroup at the micelle/water interface and  $l$  is the length of the hydrophobic tail. Globular micelles are formed with  $P < 1/3$ . Surfactants with  $1/3 < P < 1/2$  rather form cylindrical assemblies, such as wormlike micelles. When  $P > 1/2$ , we usually observe vesicles or bilayers. Addition of aromatic anions can screen the electrostatic repulsion between hydrophilic headgroups, and thus decrease the effective headgroup surface  $a$ . Aromatic salts embedded in the micelles modifies the volume of single surfactant as well, resulting in the increase of the packing parameter. As a result, micellar aggregates grow into long, flexible micelles, referred to as “wormlike” or “threadlike” micelles.

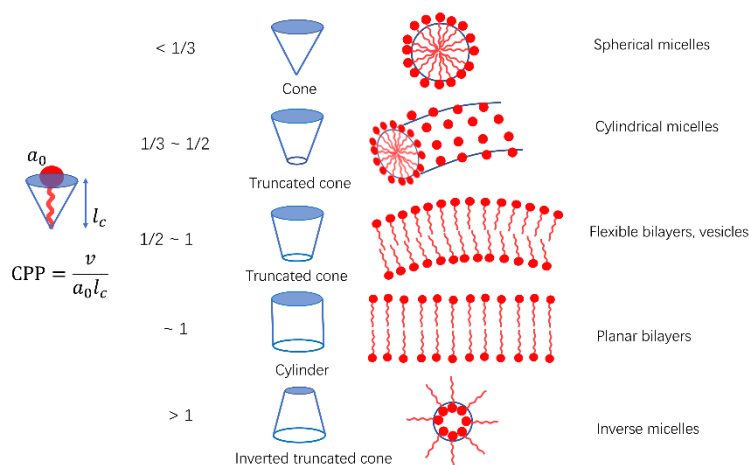


Figure 17 Molecular shapes and critical packing parameter (CPP) of surfactants.

The addition of Azo-containing derivatives into such systems makes it possible to switch ‘on’ or switch ‘off’ the viscoelastic properties by simple light irradiation, which may have potential applications in recirculating systems. There have been several studies to control the formation and the disruption of wormlike micelles by light stimulus. Sakai et al.<sup>58</sup> studied the rheological properties of a photoresponsive wormlike systems consisting of CTAB, an Azo-surfactant ( $C_4AzoC_2TAB$ ) and NaSal in a molar ratio 1:0.2:1. Addition of *trans*- $C_4AzoC_2TAB$  to a wormlike solution of CTAB/NaSal 1/1 further increased the viscosity  $\eta_0$  from 60 Pa·s to 100 Pa·s. Under UV light irradiation, the viscosity of the three components mixture decreases dramatically (100 Pa s to 0.1 Pa s), indicating a clear modification of the shape of the aggregates. However, there was no direct

structural studies on these systems. They finally assumed that the *trans* form of the Azo-surfactant was easier to incorporate into wormlike micelles of CTAB/NaSal due to the linear structure. While, the bent *cis* form is likely to destroy the network organisation.

Takahashi et al.<sup>59</sup> reported systems made of CTAB and sodium [4-(4-butylphenylazo)phenoxy]acetate (C<sub>4</sub>AzoNa), which showed an opposite light-response behaviour (Figure 18). A highly viscous mixture was formed upon UV irradiation while the viscosity decreased significantly with visible light irradiation (from 10 Pa s to 0.01 Pa s). They suggested that when the *trans*-C<sub>4</sub>AzoNa is packed linearly in the globular aggregates, the CPP value is < 1/3 for the mixture, while it is increased for bulky *cis*-C<sub>4</sub>AzoNa, favouring the formation of wormlike micelles.

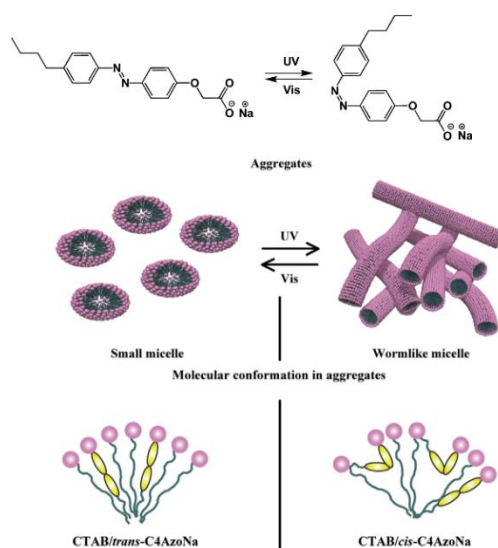


Figure 18 Photoisomerization of C<sub>4</sub>AzoNa and possible mechanism for the formation and disruption of wormlike micelles by light irradiation. Adapted from Ref 59.

Another systems composed of a cationic surfactant erucyl bis(2-hydroxyethyl)methyl ammonium chloride (EHAC) and an Azo derivative 4-azobenzenecarboxylic acid (ACA) (in its salt form) were investigated by Oh et al.<sup>60</sup> (Figure 19). The strong binding between *trans*-ACA and EHAC favours a cylinder like geometry leading to the formation of unilamellar vesicles with low viscosity. After UV light irradiation, *cis*-ACA interacts with the hydrophilic region of EHAC, leading to a truncated-cone geometry. Elongated micelles were thus formed resulting in a 5 orders of magnitude increase in viscosity (from 3 mPa·s to 500 Pa·s).

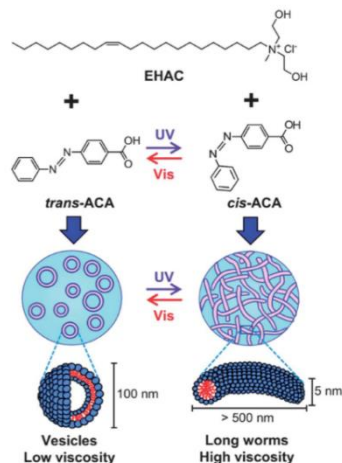


Figure 19 Structure of EHAC, ACA and proposed mechanism for reversible photorheological fluids. Adapted from Ref 60.

### II.2.3 Oppositely charged Polymer/Azo-surfactant complexes

Surfactants have been widely used in association with oppositely charged macromolecules in aqueous solution. As mentioned in Chap I.4, the complexation originates from the electrostatic and the hydrophobic interactions, resulting in various physicochemical properties and structural organizations, such as necklace, bilayer and spherical micelles.

The complexes are readily formed in a non-covalent way by simply mixing the two components; this strategy offers a facile access to photo-tunable 'smart' systems. The phase behaviour of the complexes usually depends on the charge ratio. Stoichiometric complexes (1:1) are generally highly stable (but not soluble) and precipitate. Interesting liquid crystal properties for these systems have been reported<sup>61,62</sup>.

Nevertheless, there is little work of Azo-surfactant/PE complexes in aqueous solution. Lee et al.<sup>63</sup> studied a photoresponsive system composed of a hydrophobically modified poly(acrylic acid) (HM-PAA) and a cationic Azo-surfactant (Figure 20 a). In these systems, micellar aggregates started at the critical aggregation concentration (CAC). The cooperative binding continued until the viscosity of mixtures reached a maximum. This rise of viscosity is due to the solubilisation of dodecyl chains grafted on HM-PAA in micellar aggregates: the aggregates act as cross-linkers for HM-PAA chains. The reversible change of viscosity can be controlled by alternative UV and visible light irradiation. Later, they investigated the structural organization of pure micellar aggregates and HM-PAA/Azo-surfactant mixtures by small-angle neutron scattering (Figure 20 b)<sup>50</sup>.



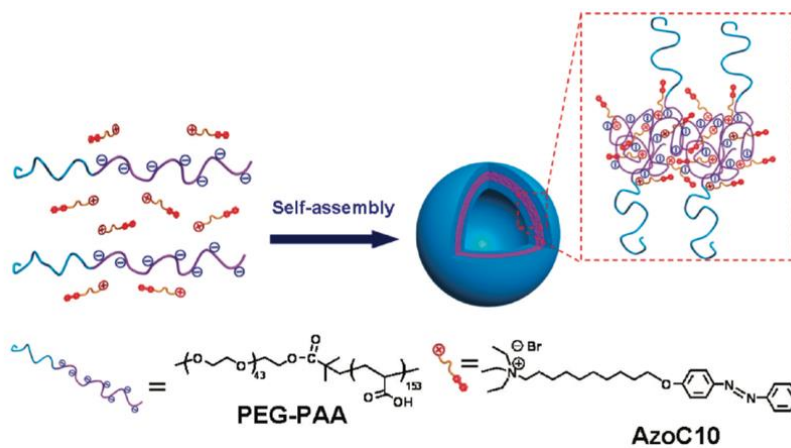


Figure 21 Schematic representation of the self-assembly of the block ionomer complex vesicles.  
Adapted from Ref 64.

## References:

- (1) Eastoe, J.; Dominguez, M. S.; Wyatt, P.; Beeby, A.; Heenan, R. K. Properties of a Stilbene-Containing Gemini Photosurfactant: Light-Triggered Changes in Surface Tension and Aggregation. *Langmuir* **2002**, *18* (21), 7837–7844.
- (2) Basilio, N.; García-Río, L. Photoswitchable Vesicles. *Curr. Opin. Colloid Interface Sci.* **2017**, *32*, 29–38.
- (3) Bandara, H. M. D.; Burdette, S. C. Photoisomerization in Different Classes of Azobenzene. *Chem. Soc. Rev.* **2012**, *41* (5), 1809–1825.
- (4) Xiao, P.; Zhang, J.; Zhao, J.; Stenzel, M. H. Light-Induced Release of Molecules from Polymers. *Top. Vol. Polym. Chem.* **2017**, *74*, 1–33.
- (5) Yu, H.; Li, J.; Wu, D.; Qiu, Z.; Zhang, Y. Chemistry and Biological Applications of Photo-Labile Organic Molecules. *Chem Soc Rev* **2010**, *39* (2), 464–473.
- (6) Li, L.; Scheiger, J. M.; Levkin, P. A. Design and Applications of Photoresponsive Hydrogels. *Adv. Mater.* **2019**, *31* (26), 1807333.
- (7) Irie, M.; Sakemura, K.; Okinaka, M.; Uchida, K. Photochromism of Dithienylethenes with Electron-Donating Substituents. *J. Org. Chem.* **1995**, *60* (25), 8305–8309.
- (8) Xiao, S.; Yi, T.; Li, F.; Huang, C. A Multi-Photo Responsive Photochromic Dithienylethene Containing Coumarin Derivative. *Tetrahedron Lett.* **2005**, *46* (52), 9009–9012.
- (9) Stumpel, J. E.; Ziólkowski, B.; Florea, L.; Diamond, D.; Broer, D. J.; Schenning, A. P. H. J. Photoswitchable Ratchet Surface Topographies Based on Self-Protonating Spiropyran–NIPAAm Hydrogels. *ACS Appl. Mater. Interfaces* **2014**, *6* (10), 7268–7274.
- (10) Ziólkowski, B.; Florea, L.; Theobald, J.; Benito-Lopez, F.; Diamond, D. Self-Protonating Spiropyran-Co-NIPAM-Co-Acrylic Acid Hydrogel Photoactuators. *Soft Matter* **2013**, *9* (36), 8754.
- (11) Klajn, R. Spiropyran-Based Dynamic Materials. *Chem Soc Rev* **2014**, *43* (1), 148–184.
- (12) Griffiths, J. II. Photochemistry of Azobenzene and Its Derivatives. *Chem. Soc. Rev.* **1972**, *1* (4), 481–493.
- (13) HARTLEY, G. S. The Cis-Form of Azobenzene. *Nature* **1937**, *140* (3537), 281–281.
- (14) Atkinson, E. R. The Chemistry of Synthetic Dyes. Volume 1 (Venkataraman, K.). *J. Chem. Educ.* **1952**, *29* (8), 426.
- (15) Kang, H.-C.; Lee, B. M.; Yoon, J.; Yoon, M. Synthesis and Surface-Active Properties of New Photosensitive Surfactants Containing the Azobenzene Group. *J. Colloid Interface Sci.* **2000**, *231* (2), 255–264.
- (16) Benkhaya, S.; M'rabet, S.; El Harfi, A. Classifications, Properties, Recent Synthesis and Applications of Azo Dyes. *Heliyon* **2020**, *6* (1), e03271.
- (17) Beharry, A. A.; Woolley, G. A. Azobenzene Photoswitches for Biomolecules. *Chem. Soc. Rev.* **2011**, *40* (8), 4422.

- (18) Crecca, C. R.; Roitberg, A. E. Theoretical Study of the Isomerization Mechanism of Azobenzene and Disubstituted Azobenzene Derivatives. *J. Phys. Chem. A* **2006**, *110* (26), 8188–8203.
- (19) Magee, J. L.; Shand, W.; Eyring, H. Non-Adiabatic Reactions. Rotation about the Double Bond\*. *J. Am. Chem. Soc.* **1941**, *63* (3), 677–688.
- (20) Curtin, D. Y.; Grubbs, E. J.; McCarty, C. G. Uncatalyzed Syn-Anti Isomerization of Imines, Oxime Ethers, and Haloimines<sup>1</sup>. *J. Am. Chem. Soc.* **1966**, *88* (12), 2775–2786.
- (21) Asano, T.; Okada, T.; Shinkai, S.; Shigematsu, K.; Kusano, Y.; Manabe, O. Temperature and Pressure Dependences of Thermal Cis-to-Trans Isomerization of Azobenzenes Which Evidence an Inversion Mechanism. *J. Am. Chem. Soc.* **1981**, *103* (17), 5161–5165.
- (22) Pozhidaeva, N.; Cormier, M.-E.; Chaudhari, A.; Woolley, G. A. Reversible Photocontrol of Peptide Helix Content: Adjusting Thermal Stability of the Cis State. *Bioconjug. Chem.* **2004**, *15* (6), 1297–1303.
- (23) Konrad, D. B.; Frank, J. A.; Trauner, D. Synthesis of Redshifted Azobenzene Photoswitches by Late-Stage Functionalization. *Chem. – Eur. J.* **2016**, *22* (13), 4364–4368.
- (24) Dong, M.; Babalhavaeji, A.; Samanta, S.; Beharry, A. A.; Woolley, G. A. Red-Shifting Azobenzene Photoswitches for in Vivo Use. *Acc. Chem. Res.* **2015**, *48* (10), 2662–2670.
- (25) Dong, M.; Babalhavaeji, A.; Collins, C. V.; Jarrah, K.; Sadovski, O.; Dai, Q.; Woolley, G. A. Near-Infrared Photoswitching of Azobenzenes under Physiological Conditions. *J. Am. Chem. Soc.* **2017**, *139* (38), 13483–13486.
- (26) Rau, H. Spectroscopic Properties of Organic Azo Compounds. *Angew. Chem. Int. Ed. Engl.* **1973**, *12* (3), 224–235.
- (27) Sadovski, O.; Beharry, A. A.; Zhang, F.; Woolley, G. A. Spectral Tuning of Azobenzene Photoswitches for Biological Applications. *Angew. Chem. Int. Ed.* **2009**, *48* (8), 1484–1486.
- (28) Beharry, A. A.; Sadovski, O.; Woolley, G. A. Azobenzene Photoswitching without Ultraviolet Light. *J. Am. Chem. Soc.* **2011**, *133* (49), 19684–19687.
- (29) Shirota, Y.; Moriwaki, K.; Yoshikawa, S.; Ujike, T.; Nakano, H. 4-[Di(Biphenyl-4-Yl)Amino]Azobenzene and 4,4'-Bis[Bis(4'-Tert-Butylbiphenyl-4-Yl)Amino]Azobenzene as a Novel Family of Photochromic Amorphous Molecular Materials. *J. Mater. Chem.* **1998**, *8* (12), 2579–2581.
- (30) Rau, H.; Rötger, D. Photochromic Azobenzenes Which Are Stable in the Trans and Cis Forms. *Mol. Cryst. Liq. Cryst. Sci. Technol. Sect. Mol. Cryst. Liq. Cryst.* **1994**, *246* (1), 143–146.
- (31) Tamai, N.; Miyasaka, H. Ultrafast Dynamics of Photochromic Systems. *Chem. Rev.* **2000**, *100* (5), 1875–1890.
- (32) Rau, H. Further Evidence for Rotation in the  $\pi, \pi^*$  and Inversion in the  $n, \pi^*$  Photoisomerization of Azobenzenes. *J. Photochem.* **1984**, *26* (2), 221–225.

- (33) Tabor, R. F.; Pottage, M. J.; Garvey, C. J.; Wilkinson, B. L. Light-Induced Structural Evolution of Photoswitchable Carbohydrate-Based Surfactant Micelles. *Chem. Commun.* **2015**, 51 (25), 5509–5512.
- (34) Barrett, C. J.; Mamiya, J.; Yager, K. G.; Ikeda, T. Photo-Mechanical Effects in Azobenzene-Containing Soft Materials. *Soft Matter* **2007**, 3 (10), 1249–1261.
- (35) Pang, X.; Lv, J.; Zhu, C.; Qin, L.; Yu, Y. Photodeformable Azobenzene-Containing Liquid Crystal Polymers and Soft Actuators. *Adv. Mater.* **2019**, 31 (52), 1904224.
- (36) Blayo, C.; Houston, J. E.; King, S. M.; Evans, R. C. Unlocking Structure–Self-Assembly Relationships in Cationic Azobenzene Photosurfactants. *Langmuir* **2018**, 34 (34), 10123–10134.
- (37) Shang, T.; Smith, K. A.; Hatton, T. A. Self-Assembly of a Nonionic Photoresponsive Surfactant under Varying Irradiation Conditions: A Small-Angle Neutron Scattering and Cryo-TEM Study. *Langmuir* **2006**, 22 (4), 1436–1442.
- (38) QIN, C.-G.; LU, C.-X.; OUYANG, G.-W.; QIN, K.; ZHANG, F.; SHI, H.-T.; WANG, X.-H. Progress of Azobenzene-Based Photoswitchable Molecular Probes and Sensory Chips for Chemical and Biological Analysis. *Chin. J. Anal. Chem.* **2015**, 43 (3), 433–443.
- (39) Yi, Q.; Sukhorukov, G. B. UV-Induced Disruption of Microcapsules with Azobenzene Groups. *Soft Matter* **2014**, 10 (9), 1384–1391.
- (40) Wang, D.; Wang, X. Amphiphilic Azo Polymers: Molecular Engineering, Self-Assembly and Photoresponsive Properties. *Top. Issue Polym. Self-Assem.* **2013**, 38 (2), 271–301.
- (41) Mori, T.; Yuyama, K.; Narita, K.; Minagawa, K.; Haraguchi, M.; Tanaka, M. Preparation of Nano- and Microparticles through Self-Assembly of Azobenzene-Dependent Ionomers. *J. Appl. Polym. Sci.* **2006**, 100, 3913–3918.
- (42) Wang, X.; Wu, L.-F.; Zhou, Q.-X.; Li, L.; Balasubraminian, S.; Kumar, J.; Tripathy, S. K. Study on Photodynamic and Photoresponsive Azo Polyelectrolytes. *Chin. J. Polym. Sci. Engl. Ed.* **2000**, 18, 337–342.
- (43) Li, Y.; Deng, Y.; Tong, X.; Wang, X. Formation of Photoresponsive Uniform Colloidal Spheres from an Amphiphilic Azobenzene-Containing Random Copolymer. *Macromolecules* **2006**, 39 (3), 1108–1115.
- (44) Li, N.; Li, Y.; Wang, X. Photoresponsive Submicron-Sized Hollow Spheres Obtained from Amphiphilic Azobenzene-Containing Random Copolymer. *Polymer* **2012**, 53 (18), 3975–3985.
- (45) Wang, G.; Tong, X.; Zhao, Y. Preparation of Azobenzene-Containing Amphiphilic Diblock Copolymers for Light-Responsive Micellar Aggregates. *Macromolecules* **2004**, 37 (24), 8911–8917.
- (46) Pouliquen, G.; Tribet, C. Light-Triggered Association of Bovine Serum Albumin and Azobenzene-Modified Poly(Acrylic Acid) in Dilute and Semidilute Solutions. *Macromolecules* **2006**, 39 (1), 373–383.

- (47) Ruchmann, J.; Fouilloux, S.; Tribet, C. Light-Responsive Hydrophobic Association of Surfactants with Azobenzene-Modified Polymers. *Soft Matter* **2008**, *4* (10), 2098.
- (48) Hayashita, T.; Kurosawa, T.; Miyata, T.; Tanaka, K.; Igawa, M. Effect of Structural Variation within Cationic Azo-Surfactant upon Photoresponsive Function in Aqueous Solution. *Colloid Polym. Sci.* **1994**, *272* (12), 1611–1619.
- (49) Akamatsu, M.; FitzGerald, P. A.; Shiina, M.; Misono, T.; Tsuchiya, K.; Sakai, K.; Abe, M.; Warr, G. G.; Sakai, H. Micelle Structure in a Photoresponsive Surfactant with and without Solubilized Ethylbenzene from Small-Angle Neutron Scattering. *J. Phys. Chem. B* **2015**, *119* (18), 5904–5910.
- (50) Lee, C. T.; Smith, K. A.; Hatton, T. A. Small-Angle Neutron Scattering Study of the Micellization of Photosensitive Surfactants in Solution and in the Presence of a Hydrophobically Modified Polyelectrolyte<sup>†</sup>. *Langmuir* **2009**, *25* (24), 13784–13794.
- (51) Lund, R.; Brun, G.; Chevallier, E.; Narayanan, T.; Tribet, C. Kinetics of Photocontrollable Micelles: Light-Induced Self-Assembly and Disassembly of Azobenzene-Based Surfactants Revealed by TR-SAXS. *Langmuir* **2016**, *32* (11), 2539–2548.
- (52) Koźlecki, T.; Sokołowski, A.; Wilk, K. A. Surface Activity and Micelle Formation of Anionic Azobenzene-Linked Surfactants. *Langmuir* **1997**, *13* (26), 6889–6895.
- (53) Shang, T.; Smith, K. A.; Hatton, T. A. Photoresponsive Surfactants Exhibiting Unusually Large, Reversible Surface Tension Changes under Varying Illumination Conditions. *Langmuir* **2003**, *19* (26), 10764–10773.
- (54) Shikata, Toshiyuki.; Hirata, Hirotaka.; Kotaka, Tadao. Micelle Formation of Detergent Molecules in Aqueous Media: Viscoelastic Properties of Aqueous Cetyltrimethylammonium Bromide Solutions. *Langmuir* **1987**, *3* (6), 1081–1086.
- (55) Shikata, Toshiyuki.; Hirata, Hirotaka.; Kotaka, Tadao. Micelle Formation of Detergent Molecules in Aqueous Media: Viscoelastic Properties of Aqueous Cetyltrimethylammonium Bromide Solutions. *Langmuir* **1987**, *3* (6), 1081–1086.
- (56) Kreke, P. J.; Magid, L. J.; Gee, J. C. <sup>1</sup>H and <sup>13</sup>C NMR Studies of Mixed Counterion, Cetyltrimethylammonium Bromide/Cetyltrimethylammonium Dichlorobenzoate, Surfactant Solutions: The Intercalation of Aromatic Counterions. *Langmuir* **1996**, *12* (3), 699–705.
- (57) Šarac, B.; Cerkovnik, J.; Ancian, B.; Mériquet, G.; Roger, G. M.; Durand-Vidal, S.; Bešter-Rogač, M. Thermodynamic and NMR Study of Aggregation of Dodecyltrimethylammonium Chloride in Aqueous Sodium Salicylate Solution. *Colloid Polym. Sci.* **2011**, *289* (14), 1597–1607.
- (58) Sakai, H.; Orihara, Y.; Kodashima, H.; Matsumura, A.; Ohkubo, T.; Tsuchiya, K.; Abe, M. Photoinduced Reversible Change of Fluid Viscosity. *J. Am. Chem. Soc.* **2005**, *127* (39), 13454–13455.
- (59) Takahashi, Y.; Yamamoto, Y.; Hata, S.; Kondo, Y. Unusual Viscoelasticity Behaviour in Aqueous Solutions Containing a Photoresponsive Amphiphile. *J. Colloid Interface Sci.* **2013**, *407*, 370–374.

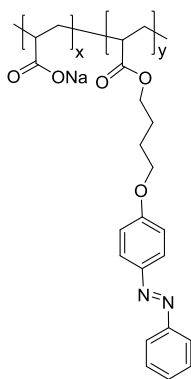
- (60) Oh, H.; Ketner, A. M.; Heymann, R.; Kesselman, E.; Danino, D.; Falvey, D. E.; Raghavan, S. R. A Simple Route to Fluids with Photo-Switchable Viscosities Based on a Reversible Transition between Vesicles and Wormlike Micelles. *Soft Matter* **2013**, *9* (20), 5025–5033.
- (61) Zhang, Q.; Bazuin, C. G. Liquid Crystallinity and Other Properties in Complexes of Cationic Azo-Containing Surfactomesogens with Poly(Styrenesulfonate). *Macromolecules* **2009**, *42* (13), 4775–4786.
- (62) Tibirna, C. M.; Diouf, P. N. Mixtures of Tertiary Amine Functionalized Azo-Containing Mesogens with Acid-Functionalized Polymers. *Polymer* **2008**, *49* (1), 241–253.
- (63) Lee, C. Ted; Smith, K. A.; Hatton, T. A. Photoreversible Viscosity Changes and Gelation in Mixtures of Hydrophobically Modified Polyelectrolytes and Photosensitive Surfactants. *Macromolecules* **2004**, *37* (14), 5397–5405.
- (64) Wang, Y.; Han, P.; Xu, H.; Wang, Z.; Zhang, X.; Kabanov, A. V. Photocontrolled Self-Assembly and Disassembly of Block Ionomer Complex Vesicles: A Facile Approach toward Supramolecular Polymer Nanocontainers. *Langmuir* **2010**, *26* (2), 709–715.

# Chapter III. Synthesis, characterizations and sample preparation

## III.1 Polyelectrolytes

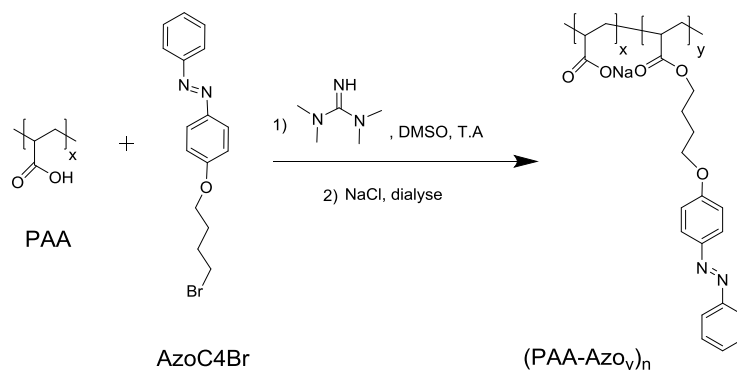
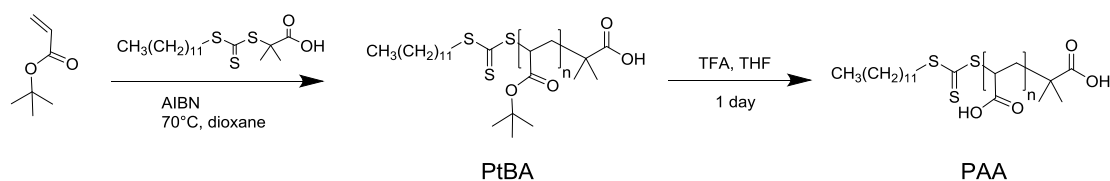
### III.1.1 Target compounds and synthetic scheme

Scheme 1 represents the structure of the PEs synthesized in this thesis. The polymer has a poly(acrylate) backbone with azobenzene linked through a short spacer as side groups. These polymers are named **(PAA-Azo<sub>y</sub>)<sub>n</sub>**, where *y* is the molar fraction of units bearing an azo group and *n* is the number-average degree of polymerization.



Scheme 1 Structure of (PAA-Azo<sub>y</sub>)<sub>n</sub>.

These polymers were synthesized by the synthetic route shown in Scheme 2. The main chain polymer was prepared by controlled polymerization of *tert*-butyl acrylate (tBA) by RAFT to generate well-defined poly(*tert*-butyl acrylate) (PtBA) polymers. Subsequently, the acidolysis of PtBA yielded the polyacrylic acid (PAA). The salt form (NaPAA) was obtained by the dialysis of PAA in excess of NaOH. PAA was esterified by AzoC4Br, a brominated derivative of azobenzene.



Scheme 2 Synthetic route to the polymers  $(\text{PAA-Azo}_y)_n$ .

We will first give a brief overview of the RAFT polymerization, and then, present the results of our polymerizations and the characterization of the targeted polymers. In the following part we will expose the synthesis of Azo derivatives and their grafting on the polymer.

### III.1.2 Controlled radical polymerization RAFT

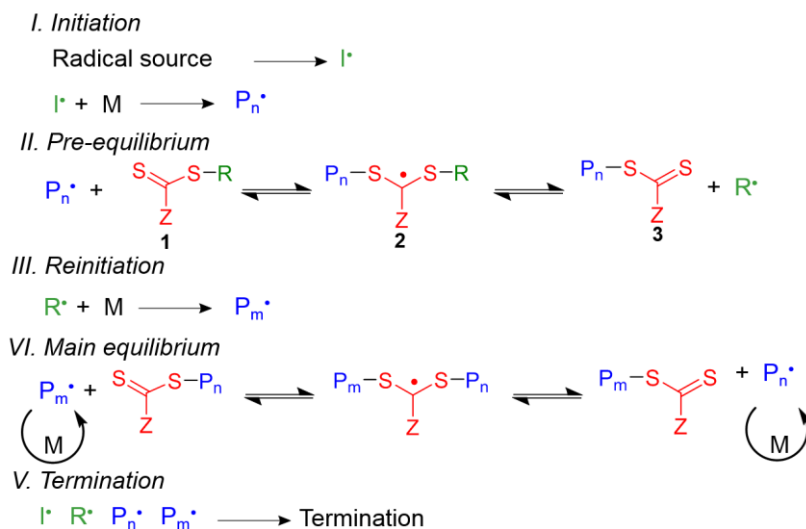
#### III.1.2.1 Principle

As said before, the main chain polymer is synthesized by RAFT. We remind briefly the principles and the properties of this method of polymerization.

First reported by Rizzardo *et al.* in 1998,<sup>1</sup> reversible addition-fragmentation chain transfer (RAFT) polymerization is a controlled radical polymerization, which means that it has the three essential properties: the mass of the polymer can be controlled, the polydispersity is low, and it the polymerization centres remains active throughout the polymerization (living polymerization). The last property is essential to build well-defined architectures such as graft copolymers, block copolymers, dendrimers and stars. RAFT polymerization can be implemented to a wide variety of functional monomers, providing good control over the polymerization of most vinyl monomers available to free radical polymerization (*i.e.*, styrene, butadiene, (meth)acrylates, (meth)acrylamide, vinyl acetate, vinyl chloride). Additionally, RAFT can be performed in various reaction media including organic solvents, aqueous solutions and dispersed phases. RAFT polymerization

however shows some limitation such as a relative high cost for chains transfer agent, odour and colour of synthesized polymers and thermal stability of thiocarbonylthio groups.

RAFT relies on a reversible equilibrium between active and dormant polymer chains. Therefore, RAFT belongs to the family of reversible-deactivation radical polymerizations (RDRP). In RAFT polymerization, the reversible deactivation equilibrium is mediated by a chain transfer agent, also called RAFT agent, which hence plays a key role to control the polymerization. Common RAFT agents are thiocarbonylthio compounds including aromatic dithioesters, trithiocarbonates, dithiocarbamates and xanthates. In RAFT, the chain transfer is degenerative: there is no creation of radicals. Therefore, an external source of radicals is required to maintain a constant rate of polymerization, which is very different from other RDRP methods. Typically, radical initiators such as azobisisobutyronitrile (AIBN) and 4,4'-azobis(4-cyanovaleric acid) (ACVA) can be used<sup>2,3</sup>. RAFT can also to be initiated by redox agents<sup>4,5</sup> or by light irradiation<sup>6</sup>.

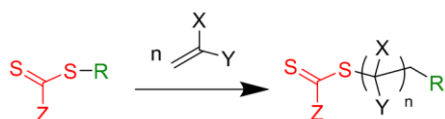


Scheme 3 Proposed Mechanism of Reversible Addition–Fragmentation Chain Transfer Polymerization

The mechanism of RAFT is presented in Scheme 3. The initiator first decomposes to form radicals  $I^\bullet$  which react with single monomers to yield a propagating radical chains  $P_n^\bullet$ . Then,  $P_n^\bullet$  adds to the chain transfer agent **1** to form an intermediate **2** which may provide two types of fragmentation. The intermediate **2** can either reform starting species (RAFT agent and  $P_n^\bullet$ ) or fragment into a new radical  $R^\bullet$  and a macro-RAFT agent **3** (a dormant chain). In the next step, the leaving radical group ( $R^\bullet$ ) reacts with another monomer to reinitiate polymerization forming new propagating radical ( $P_m^\bullet$ ). Unlike in conventional radical

polymerization, the growing chains are end protected by the RAFT agents, which impedes the termination reactions and allow the chains to grow as long as monomer is present and controls the chain length. Moreover, a rapid equilibrium is established between the propagating radicals ( $P_n\cdot$  and  $P_m\cdot$ ) and the dormant species allowing all the chains to grow equally resulting in a low polydispersity.

From a global point of view, RAFT polymerization can be regarded as the insertion of monomers between the S-R bond of the RAFT agent **1** (Scheme 4). The majority of the chains are ended by thiocarbonylthio group ("living" chain end) which offers the possibility of chain extension with a second type of monomer as well as various post-polymerization modifications: it allows to synthesize different architectures. The Z- and R- groups of RAFT agent should be carefully selected to ensure that the C=S bond is more reactive to radical addition than the C=C bond of the monomer. The rate of fragmentation of the intermediate radical **2** and the reactivity of the C=S bond toward radical addition is mainly related to Z- group. R- group should be an excellent leaving group when the propagating radical is added to the C=S bond of RAFT agent and enables to reinitiate polymerization rapidly and efficiently to avoid rate retardation. Guides to select the Z- and R- groups for different monomers are available in many reviews<sup>7-10</sup>.



Scheme 4 The overall RAFT process.

### III.1.2.2 Reaction conditions

The RAFT polymerization conditions are the same as those of conventional free radical polymerization. The same initiator, temperature and solvent are used, in addition to an appropriate RAFT agent. Three stoichiometric ratios must be adjusted for a successful RAFT polymerization.

#### 1) $[M]_0/[RAFT]_0$

$[M]_0$  is the initial concentration in monomer and  $[RAFT]_0$  the concentration in RAFT agent. When the reaction is controlled, each RAFT agent generates one polymer chain. When the reaction is complete, all the monomers are incorporated in the chains. Therefore the  $[M]_0/[RAFT]_0$  ratio is the number of monomers per chain. It equals to the theoretical number-average degree of polymerization  $DP_n$ .

This is how  $DP_n$  and hence, the number-average molar mass  $M_n$  can be predicted and targeted before polymerization.

In the course of the reaction, before completion, the expressions for  $M_n$  and  $DP_n$  are given by the following equations.<sup>11,12</sup>

$$DP_n(t) = \frac{[M]_0 - [M]_t}{[RAFT]_0} = p \frac{[M]_0}{[RAFT]_0} \quad (1)$$

$$M_n = \frac{[M]_0 - [M]_t}{[RAFT]_0} \times m_M + m_{RAFT} \quad (2)$$

where  $[M]_t$  is the concentration of monomer at time  $t$ ,  $p$  the conversion rate of polymer,  $m_M$  and  $m_{RAFT}$  the molar weight of the monomer and the RAFT agent.

These equations indicate that if the reaction is controlled,  $DP_n$  and  $M_n$  should vary linearly with monomer conversion. RAFT process offers a good molecular weight control over a range from 1000 to 100000 g mol<sup>-1</sup>. Higher molecular weights are also accessible with specific reaction conditions.

### 2) $[RAFT]_0/[Initiator]_0$

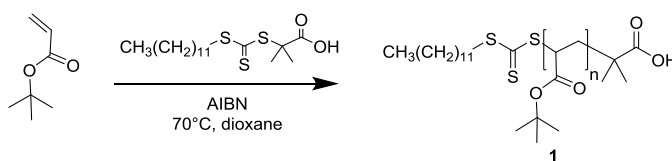
The ratio of RAFT agent to initial radical source affects the control of the molecular-weight evolution. The initiator concentration should be chosen to offer a balance between an acceptable rate of polymerization and an acceptable level of dead chains<sup>12</sup>. Usually  $[RAFT]_0/[Initiator]$  varies from 5 to 10.<sup>10</sup>

### 3) $[M]_0/[Initiator]$

As for conventional free radical polymerization, the rate of polymerization depends on the ratio of monomer to initiator. These ratios are usually reported as  $[M]/[RAFT\ agent]/[Initiator]$  in many articles. The composition  $[M]/[RAFT\ agent]/[Initiator]$  must be optimized to reach the best compromise.

## III.1.3 Synthesis of the PAA chains

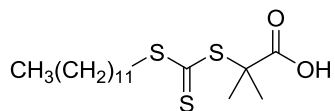
Polymerization procedure is based on a previously reported method<sup>13</sup>.



Scheme 5 Synthesis of PtBA 1 by RAFT

The inherent properties of the RAFT agent (choice of Z- and R- group in

Scheme 4) and the reactivity of monomers both affect the equilibrium of this addition-fragmentation process<sup>14</sup>. We have chosen to work with trithiocarbonates since they have proved to be efficient RAFT agents for the polymerization of acrylates. We have also chosen to work with a commercially available trithiocarbonate type agent (Scheme 6).



Scheme 6 Structure of 2-(Dodecylthiocarbonothioylthio)-2-methylpropionic acid.

We have targeted two different polymers: a short one and a long one. The composition  $[M]/[RAFT\ agent]/[Initiator]$  was optimized to obtain the best compromise between rate of polymerization and control. The best compositions were 90:1:0.07 for the polymerization of low molecular weight poly(*tert*-butyl acrylate) (PtBA). More initiator was required for higher molecular weight PtBA to provide an appropriate polymerization rate. The ratio was adjusted to 1250:1:0.5 for longer chain length PtBA. The theoretical  $DP_n$  of the corresponding the polymers are therefore 90 and 1250 for complete conversion ( $p = 1$ ).

### III.1.3.1 Kinetics measurements of the polymerization

The kinetic of polymerization was monitored by <sup>1</sup>H NMR and SEC. As shown in Figure 1, peaks at 6.26 ppm, 6.01 ppm and 5.68 ppm correspond to the three acrylate protons. The integrals of these peaks were normalized to the intensity of an internal standard. The normalized integrals decrease with the consumption of monomers during the polymerization. To determine the conversion rate of tBA monomers, we followed the normalized integral of the peak at 5.68 ppm.

$$\frac{[M]_t}{[M]_0} = \frac{I_t}{I_0} \quad (3)$$

$$p = 1 - \frac{[M]_t}{[M]_0} = 1 - \frac{I_t}{I_0} \quad (4)$$

where  $[M]_0$  initial concentration of tBA,  $I_0$  integral of the peak at  $t_0$

$[M]_t$  concentration of tBA at time t,  $I_t$  integral of the peak at t

p conversion rate

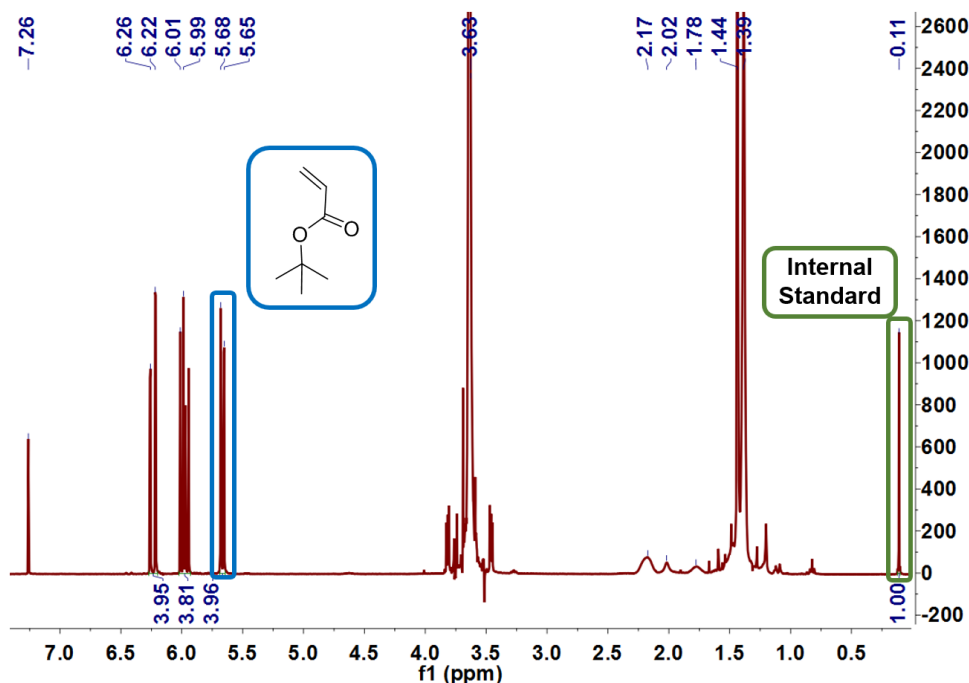


Figure 1 <sup>1</sup>H NMR in CDCl<sub>3</sub> of polymerization of tBA.

The evolution of the molar mass was monitored by SEC. When combining this information with <sup>1</sup>H NMR kinetic results, we can plot the evolution of the apparent number-average molar mass  $M_n$  as a function of monomer conversion  $p$ .

The kinetic plots for short and long PtBA chains are presented in Figure 2 and Figure 3 respectively. The kinetic rates (Figure 2a and Figure 3a) display a first-order behaviour after an induction period of 40 min, which means that the global polymerization rate is constant after 40 min. The induction period is often observed at the beginning of RAFT polymerization and is attributed to the preequilibrium step of RAFT process as discussed in the introduction on RAFT<sup>14</sup>.

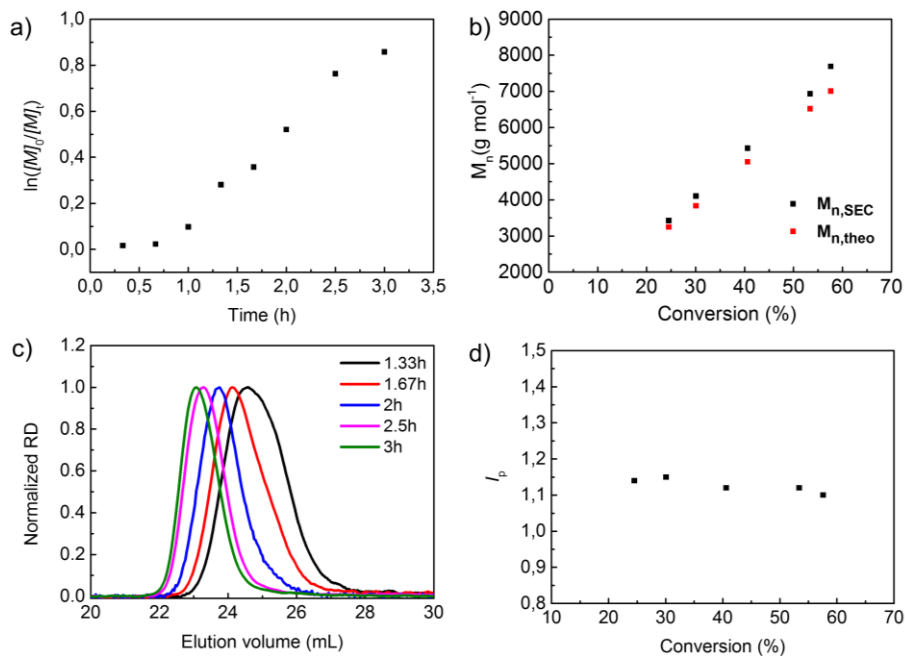


Figure 2 Kinetic plots for PtBA<sub>54</sub>RAFT ( $[tBA]/[RAFT\ agent]/[AIBN]=90:1:0.07$ ). a)  $\ln([M]_0/[M]_t)$  as a function of polymerization time determined by <sup>1</sup>H NMR. b)  $M_n$  obtained by SEC as a function of monomer conversion. c) SEC traces for different polymerization times. d) Polydispersity index  $I_p$  as a function of monomer conversion.

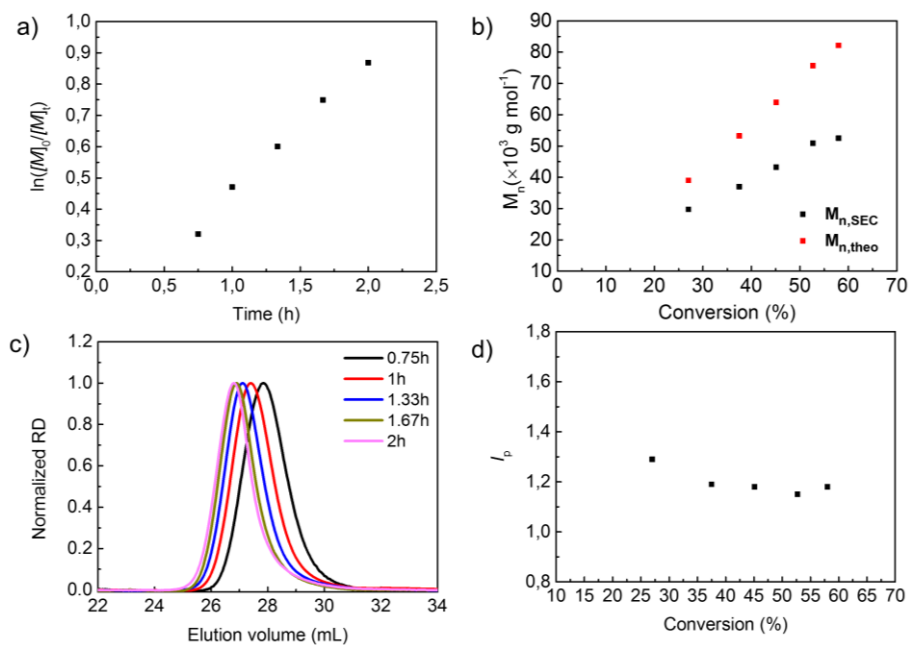


Figure 3 Kinetics plots for PtBA<sub>738</sub>RAFT ( $[tBA]/[RAFT\ agent]/[AIBN]=1250:1:0.5$ ). a)  $\ln([M]_0/[M]_t)$  as a function of polymerization time determined by <sup>1</sup>H NMR. b)  $M_n$  obtained by SEC as a function of monomer conversion. c) SEC traces for different polymerization times. d) Polydispersity index  $I_p$  as a function of monomer conversion.

Figure 2c and Figure 3c show the evolution of the molar mass  $M_{n,SEC}$  measured by SEC. It increases linearly with the monomer conversion (Figure 2b and Figure 3b), which confirms the controlled growth of chain length. It can be compared with the theoretical  $M_{n,theo}$  as calculated by Eq. (2).

For the short polymer, there is a good agreement between the measured molar mass  $M_{n,SEC}$  values and the theoretical  $M_{n,theo}$  values. For the long polymer, the masses measured by SEC are lower than the theoretical ones. This effect may be attributed to the difference in hydrodynamic volume between PtBA and the molecular weight standard poly(methyl methacrylate). It could be also attributed to the loss of living radicals due to a higher rate of initiator.

Finally, Figure 2d and Figure 3d show that the polydispersity is constant and remains low, thus confirming a controlled radical polymerization. It is around 1.1 for the low masses and 1.2 for the high masses.

In conclusion, the kinetics studies show that the polymerization is controlled. The molar mass can be reached by adjusting the  $[M]_0/[RAFT]_0$  ratio and the conversion rate; the polydispersities are quite low.

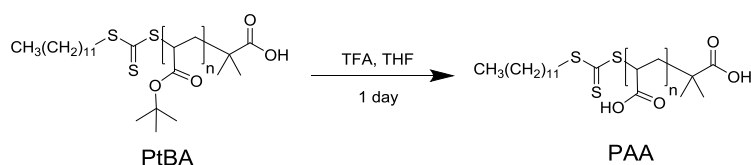
The polymerization advancement  $p$  was followed by NMR, and the reactions were stopped at  $p \sim 60\%$ . The expected theoretical degrees of polymerization are therefore:

$$DP_n = 0.6 \frac{[M]_0}{[RAFT]_0} \quad (5)$$

This gives a degree of polymerization of 54 for short chains and 738 for long chains. Hence the synthesized PtBA are labelled after the theoretical masses PtBA<sub>54RAFT</sub> and PtBA<sub>738RAFT</sub>. The measurements of the masses by SEC are summarized in Table 1.

### III.1.3.2 Acidolysis of PtBA

This acidolysis is carried out by TFA in MeOH at room temperature. This step does not necessitate purification since the solvent and TFA can be evaporated under vacuum.



Scheme 7 Acidolysis of PtBA

The polymer was converted to its salt form by neutralization with aqueous

NaOH and dialysis. To be coherent with previous notations, PAA chains obtained from acidolysis of PtBA are noted PAA<sub>54RAFT</sub> and PAA<sub>738RAFT</sub> thereafter. Unmodified NaPAA chains (NaPAA<sub>54RAFT</sub> and NaPAA<sub>738RAFT</sub>) were obtained by dialysis and used as reference in the structural studies (SAXS).

### III.1.3.3 Molar mass distribution summary

SEC plots in Figure 4 demonstrate the narrow distribution of the synthesized polymers. The molar masses of the different polymers are summarized in Table 1. The  $DP_n$  was estimated from SEC measurements ( $DP_n = M_{n,SEC}/M_0$ ), where  $M_{n,SEC}$  is the number average molar mass obtained by SEC and  $M_0$  is the molar mass of monomer.

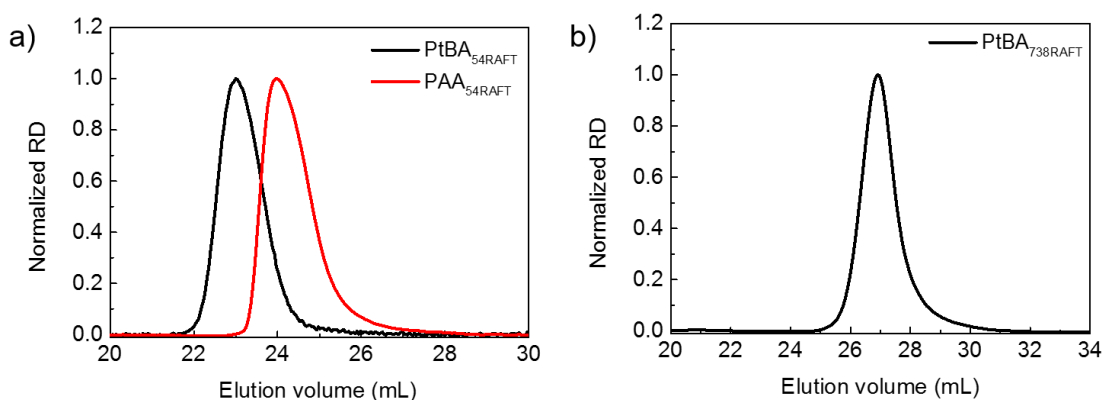


Figure 4 SEC curves of polymers synthesized by RAFT

	$M_w$ (g·mol <sup>-1</sup> )	$M_n$ (g·mol <sup>-1</sup> )	$I_p$	$DP_n$ determined by SEC	<i>Theoretical</i> $DP_n$ at $p = 60\%$ (RMN)
PtBA <sub>54RAFT</sub>	8700	7900	1.10	62	54
PAA <sub>54RAFT</sub>	4650	4200	1.12	60	54
PtBA <sub>738RAFT</sub> <sup>a</sup>	78100	62800	1.18	490	738
PAA <sub>23sigma</sub> <sup>b</sup>	2300	1650	1.40	23	/

Table 1 The weight average molar mass ( $M_w$ ), number average molar mass ( $M_n$ ), polydispersity index ( $I_p$ ,  $I_p = M_w/M_n$ ), number average degree of polymerization ( $DP_n$ ) obtained by SEC ( $DP_n = M_{n,SEC}/M_0$ ) and theoretical  $DP_n$  from Eq.(5). (a. PAA<sub>738RAFT</sub> chains can't be measured correctly due to the strong interaction with SEC column. b. PAA<sub>23sigma</sub> is a commercial PAA purchased from Sigma.)

### III.1.3.4 Water contents in NaPAA

PEs are hygroscopic. The water contents (w/w%) of the PE powders were measured by thermogravimetric analysis (TGA) and are given in Table 2. The mass fraction of water was taken into account in the preparation of the solutions.

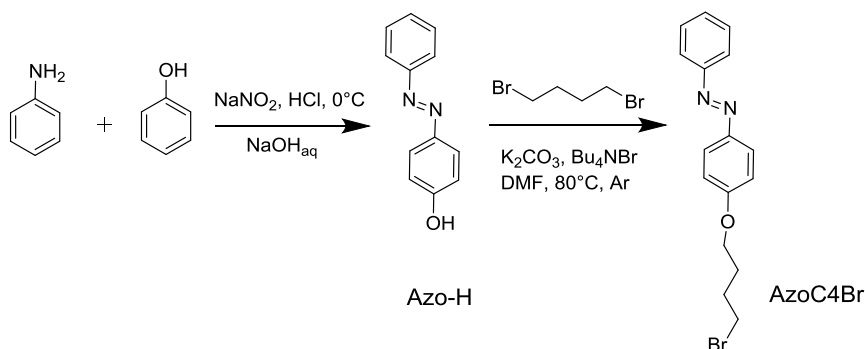
Sample	(w/w%)
NaPAA <sub>23sigma</sub>	19.2 %
NaPAA <sub>54RAFT</sub>	12.9 %
NaPAA <sub>738RAFT</sub>	20.3 %

Table 2 Water contents in NaPAA (NaPAA<sub>23sigma</sub> was obtained from the dialysis of a commercial PAA<sub>23sigma</sub> in presence of excess of NaOH)

## III.1.1 Modification of PAA by azobenzene bearing groups

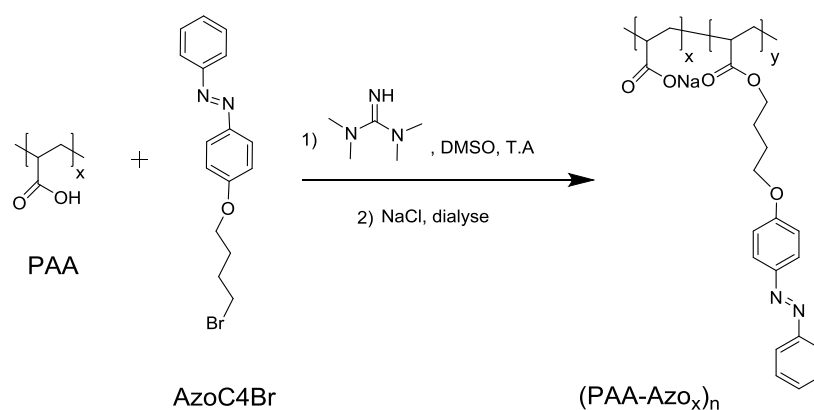
### III.1.1.1 Syntheses

As shown in the Scheme 2, PAA was modified with bromide AzoC<sub>4</sub>Br. This reagent was synthesized by the procedure reported by Wang et al.<sup>15</sup> (Scheme 8). The phenol-azobenzene (Azo-H) was synthesized by azoic coupling between phenol and aniline. The resulting phenol was etherified by butylene dibromide to form AzoC<sub>4</sub>Br. The final compound is formed with an overall yield of 50 % at the scale of 5 g.



Scheme 8 Synthesis of AzoC<sub>4</sub>Br.

AzoC<sub>4</sub>Br was grafted to PAA randomly via esterification promoted by strong organic base 1,1,3,3-tetramethylguanidine (TMG) (Scheme 9). The method was adapted from the work of Li et al.<sup>16</sup>



Scheme 9 Synthesis procedure of azo containing sodium polyacrylate (PAA-Azo<sub>x</sub>)<sub>n</sub>

Azo functionalized sodium polyacrylate with different degrees of polymerization and Azo fractions were synthesized. We esterified two different kinds of PAA by this reaction: a commercial low molecular mass PAA ( $M_w$  2276 g mol<sup>-1</sup>,  $M_n$  1648 g mol<sup>-1</sup>,  $I_p$  1.40,  $DP_n$  23 determined by SEC analysis, Sigma) and the well-defined PAA chains synthesized by RAFT.

Esterifications were carried out with AzoC4Br amounts between 0.05 to 0.7 equivalent. It turns out that below 0.5 equiv., the grafting is quantitative. With higher Azo fractions, hydrophobically modified polyions are no longer soluble in aqueous solution, especially for high molecular mass PAA chains. To keep the solubility in aqueous solution and have an effective photo-response, the molar rate of azo units was chosen in between 10 % and 15 %.

**Nomenclature:** Azo modified PAA chains are named (PAA-Azo<sub>y</sub>)<sub>n</sub>, where  $y$  is the molar fraction of grafted Azo units and  $n$  is the number-average degree of polymerization. Subscript RAFT and Sigma were added to the name to recall the origin of the PAA (RAFT synthesis or commercial product).

### III.1.1.2 Determination of azo grafting fraction $\tau_{azo}$

Since the synthesis procedure includes several steps, it is necessary to check the grafting rates in the final products. This has been realized by  $^1\text{H}$  NMR and UV-Vis spectroscopy.

#### Determination of the Azo content by NMR:

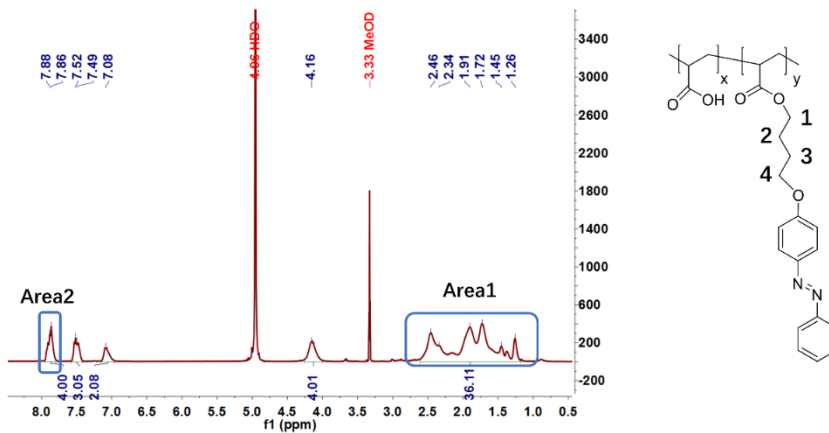


Figure 5  $^1\text{H}$  NMR spectra of  $(\text{PAA-AzO}_{0.11})_{42\text{Sigma}}$  (acid form) in MeOD.

The Azo molar fraction  $\tau_{azo}$  was estimated readily by integration of characteristic peaks. One example of NMR spectra measured on  $(\text{PAA-AzO}_{0.11})_{42\text{Sigma}}$  is presented in Figure 5. The integral (Area1) from 1.26 ppm to 2.46 ppm corresponds to the 4y protons in positions C2, C3, and to the three backbone protons of PAA chains. The integral (Area2) at 7.88 ppm corresponds to the 4y aromatic protons of the Azo group.

$$x + y = 1 \quad (6)$$

$$R = \frac{\text{Area2}}{\text{Area1}} = \frac{4y}{3 + 4y} \quad (7)$$

The molar fraction of Azo units  $\tau_{azo}$  is given by:

$$\tau_{azo} = y = \frac{3}{4} \times \frac{R}{1 - R} \quad (8)$$

#### Determination of the azo content by UV-Vis:

UV-Vis spectroscopy is a more accurate technique to determine the molar fraction of azo units. The Azo groups of the polymers are the only UV-active part of the polymer. So, the absorbance ( $A$ ) of Azo-containing polyions solution is directly proportional to the concentration of azo units (Beer-Lamber law).

$$A = \epsilon lc$$

where  $A$  is the measured absorbance;  $l$  (cm) is the path length through the

sample ( $l = 1$  cm);  $c$  ( $\text{mol L}^{-1}$ ) is the concentration of the absorbing species;  $\varepsilon$  ( $\text{L mol}^{-1} \text{cm}^{-1}$ ) is the molar absorption coefficient of the azo group.  $\varepsilon$  at the maximum absorption (349 nm) was determined in a mixture of THF/H<sub>2</sub>O (1/1 in v/v) to ensure the solubility of both AzoC4Br and azo-containing sodium polyacrylates. The found value is  $21278 \pm 221$  ( $\text{L mol}^{-1} \text{cm}^{-1}$ ).

Solutions of  $(\text{PAA-Azo}_y)_n$  were prepared at precise and appropriate concentrations and their absorbance at 349 nm were measured. The molar fraction of Azo unit in the polymer can be calculated by equation:

$$\tau_{azo} = \frac{1}{1 + \frac{1}{M_1} \left( \frac{m\varepsilon l}{AV} - M_2 \right)} \quad (9)$$

where  $m$  (mg) is the mass of azo containing polymer used for solution preparation;  $V$  (mL) is the total volume of the prepared solution;  $A$  is the measured absorbance;  $M_1$  ( $\text{g.mol}^{-1}$ ) is the molar mass of the non-functionalized monomers;  $M_2$  ( $\text{g.mol}^{-1}$ ) is the molar mass of the functionalized monomers.

The details of these two calculation methods are given in appendix a) and b).

#### Measured $\tau_{azo}$ values for Azo-modified polymers:

The values are summarized in Table 3.

Synthesized polymer	$\tau_{azo}$ by NMR	$\tau_{azo}$ by UV-Vis
(PAA-AZO <sub>0.11</sub> ) <sub>42</sub> Sigma	$9.0 \pm 1.9$ %	$10.7 \pm 0.4$ %
(PAA-AZO <sub>0.15</sub> ) <sub>39</sub> Sigma	$18.0 \pm 3.3$ %	$15.1 \pm 1.5$ %
(PAA-AZO <sub>0.15</sub> ) <sub>54</sub> RAFT	$13.7 \pm 2.6$ %	$15.0 \pm 0.6$ %
(PAA-AZO <sub>0.11</sub> ) <sub>738</sub> RAFT	$9.3 \pm 1.5$ %	$11.4 \pm 0.3$ %

Table 3  $\tau_{azo}$  determined by NMR and UV-Vis

The NMR results are consistent with that of UV-Vis.  $\tau_{azo}$  values determined by UV-Vis spectroscopy are more accurate and thus used in the nomenclature of azo-containing polymers  $(\text{PAA-Azo}_y)_n$  ( $y = \tau_{azo}$ ).

For the synthesized chains, the Azo fraction in the final product is equal to the equivalent number of Azo units introduced initially in the reaction media, which means a quantitative grafting reaction and no loss of Azo during purification. Concerning the Azo-polymers obtained from commercial PAA with a high polydispersity, the final molar fraction of Azo units is lower than the number of equivalents added in the reaction. This is probably related to the fact that part of

Azo units were grafted to oligomers that were removed during the dialysis procedure.

### III.1.1.3 Measurements of the molar masses of (PAA-Azo<sub>v</sub>)<sub>n</sub>

All the azo modified polymers in acid form were analysed by SEC (Table 4).

	$M_w$ (g·mol <sup>-1</sup> )	$M_n$ (g·mol <sup>-1</sup> )	$I_p$	$DP_n$ by SEC	$DP_n$ (theoretical)*	$\tau_{water}$	$\langle M \rangle$ (g·mol <sup>-1</sup> )
(PAA-Azo <sub>0.11</sub> ) <sub>42Sigma</sub>	5800	4400	1.3 3	42	/	17.0	104.2
(PAA-Azo <sub>0.15</sub> ) <sub>39Sigma</sub>	5700	4500	1.2 6	39	/	15.1	115.9
(PAA-Azo <sub>0.15</sub> ) <sub>54RAFT</sub>	7700	6900	1.1 3	56	54	16.2	115.9
(PAA-Azo <sub>0.1</sub> ) <sub>738RAFT</sub>	76100	60600	1.2 6	595	738	15.5	104.2

Table 4 Results of azo containing sodium polyacrylates: weight-average molecular weight ( $M_w$ ), number-average molecular weight ( $M_n$ ), polydispersity index ( $I_p = M_w / M_n$ ) and degree of polymerization ( $DP_n$ ),  $\langle M \rangle$  average molar mass for polymers in acid form.

\* Theoretical values of unmodified PAA chains: we considered that the grafting of azo group does not change the  $DP_n$  of PAA synthesized by RAFT.

Since the starting polymer PAA<sub>23Sigma</sub> has two main populations and certainly contains oligomers, (PAA-Azo<sub>0.11</sub>)<sub>42Sigma</sub> also has a large polydispersity and shows two populations as well as seen in Figure 6a. However, part of small oligomers were certainly eliminated during the dialysis procedure. That explains why the average degree of polymerization is larger for the modified polymers (PAA-Azo<sub>0.11</sub>)<sub>42Sigma</sub> ( $DP_n = 42$ ) than for the initial PAA<sub>23Sigma</sub> chains ( $DP_n = 23$ ). For the same reason the polydispersity decreases after grafting (from 1.4 to 1.3).

(PAA-Azo<sub>0.15</sub>)<sub>54RAFT</sub> and (PAA-Azo<sub>0.11</sub>)<sub>738RAFT</sub> polymers synthesized from well-defined PAA retain a narrow polydispersity as shown in Figure 6b and Figure 6c. The difference in elution volumes is directly related to the grafting of azo groups. PAA<sub>738RAFT</sub> is not shown in Figure 6c, since the high molecular weight PAA chains cannot be measured correctly by SEC (carboxylic acid groups interacted strongly with the SEC column or the solubility weakens for high molar mass PAA).

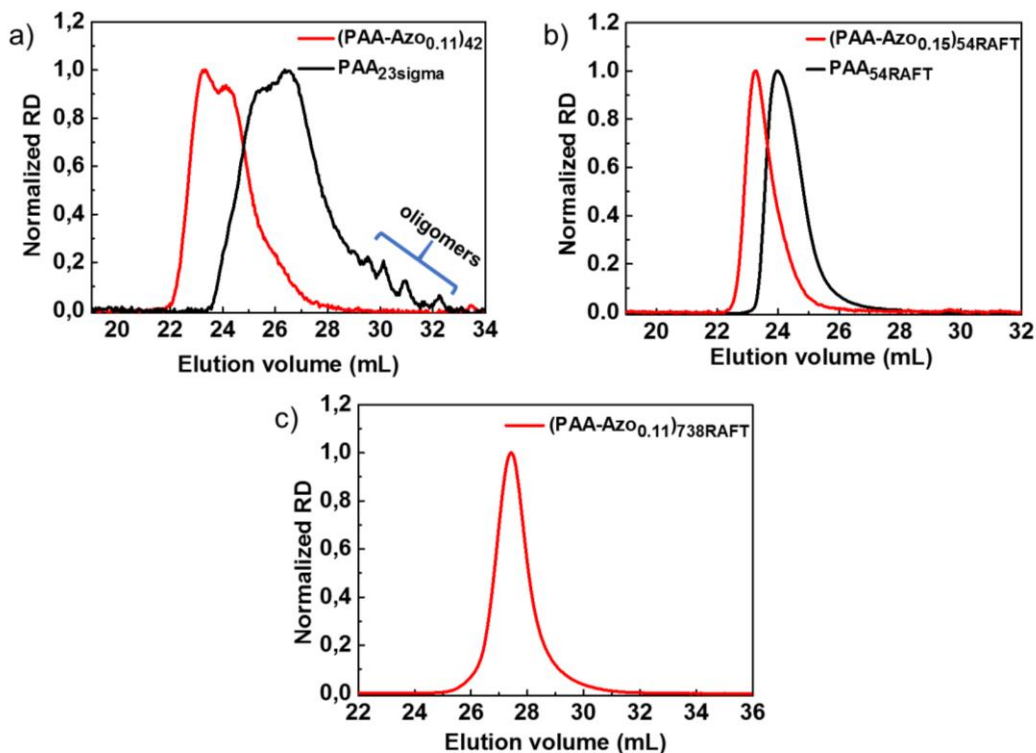


Figure 6 SEC curves of a) PAA<sub>23sigma</sub> and (PAA-AzO<sub>0.11</sub>)<sub>42sigma</sub>. b) PAA<sub>54RAFT</sub> and (PAA-AzO<sub>0.15</sub>)<sub>54RAFT</sub>. c) (PAA-AzO<sub>0.11</sub>)<sub>738RAFT</sub>. All GPC data were done with acid forms.

### III.1.2 Conclusion

The targeted polymers were synthesized with a controlled mass and a controlled polymerization rate at the scale of 1 g. The backbone was synthesized by RAFT polymerization of tBA which yielded a soluble polymer, easy to characterize by SEC at this step. Acidolysis of the polymer and neutralization occurs with conservation of  $DP_n$ . Finally, the grafting rate can be achieved quantitatively for grafting rates lower than 50 % per mol.

### III.1.3 Experimental procedures for the polyelectrolyte syntheses.

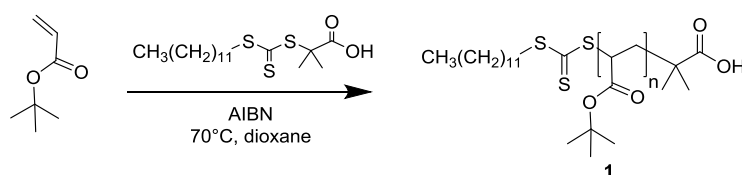
#### III.1.3.1 General

**NMR:** NMR spectra were recorded on a Bruker Avance 400 spectrometer operating at 400 MHz for  $^1\text{H}$  and 100 MHz for  $^{13}\text{C}$ .

**FTIR:** The IR spectra were measure with a Bruker Vertex 70 spectrophotometer equipped with a DTGS detector and on a Smith ATR-diamond stage of type DuraSample IR II.

**Elemental analysis and mass spectra** were performed at the “service d’analyses” of the “Faculté de Chimie”, Strasbourg

### III.1.3.2 Polymerization of *tert*-butyl acrylate (tBA)



*tert*-Butyl acrylate (tBA) was passed through a column of basic alumina to remove inhibitors prior to use. For the synthesis of PtBA with a low molecular weight (7900 g·mol<sup>-1</sup> as determined by SEC), tBA (7.00 g, 54.62 mmol), CTA (220 mg, 610 μmol), AIBN (6.98 mg, 60 μmol) were dissolved in 1,4-dioxane (19 ml). Hexamethylcyclotrisiloxane (118 mg) was added as an internal standard. The mixture was deoxygenated by bubbled argon for 40 min. The reaction flask was then immersed in a preheated oil bath at 65 °C and allowed to stir for 3 hrs. Upon completion, the solution was opened to air and cooled to room temperature. The solvent 1,4-dioxane was removed by evaporation. The polymer was redissolved in 10 ml THF and precipitated in 150 ml MeOH/H<sub>2</sub>O 7/3, centrifuged and dried. The obtained polymer **1** is a yellow solid (3.62 g, 75% yield).

A similar procedure was followed for the synthesis of PtBA with a high molecular weight (62788 g·mol<sup>-1</sup> as determined by SEC), with the following amounts tBA (10 g, 78.02 mmol), CTA (22.9 mg, 0.062 mmol), AIBN (5.1 mg, 0.031 mmol), and stirring at 70 °C for 2 hrs. The resulting polymer was redissolved in 60 ml THF and precipitated in 450 ml MeOH / Water 9/1, centrifuged and dried. The obtained polymer **1** is a pale-yellow solid (4.77 g, 85% yield). <sup>1</sup>H NMR (400 MHz, CDCl<sub>3</sub>) δ 2.21 (s, backbone CH), 1.83 – 1.26 (m, backbone CH<sub>2</sub>, COOC(CH<sub>3</sub>)<sub>3</sub>). <sup>13</sup>C NMR (100 MHz, CDCl<sub>3</sub>) δ 174.31-173.82 (COOC(CH<sub>3</sub>)<sub>3</sub>), 80.47 – 80.57 (COOC(CH<sub>3</sub>)<sub>3</sub>), 42.47 – 41.72 (backbone CH), 37.53 – 35.98 (backbone CH<sub>2</sub>), 28.09-28.23 (COOC(CH<sub>3</sub>)<sub>3</sub>). ATR-IR (cm<sup>-1</sup>) ν<sub>max</sub>: 2978 (ν<sub>as</sub> CH<sub>3</sub>), 2933 (ν<sub>as</sub> CH<sub>2</sub>), 1725 (C=O), 1479 (δ CH<sub>2</sub>), 1457 (δ<sub>as</sub> CH<sub>3</sub>), 1448 (δ<sub>as</sub> CH<sub>3</sub>), 1393 and 1365 (δ<sub>s</sub> CH<sub>3</sub> tBu), 1256 (C-O).

### III.1.3.3 Kinetic measurements by NMR and GPC

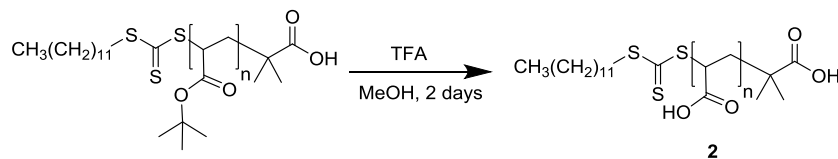
The syringe was deoxygenated with argon 3 times before withdrawing. Aliquots of 0.1 ml of the reaction medium were withdrawn every 30 min (50 μL for NMR, 50 μL for SEC) and cooled immediately by liquid azote bath to stop the polymerization.

Analysis by NMR: The 50 μL aliquot was diluted in CDCl<sub>3</sub> and analyzed by

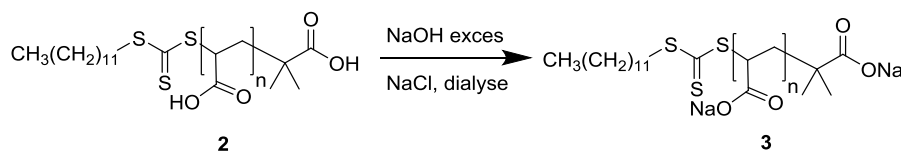
NMR. Hexamethylcyclotrisiloxane was used as an internal standard.

Analysis by SEC: the 50  $\mu\text{L}$  aliquot was analyzed by SEC, according to the experimental procedure described in chapter IV (techniques).

#### III.1.3.4 aciolysis and dialysis

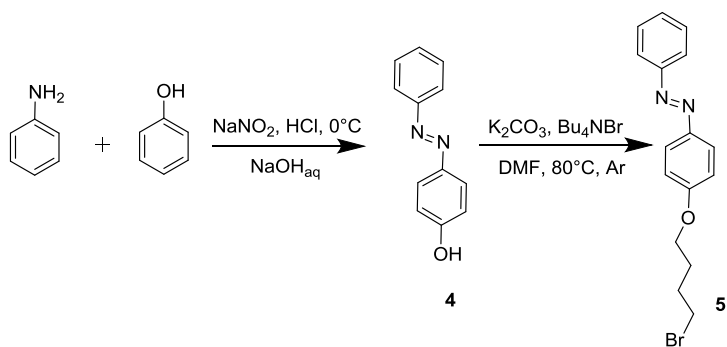


PtBA **1** (1 g) was dissolved in a mixture of TFA (20 ml) and MeOH (10 ml). The mixture was stirred at room temperature for 2 days. Most of TFA and THF were evaporated and the residue lyophilized to afford Polyacrylic acid (PAA) **2**.  $^1\text{H}$  NMR (400 MHz,  $\text{D}_2\text{O}$ )  $\delta$  2.35 (s, backbone CH), 1.88 – 1.20 (m, backbone  $\text{CH}_2$ ). ATR-IR ( $\text{cm}^{-1}$ )  $\nu_{\text{max}}$ : 2921 ( $\nu_{\text{as}} \text{CH}_2$ ), 2850 ( $\nu_{\text{s}} \text{CH}_2$ ), 1698 ( $\nu \text{C}=\text{O}$  acid), 1453 ( $\delta \text{CH}_2$ ), 1161 (C-O).



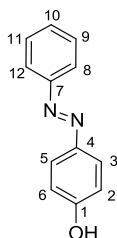
PAA **2** was dissolved in aqueous solution (15 mL) with an excess of NaOH (pH=9) and dialyzed against Milli-Q water for 3 days in a regenerated cellulose membrane (molecular weight-cutoff MWCO = 1 kD). Milli-Q water was refreshed every day. Sodium polyacrylate (NaPAA) **3** power was obtained by lyophilization.  $^1\text{H}$  NMR (400 MHz,  $\text{D}_2\text{O}$ )  $\delta$  3.71 (m, backbone CH,  $\text{CH}_2$ ), 2.42-1.29 (m, backbone CH,  $\text{CH}_2$ ). ATR-IR (neat solid) ( $\text{cm}^{-1}$ )  $\nu_{\text{max}}$ : 2920 ( $\nu_{\text{as}} \text{CH}_2$ ), 2853 ( $\nu_{\text{s}} \text{CH}_2$ ), 1554 ( $\nu_{\text{as}} \text{CO}_2^-$ ), 1452 ( $\delta \text{CH}_2$ ), 1404 ( $\nu_{\text{s}} \text{CO}_2^-$ ). Part of NaPAA is kept without further modification and is used as reference for the study of azo containing sodium polyacrylate.

### III.1.3.5 Azo motif AzoC<sub>4</sub>Br synthesis



#### 4-(phenyldiazenyl)phenol (Azo-H) (**4**):

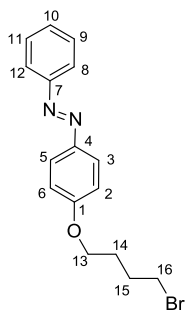
In a three-necked flask, a solution of 8 ml conc. HCl and 8 ml of deionized water was cooled to  $0^\circ\text{C}$ . Aniline (2.50 g, 26.8 mmol) was added with stirring. Then sodium nitrite (2.00 g, 29 mmol) dissolved in 10 ml of water was slowly added at  $0^\circ\text{C}$ . The mixture was stirred for 20 min at  $0^\circ\text{C}$ . A solution of phenol (2.52 g, 26.8 mmol) in aq. NaOH (10 wt. %, 25 mL) was added slowly in the reaction medium and stirred for 1 h at  $0^\circ\text{C}$ . The product was recovered by filtration and recrystallized from EtOH/ $\text{H}_2\text{O}$  (6 /1). Purification of the solid by column chromatography (100% DCM) afforded **4** as a yellow solid (4.11 g, 78% yield).  $^1\text{H}$  NMR (400 MHz,  $\text{CDCl}_3$ )  $\delta$  7.93 – 7.83 (m, 4H, **H3-Ar**, **H5-Ar**, **H8-Ar**, **H12-Ar**), 7.55 – 7.39 (m, 3H, **H9-Ar**, **H10-Ar**, **H11-Ar**), 6.98 – 6.91 (m, 2H, **H2-Ar**, **H6-Ar**).  $^{13}\text{C}$  NMR (100 MHz,  $\text{CDCl}_3$ )  $\delta$  158.42 (C1), 152.76 (C7), 147.31 (C4), 130.61 (C10), 129.20 (C9, C11), 125.20 (C3, C5), 122.71 (C8, C12), 115.96 (C2, C6). Melting point:  $76^\circ\text{C}$ . HRMS (ESI<sup>+</sup>)  $m/z$  199.086056 (calcd for  $\text{C}_{12}\text{H}_{10}\text{N}_2\text{O}$  199.086589). ATR-IR ( $\text{vcm}^{-1}$ )  $\nu_{\text{max}}$ : 3110 ( $\nu$  O-H), 3070 ( $\nu$ C-H aromatic), 1587 ( $\nu$ C=C aromatic), 1415 ( $\nu$ N=N), 1273 (aryl-O), 1143 (O- $\text{CH}_2$ ), 847 ( $\gamma$  C-H aromatic). Anal. Found: C, 72.51; H, 5.07; N, 14.13 (calcd for  $\text{C}_{12}\text{H}_{10}\text{N}_2\text{O}$ : C, 72.71; H, 5.09; N, 14.13).



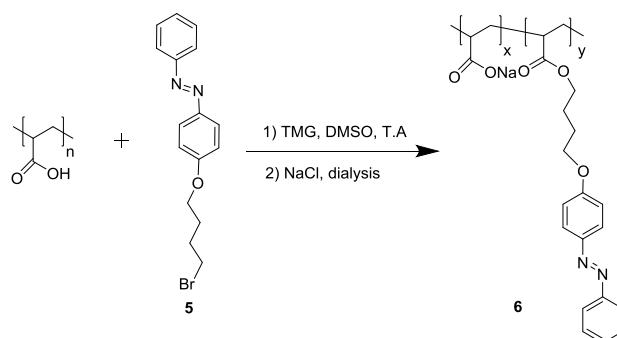
#### 1-(4-(4-bromobutoxy)phenyl)-2-phenyldiazene (AzoC<sub>4</sub>Br) (**5**):

Compound **4** (5 g, 25 mmol), 1,4-dibromobutane (27.23 g, 130 mmol) and  $\text{K}_2\text{CO}_3$  (17.43 g, 130 mmol) were dissolved in 20 ml DMF. The mixture was heated at  $80^\circ\text{C}$  under argon for 3 h. After cooling down to room temperature, excess

$K_2CO_3$  was removed by filtration. Then the mixture was precipitated in 500 ml MeOH and kept in the fridge (4 °C) for 2 days. The crude product was recovered by filtration and purified by column chromatography ( $SiO_2$ , DCM) to yield pure **5** as an orange solid (5.59 g, 67% yield).  $^1H$  NMR (400 MHz,  $CDCl_3$ )  $\delta$  7.95 – 7.85 (m, 4H, **H3**-Ar, **H5**-Ar, **H8**-Ar, **H12**-Ar), 7.54 – 7.41 (m, 3H, **H9**-Ar, **H10**-Ar, **H11**-Ar), 7.02 (m, 2H, **H2**-Ar, **H6**-Ar), 4.09 (t,  $J = 6.0$  Hz, 2H, Ar- $OCH_2$ ), 3.51 (t,  $J = 6.5$  Hz, 2H,  $CH_2$ -Br), 2.15 – 1.95 (m, 4H,  $OCH_2-CH_2-CH_2-CH_2Br$ ).  $^{13}C$  NMR (100 MHz,  $CDCl_3$ )  $\delta$  161.48 (C6), 152.90 (C7), 147.16 (C4), 130.52 (C10), 129.17 (C9, C10), 124.90 (C3, C5), 122.70 (C8, C12), 114.80 (C6, C2), 67.33 (Ar- $OCH_2$ ), 33.52 ( $CH_2$ -Br), 29.55 ( $CH_2-CH_2Br$ ), 27.98 (Ar $OCH_2CH_2$ ). MP: 79 °C. HRMS (ESI<sup>+</sup>)  $m/z$  333.061842 (calcd for  $C_{16}H_{17}BrN_2O$  333.059702). ATR-IR (vcm<sup>-1</sup>): 3073 ( $\nu$ C-H aromatic), 2953, 2942, 2913 and 2973 ( $\nu$   $CH_2$ ), 1583 (C=C aromatic), 1436 (N=N), 1255 (aryl-O), 1146 (O- $CH_2$ ), 830 (C-H aromatic), 735 (rock- $(CH_2)_4$ ). Anal. Found: C, 57.53; H, 5.07; N, 8.41 (calcd for  $C_{16}H_{17}BrN_2O$ : C, 57.67; H, 5.14; N, 8.41).



### III.1.3.6 (PAA-Azo<sub>y</sub>)<sub>n</sub> synthesis

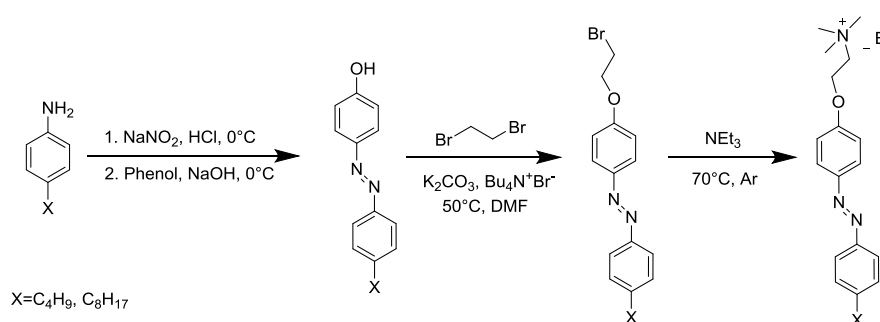


PAA (0.5 g, 6.9 mmol, 1 eq) and AzoC<sub>4</sub>Br **5** (0.36 g, 1.1 mmol, 0.15 eq) were dissolved in DMSO (7 ml). 1.7 ml of 1,1,3,3-tetramethylguanidine (TMG) (1.6 g, 13.9 mmol, 2 eq) was added to the reaction medium. The mixture was stirred at room temperature for 4 hrs. The crude product was precipitated in 150 ml acetone to remove most of the DMSO, then centrifuged and dried. The crude was redissolved in water. The pH was adjusted between 8 and 9 by addition of aq. NaOH. A large excess of NaCl (20 eq) was added for ion exchange. The mixture

was transferred into a pretreated dialysis membrane tube (MWCO 1 kD). The dialysis tube was put in a beaker containing 1 L Milli-Q water. Milli-Q water was refreshed every day until the conductivity of water was constant. The final product **6** in ionic form was obtained by lyophilization (yellow powder, 0.44 g, 53% yield).  $^1\text{H}$  NMR (400 MHz, MeOD)  $\delta$  7.83 (s, 4H, **H-Ar**), 7.45 (s, 3H, **H-Ar**), 7.02 (m, 2H, **H-Ar**), 4.11 (s, 4H, Ar-OCH<sub>2</sub>, COOCH<sub>2</sub>), 2.44 – 1.16 (m, 26H, backbone CH, COOCH<sub>2</sub>CH<sub>2</sub>CH<sub>2</sub>).  $^{13}\text{C}$  NMR (100 MHz, MeOD)  $\delta$  178.45 (**COOH**), 154.08 (**C-Ar**), 148.11 (**C-Ar**), 131.55 (**C-Ar**), 130.19(**C-Ar**), 125.84 (**C-Ar**), 123.66 (**C-Ar**), 115.99 (**C-Ar**), 69.02 (OCH<sub>2</sub>), 43.16 – 42.61 (backbone **CH**), 27.02 – 26.34, 23.74 (backbone **CH**<sub>2</sub>, Azo-OCH<sub>2</sub>CH<sub>2</sub>CH<sub>2</sub>CH<sub>2</sub>O-). IR (cm<sup>-1</sup>)  $\nu_{\text{max}}$ : 2953, 2919 and 2978 ( $\nu$  CH), 1725 (C=O ester), 1605 (C=C aromatic), 1368 ( $\delta$  CH<sub>2</sub>), 1256 (C-O ester), 1143 (C-O COOH), 847 (C-H aromatic), 754.

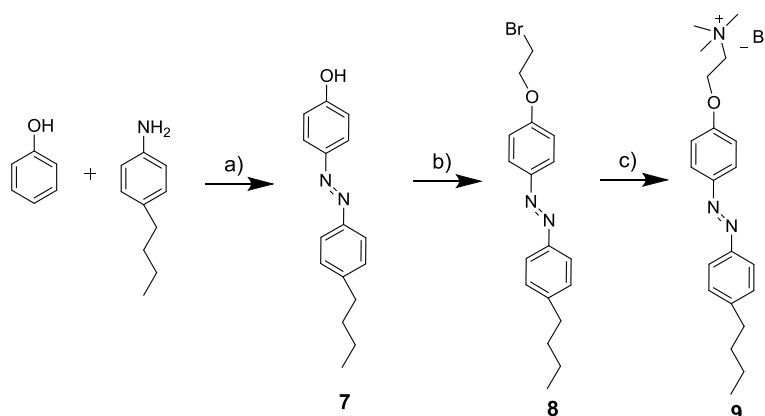
### III.2 Azo-containing surfactants

Azo-containing surfactants (Azo-surfactant) were obtained according to a published procedure,<sup>17–19</sup> indicated in Scheme 10. The synthesis started with the azo coupling reaction between alkyl-aniline and phenol, followed by the addition of a two-carbon spacer and the introduction of a quaternary ammonium head. Two Azo-surfactants with different chain lengths (4Azo2TAB and 8Azo2TAB) were synthesized.



Scheme 10 General synthesis procedure of the azobenzene surfactants

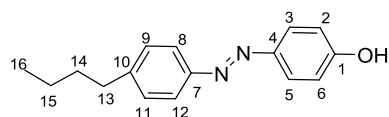
### III.2.1 4Azo2TAB



Scheme 11 Synthesis of **9**. a)  $\text{NaNO}_2$ ,  $\text{HCl}$ ,  $0\text{ }^\circ\text{C}$ ; b)  $\text{K}_2\text{CO}_3$ ,  $\text{Bu}_4\text{NBr}$ ,  $\text{DMF}$ ,  $50\text{ }^\circ\text{C}$ ; c)  $\text{NEt}_3$ ,  $\text{THF}$ ,  $70\text{ }^\circ\text{C}$  under argon.

#### 4-butyl-(4'-hydroxy)azobenzene ( $\text{C}_4\text{AzoOH}$ ) (**7**):

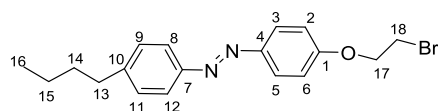
In a three-necked flask, aniline (4.0 g, 26.6 mmol) was dispersed in 80 ml  $\text{HCl}$  aqueous solution ( $1\text{ mol L}^{-1}$ ) at  $0\text{ }^\circ\text{C}$ . Sodium nitrite (2.0 g, 29.0 mmol) in 10 ml water was slowly added. The mixture was left to react for 30 min at  $0\text{ }^\circ\text{C}$ . Then 25 ml of phenol (2.5 g, 26.6 mmol) in 10%wt  $\text{NaOH}$  was introduced dropwise in the reaction mixture at  $0\text{ }^\circ\text{C}$  and stirred thoroughly during 10 hrs. The crude product was recovered by filtration and evaporated under vacuum. The filtrate was recrystallized in a minimum volume of *n*-heptane and then chromatographed ( $\text{SiO}_2$ ,  $\text{DCM}$ ) to afford (**7**) an orange solid (3.7 g, 55% yield).  $^1\text{H NMR}$  (400 MHz,  $\text{CDCl}_3$ )  $\delta$  7.86 (d,  $J = 9.0\text{ Hz}$ , 2H, H3-Ar, H5-Ar), 7.79 (d,  $J = 8.4\text{ Hz}$ , 2H, H8-Ar, H12-Ar), 7.30 (d,  $J = 8.5\text{ Hz}$ , 2H, H9-Ar, H11-Ar), 6.94 (d,  $J = 9.0\text{ Hz}$ , 2H, H2-Ar, H6-Ar), 2.68 (t,  $J = 7.8\text{ Hz}$ , 2H,  $\text{CH}_2\text{-Ar}$ ), 1.71 – 1.58 (m, 2H,  $\text{CH}_2\text{-CH}_2\text{Ar}$ ), 1.45 – 1.32 (m, 2H,  $\text{CH}_2\text{-CH}_2\text{CH}_2\text{Ar}$ ), 0.94 (t,  $J = 7.3\text{ Hz}$ , 3H,  $\text{CH}_3$ ).  $^{13}\text{C NMR}$  (100 MHz,  $\text{CDCl}_3$ )  $\delta$  158.04 (C1), 151.08 (C7), 147.45 (C4), 146.08 (C10), 129.21 (C9, C11), 124.94 (C3, C5), 122.69 (C8, C12), 115.89 (C2, C6), 35.71 ( $\text{CH}_2\text{-Ar}$ ), 33.62 ( $\text{CH}_2\text{-CH}_2\text{Ar}$ ), 22.49 ( $\text{CH}_2\text{-CH}_2\text{CH}_2\text{Ar}$ ), 14.10 ( $\text{CH}_3$ ). HRMS ( $\text{ESI}^+$ )  $m/z$  255.147731 (calcd for  $\text{C}_{16}\text{H}_{17}\text{BrN}_2\text{O}$ : 255.149190). Anal. Found: C, 73.61; H, 7.19; N, 10.77. (calcd for  $\text{C}_{16}\text{H}_{17}\text{BrN}_2\text{O}$ : C, 75.56; H, 7.13; N, 11.01).



#### 4-butyl-(4'-(2-bromoethyl)phenyl)azobenzene ( $\text{C}_4\text{AzoC}_2\text{Br}$ ) (**8**):

Compound **7** (2.0 g, 7.9 mmol), 1,2-dibromoethane (7.0 ml, 78.6 mmol),  $\text{K}_2\text{CO}_3$  (10.3 g, 78.6 mmol) and  $\text{Bu}_4\text{NBr}$  (100 mg) were introduced in 20 ml  $\text{DMF}$ .

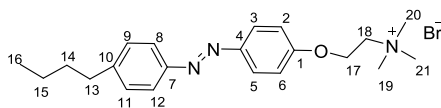
The mixture was heated at 50 °C under argon during 24 hrs. K<sub>2</sub>CO<sub>3</sub> solid was removed by filtration. Most of solvent were removed by extraction with EtOAc and water. The residue was precipitated in 300 ml of cold MeOH. The crude product was filtrated and evaporated under vacuum. After a purification by column chromatography (SiO<sub>2</sub>, DCM), the final product (**8**) is a yellow solid (2.5 g, 86% yield). <sup>1</sup>H NMR (400 MHz, CDCl<sub>3</sub>) δ 7.90 (d, J = 9.0 Hz, 2H, H3-Ar, H5-Ar), 7.80 (d, J = 8.4 Hz, 2H, H8-Ar, H12-Ar), 7.31 (d, J = 8.5 Hz, 2H, H9-Ar, H11-Ar), 7.02 (d, J = 9.0 Hz, 2H, H2-Ar, H6-Ar), 4.38 (t, J = 6.4 Hz, 2H, ArO-CH<sub>2</sub>), 3.68 (t, J = 6.3 Hz, 2H, ArOCH<sub>2</sub>-CH<sub>2</sub>-Br), 2.68 (t, J = 7.6 Hz, 2H, CH<sub>2</sub>Ar), 1.71 – 1.58 (m, 2H, CH<sub>2</sub>-CH<sub>2</sub>Ar), 1.45 – 1.31 (m, 2H, CH<sub>2</sub>-CH<sub>2</sub>CH<sub>2</sub>Ar), 0.94 (t, J = 7.3 Hz, 3H, CH<sub>3</sub>). <sup>13</sup>C NMR (100 MHz, CDCl<sub>3</sub>) δ 160.33 (C1), 151.10 (C7), 147.66 (C10), 146.15 (C4), 129.21 (C9, C11), 124.75 (C3, C5), 122.73 (C8, C12), 115.03(C2, C6), 68.16 (ArO-CH<sub>2</sub>), 35.71 (CH<sub>2</sub>Ar), 33.62 (CH<sub>2</sub>-CH<sub>2</sub>Ar), 28.94 (ArOCH<sub>2</sub>-CH<sub>2</sub>), 22.49 (CH<sub>2</sub>-CH<sub>2</sub>CH<sub>2</sub>Ar), 14.10 (CH<sub>3</sub>). HRMS (ESI<sup>+</sup>) m/z 361.090751 (calcd for C<sub>18</sub>H<sub>21</sub>BrN<sub>2</sub>O 361.091002). Anal. Found: C, 59.83; H, 5.91; N, 7.67. (calcd for C<sub>18</sub>H<sub>21</sub>BrN<sub>2</sub>O: C, 59.84; H, 5.86; N, 7.75).



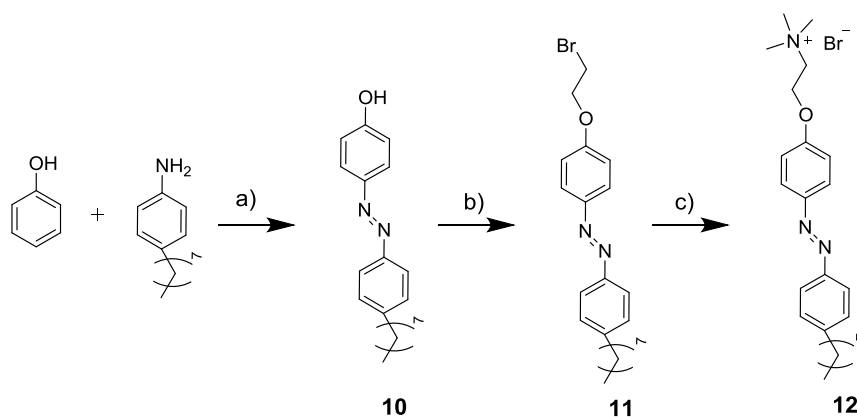
2-(4-(4-butylphenyl)diazenylphenoxy)ethyltrimethylammonium bromide (4Azo2TAB) (**9**):

Compound **8** (1.1 g, 3.1 mmol) and a solution of trimethylamine in ethanol (3.3 ml, 3 mol L<sup>-1</sup>) were dissolved in 10 ml THF. The mixture was stirred at 70 °C under argon during 24 hrs. After cooling to room temperature, the precipitate was filtrated and recrystallized from EtOAc/EtOH (8/3) at 90 °C to afford (**9**) an orange solid (1.0 g, 79% yield). <sup>1</sup>H NMR (400 MHz, CDCl<sub>3</sub>) δ 7.90 (d, J = 9.0 Hz, 2H, H3-Ar, H5-Ar), 7.79 (d, J = 8.3 Hz, 2H, H8-Ar, H12-Ar), 7.29 (d, J = 8.4 Hz, 2H, H9-Ar, H11-Ar), 7.03 (dd, J = 9.1, 0.0 Hz, 2H, H2-Ar, H6-Ar), 4.62 – 4.54 (m, 2H, ArO-CH<sub>2</sub>), 4.41 – 4.32 (m, 2H, ArOCH<sub>2</sub>-CH<sub>2</sub>), 3.62 (s, 9H, N(CH<sub>3</sub>)<sub>3</sub>), 2.67 (t, J = 7.7 Hz, 2H, CH<sub>2</sub>Ar), 1.68 – 1.58 (m, 2H, CH<sub>2</sub>-CH<sub>2</sub>Ar), 1.44 – 1.30 (m, 2H, CH<sub>2</sub>-CH<sub>2</sub>CH<sub>2</sub>Ar), 0.93 (t, J = 7.3 Hz, 3H, CH<sub>3</sub>). <sup>13</sup>C NMR (100 MHz, CDCl<sub>3</sub>) δ 158.87 (C1), 150.93 (C7), 148.14 (C10), 146.46 (C4), 129.23 (C9, C11), 124.90 (C3, C5), 122.82 (C8, C12), 114.90 (C2, C6), 65.18 (ArOCH<sub>2</sub>-CH<sub>2</sub>-N(CH<sub>3</sub>)<sub>3</sub>), 62.76 (ArO-CH<sub>2</sub>), 54.99 (N(CH<sub>3</sub>)<sub>3</sub>), 35.70 (CH<sub>2</sub>Ar), 33.56 (CH<sub>2</sub>-CH<sub>2</sub>Ar), 22.47 (CH<sub>2</sub>-CH<sub>2</sub>CH<sub>2</sub>Ar), 14.07 (CH<sub>3</sub>). ATR-IR (diamond) ν<sub>max</sub>: 3009 (C-H aromatic), 2955 (ν<sub>as</sub> CH<sub>3</sub>), 2932 (ν<sub>as</sub> CH<sub>2</sub>), 2870 (ν<sub>s</sub> CH<sub>3</sub>), 2857 (ν<sub>s</sub> CH<sub>2</sub>), 1595 (νC=C aromatic), 1485 (νN=N),

1244 (aryl-O), 1159 (O-CH<sub>2</sub>), 858 ( $\gamma$  CH aromatic). HRMS (ESI<sup>+</sup>) m/z 340.239121 (calcd for C<sub>21</sub>H<sub>30</sub>N<sub>3</sub>O<sup>+</sup> 340.238339). Anal. Found: C, 59.88; H, 7.17; N, 9.94. (calcd for C<sub>21</sub>H<sub>30</sub>BrN<sub>3</sub>O: C, 60.00; H, 7.19; N, 10.00).



### III.2.2 8Azo2TAB

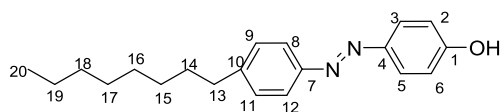


Scheme 12 Synthesis of **12**. a) NaNO<sub>2</sub>, HCl, 0 °C; b) K<sub>2</sub>CO<sub>3</sub>, Bu<sub>4</sub>NBr, DMF, 50 °C; c) NEt<sub>3</sub>, THF, 70 °C under argon.

#### 4-((4-octylphenyl)diazenyl)phenol (C<sub>8</sub>AzoOH) (**10**):

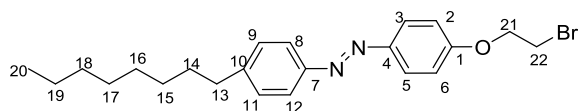
4-octylaniline (2.9 g, 14.1 mmol) was dispersed in 80 ml of 1 M HCl solution and 20 ml EtOH at 0 °C. Sodium nitrite (1.0 g, 14.1 mmol) in 10 ml water was slowly added. The mixture was left to react for 30 min at 0 °C. Then 30 ml of phenol (1.3 g, 14.1 mmol) in 10% wt NaOH was introduced dropwise in the reaction mixture at 0 °C and stirred thoroughly during 10 hrs. The crude product was recovered by extraction EtOAc/H<sub>2</sub>O. Then the organic layers were washed with NaOH aqueous solution in order to remove the no reacted phenol. The combined organic layers were dried (MgSO<sub>4</sub>) and concentrated under vacuum. Chromatography (SiO<sub>2</sub>, Cyclohexane/ EtOAc, 0/100 to 7/3) afforded (**10**) an orange solid (0.53 g, 12% yield). <sup>1</sup>H NMR (400 MHz, CDCl<sub>3</sub>)  $\delta$  7.86 (d, *J* = 8.9 Hz, 2H, H3-Ar, H5-Ar), 7.79 (d, *J* = 8.4 Hz, 2H, H8-Ar, H12-Ar), 7.30 (d, *J* = 8.3 Hz, 2H, H9-Ar, H11-Ar), 6.94 (d, *J* = 8.9 Hz, 2H, H2-Ar, H6-Ar), 2.67 (t, *J* = 7.6 Hz, 2H, H13), 1.71 – 1.59 (m, 2H, H14), 1.40 – 1.19 (m, 10H, H15-H19), 0.88 (t, *J* = 6.8 Hz, 3H, H20). <sup>13</sup>C NMR (100 MHz, CDCl<sub>3</sub>)  $\delta$  158.02 (C1), 151.08 (C7), 147.46 (C10), 146.13 (C4), 129.20 (C9, C11), 124.94 (C3, C5), 122.70 (C8, C12), 115.88 (C2, C6), 36.02 (C13), 32.03 (C14), 31.49 (C15), 29.62 (C16), 29.45 (C17), 29.41

(C18), 22.82 (C19), 14.26 (C20). HRMS (ESI<sup>+</sup>) *m/z* 311.210913 (calcd for C<sub>20</sub>H<sub>26</sub>N<sub>2</sub>O 311.211790). Anal. Found: C, 77.10; H, 8.55; N, 9.01. (calcd for C<sub>20</sub>H<sub>26</sub>N<sub>2</sub>O C, 77.38; H, 8.44; N, 9.03).



1-(4-(2-bromoethoxy)phenyl)-2-(4-octylphenyl)diazene (C<sub>8</sub>AzoC<sub>2</sub>Br) (**11**):

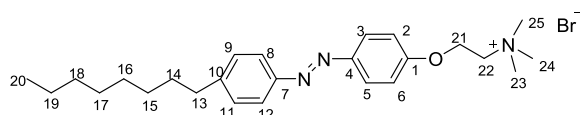
Compound **10** (5.0 g, 16.1 mmol), 2-dibromoethane (1.2 ml, 16.1 mmol), K<sub>2</sub>CO<sub>3</sub> (1.9 g, 16.1 mmol) and Bu<sub>4</sub>NBr (10 mg) were introduced in 10 ml DMF. The mixture was heated at 50 °C under argon during 26 hrs. K<sub>2</sub>CO<sub>3</sub> solid was removed by filtration. Most of solvent were removed by extraction with EtOAc and water. Then the residue was precipitated into 300 ml of cold MeOH. The crude product was filtrated and evaporated under vacuum. Chromatography (SiO<sub>2</sub>, DCM) afforded (**11**) as a yellow solid (0.50 g, 74% yield). <sup>1</sup>H NMR (400 MHz, CDCl<sub>3</sub>) δ 7.90 (d, *J* = 9.0 Hz, 2H, H3-Ar, H5-Ar), 7.80 (d, *J* = 8.4 Hz, 2H, H8-Ar, H12-Ar), 7.30 (d, *J* = 8.4 Hz, 2H, H9-Ar, H11-Ar), 7.02 (d, *J* = 9.0 Hz, 2H, H2-Ar, H6-Ar), 4.36 (t, *J* = 6.3 Hz, 2H, H21), 3.68 (t, *J* = 6.3 Hz, 2H, H22), 2.67 (t, *J* = 7.8 Hz, 2H, H13), 1.69 – 1.61 (m, 2H, H14), 1.39 – 1.21 (m, 10H, H15-H19), 0.88 (t, *J* = 7.1 Hz, 3H, H20). <sup>13</sup>C NMR (101 MHz, CDCl<sub>3</sub>) δ 160.34 (C1), 151.10 (C7), 147.68 (C4, C10), 129.21 (C9, C11), 124.75 (C3, C5), 122.73 (C8, C12), 115.03 (C2, C6), 68.17 (C21), 36.03 (C13), 32.03 (C18), 31.49 (C14), 29.62 (C15), 29.45 (C16), 29.41 (C17), 28.93 (C22), 22.82 (C19), 14.26 (C20). HRMS (ESI<sup>+</sup>) *m/z* 417.150597 (calcd for C<sub>22</sub>H<sub>29</sub>BrN<sub>2</sub>O 417.153602). Anal. Found: C, 63.79; H, 7.16; N, 6.76. (calcd for C<sub>22</sub>H<sub>29</sub>BrN<sub>2</sub>O C, 63.31; H, 7.00; N, 6.71).



N,N,N-trimethyl-2-(4-((4-octylphenyl)diazenyl)phenoxy)ethan-1-aminium bromide (8Azo2TAB) (**12**):

Compound **11** (0.50 g, 1.2 mmol) and a solution of trimethylamine in ethanol (1.2 ml, 3 mol L<sup>-1</sup>) were dissolved in 5 ml THF. The mixture was stirred at 70 °C under argon for two days. After cooling to room temperature, the precipitate was filtrated and recrystallized from EtOAc/MeOH (3/1) at 90 °C to afford (**12**) as an orange solid (0.37 g, 64% yield). <sup>1</sup>H NMR (400 MHz, CDCl<sub>3</sub>) δ 7.91 (d, *J* = 9.0 Hz, 2H, H3-Ar, H5-Ar), 7.80 (d, *J* = 8.4 Hz, 2H, H8-Ar, H12-Ar), 7.30 (d, *J* = 8.5 Hz, 2H, H9-Ar, H11-Ar), 7.04 (d, *J* = 9.1 Hz, 2H, H2-Ar, H6-Ar), 4.52 (m, 2H, H21), 4.33 (m, 2H, H22), 2.67 (t, *J* = 7.6 Hz, 2H, H13), 1.66 (m, 2H, H14), 1.37 – 1.22

(m, 10H, H15-H19), 0.88 (t,  $J = 7.1$  Hz, 3H, H20).  $^{13}\text{C}$  NMR (101 MHz,  $\text{CDCl}_3$ )  $\delta$  158.81 (C1), 150.95 (C7), 148.22 (C4), 146.56 (C10), 129.24 (C9, C11), 124.94 (C3, C5), 122.85 (C8, C12), 114.87 (C2, C6), 65.21 (C21), 62.79 (C22), 55.10 (C23, C24, C25), 36.04 (C13), 32.02 (C18), 31.46 (C14), 29.60 (C15), 29.44 (C16), 29.40 (C17), 22.81 (C19), 14.25 (C20). ATR-IR (diamond)  $\nu_{\text{max}}$ : 3011 ( $\nu$  CH aromatic), 2954 ( $\nu_{\text{as}}$   $\text{CH}_3$ ), 2923 ( $\nu_{\text{as}}$   $\text{CH}_2$ ), 2851 ( $\nu_{\text{s}}$   $\text{CH}_2$ ), 1596 ( $\nu$  C=C aromatic), 1469 ( $\nu$  N=N), 1251 (aryl-O), 1108 (O- $\text{CH}_2$ ), 840 ( $\gamma$  C-H aromatic). HRMS (ESI $^+$ )  $m/z$  396.298201 (calcd for  $\text{C}_{25}\text{H}_{38}\text{N}_3\text{O}^+$ : 396.300939). Anal. Found: C, 62.98; H, 8.14; N, 8.84. (calcd for  $\text{C}_{25}\text{H}_{38}\text{BrN}_3\text{O}$ : C, 63.02; H, 8.04; N, 8.82).



### III.3 Sample preparations

#### III.3.1 Polyelectrolyte aqueous solutions

Salt-free aqueous solutions of PEs were prepared by dissolving PEs powders in ultrapure water. Very low concentrations were obtained from the dilution of concentrated solutions. The mass of residual water in dry PEs was considered during concentration calculation. Solutions were stirred one hour and then stored in dark place at room temperature at least 2 days before measurements. The same procedure was followed for surfactant solution preparation.

#### III.3.2 Polyelectrolyte/Surfactant complexes solutions

PEs and azo-surfactants solutions were prepared separately by dissolving powders in ultrapure water. PE/surfactant solutions were obtained by mixing initial PEs and surfactant solutions at desired concentrations under strong stirring. Solutions were kept in dark place at room temperature at least 3 days before measurements.

#### III.3.3 Azo-surfactant/Aromatic salt solutions

Azo-surfactant and salt solutions were prepared separately and mixed under strong stirring. The viscous mixture was further homogenized by ultrasound and kept in dark for 3 days. It is however impossible to transfer this preparation directly due to its high viscosity. It was therefore irradiated by UV light to provoke the transition to a fluid phase and then injected into in NMR tube or glass capillary for SAXS measurements. Next, blue light was applied to initiate the inverse

photoisomerization. Samples were kept in dark 3 days for equilibrium.

## References:

- (1) Chiefari, J.; Chong, Y. K. (Bill); Ercole, F.; Krstina, J.; Jeffery, J.; Le, T. P. T.; Mayadunne, R. T. A.; Meijs, G. F.; Moad, C. L.; Moad, G.; Rizzardo, E.; Thang, S. H. Living Free-Radical Polymerization by Reversible Addition–Fragmentation Chain Transfer: The RAFT Process. *Macromolecules* **1998**, *31* (16), 5559–5562.
- (2) Gody, G.; Maschmeyer, T.; Zetterlund, P. B.; Perrier, S. Rapid and Quantitative One-Pot Synthesis of Sequence-Controlled Polymers by Radical Polymerization. *Nat. Commun.* **2013**, *4* (1), 2505.
- (3) Gody, G.; Maschmeyer, T.; Zetterlund, P. B.; Perrier, S. Exploitation of the Degenerative Transfer Mechanism in RAFT Polymerization for Synthesis of Polymer of High Livingness at Full Monomer Conversion. *Macromolecules* **2014**, *47* (2), 639–649.
- (4) Bai, W.; Zhang, L.; Bai, R.; Zhang, G. A Very Useful Redox Initiator for Aqueous RAFT Polymerization of N-Isopropylacrylamide and Acrylamide at Room Temperature. *Macromol. Rapid Commun.* **2008**, *29* (7), 562–566.
- (5) Martin, L.; Gody, G.; Perrier, S. Preparation of Complex Multiblock Copolymers via Aqueous RAFT Polymerization at Room Temperature. *Polym. Chem.* **2015**, *6* (27), 4875–4886.
- (6) Chen, M.; Zhong, M.; Johnson, J. A. Light-Controlled Radical Polymerization: Mechanisms, Methods, and Applications. *Chem. Rev.* **2016**, *116* (17), 10167–10211.
- (7) D. J. Keddie et al. RAFT Agent Design and Synthesis. *Macromolecules* **2012**, *45*, 5321–5342.
- (8) Keddie, D. J. A Guide to the Synthesis of Block Copolymers Using Reversible-Addition Fragmentation Chain Transfer (RAFT) Polymerization. *Chem. Soc. Rev.* **2014**, *43* (2), 496–505.
- (9) Tian, X.; Ding, J.; Zhang, B.; Qiu, F.; Zhuang, X.; Chen, Y. Recent Advances in RAFT Polymerization: Novel Initiation Mechanisms and Optoelectronic Applications. *Polymers* **2018**, *10* (3), 318.
- (10) Perrier, S. *50th Anniversary Perspective*: RAFT Polymerization—A User Guide. *Macromolecules* **2017**, *50* (19), 7433–7447.
- (11) Chong, Y. K.; Krstina, J.; Le, T. P. T.; Moad, G.; Postma, A.; Rizzardo, E.; Thang, S. H. Thiocarbonylthio Compounds in Free Radical Polymerization with Reversible Addition-Fragmentation Chain Transfer (RAFT Polymerization). Role of the Free-Radical Leaving Group (R). *Macromolecules* **2003**, *36* (7), 2256–2272.
- (12) Moad, G.; Rizzardo, E.; Thang, S. H. Radical Addition–Fragmentation Chemistry in Polymer Synthesis. *Polymer* **2008**, *49* (5), 1079–1131.
- (13) Barlow, T. R.; Brendel, J. C.; Perrier, S. Poly(Bromoethyl Acrylate): A Reactive Precursor for the Synthesis of Functional RAFT Materials. *Macromolecules* **2016**, *49* (17), 6203–6212.
- (14) Perrier, S.; Barner-Kowollik, C.; Quinn, J. F.; Vana, P.; Davis, T. P. Origin of Inhibition Effects in the Reversible Addition Fragmentation Chain Transfer (RAFT) Polymerization of Methyl Acrylate. *Macromolecules* **2002**, *35* (22), 8300–8306.

- (15) Wang, Y.; Ma, N.; Wang, Z.; Zhang, X. Photocontrolled Reversible Supramolecular Assemblies of an Azobenzene-Containing Surfactant with  $\alpha$ -Cyclodextrin. *Angew. Chem. Int. Ed.* **2007**, *46* (16), 2823–2826.
- (16) Li, Q.; Bao, Y.; Wang, H.; Du, F.; Li, Q.; Jin, B.; Bai, R. A Facile and Highly Efficient Strategy for Esterification of Poly(Meth)Acrylic Acid with Halogenated Compounds at Room Temperature Promoted by 1,1,3,3-Tetramethylguanidine. *Polym. Chem.* **2013**, *4* (9), 2891.
- (17) Jia, K.; Zhang, X.; Zhang, L.; Yu, L.; Wu, Y.; Li, L.; Mai, Y.; Liao, B. Photoinduced Reconfiguration of Complex Emulsions Using a Photoresponsive Surfactant. *Langmuir* **2018**, *34* (38), 11544–11552.
- (18) Sun, T.; Wang, Q.; Bi, Y.; Chen, X.; Liu, L.; Ruan, C.; Zhao, Z.; Jiang, C. Supramolecular Amphiphiles Based on Cyclodextrin and Hydrophobic Drugs. *J. Mater. Chem. B* **2017**, *5* (14), 2644–2654.
- (19) Song, B.; Zhao, J.; Wang, B.; Jiang, R. Synthesis and Self-Assembly of New Light-Sensitive Gemini Surfactants Containing an Azobenzene Group. *Colloids Surf. Physicochem. Eng. Asp.* **2009**, *352* (1–3), 24–30.

# Chapter IV. Analysis techniques

## IV.1 UV and Blue light irradiation

### IV.1.1 Light sources

Optical radiation device is an important part for the study of photoresponsive systems. The wavelength, light-emitting intensity and the setup influence the photoconversion and the photostationary state. Most popular UV sources used with photoresponsive systems are mercury lamps<sup>1-3</sup>, filtered UV tubes<sup>4,5</sup>, optical fibers<sup>6-8</sup> and UV LEDs<sup>7</sup>.

Mercury arc lamps offer a large range of wavelengths (200 nm - 2500 nm). Additional filters are needed to select specific wavelengths. Mercury arc lamps have a large lighting area and may emit dangerous levels of UV radiation. Hence manipulations must be done with care.

Alternatively, UV tubes, optical fibbers coupled with laser (or diodes devices), or simple UV LEDs can deliver UV light in a safer way. Filtered UV tubes have a large spectral distribution. They have a sufficient lighting area and can be handled easily. Optical fibbers associated to laser have gained increasing interest because they can easily transmit UV light on very small areas. Nevertheless, their limited lighting surface can also be a disadvantage. UV LEDs own low energy consumption, a concentrated narrow beam and high effective luminous efficiency. They offer a large range of wavelength, with a narrow wavelength distribution. Even though the lighting area of UV LED is not very large, it's possible to assemble several units and to create a suitable setup for the experiments.

A filtered UV tubes (365 nm) with a large wavelength distribution was used at the beginning. The lightened area is sufficiently large for illuminating NMR tubes and UV-Vis cuvettes. One limitation of UV tubes lamp is that the irradiation can only be applied on one side of the sample. Another limitation is the heat dissipation which might warm up the sample after a long irradiation period (that can affect the isomerization process of azobenzene). Hence, samples were illuminated at 10 cm away from UV tubes in practice. UV tubes are more suitable for dilute solutions and short time irradiation.

UV LEDs with a narrow viewing angle (15°) were used in most of the experiments. The spectra distribution is centred at 365 nm with a narrow

wavelength distribution (363 – 370 nm at half-maximum). They were arranged in different ways according to the nature of the measurements. Different setups will be presented in the following part. No heating problems were observed. Samples can be put very close to the LEDs to improve the irradiance.

The radiant flux received per unit area (irradiance) were measured with a photodiode power meter (ThorLabs PM130D) for different sources and typical setups (Table 1).

UV sources	Distance between light source and sample (cm)	Irradiance (mW/cm <sup>2</sup> )
Filtered UV tubes	10	0.7
UV LED	0.5	1.3
Blue LED	0.5	7.9

Table 1 Irradiance with different light sources.

Setup	Irradiance for UV LEDs (mW/cm <sup>2</sup> )	Irradiance for Blue LEDs (mW/cm <sup>2</sup> )
SAXS	2.0	7.9
SANS	1.3	8.1
UV-Vis/NMR	0.35	3.8

Table 2 Irradiance for different setups. (Measured at a distance of 0.5 cm for SAXS and UV-Vis, 1 cm for SANS).

#### IV.1.2 Comparison between UV tubes and UV LEDs irradiation

The *trans/cis* ratio is highly sensitive to the irradiation setup (intensity, wavelength distribution). In order to find the most adapted UV illumination conditions, comparisons between UV tube and UV LEDs irradiation were realized by <sup>1</sup>H NMR and UV-Vis measurements. We present here some examples of different systems.

##### By NMR

NMR measurements under light stimulus were carried out for two Azo-surfactant solutions in D<sub>2</sub>O (4Azo2TAB at 50 mM and 8.6 mM). The LED irradiation setup is composed of 8 LEDs (4 LEDs on each side of the sample) put close to the sample. The UV tubes (that can only irradiate from one side of the sample) is

set at a distance of 10 cm. Samples in glass NMR tubes with a diameter of 5 mm were irradiated by LEDs or UV tubes until the *trans/cis* composition remained unchanged.

Figure 1 shows the NMR spectra of 4Azo2TAB 50 mM in D<sub>2</sub>O before and after light stimulus (UV or blue LEDs). Pure *trans* and their *cis* isomers solutions show clearly distinct peaks (Figure 1 red curve for dark and green curve for UV). Therefore, the molar fraction of *trans* isomers  $x_{trans}$  at photostationary state is estimated by the integral of the *trans* and the corresponding *cis* peaks. The interpretation of NMR peaks and the method of  $x_{trans}$  calculation is given in Chap VI.2.2.2.

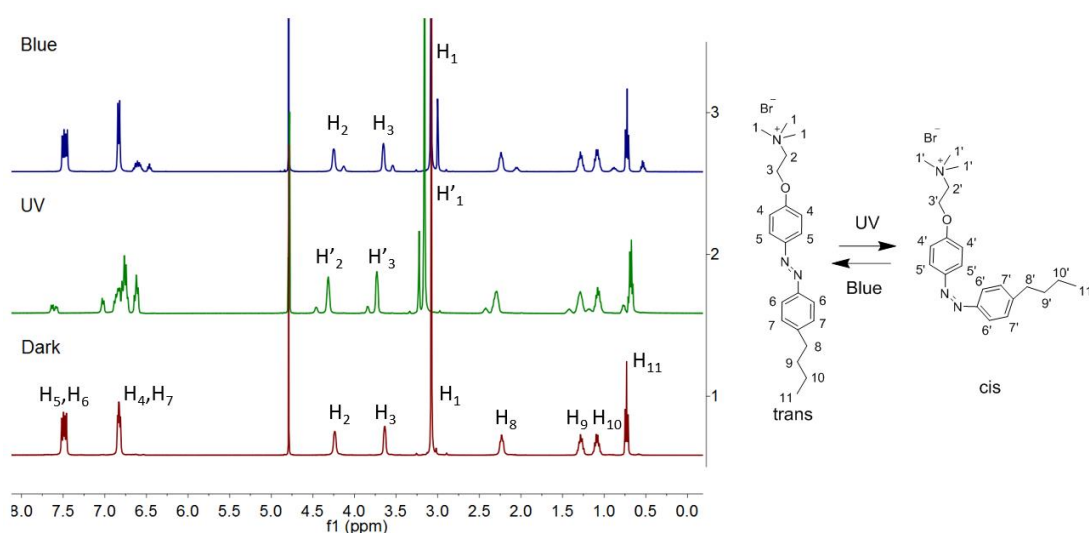


Figure 1 <sup>1</sup>H NMR spectra of 4Azo2TAB 50mM in D<sub>2</sub>O (dark) before and after light irradiation (UV, blue LEDs).

The molar fraction of *trans* isomers in the photostationary state  $x_{trans}$  values determined by NMR are given in Table 3. For 50 mM 4Azo2TAB solution, 33% of *trans* isomers are still present after 4 h exposure to UV tube. The *trans* fraction even Dark increases to 40% after 21 h probably due to lamp heat dissipation problems. For the same solution, only 15% of *trans* isomers are present after 3 h UV LEDs irradiation. For a less concentrated solution close to the CMC of *cis* isomers,  $x_{trans}$  values are lower than those obtained with the 50 mM solution and the steady state is reached faster.

$x_{trans}$	UV tubes	UV LED	Blue LED
4Azo2TAB 50mM in D <sub>2</sub> O	33 %	15 %	82 %
4Azo2TAB 8.6 mM in D <sub>2</sub> O	12 %	8 %	82 %

Table 3  $x_{trans}$  of 4Azo2TAB determined by NMR.

## By UV-Vis

We plot the variation of the UV absorption spectra of 4Azo2TAB/PSS complexes using different light irradiations setups in Figure 2. The concentration (PSS/4Azo2TAB 100/50 mM) used for structural studies is too high to be measured directly by UV-Vis spectroscopy directly, a dilution is needed prior to the experiments. The *trans* form presents a maximum adsorption band at 347 nm. Upon UV irradiation, this band decreases and shifts progressively to lower wavelength and a band increases at 438 nm. Two isosbestic points are present, which reflect that the absorption spectrum is a linear combination of the pure *trans* and pure *cis* absorption spectra. We can therefore extract the *trans/cis* ratio from the UV-Vis spectrum at any irradiation time. The details of the method are given in Chap VI.3.2.

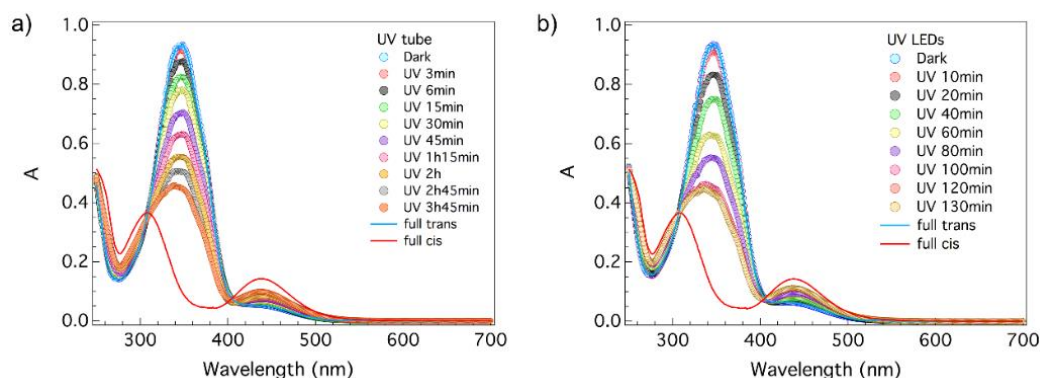


Figure 2 Variation of absorption under a) UV tube irradiation; b) UV LEDs irradiation.

$x_{trans}$  values for all intermediate states as a function of the irradiation time are plotted in Figure 3.  $x_{trans}$  at the stationary state is 39% with UV LEDs and 42% with UV tubes. The *trans/cis* photoisomerization is clearly faster under UV LEDs irradiation than under UV tubes and the equilibrium state is richer in *cis* isomers.

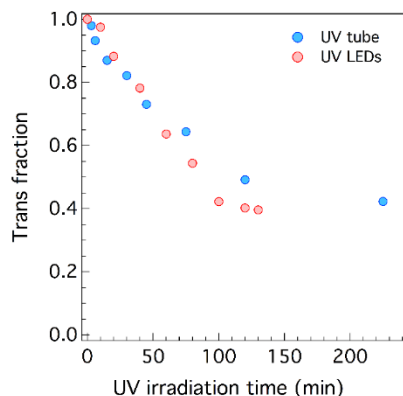


Figure 3 Evolution of the *trans* fraction for 4Azo2TAB/PSS complexes (50 mM/100 mM) under UV light irradiation. Red curve: irradiation by UV LEDs; Blue curve: irradiation by UV tubes. The concentrated solution was diluted 1000 times prior to measurements.

### Conclusion

$x_{trans}$  at the stationary state depends on the irradiation wavelength and the irradiance of UV sources. UV LEDs and UV tubes wavelength are both centred at 365 nm. But the spectral distribution of UV tubes is larger and contains undesired wavelength (such as blue light), which may cause the inverse *cis* to *trans* isomerization.  $x_{trans}$  values determined for UV tubes are always higher than that found for UV LEDs.

The kinetic of photoconversion is proportional to the irradiance of light source (radiative flux received per unit area) and therefore, to the light source and its distance to the sample. Due to the heat dissipation problem, samples are put at 10 cm away from the UV tubes. In contrast samples can be put close to the UV LEDs, which further enhances the irradiance. The equilibrium state is achieved faster with UV LEDs. UV LEDs are therefore more efficient and more adapted to our experiments.

The sample concentration may also affect the *trans* fraction because the Azo moiety has a very strong absorbance. This will be discussed in Chapter VI.

Blue light is used to induce the phototransition from *cis* to *trans* state. Several tests were performed with incandescent lamp. Heating problems were observed. We finally used blue LEDs (465 nm) in the same way as UV LEDs for the back transformation from *cis* to *trans* isomers. The final composition  $x_{trans}$  after blue light irradiation is estimated in the same way as for UV irradiation.

## IV.2 Small-Angle X-ray and Neutron Scattering

### IV.2.1 Generalities

Small-Angle Neutron Scattering (SANS) and Small-Angle X-ray Scattering techniques (SAXS) are well-suited techniques to determine the structural organization in soft matter, from self-assembled systems to colloidal and polymer solutions<sup>9,18</sup>. SAXS and SANS can probe distances from a few angstroms to tens of hundred nanometres, giving information about the shape and size of the objects as well as their mutual organization.

For PEs and surfactants in solution, we measure the total differential scattering cross section of the solute  $\Sigma(\vec{q})$  that contains all the information about the structural organization, and a background (solvent scattering and incoherent scattering in SANS) that needs to be subtracted. The intensity is measured as a function of the scattering vector  $\vec{q}$  defined as  $q = 4\pi \sin(\theta/2) / \lambda$  where  $\theta$  is the scattering angle and  $\lambda$  the wavelength.

The scattering cross section of the solute per unit volume  $\Sigma(\vec{q})$  (in  $\text{cm}^{-1}$ ) or more simply, the intensity, depends on the structural organization of the elementary scatterers (monomers, surfactants, ions...) and writes:

$$\Sigma(\vec{q}) = \frac{1}{V} \sum_{i,j} K_i K_j \langle \exp[i\vec{q}(\vec{r}_i - \vec{r}_j)] \rangle \quad K_i = a_i - a_s \frac{v_i}{v_s} \quad (1)$$

$\vec{r}_i$  and  $\vec{r}_j$  are the positions of the scatterers  $i$  and  $j$ ,  $K_i$  and  $K_j$  are their contrast lengths (cm) relative to the solvent  $s$ .  $a_i$  and  $a_s$  are the coherent scattering lengths (cm) of the scatterers  $i$  and the solvent, and  $v_i$  and  $v_s$ , are their partial molar volumes ( $\text{cm}^3 \text{mol}^{-1}$ ). These partial molar volumes can be determined from density measurements or estimated by incremental volumes. It is usually more convenient to introduce the scattering length density of the scatterers  $\rho$  (or SLD in  $\text{cm}^{-2}$ ):

$$\rho = \frac{a}{v} N_a \quad (2)$$

with  $N_a$  the Avogadro number.

For an isotropic two components system made of PEs and surfactants in aqueous solution (we neglect here the contribution of the counterions) and considering monomer-monomer, surfactant-surfactant and monomer-surfactants pairs in equation (1), the scattering cross section split in three distinct terms

$$\Sigma(q) = K_m^2 S_{mm} + K_{Surf}^2 S_{SurfSurf}(q) + 2K_m K_{Surf} S_{mSurf}(q) \quad (3)$$

with

$$\begin{cases} K_m = a_m - a_s \frac{v_m}{v_s} = \frac{v_m}{N_a} (\rho_m - \rho_s) \\ K_{Surf} = a_{Surf} - a_s \frac{v_{Surf}}{v_s} = \frac{v_{Surf}}{N_a} (\rho_{Surf} - \rho_s) \end{cases} \quad (4)$$

$S_{mm}$ ,  $S_{SurfSurf}$  and  $S_{mSurf}$  are the partial structure functions related to the monomers ( $m$ ), the surfactants ( $Surf$ ) and monomers-surfactants ( $mSurf$ ). They contain all the information on the structural arrangement of monomers, ( $S_{mm}$ ), surfactants ( $S_{SurfSurf}$ ), as well as their mutual organisation (cross term  $S_{mSurf}$ ).

Using neutron scattering and isotopic labelling, it is possible to vary the SLD of the water by mixing  $H_2O$  and  $D_2O$ . With a deuterated volume fraction  $\phi_D$ , the corresponding SLD  $\rho_{H_2O/D_2O}$  writes

$$\rho_{H_2O/D_2O} = (1 - \phi_D)\rho_{H_2O} + \phi_D\rho_{D_2O} \quad (5)$$

By choosing the right composition  $\phi_D$ , it is possible to match the SLD of component A and therefore, to mask its contribution to the scattered intensity ( $\rho_{H_2O/D_2O} = \rho_A$ ,  $K_A = 0$ ,  $K_A^2 S_{AA}(q) = 0$ ,  $K_A K_B S_{AB}(q) = 0$ ). The structure function of the other component B is then revealed ( $\sum(q) = K_B^2 S_{BB}(q) \neq 0$ ). This contrast matching method or more generally, the contrast variation is really unique in neutron scattering. With X-rays we are usually in a situation where all the structure functions contribute to the scattered intensity.

For polymeric chains, micelles and their complexes, each structure function contains two contributions. One originates from interferences between scatterers in the same “object” (form factor), and one from interferences between scatterers in different objects (structure factor). The form factor (associated to intra-object correlations) enables to characterize the size and the shape of the assembly while the structure factor (inter-object correlations) gives information about their dispersion state. The later therefore directly reflects the interaction between the objects.

In our systems composed of PEs, surfactants and their mixtures, we observe the formation of globular as well as cylindrical particles. The “colloidal description” is often more appropriate to analyse the scattered intensity

$$\sum(q) = I(q) = \phi \Delta\rho^2 V P(q) S(q) \quad (6)$$

where  $\phi$  is the volume fraction of the particles,  $V$  their volume and  $\Delta\rho^2$  the contrast factor ( $\Delta\rho = \rho_{particle} - \rho_s$ ).  $P(q)$  is the normalized form factor ( $P(q=0) = 1$ ).  $S(q)$  is the structure factor.

## IV.2.2 Form factor

For very dilute systems, or more generally when inter-particles correlations are negligible,  $S(q)=1$ , only the form factor  $P(q)$  contributes to the intensity.

The spatial resolution is inversely proportional to the scattering vector  $q$ . Different geometrical information can be found according to the  $q$  range of observation and the typical size  $R_g$  (radius of gyration) of the particle (Figure 4).

For  $q \rightarrow 0$  (violet zone in Figure 4), the object can be considered as punctual with respect to the spatial resolution: only global properties can be determined. Since  $P(q) \rightarrow 1$ ,  $\Sigma(q) = \phi \Delta \rho^2 V$ , we can extract the volume of the objects, and therefore the degree of polymerization for polymers in solution.

For  $qR_g < 1$  (red zone in Figure 4), we are in the Guinier regime. We find a plateau at low  $q$ . The reduction of the intensity around  $qR_g \approx 1$  allows to determine the radius of gyration  $R_g$ .

For  $qR_g > 1$ , we enter in the intermediate regime (blue zone in Figure 4). The scattered intensity scales as  $q^{-\alpha}$ , where  $\alpha$  is related to the shape of the object. For example,  $\alpha = 1$  for an infinite rod, 2 for a Gaussian chain. If the geometry of the object is well defined (sphere, ellipsoid, cylinder with low polydispersity), additional characteristic oscillations are observed in the regime and can be analysed on the basis of analytical form factors.

In the high- $q$  regime (Porod regime, green zone in Figure 4), we probe the interface of the objects. For a smooth interface, the intensity usually varies as  $q^{-4}$ .

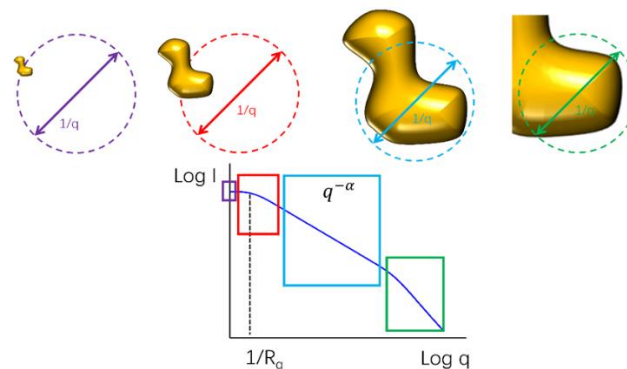


Figure 4 Form factor  $P(q)$  and corresponding range of observation in real space. Adapted from Ref 9.

## IV.2.3 Scattering length densities (SLD)

The SLDs of the different components are key parameters in small-angle scattering. This knowledge is important to prepare the experiments, but also, to correctly analyse the data. The SLD determination is based on scattering length

and the partial molar volume of the molecules.

#### IV.2.3.1 Scattering length of molecules or monomers

The X-ray scattering length  $b_x$  is proportional to the total number of electrons  $Z_e$  (that increases linearly with the atomic number  $Z$ ) of the molecule.

$$b_{x\ total}(10^{-13}\text{ cm}) = r_e \times Z_e = 2.82 \times Z_e \quad (7)$$

where  $r_e = 2.82 \cdot 10^{-13}$  cm is the classical radius of the electron.

Values for common elements are given in Table 4.

The neutron coherent scattering length of atoms  $b_N$  are available in many articles or books. The neutron scattering length of a molecule is equal to the sum of the  $b_i$  over all the atoms in the molecule:

$$b_{N\ total}(10^{-13}\text{ cm}) = \sum b_{Ni} \quad (8)$$

Atoms	$M$ (g mol <sup>-1</sup> )	$b_N$ (10 <sup>-13</sup> cm)	$b_x$ (10 <sup>-13</sup> cm)
C	12.011	6.646	16.92
N	14.0	9.36	19.74
H	1.008	-3.739	2.82
D	2.014	6.671	2.82
O	15.999	5.803	22.56
S	32.06	2.847	45.12
Br	79.904	6.795	98.7
Na	22.99	6.795	31.02

Table 4 Neutron and X-ray scattering lengths of atoms  $b_N$  and  $b_x$

#### IV.2.3.2 Partial molar volumes of molecules or monomers

The partial molar volume is a thermodynamic quantity which is intimately related to the solute-solvent interactions. It corresponds basically to the overall volume variation of a solution induced by the dissolution of a solute. We should note that if the volume of a substance cannot be negative, the partial molar volume can be. An example is the dissolution of a strong electrolyte in water. The water molecules in the solvation shell around the ions are physically closer than in bulk pure water resulting in a global volume decrease.

The partial molar volume  $v$  (cm<sup>3</sup> mol<sup>-1</sup>) of a molecule can be obtained by density measurements (when possible) or with the incremental volume method.

Molecules are then divided in different chemical parts of known partial molar volumes. By considering the additivity of the partial molar volumes  $v_{0i}$

$$v = \sum v_{0i} \quad (8)$$

Azo-surfactants can be divided into several parts as shown in Figure 5 (alkyl tail, azobenzene core, oxy group, small alkyl spacer and polar head). The partial molar volumes of each chemical group are summarized in Table 5. The volume associated to the polar head is deduced from the partial molar volume of the cetyltrimethyl ammonium bromide (CTAB)<sup>10</sup> in the micellar state by considering

$$v_{CTAB} = v_{C_{16}H_{33}} + v_{(CH_3)_3N^+} + v_{Br^-} = 365.4 \text{ cm}^3 \text{ mol}^{-1} \quad (9)$$

- **Azo-surfactant:** 4Azo2TAB and 8Azo2TAB

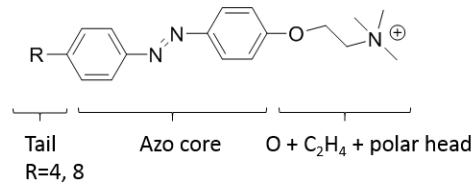


Figure 5 Chemical structure of Azo-surfactant.

	$v$ ( $\text{cm}^3 \text{ mol}^{-1}$ )
$C_4H_9$	81.3
$C_8H_{17}$	146.1
$C_2H_4$	32.6
oxo	5.48
$(CH_3)_3N^+$	59.6
azobenzene	106.0

Table 5 Partial molar volume of different chemical groups<sup>10-12</sup>.

#### IV.2.3.3 Scattering length density of molecules or monomers

The scattering length density  $\rho$  ( $\text{cm}^{-2}$ ) of a molecule is given by

$$\rho = \frac{a}{v} N_A \quad (10)$$

or more explicitly

$$\rho(10^{10} \text{ cm}^{-2}) = \frac{a(10^{-13} \text{ cm})}{v(\text{cm}^3 \text{ mol}^{-1})} \times 6.022(10^{23} \text{ mol}^{-1}) \quad (11)$$

where  $N_A$  ( $\text{mol}^{-1}$ ) is the Avogadro's number,  $a$  ( $\text{cm}^{-1}$ ) and  $v$  ( $\text{cm}^3 \text{ mol}^{-1}$ ) are

the scattering length and the partial molar volume.

The scattering length densities, scattering lengths and partial molar volumes (X-rays and neutron) for all the molecules and monomers used in this thesis are presented in Table 6 and on Figure 6 (for SANS experiments). Calculations are given for the ionized forms only. The contribution of the counterions Na<sup>+</sup> and Br<sup>-</sup> are negligible for SANS experiments. It is no longer the case for SAXS measurements.

	$\nu$ (cm <sup>3</sup> mol <sup>-1</sup> )	$b_x$ (10 <sup>-13</sup> cm)	$\rho_x$ (10 <sup>+10</sup> cm <sup>-2</sup> )	$b_N$ (10 <sup>-13</sup> cm)	$\rho_N$ (10 <sup>+10</sup> cm <sup>-2</sup> )
H <sub>2</sub> O	18.07	28.2	9.4	-1.68	-0.56
D <sub>2</sub> O	18.07	28.2	9.4	19.15	6.38
4Azo2TA <sup>+</sup>	284.97	518.88	10.97	61.28	1.295
8Azo2TAB <sup>+</sup>	349.76	609.12	10.49	57.95	0.998
PSS <sub>H</sub> <sup>-</sup>	114	270.72	14.30	47.25	2.51
PSS <sub>D</sub> <sup>-</sup>	114	270.72	14.30	120.12	6.35
PAA <sup>-</sup>	29.1	107.16	22.18	20.33	4.21
PAA <sup>-</sup> -Azo <sub>0.11</sub>	48.6	148.73	18.44	-	-
PAA <sup>-</sup> -Azo <sub>0.15</sub>	58.1	163.84	17.73	-	-
Sal <sup>-</sup>	100.3	203.0	12.19	45.24	2.715
BenSulf	109.2	231.2	12.76	41.437	2.286
Na <sup>+</sup>	-6.6	28.2	-25.65	3.63	-3.302
Br <sup>-</sup>	30.1	101.5	20.30	6.80	1.36

Table 6 Summary of the different compounds involved in this thesis<sup>13-15</sup>.  $\nu$  (cm<sup>3</sup> mol<sup>-1</sup>) partial molar volume,  $b_x$  (cm) X-ray scattering length,  $\rho_x$  (cm<sup>-2</sup>) X-ray scattering length density,  $b_N$  (cm) neutron scattering length,  $\rho_N$  (cm<sup>-2</sup>) neutron scattering length density. Values for PAA<sup>-</sup>, azo-containing PAA are calculated according to the method described in IV.2.3.

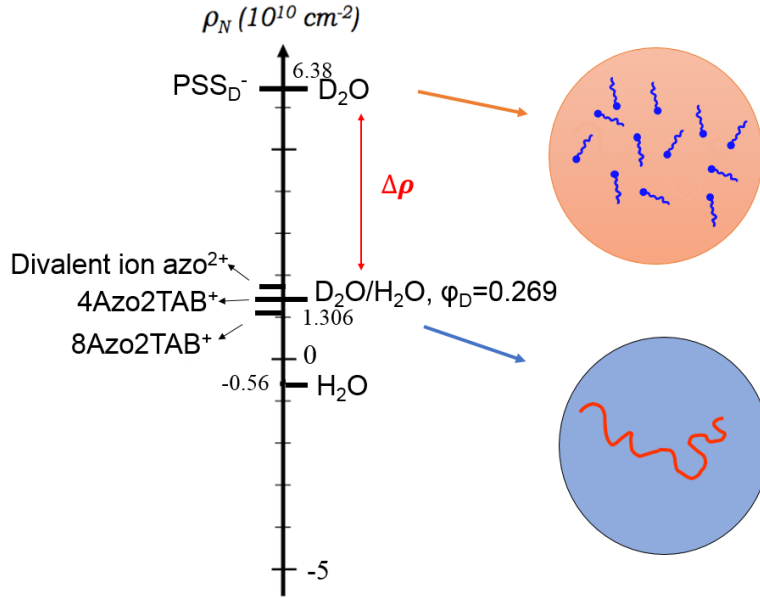


Figure 6 Contrast variation for PSS/Azo-surfactant complexes. The cartoons represent what is mainly seen with SANS using deuterated PSS and hydrogenated surfactant for  $\rho_s = 6.38$  and  $1.306 \cdot 10^{10} \text{ cm}^{-2}$ .

#### IV.2.3.4 Fitting models

For the different systems forming aggregates, we analysed the scattered intensity on the basis of the general equation

$$I(q) = \phi \Delta \rho^2 V P(q) S(q) \quad (12)$$

Experimental data have been fitted on the absolute scale using the NCNR SANS package developed by NIST Center for Neutron Research and running with the Igor Pro software. Different models of the library have been used and/or modified. We briefly present here the most important form factors we used as well as their adjustable parameters.

#### Spherical and core-shell spherical models

The form factor for a homogenous sphere (also called one shell spherical model) of radius  $R$  is given by

$$P_S(q, R) = \left[ 3 \frac{\sin(qR) - (qR) \cos(qR)}{(qR)^3} \right]^2 \quad (13)$$

For a core-shell model with a core radius  $R_c$ , a shell radius  $R_s$ , and SLD  $\rho_c$  and  $\rho_s$ , in a solvent of scattering length density  $\rho_{solv}$ , the form factor  $P(q)$  is

$$P(q, R) = \left[ \frac{(\rho_s - \rho_{solv}) V_s F_S(q, R_s) + (\rho_c - \rho_s) V_c F_S(q, R_c)}{(\rho_s - \rho_{solv}) V_s + (\rho_c - \rho_s) V_c} \right]^2 \quad (14)$$

With

$$F_S(q, R) = \left[ 3 \frac{\sin(qR) - (qR) \cos(qR)}{(qR)^3} \right] \quad (15)$$

The adjustable parameters for the fits are the volume fraction, the core radius and the shell thickness, the SLDs of the core, the shell and the solvent (fixed value), as well as a background.

The homogeneous sphere model has been used to fit the scattering of PAA-Azo copolymers (long chains). It has been combined with a Gaussian polydispersity and a structure factor  $S(q)$  developed for charged colloids in a repulsive screened Coulombic potential.

### **Ellipsoid of revolution and core-shell ellipsoids**

For a uniform ellipsoid of revolution (also call one shell ellipsoid) with semi-axis  $R$ ,  $R$  and  $\varepsilon R$  (where  $\varepsilon$  is the ellipticity)

$$P(q, R, \varepsilon) = \int_0^{\pi} P_S(q, r(R, \varepsilon, \alpha)) \sin \alpha d\alpha \quad (16)$$

with

$$r(R, \varepsilon, \alpha) = R \sqrt{\sin^2 \alpha + \varepsilon^2 \cos^2 \alpha} \quad (17)$$

The adjustable parameters for the fits are the volume fraction, the semi-radius along the symmetry (or rotation) axis ( $\varepsilon R$ ), the semi-radius in the equatorial plane ( $R$ ), the SLDs of the particle and the solvent (fixed value) as well as a background. This model applies to oblate ( $\varepsilon < 1$ ), prolate ( $\varepsilon > 1$ ), or spherical ( $\varepsilon = 1$ ) particles. Semi-radius in the equatorial plane and along the symmetry axis ( $R$  and  $\varepsilon R$ ) are also called major and minor (oblate situation) or minor and major (prolate situation) according the ellipticity value.

This model has been used to fit the scattering of surfactant micelles in combination with a structure factor  $S(q)$  developed for charged colloids in a repulsive screened Coulombic potential.

The model for the core-shell ellipsoid is a variant the homogeneous model. The adjustable parameters for the fits are the volume fraction, the major and minor core radius, the major and minor shell radius, the SLDs of the core, the shell and the solvent (fixed value) and a background. The shell thickness was let free in the two directions (major, minor) or kept constant.

This model has been used to fit the scattering of surfactant micelles with neutron and X-rays and the intensity of PE/surfactant complexes. For the micelles,

this model was combined to a structure factor  $S(q)$  developed for charged colloids in a repulsive screened Coulombic potential.

### **Cylindrical model with elliptic section and core-shell variant**

For an elliptical cylinder on length  $H$ , a minor axis  $a$  and a major axis  $\varepsilon a$  ( $\varepsilon$  is the ellipticity) with no preferred orientation the form factor is

$$P(q) = \int_0^{\frac{\pi}{2}} F^2(q, \alpha, \psi) \sin \alpha d\alpha \quad (18)$$

with

$$F(q, \alpha, \psi) = 2 \frac{J_1(x) \sin(y)}{xy} \quad (19)$$

and

$$x = q \sin \alpha [(\varepsilon a)^2 \sin^2 \psi + a^2 \cos^2 \psi]^{\frac{1}{2}} \quad (20)$$

$$y = q \frac{L}{2} \cos(\alpha) \quad (21)$$

where  $J_1(x)$  is the Bessel function of the first kind and first order.

The adjustable parameters for the fits are the volume fraction, the minor radius, the ellipticity  $e$ , the length of the cylinder, the SLDs of the particle and the solvent (fixed value), as well as a background.

This model has been used to fit the scattering of wormlike micelles. Due to the very long size of the aggregates, the length  $H$  cannot be determined and has been fixed to an arbitrary value.

The core-shell elliptic model is a variant the homogeneous model. The adjustable parameters for the fits are the volume fraction, the major core, the ellipticity, the SLDs of the core, the shell and the solvent (fixed value), and a background. A single ellipticity has been introduced in the model. The shell thickness is therefore not identical in the direction of the short and the long axis.

This model has been used to fit the scattering of surfactant and of wormlike micelles by SAXS.

### **Pearl-necklace model**

In order to fit the scattering of PE/surfactant complexes, we need to determine the intensity scattered by a pearl-necklace assembly. Our simplified model is based on the form factor initially developed for hydrophobic PEs<sup>16</sup>. In this model,

$N$  pearls are located on the segments (size  $A$ ) of a freely jointed chain. For simplicity, we ignore the scattering of the connecting segments and only consider the contribution of the pearls. If  $P_{pearl}(q)$  is the form factor a one pearl of volume  $V_{pearl}$ , the intensity scattered by a pearl-necklace containing  $N$  pearls (considering  $S(q)=1$ ) is given by

$$I_{pearl\ necklace}(q) = \phi \Delta \rho^2 V_{pearl} P_{pearl}(q) Interf(q) \quad (22)$$

with

$$Interf(q) = \frac{2}{N} \left[ \frac{N}{1 - \frac{\sin(qA)}{qA}} - \frac{N}{2} - \frac{1 - \left(\frac{\sin(qA)}{qA}\right)^N}{\left(1 - \frac{\sin(qA)}{qA}\right)^2} \frac{\sin(qA)}{qA} \right] \quad (23)$$

$Interf(q)$  is the interference function between the pearls along a single necklace.

This model has been used to fit the scattering of PE/surfactant complexes. We used the core-shell ellipsoid model for  $P_{pearl}(q)$ . The adjustable parameters combine those of  $P_{pearl}(q)$  but also, those of the interference functions: the number of pearls and the average distance between them. Note that  $N$  cannot really be fitted and must be an integer. It is therefore changed manually until the fit quality is improved.

#### IV.2.3.5 Structure factor $S(q)$

In our systems, electrostatic interaction plays a key role in the stabilisation of the solution. Repulsions are usually responsible for the presence of a peak in the scattered intensity. In order to analyse correctly the data, we have often combined the form factors with a structure factor  $S(q)$  developed for charged micelles and colloids in a repulsive screened Coulombic potential<sup>16,17</sup>.

The adjustable parameters combine those of  $P(q)$  and those of the structure factor  $S(q)$ : the volume fraction, the radius of the particles, the salt concentration, the charge number (in  $e$  units), the temperature (fixed) and the dielectric constant (fixed).

This structure factor has been used to fit the scattered intensity of surfactant micelles (using an ellipsoid form factor) as well as the spherical particles found in PAA-Azo modified polymers(core-shell spherical particle). For this system,  $S(q)$  was associated to the form factor or core-shell spherical particles.

## IV.2.4 SAXS experimental conditions and illumination protocol

### IV.2.4.1 SAXS instrument

SAXS measurements were performed at the Institut Charles Sadron on a Rigaku diffractometer installed on a microfocus rotating anode generator (Micromax™-007 HF) operating at 40 kV, 30 mA. The beam was monochromatized (wavelength = 1.54 Å) and collimated with a confocal Max-Flux Optics™ (Osmics, Inc.) combined with a three pinholes system. The scattered intensity was measured as a function of the magnitude of the scattering vector with a 2D multiwires detector located at  $d = 0.81$  m from the sample position ( $0.01 \text{ \AA}^{-1} < q < 0.33 \text{ \AA}^{-1}$ ). Scattering patterns were treated according to the usual procedures for isotropic scattering. Glass and quartz capillaries (1mm in diameter) were used as sample containers. Scattering from pure water and empty capillary were also measured and subtracted to the sample measurements. Intensities were converted into absolute scale with a calibrated Lupolen standard. Scattering vectors were calibrated using the diffraction peaks of a silver behenate powder. Experimental resolution was measured on a Bragg peak of tricosane sample. Except for relaxation studies, the illumination was always maintained during SAXS measurements. Experiments were performed in vacuum at room temperature.

### IV.2.4.2 Illumination setup and protocols

Two UV or blue LEDs were fixed above and below the capillary (2 mm apart) to illuminate the sample *in situ* (Figure 7). The concentration of Azo in solutions varies from 15 mM to 150 mM. In order to ensure the equilibrium state is reached, measurements were done regularly until the scattered intensity is stabilized. The irradiation time needed to reach the stationary state depends on the chromophore concentration, but also on the structure of the solutions. In this final state, the structure is believed to be homogeneous in the sample. Unintended effects may appear in highly viscous solutions or in thick samples for which the diffusion process is not able to homogenize the system in a reasonable time, or before the chromophore relax to their *trans* state. For low concentration chromophore solutions, an equilibrium period of 40 - 60 min is necessary (10 min/measurement during the transition regime).

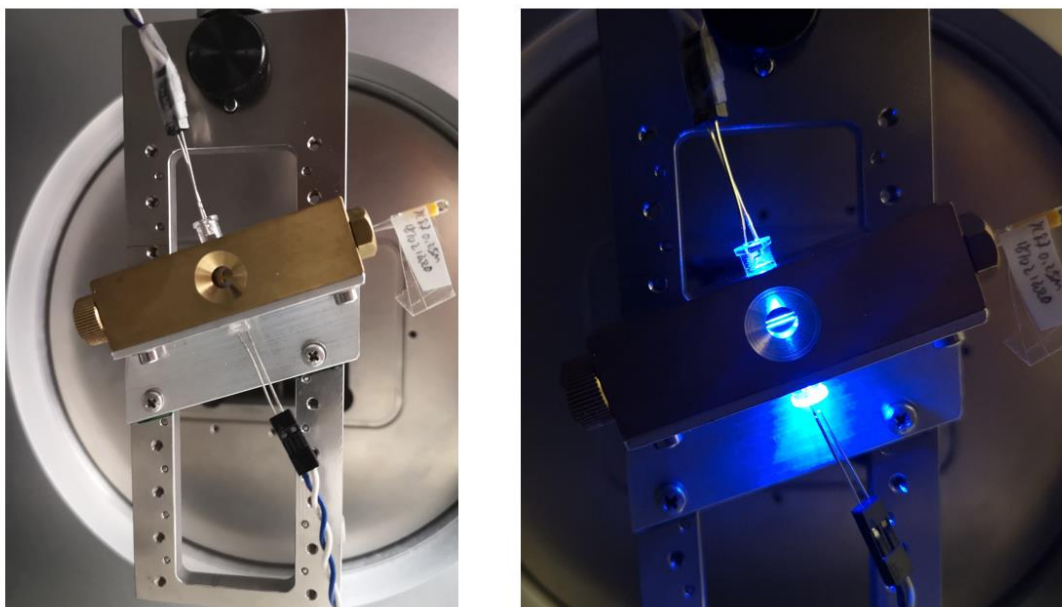


Figure 7 In situ light irradiation setup for SAXS experiments (blue light).

For concentrated solutions or particular compositions, longer irradiation time is needed. To be more efficient, the whole capillary was pre-irradiated by 8 LEDs during 1 - 2 hours before being introduced in the SAXS instrument (Figure 8).

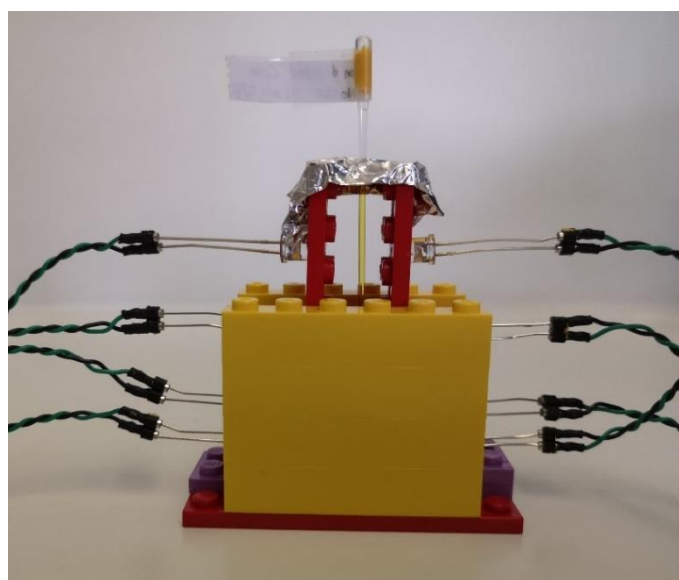


Figure 8 External pre-illumination by 8 LEDs for SAXS samples.

For thermal relaxation studies, we also need to probe an 'homogeneous irradiated system' on the time scale of the measurement. Using the "classical" irradiation device in the diffractometer (Figure 7), the initially irradiated zone is of the order of 5 mm along the capillary without pre-irradiation. We must avoid the

diffusion effect between molecules initially in the irradiated zone (majority of *cis* conformation) and in the non-irradiated zone (*trans* conformation). For that reason, samples were pre-illuminated outside with 8 LED until the stationary state is reached, installed in the sample holder and then left to relax in dark.

We may wonder if the measurement using outside pre-illumination has the same final state as with a direct in-situ irradiation. The UV plots of wormlike micelles (8Azo2TAB/NaSal) obtained with the two irradiation ways are given in Figure 9. No difference is observed between these illumination methods. Even if the exchange between the irradiated zone and the non-irradiated zone exists during the measurement, this does not seem to influence the *trans/cis* ratio at equilibrium state for this sample.

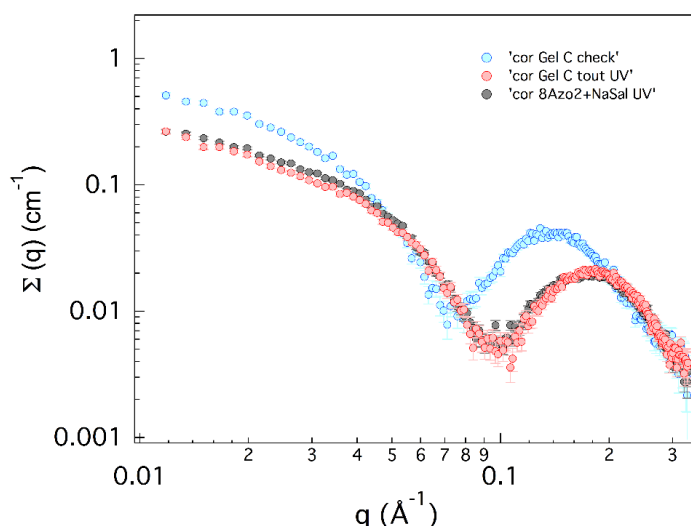


Figure 9 Comparison of SAXS curves of 8Azo2TAB/NaSal (75 mM/62.5 mM) irradiated by different ways: only with two UV LEDs in situ (black curve) and pre-illumination of the whole capillary with UV LEDs plus two UV LEDs in situ (red curve).

#### IV.2.4.3 Experimental conditions

##### **Borosilicate and quartz glass capillaries**

Borosilicate and quartz glass capillaries were tested under UV by SAXS. While the absorption of borosilicate is a little higher than that of quartz, the final state probed by SAXS is nearly identical (Figure 10). For cost reason, most of the SAXS experiments were done with borosilicate capillaries.

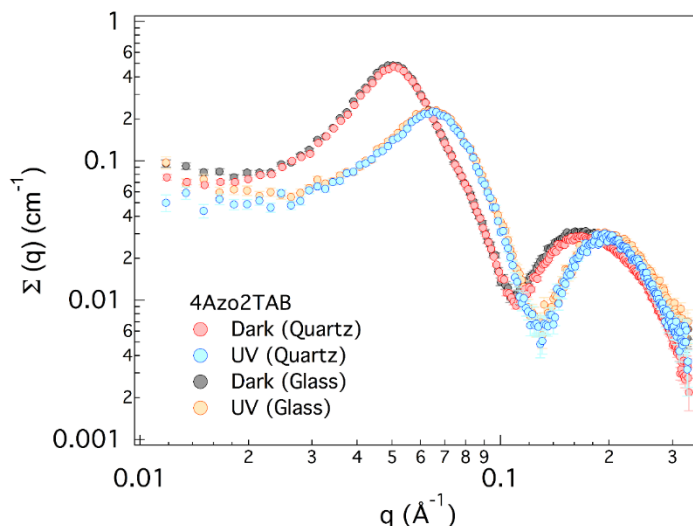


Figure 10 SAXS curves of 4Azo2TAB 50 mM measured in glass (borosilicate) and quartz capillary.

### Diameter of the capillary and sample preparation

The diameter of the capillary (sample thickness) may influence the *trans/cis* composition at the final state because the Azo moiety absorbs enormously the incident UV light. The homogenization of the solution requires the diffusion of the chromophores (and therefore the diffusion of the micellar aggregates in which they are embedded) over the thickness of the sample. For high azobenzene content, high viscous systems and large diameter, the homogenization may be difficult to achieve. The apparent final state measured on surfactant/PE complexes at relatively high concentration (4Azo2TAB/PSS, 50 mM/100 mM) in 1.5 mm capillary show large difference at large  $q$  values with respect to the 1 mm capillary. The oscillation around  $0.2 \text{ \AA}^{-1}$  (characteristic of the micellar aggregate) is shifted to low  $q$  upon UV irradiation (*i.e.*, closer to the dark solution) for the largest diameter capillary (yellow curve in Figure 11). This is consistent with final state in which *cis/trans* ratio is reduced. This capillary diameter effect on the final state is also possible with the 1 mm diameter capillary. However, the final state is identical to that measured on the same sample at lower concentration. It seems therefore unlikely. 1 mm capillary appears as the best compromise for measurements under light stimulus.

We remark that the real diameters of capillaries vary from one to the other (0.85 mm to 1.2 mm). Their thicknesses were measured individually by optical microscopy. It is an important parameter for the conversion of the scattered intensity to the absolute scale.

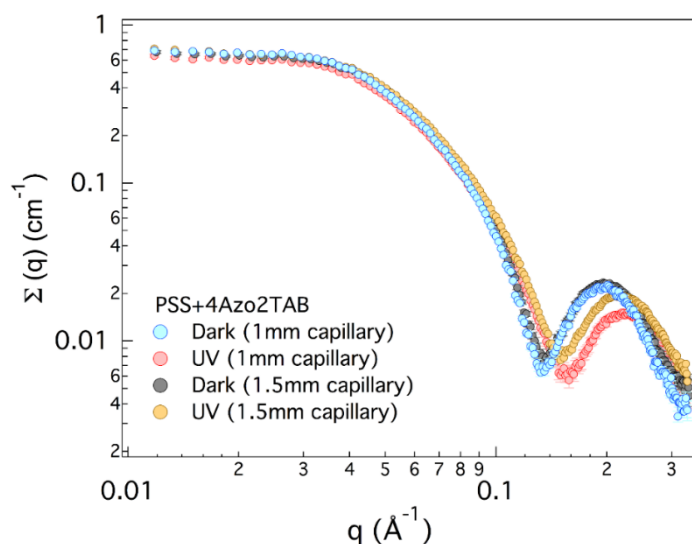


Figure 11 SAXS curves of 4Azo2TAB/PSS (50mM/100mM) complexes with capillaries of different diameters.

## IV.2.5 SANS experimental conditions and illumination protocol

### IV.2.5.1 SANS instrument

SANS measurements were carried out on the PAXY diffractometer at Laboratoire Léon Brillouin (CEA Saclay, France). Three configurations (sample to detector distance/wavelength) were used (1 m/ 5 Å, 3 m/5 Å, 5 m/8.5 Å) covering a  $q$  range from  $5 \cdot 10^{-3}$  to  $0.45 \text{ \AA}^{-1}$ . Samples were loaded in quartz cell (Hellma) of 1 mm path length. The temperature was controlled and fixed to  $22^\circ\text{C}$ . Data were corrected and set in absolute scale using the *PASINET* software developed at LLB.

### IV.2.5.2 Illumination setup

Sample irradiation was performed *in situ* using a multi-LED setup developed at the LLB. This system is made of ten LEDs arranged circularly on one side of the sample (1 cm apart) and surrounding the neutron beam. Additional LEDs were installed at other positions of the sample changer to pre-illuminate the samples if required. Each measurement under UV were repeated several times and compared to ensure that the equilibrium state is reached.

Additionally, some samples were pre-irradiated by UV tubes or LEDs outside the instrument and stirred several times before their installation on the sample changer. This helps to homogenise quickly the sample and thus reduce the irradiation time *in situ*. The irradiation time required to reach the equilibrium state

was estimated from precise kinetic measurements on representative samples (micelles, PE-micelles).

The presence of external light sources in the close environment might slightly influence the *trans/cis* ratio at the equilibrium. Two distinct experiments have been performed at the LLB on these systems. In the second experiment, the sample was sheltered by an umbrella with anti-UV coating.

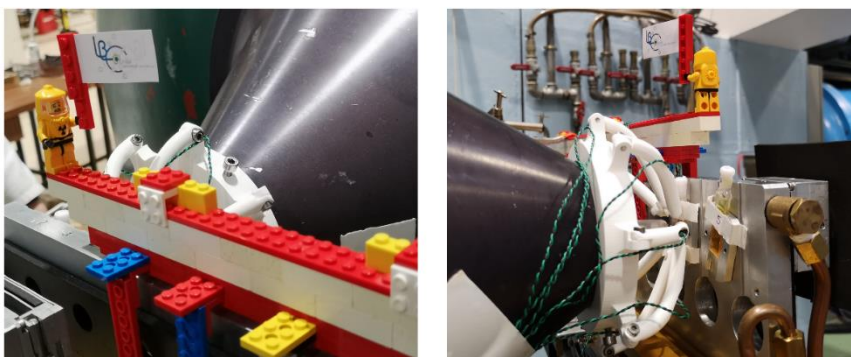


Figure 12 Illumination device for SANS measurements.

### IV.3 NMR

NMR spectra were recorded on a Bruker NMR spectrometer operating at 400 MHz ( $^1\text{H}$ ) or 100 MHz ( $^{13}\text{C}$ ). This technique is used to check the purity of the synthesised surfactants and to determine the *cis/trans* fraction of the solutions in the steady state. NMR tubes (5 mm in diameter) were kept in dark during 2 days prior to the measurements to reveal the signature of pure *trans* isomers. UV irradiation was performed by 8 UV LEDs close to the NMR tube or by UV tubes located at a distance of 5 mm around the NMR tube. Homogenization was done several times during the irradiation.

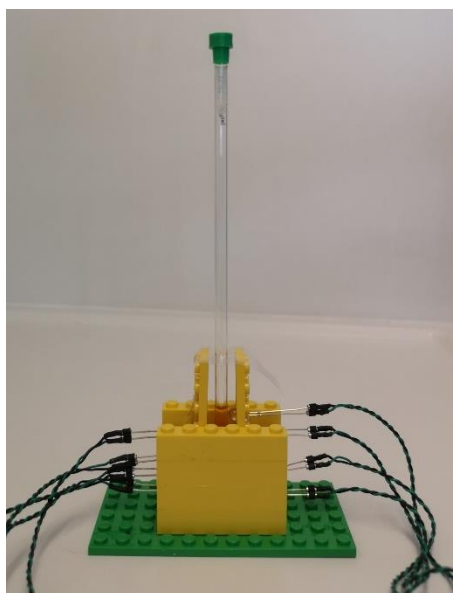


Figure 13 Irradiation of NMR tubes.

## IV.4 Size Exclusion Chromatography (SEC)

Molar mass and polydispersity index ( $I_p$ ) of polymers were determined with size-exclusion chromatography using THF as eluent and toluene as flow rate marker. The flow rate was 1.0 mL/min. All the sodium polyacrylate and azo-functionalized polyacrylate were measured in their acid form. Equipment in THF for small polymers and oligomers has 4 PLGel monoporosity columns: 50 Å, 100 Å, 500 Å, 1000 Å (granulometry = 5 mm; length = 30 cm, internal diameter = 7.5 mm) which ensures a separation range from 100 to 60 000 g/mol. The PMMA calibration is established with 9 Polymer Lab. standards (molar masses between 550 and 27 600 g/mol). The detection is achieved with a Shimadzu RID-10A refractometer and a Shimadzu SPD-20A UV detector.

Equipment in THF for longer polymers has PLGel mixed C columns (particles size = 5 µm; length = 30 cm; internal diameter = 7.5 mm) with a separation range of 1 000 - 2 million g/mole. Molar masses are calculated with PMMA standard calibrations (molar masses from 1310 to 1577 000 g/mol). Detection is carried out with a Shimadzu SPD-M20A diode array UV detector, an Optilab T-REX refractometer (Wyatt Techn), a Viscostar-II viscometer (Wyatt Techn) and a TREOS light scattering detector (Wyatt Techn).

## IV.5 UV-Vis absorption spectroscopy

UV-Vis absorption measurements were carried out on a Perkin Elmer Lambda

25 spectrometer using standard quartz cells (Hellma OS) with an optical path length of 10 mm. Spectra were recorded in the range of 250 - 700 nm. Absorbance from pure water was systematically subtracted from sample measurements. This technique is used to determine the trans/cis molar fraction of the chromophores and can only be used with very low absorbance solutions.

For higher concentration solutions (as for samples for structural studies), a dilution is needed prior to the measurements. A small fraction of the solution was collected, diluted 1000 to 2000 times and analysed immediately on the spectrophotometer.

UV-Visible spectroscopy was also used to investigate the photoisomerization process during the transition regime until the steady state is reached as well as during the thermal relaxation.

The irradiation setup for quartz cell is presented in Figure 14. The sample is illuminated by 4 LEDs on both sides of the cell.

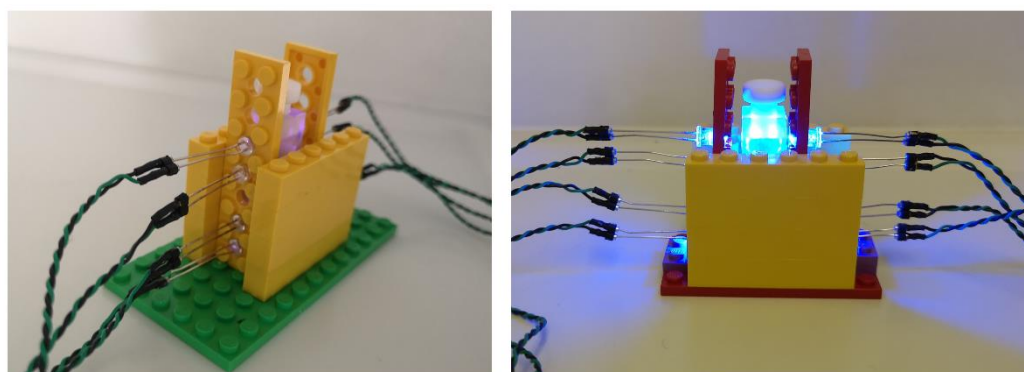


Figure 14 Irradiation of UV-Vis samples by LEDs.

At the very beginning, several measurements were carried out with UV tubes in order to compare with UV LED irradiation. Sample were placed at 10 cm away from the UV tubes to avoid heat dissipation problems (Figure 15). However, we abandoned this illumination method and chose to use the more efficient UV LEDs setup.



Figure 15 Irradiation setup with UV tubes for UV-Vis measurement.

## IV.6 Surface tension measurements

The surface tension measurements were performed on a Kibron tensiometer using a small sample cup (3 mL). Millipore water was used for calibration. Azo-surfactant solutions with accurate concentrations were prepared and kept 2 days in the dark state for equilibrium. For the measurement of the *cis*-form, the solution was pre-irradiated by 8 UV LEDs at a distance of 5 mm in a quartz cell (Hellma OS, 10 mm path length) with stirring (Figure 14). The irradiation time depends on the sample concentration and ranged from 4 h to 20 h. The irradiated solution was transferred in the plastic cuvette just before the measurement. Four LEDs were set above the cuvette to maintain the *cis*-form state during measurement (Figure 16). The critical micellar concentration (CMC) value was determined by the plot of  $\gamma$  as a function of  $\ln c$ .

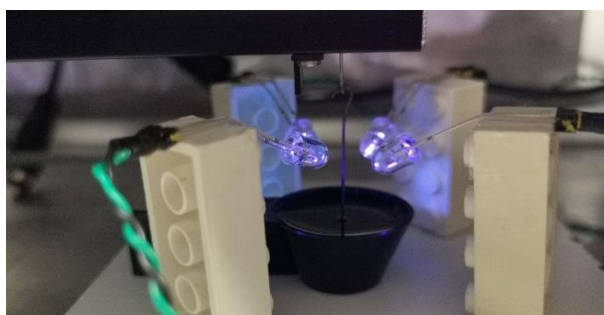


Figure 16 Irradiation Setup for surface tension measurements.

## IV.7 Thermogravimetric analysis (TGA)

Polyelectrolytes are usually hygroscopic and contain typically about 10 - 20% by weight of moisture. It is important to know the water content in the lyophilised powder to get accurate solution concentrations. The residual water contents in PE

(PSS, PAA, azo-modified PAA), but also azo-surfactants and other used products were determined by TGA. Thermogravimetric analysis was carried out with a thermal analyzer (TGA 2 STAR System METTLER TOLEDO) under nitrogen atmosphere at a heating rate of 10 °C/min.

## IV.8 Transmission electron microscopy (Cryo-TEM)

Cryo-TEM measurements have been carried out at the ICS and at DTU (Denmark). Measurements at the ICS have been performed on samples in dark (PAA-Azo and PE/Azo-surfactant complexes). Experiments carried out at DTU on Azo-surfactant/co-surfactant solutions have been realised on samples in dark and under UV radiation.

Images were obtained on samples vitrified in a plunge freezer. The chamber was held at 20°C and the relative humidity at 80%. A 3µl drop was deposited onto a lacey carbon film covered grid (Ted Pella) rendered hydrophilic using a Quorum glow discharge unit (Quorum Q150T ES). The grid is automatically bottled to form a thin film which is plunged in liquid ethane hold at -190°C by liquid nitrogen. In that way a vitrified film is obtained in which the native structure of the system is preserved. The grid was mounted onto a cryo holder (Galan 626) and observed under low dose conditions in a Tecnai G2 microscope (FEI) at 200 kV. Images were acquired using a Gatan Oneview camera (DTU) and a FEI Eagle 2k-2k ssCCD camera (ICS). For measurement under UV radiation, the solution was irradiated directly in its dial during 4 hours (Figure 17) before collecting the necessary volume for sample preparation.

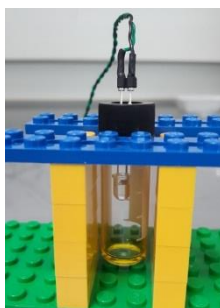


Figure 17 Irradiation setup for Cryo-TEM experiments.

## References:

- (1) Shimogaki, T.; Oshita, S.; Matsumoto, A. Intercalation of Mono- and Difunctional Azobenzenes as Photoresponsible Guest Molecules into Poly(Muconic Acid) Host Crystals. *Macromol. Chem. Phys.* **2011**, *212* (16), 1767–1777.
- (2) Sakai, H.; Orihara, Y.; Kodashima, H.; Matsumura, A.; Ohkubo, T.; Tsuchiya, K.; Abe, M. Photoinduced Reversible Change of Fluid Viscosity. *J. Am. Chem. Soc.* **2005**, *127* (39), 13454–13455.
- (3) Pouliquen, G.; Tribet, C. Light-Triggered Association of Bovine Serum Albumin and Azobenzene-Modified Poly(Acrylic Acid) in Dilute and Semidilute Solutions. *Macromolecules* **2006**, *39* (1), 373–383.
- (4) Fang, L.; Han, G.; Zhang, J.; Zhang, H.; Zhang, H. Synthesis of Well-Defined Easily Crosslinkable Azobenzene Side-Chain Liquid Crystalline Polymers via Reversible Addition–Fragmentation Chain Transfer Polymerization and Photomechanical Properties of Their Post-Crosslinked Fibers. *Eur. Polym. J.* **2015**, *69*, 592–604.
- (5) Wu, L.; Tuo, X.; Cheng, H.; Chen, Z.; Wang, X. Synthesis, Photoresponsive Behavior, and Self-Assembly of Poly(Acrylic Acid)-Based Azo Polyelectrolytes. *Macromolecules* **2001**, *34* (23), 8005–8013.
- (6) Peng, S.; Guo, Q.; Hartley, P. G.; Hughes, T. C. Azobenzene Moiety Variation Directing Self-Assembly and Photoresponsive Behavior of Azo-Surfactants. *J Mater Chem C* **2014**, *2* (39), 8303–8312.
- (7) Lund, R.; Brun, G.; Chevallier, E.; Narayanan, T.; Tribet, C. Kinetics of Photocontrollable Micelles: Light-Induced Self-Assembly and Disassembly of Azobenzene-Based Surfactants Revealed by TR-SAXS. *Langmuir* **2016**, *32* (11), 2539–2548.
- (8) Khoukh, S.; Tribet, C.; Perrin, P. Screening Physicochemical Parameters to Tuning the Reversible Light-Triggered Control of Emulsion Type. *Colloids Surf. Physicochem. Eng. Asp.* **2006**, *288* (1–3), 121–130.
- (9) Cousin, F. Small Angle Neutron Scattering. *EPJ Web Conf.* **2015**, *104*, 01004.
- (10) Corkill, J. M.; Goodman, J. F.; Walker, T. Partial Molar Volumes of Surface-Active Agents in Aqueous Solution. *Trans. Faraday Soc.* **1967**, *63* (0), 768–772.
- (11) Marcus, Y. The Standard Partial Molar Volumes of Ions in Solution. Part 4. Ionic Volumes in Water at 0–100 °C. *J. Phys. Chem. B* **2009**, *113* (30), 10285–10291.
- (12) Tanford, C. Micelle Shape and Size. *J. Phys. Chem.* **1972**, *76* (21), 3020–3024.
- (13) Van der Maarel, J. R. C.; Groot, L. C. A.; Hollander, J. G.; Jesse, W.; Kuil, M. E.; Leyte, J. C.; Leyte-Zuiderweg, L. H.; Mandel, M.; Cotton, J. P. On the Charge Distribution in Aqueous Poly(Styrenesulfonic Acid) Solutions. A Small-Angle Neutron Scattering Study. *Macromolecules* **1993**, *26* (26), 7295–7299.
- (14) Takeshita, K.; Hirota, N.; Terazima, M. Enthalpy Changes and Reaction Volumes of Photoisomerization Reactions in Solution: Azobenzene and p-Coumaric Acid. *J. Photochem. Photobiol. Chem.* **2000**, *134* (1), 103–109.
- (15) Durchschlag, H.; Zipper, P. Calculation of the Partial Volume of Organic Compounds and Polymers. In *Ultracentrifugation*; 2007; Vol. 94, pp 20–39.

- (16) Schweins, R.; Huber, K. Particle Scattering Factor of Pearl Necklace Chains. *Macromol. Symp.* **2004**, 211 (1), 25–42.
- (17) Kline, S. R. Reduction and Analysis of SANS and USANS Data Using IGOR Pro. *J. Appl. Crystallogr.* **2006**, 39 (6), 895–900.
- (18) Combet, J. Polyelectrolytes and Small Angle Scattering. *EPJ Web of Conferences* **2018**, 188, 03001.



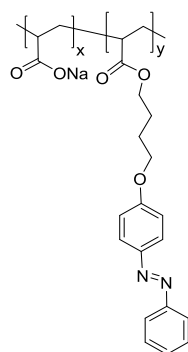
## Chapter V. Azo-functionalized polyelectrolytes

Hydrophobic and amphiphilic polymers are capable to adapt particular conformation, but also to self-assemble into different architectures such as colloidal particles and vesicles. The hydrophobic/hydrophilic balance is a key parameter to explain the formation of these structures. The addition of Azobenzene group in PEs offers the possibility to tune the hydrophobicity and further modify their architectures by simple light irradiations.

The main objective of this chapter is to understand the structural organization of Azo-polymers in aqueous solution and its variation under light irradiation. This chapter begins with the study of the photoisomerization behaviour of Azo-polymers (*trans/cis* composition at the stationary state and reversibility). Then the structure of a series of Azo-polymers at different concentrations are investigated by SAXS. Different organizations are proposed for short and long lengths Azo-polymers systems.

### V.1 Azo-containing polyelectrolytes

We have synthesized four Azo-containing sodium polyacrylates with different chain lengths and Azo molar fractions (Scheme 1). The synthesis and the characterization of Azo-polymers are presented in Chap III.1 (P 45). Just to recall that they are denoted  $(\text{PAA-Azo}_y)_n$ , where  $y$  is the molar fraction of azo units and  $n$  is the number average degree of polymerization.  $(\text{PAA-Azo}_{0.11})_{42\text{Sigma}}$  and  $(\text{PAA-Azo}_{0.15})_{39\text{Sigma}}$  are obtained from a commercial polyacrylic acid.  $(\text{PAA-Azo}_{0.15})_{54\text{RAFT}}$  and  $(\text{PAA-Azo}_{0.11})_{738\text{RAFT}}$  are obtained from a well-defined polyacrylic acid synthesized by RAFT polymerization. Their main characteristics are recalled in Table 1.



Scheme 1 Structure of  $(\text{PAA-Azo}_y)_n$ .

	$M_w$ (g.mol <sup>-1</sup> )	$M_n$ (g.mol <sup>-1</sup> )	$I_p$	$DP_n$ by SEC	$DP_n$ by NMR*	$\tau_{azo}$ (%)
(PAA-Azo <sub>0.11</sub> ) <sub>42Sigma</sub>	5800	4400	1.33	42	/	10.7
(PAA-Azo <sub>0.15</sub> ) <sub>39Sigma</sub>	5700	4500	1.26	39	/	15.1
(PAA-Azo <sub>0.15</sub> ) <sub>54RAFT</sub>	7700	6900	1.13	56	54	15.0
(PAA-Azo <sub>0.11</sub> ) <sub>738RAFT</sub>	76000	60600	1.26	595	738	11.4

Table 1 Main properties of azo containing sodium polyacrylates: weight-average molecular weight ( $M_w$ ), number-average molecular weight ( $M_n$ ), polydispersity index ( $I_p = M_w/M_n$ ) and degree of polymerization ( $DP_n$ ). (\* Values determined by NMR kinetic traces for unmodified PAA chains. We considered that the grafting of azo group does not change the  $DP_n$  of PAA synthesized by RAFT).

## V.2 Photoisomerization behaviours

Photoconversion of azo-containing polymers in aqueous solution was investigated by UV-Vis absorption spectroscopy. Several aspects including *trans/cis* ratio at the equilibrium state, but also, the photoconversion reversibility upon blue light stimulus and the thermal relaxation will be discussed in this chapter.

### V.2.1 *Trans/Cis* ratio

The *trans/cis* ratio is an important parameter that influence the final organization of photoresponsive systems. This molar fraction can be determined by UV-Visible spectroscopy measurements.

Figure 1 shows the variation of UV-Vis spectra of (PAA-Azo<sub>0.11</sub>)<sub>42Sigma</sub> aqueous solution (Azo unit concentration 0.05 mM) under UV irradiation. *Trans* isomer exhibits a strong absorption band at 338 nm corresponding to a  $\pi - \pi^*$  transition and a weak band at approximately 440 - 450 nm which is attributed to an  $n - \pi^*$  transition. Under UV irradiation, the maximum absorption at around 340 nm decreases while its position is shifted to 319 nm due to the *trans*  $\leftrightarrow$  *cis* photoisomerization of the Azo groups. Additionally, the absorbance peak centered at 437 nm increases when UV light is applied. Isosbestic points are observed at 300 and 405 nm, which is the signature of the presence of both *trans* and *cis* azo groups (two state model): all the UV-Vis spectra can be decomposed as a linear combination of pure *trans* spectrum and pure *cis* spectrum.

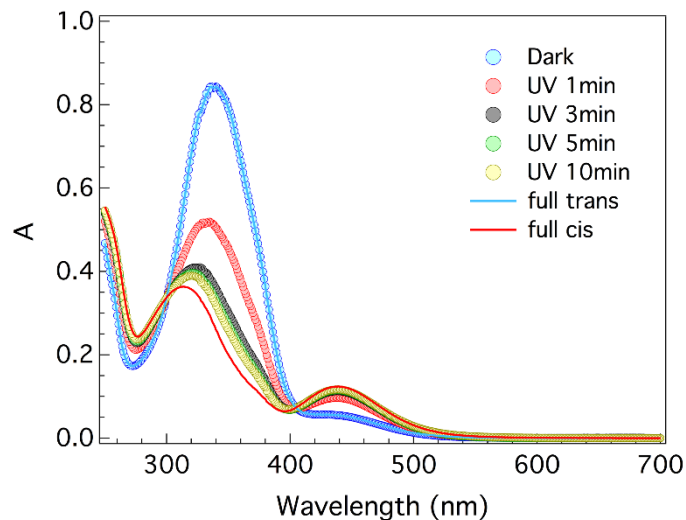


Figure 1 a) Variation of UV-Vis spectra of (PAA-Azo<sub>0.11</sub>)<sub>42Sigma</sub> for different UV irradiation time, with azo unit concentration of 0.05 mM.

In structural studies by small-angle scattering techniques, the concentrations of the solutions are much higher and cannot be directly measured by UV-visible spectroscopy. To quantify  $x_{trans}$  at the equilibrium state ( $x_{trans}^{eq}$ ) in these 'concentrated' samples, a rapid dilution is necessary prior to UV-visible absorption measurements. A series of solutions from 0.03 M to 1 M (monomer concentration) were prepared and measured. The dilution procedure and the fast manipulation probably alter the structural organization of the 'objects' in solution, but we assume that it does not change the *trans/cis* fraction of the isomers.

An example for the 1 M solution is given in Figure 2a. Concretely, 10  $\mu$ L of 1 M solution was taken out regularly, diluted 2000 times (to reach an azo unit concentration of 0.05 mM), introduced in the spectrometer and immediately measured. Each curve therefore reflects the *trans/cis* content in a 1 M solution but at different irradiation time  $t$ . Three hours of UV irradiation are required to reach the equilibrium state (yellow curve in Figure 2a). A dilute sample irradiated directly by UV light, has been measured and compared (Figure 2b). The stationary state is reached after only several minutes of UV irradiation. The kinetics of photoconversion of the 1M solution during UV irradiation is therefore much slower than that of a dilute solution.

It is possible to extract the *trans* fraction  $x_{trans}$  at any irradiation (or relaxation) time if the absorption spectra associated to the pure *trans* and pure *cis* forms are known. Since all the solutions are kept in dark for 2 days before measurements, the initial UV-Vis absorption spectra can be considered as

composed of 100% *trans* isomers. Unfortunately, a 100% *cis* isomers state can never be reached experimentally. In a dilute solution for instance, the residual amount of the *trans* isomers at equilibrium is about 8%. This value is determined from NMR analysis of Azo-surfactants and is in agreement with the value described in the thesis of Eloise Chevallier<sup>1</sup>. The pure *cis* absorption spectra can therefore be deduced from a linear combination of the spectrum at equilibrium and in dark state using:

$$A_{eq}(\lambda) = x_{trans}^{eq} A_{trans}(\lambda) + (1 - x_{trans}^{eq}) A_{cis}(\lambda) \quad (1)$$

$$\Rightarrow A_{cis}(\lambda) = \frac{A_{eq}(\lambda) - x_{trans}^{eq} A_{trans}(\lambda)}{(1 - x_{trans}^{eq})} \quad (2)$$

$$\text{with } A_{trans}(\lambda) = A_{dark}(\lambda) \text{ and } x_{trans}^{eq} = 8\%$$

The *trans/cis* ratio for the 1 M solution (at any irradiation time), or more generally for any solutions can be deduced from the absorption spectrum using:

$$A(\lambda) = x_{trans} A_{trans}(\lambda) + (1 - x_{trans}) A_{cis}(\lambda) \quad (3)$$

$A_{trans}$  and  $A_{cis}$  must be measured at the same concentration. This relationship is valid for any wavelength  $\lambda$ . The determination of  $x_{trans}$  can be therefore estimated at a single wavelength measurement  $\lambda$ .

$$x_{trans} = \frac{A(\lambda) - A_{cis}(\lambda)}{A_{trans}(\lambda) - A_{cis}(\lambda)} \quad (4)$$

Here, we preferred to fit the whole absorption spectra. There are two advantages. First, we are less sensitive to the error measurements on  $A(\lambda)$  and  $A_{trans}(\lambda)$ . The main source of uncertainty in the calculation now only comes from the estimation of  $x_{trans}^{eq}$  needed in the expression of  $A_{cis}(\lambda)$ . Second, for high concentration solutions, we need to dilute the samples. This inevitably introduces small errors in the final concentration, and therefore in the  $x_{trans}$  determination if we use other reference solutions (for full *cis* and full *trans* spectra). To overcome these problems, every measurement was renormalized with regard to the full *trans* reference to reproduce the two isosbestic points. This can only be done if we work on the whole absorption spectra and not at a single selected wavelength.

This procedure was applied on the absorption spectra in Figure 2a and Figure 2b to extract the variation of the *trans* fraction with the UV irradiation time (Figure 2c). The *trans/cis* ratio for 1 M solution is 32% at the equilibrium state while it is close to 10% for very dilute systems. We see here a direct consequence of the local organization on the photoconversion process.

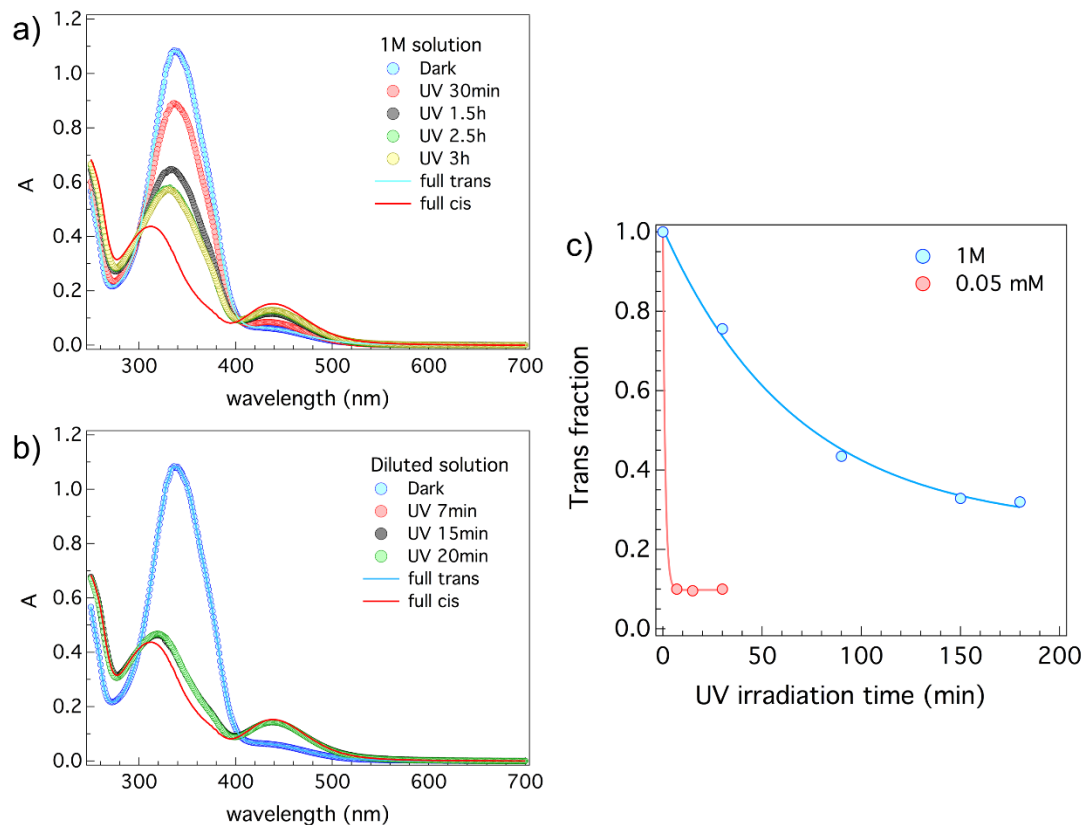


Figure 2 UV-Vis spectra of 1 M (PAA-Azo<sub>0.11</sub>)<sub>42Sigma</sub> solution as a function of the UV irradiation time  $t$ : a) 1 M solution under UV, diluted just before the measurement; b) dilute solution directly under UV; c) variation of the *trans* fraction  $x_{trans}$  vs irradiation time for a 1 M and 0.05 mM solution.

The variations of  $x_{trans}$  for solutions of concentration from 0.03 M to 1 M are presented in Figure 3. The full lines help to visualize the tendency of the variations. Despite our efforts, there are still non-negligible fluctuations caused maybe by parasite light during the withdrawn and the dilution procedure. The *trans/cis* ratio is concentration-dependent. The kinetic rate of photoisomerization decreases when the concentration increases. We notice that the final  $x_{trans}^{eq}$  values are almost identical for concentrations lower than 0.125 M. The higher the concentration, the more *trans* isomers are detected at the photostationary state<sup>2,3</sup>. The high concentration in Azo inevitably leads to a very high absorption. The equilibrium state is reached via a diffusion process. It is rather normal to find a faster kinetic for low concentration system, the structure of the solution certainly plays a role (Azo-particle, Azo-polymer) in the diffusion process. The fact that the final *trans* state also depends on the concentration is a pure consequence of the local structure in which the azo groups are inserted.

The knowledge of the *trans/cis* ratio for different concentrations is very helpful to understand the structural behaviour observed by SAXS. The experimental irradiation setup of the present UV-Vis absorption experiments was therefore designed to be as close as possible to that of SAXS measurements. Sample containers have the same thickness (1 mm) and UV LEDs are used for the irradiation. Samples were illuminated by 8 LEDs on two sides and were homogenized before the withdraw. On the SAXS instrument, UV irradiation is realized in situ by two LEDs at 2 mm from the capillary. If it is impossible to establish exactly the irradiation setup, the photoconversion investigated by UV-Vis spectroscopy provides however a good approximation of the *trans/cis* ratio in SAXS measurements.

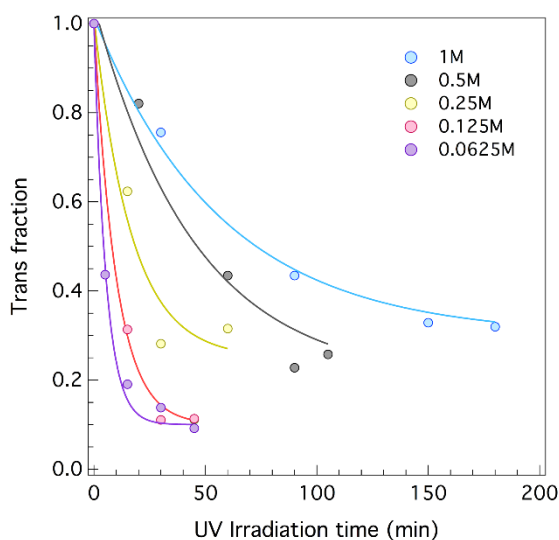


Figure 3 Variation of  $x_{trans}$  vs irradiation time for (PAA-AzO<sub>0.11</sub>)<sub>42Sigma</sub> solutions.

## V.2.2 Reversibility

In order to probe the reversibility of the photoconversion on Azo-polymers, we have measured the trans fraction  $x_{trans}^{eq}$  during several irradiation cycles on dilute solutions. The photoconversion from *trans* to *cis* is realized by UV light irradiation 365 nm while the reverse process, *cis* to *trans*, is triggered by Blue light illumination at 450 nm. Several UV-Blue irradiation cycles were applied on Azo-polymer solutions directly in the UV-Vis cuvette (1 cm path length). The *trans* fraction at the photostationary state was determined by UV-Vis spectroscopy as described in the previous paragraph. The behaviour is very similar for both long and short length Azo-polymers with the same azo unit fraction ( $\tau_{azo} = 0.11$ ). We found a good reversibility upon light stimulus (Figure 4).

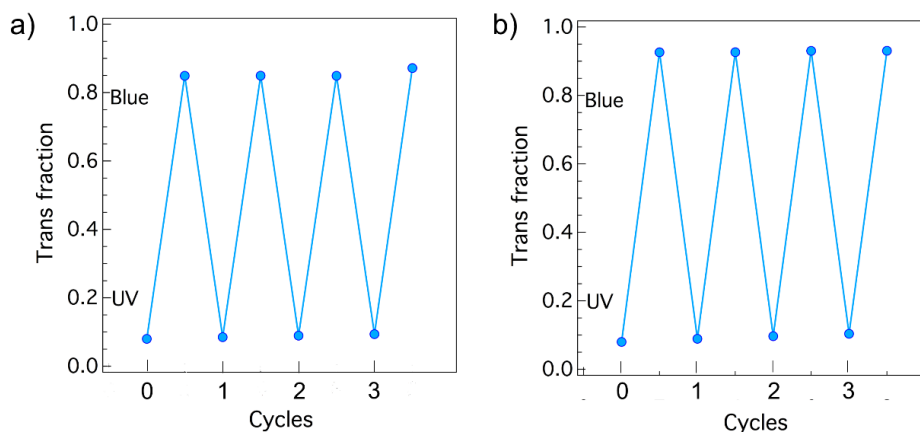


Figure 4 Reversibility *trans* ↔ *cis* measured by UV-Vis during UV-Blue irradiation cycles. The trans fraction at the stationary state is measured on: a) (PAA-Azo<sub>0.11</sub>)<sub>42Sigma</sub> (Azo unit concentration 0.056 mM); b) (PAA-Azo<sub>0.11</sub>)<sub>738RAFT</sub> (Azo unit concentration 0.05 mM).

### V.2.3 Comparison of Azo-polymers UV-Vis spectra

The UV-Vis spectra in dark state for the four synthesized Azo-polymers are given in Figure 5. The position of the absorption peak is very sensitive to the local environment of Azo groups. A blue shift is expected when the azobenzene is aggregated.<sup>4</sup> Indeed, for the same Azo fraction ( $\tau_{azo} = 0.11$ ), the long polymer (PAA-Azo<sub>0.11</sub>)<sub>738RAFT</sub> exhibits a blue shift compared to the short one (PAA-Azo<sub>0.11</sub>)<sub>42Sigma</sub> (Figure 5a). This clearly indicates that the local structural organization of Azo groups is different, and that chromophores are certainly not in contact with water for long chains (Azo are probably inserted in aggregates even at low concentration). The absorption peak of the two others short Azo-polymers with 15% Azo units are almost at the same position: the local structure is very similar at very low concentration.

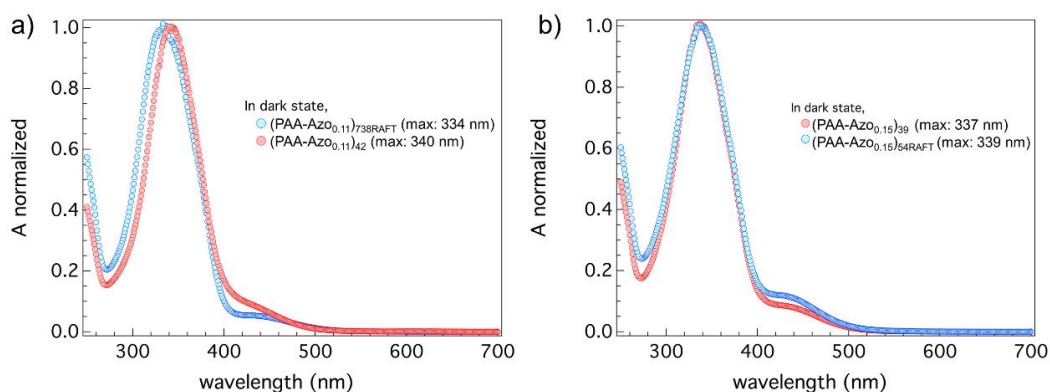


Figure 5 Normalized absorption spectra of a) long and short Azo-polymers with  $\tau_{azo} = 0.11$ ; a) two short length Azo-polymers with  $\tau_{azo} = 0.15$ . (all the spectra were measured at an Azo unit concentration around 0.05 mM ).

## V.3 Structural organization study

We have studied the four different Azo-polymers by SAXS at different concentrations, in the dark state and under UV irradiation.

The goal is to determine the structural organization of these systems and the modifications triggered by irradiation. The unmodified poly(sodium acrylate) NaPAA was also studied for comparison.

### V.3.1 Reference systems: poly(sodium acrylate) (NaPAA)

A commercial PAAH and two well-defined synthesized PAAH were ionized and purified by dialysis to obtain the salt form NaPAA. These three unmodified NaPAA are considered as reference systems for the structural study of azo-containing polyions. Figure 6 presents SAXS curves for different monomer concentrations (0.015 M to 1 M). They all exhibit a broad peak at a position  $q^*$  which is characteristic of PE solutions and electrostatic repulsions.

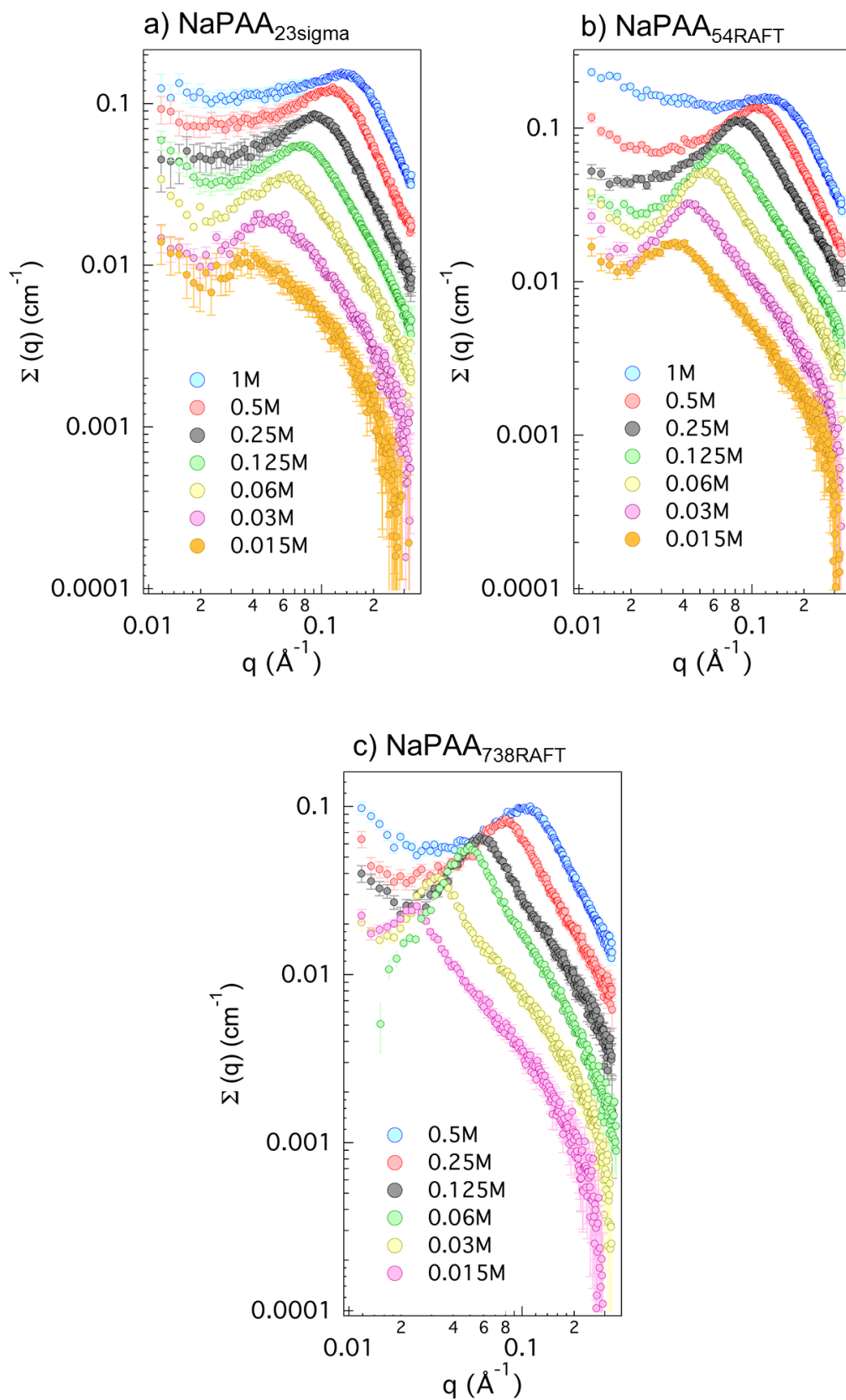


Figure 6 SAXS curves for reference PEs: NaPAA<sub>23sigma</sub>, NaPAA<sub>54Raft</sub>, and NaPAA<sub>738Raft</sub>.

Log-log plots of  $q^*$  as a function of the concentration  $c$  (monomer concentration) are presented in Figure 7 for the three PEs.  $q^*$  varies as  $c^\alpha$  with different power laws exponents  $\alpha$  (NaPAA<sub>738RAFT</sub>  $\alpha = 0.43$ ; NaPAA<sub>54RAFT</sub>  $\alpha = 0.30$ ; NaPAA<sub>23sigma</sub>  $\alpha = 0.29$ ). For NaPAA<sub>23sigma</sub> and NaPAA<sub>54RAFT</sub>,  $q^*$  varies as  $\approx c^{1/3}$ , we are in dilute regime in the whole concentration range (small chains). For NaPAA<sub>738RAFT</sub>,  $q^*$  varies roughly as  $c^{1/2}$ , we are in semidilute regime. These behaviours are expected for short and long chains of PE. NaPAA chains are therefore solubilized at the molecular level.

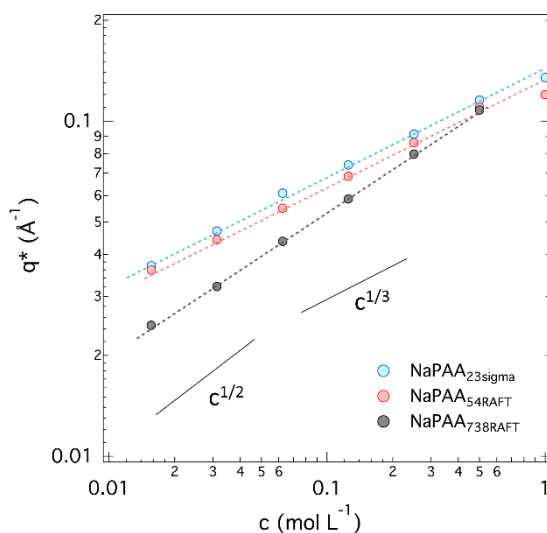


Figure 7  $q^*$  vs concentration for reference PEs: NaPAA<sub>23sigma</sub>, NaPAA<sub>54RAFT</sub> and NaPAA<sub>738RAFT</sub>.

### V.3.2 Azo polymers: general observations

The four Azo-polymers have been measured at different concentrations in dark and under blue or UV light.

Typical scattering curves at 0.25 mol L<sup>-1</sup> are presented in Figure 8 for each PE in dark and under UV (log-log and linear scales). The scattering of pure NaPAA is also presented for comparison.

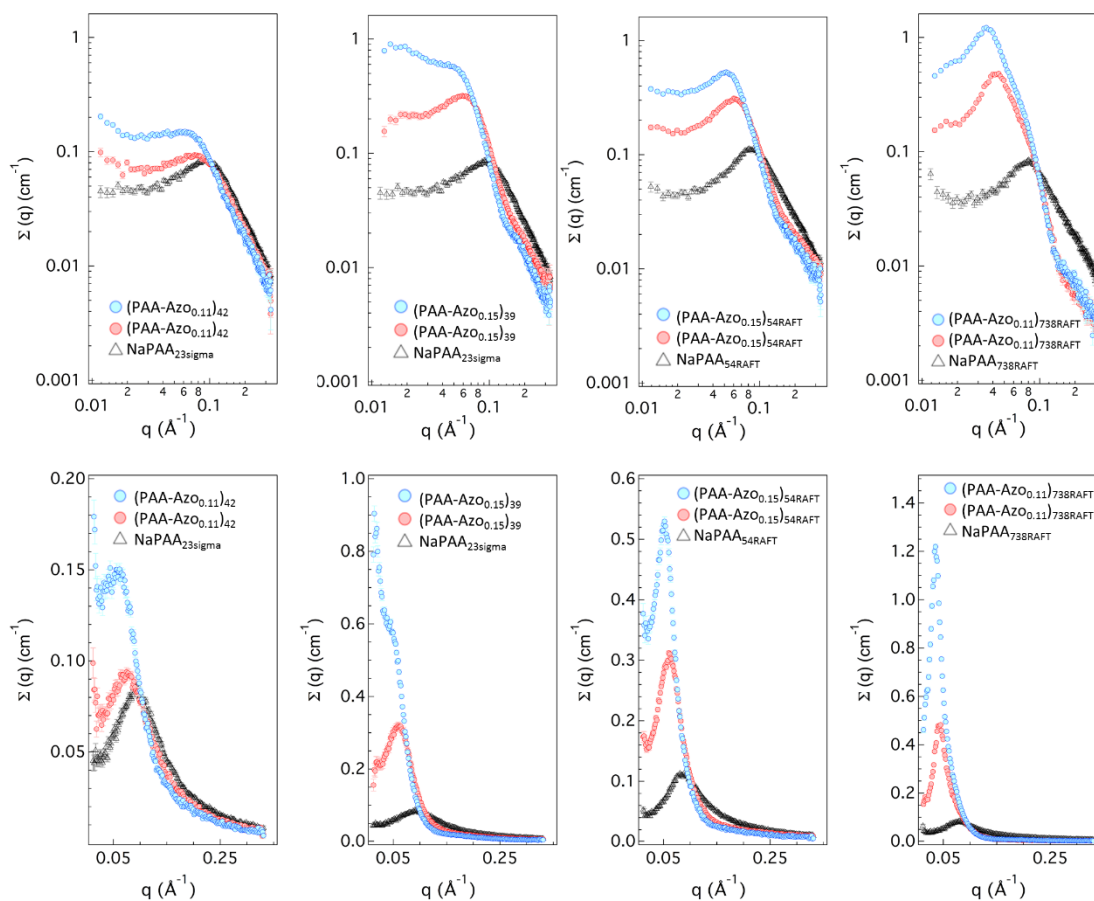


Figure 8 Scattering patterns measured on (PAA-Azo<sub>0.11</sub>)<sub>42</sub>Sigma, (PAA-Azo<sub>0.15</sub>)<sub>39</sub>Sigma, (PAA-Azo<sub>0.15</sub>)<sub>54</sub>RAFT, (PAA-Azo<sub>0.11</sub>)<sub>738</sub>RAFT at  $c = 0.25 \text{ mol L}^{-1}$  in log-log scale (up) and linear scale (down). Blue curve : dark; red curve : under UV radiation; black curve unmodified NaPAA.

The different systems show similar behaviours.

First of all, a scattering peak is still present for modified NaPAA-Azo (in dark and under UV) but its position is shifted to lower  $q$  values compared to pure NaPAA.

Second, the application of the UV radiation provokes a displacement of the peak which moves closer to that of pure NaPAA.

Third, and this is certainly the most visible effect, the UV stimulus causes a very important decrease in intensity (by a factor  $\approx 2$ , more visible on the linear scale). These observations demonstrate that our systems are highly sensitive to UV and that the photoisomerization at the molecular level scale can induce large structural modification at the mesoscopic scale.

A last point to mention concerns the shape of the scattered intensity. Modifications are observed between long and short chains, but also according to the Azo-fraction content and the concentrations. These modifications will be discussed later.

The nature of the regime of the solution (dilute, semi-dilute) is important for understanding the scattering curves and the significance of the scattering peak. According to the degree of polymerization, our unmodified NaPAA is in dilute (short chains) or in semi-dilute (long chains) regime in the whole concentration range. It is highly probable that short NaPAA-Azo will remain in dilute regime whatever their conformation and/or their association in solution. The situation is more complex for modified NaPAA-Azo with a high degree of polymerization. Everything will depend on the conformation of the chains (collapsed or extended) and their interaction with others.

In dilute regime, charged colloids usually show a correlation peak at a position  $q^*$  related to the average distance  $d$  between the center of mass of nearest neighbours. By considering a well-defined organization in solution (cubic, face-centered-cubic...), this distance only depends on the colloid concentration. For self-assembled particles, the colloid concentration now depends on the aggregation number  $N_{agg}$ . It is therefore possible to derive a relationship between the position of the correlation peak  $q^*$  and the aggregation number  $N_{agg}$ . For a face-centered-cubic structure<sup>5</sup>:

$$q^* = \frac{2\pi}{d}, d = \frac{1}{\sqrt{2}} \left( \frac{4000 \times N_{agg}}{N_{avo} \times c} \right)^{\frac{1}{3}} \times 10^8 \text{Å} \quad (4)$$

where  $N_{avo}$  is the Avogadro number, and  $c$  is the molar concentration of elementary units forming the particles ( $\text{mol L}^{-1}$ ). This is only an approximation since the maximum is not really a Bragg peak (there is no long range order in the solution). Different relationships have been proposed to relate precisely  $q^*$  to the average distance  $d$  between charged particles. However, from a phenomenological point of view, we will only consider here that  $d \approx 2\pi / q^*$  and

$$d \propto \left( \frac{N_{agg}}{c} \right)^{\frac{1}{3}}, q^* \propto \left( \frac{c}{N_{agg}} \right)^{\frac{1}{3}} \quad (5)$$

The interesting point is that the position of the peak varies as  $c^{1/3}$  if the aggregation number is constant (simple dilution law). If it not the case, this implies a variation of  $N_{agg}$  with  $c$  and therefore, a modification of the volume of the particle. This classical behaviour certainly applies to our charged systems provided that they are in dilute regime. It will help us to explain the variation of  $q^*$  with the concentration but also, during the irradiation process.

### V.3.3 Structural reversibility upon irradiation and thermal relaxation

The reversibility of the structural properties upon UV and blue irradiation was tested with SAXS. We followed the position of the maximum  $q^*$  in the photostationary states during several UV-blue irradiation cycles. The accuracy of the measurements is good enough to evidence very small variations. Typical scattering curves (dark, blue, UV) and  $q^*$  variations on short and long chains ((PAA-Azo<sub>0.15</sub>)<sub>54</sub>RAFT, (PAA-Azo<sub>0.11</sub>)<sub>738</sub>RAFT) at  $c = 0.25 \text{ mol L}^{-1}$  are presented in Figure 9 and Figure 10.

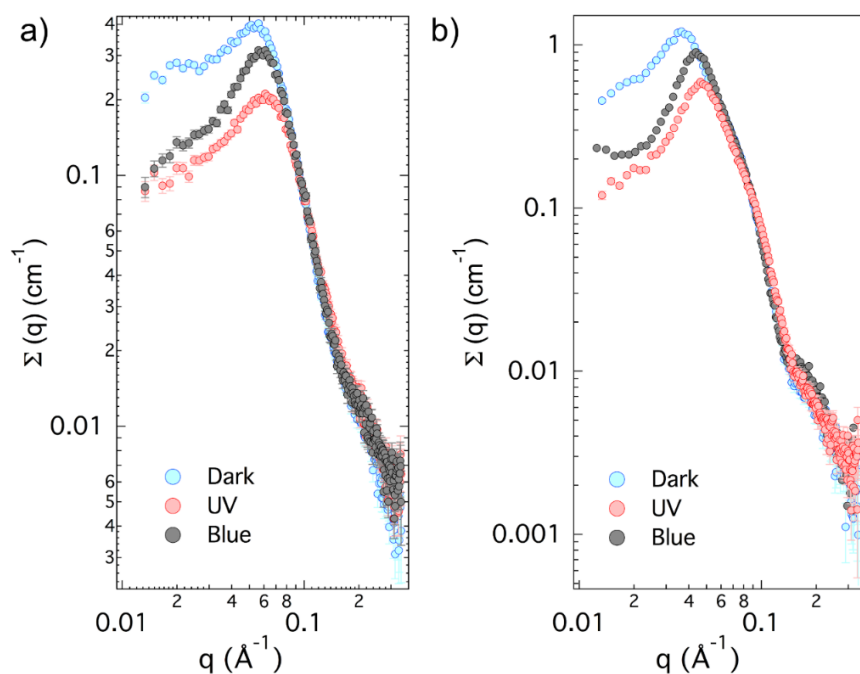


Figure 9 SAXS plots in Dark, under UV and Blue light a) 0.25 M (PAA-Azo<sub>0.15</sub>)<sub>54</sub>RAFT; b) 0.25 M (PAA-Azo<sub>0.11</sub>)<sub>738</sub>RAFT.

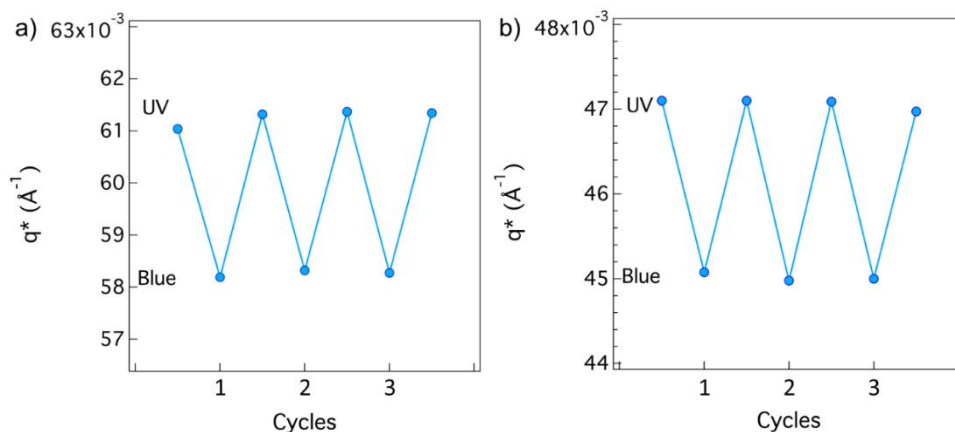


Figure 10 Peak position  $q^*$  in the photostationary state during UV and blue irradiation cycles a) 0.25 M (PAA-Azo<sub>0.15</sub>)<sub>54</sub>RAFT; b) 0.25 M (PAA-Azo<sub>0.11</sub>)<sub>738</sub>RAFT.

When samples are irradiated alternatively by UV and Blue light, the structural organization is changing leading to cyclic a variation of  $q^*$ . The reversibility of the *trans*  $\leftrightarrow$  *cis* photoconversion observed with UV-visible spectroscopy at the molecular level is also found in the macromolecular organization whatever the chain length.

Since the structural organization of the solution is intimately related to the photoconversion of the chromophores, the structure of irradiated samples should relax when UV light is stopped. The kinetics of relaxation has been monitored by SAXS by following the position of the maximum as a function of time.

The whole capillary was pre-illuminated by UV LEDs until a photostationary state is reached. Then we stopped the irradiation and measured the scattering patterns for different relaxation times. Figure 11 shows the variation of  $q^*$  with time for (PAA-Azo<sub>0.15</sub>)<sub>54</sub>RAFT and (PAA-Azo<sub>0.11</sub>)<sub>738</sub>RAFT. The fits of the decay with an exponential law ( $y_0 + Aexp^{-t/\tau}$ ), gives characteristic times of 2.1 h and 14.2 h for short and long chains respectively. It turns out that the structural organization with shorter chains (PAA-Azo<sub>0.15</sub>)<sub>54</sub>RAFT, relaxes faster than the long one (PAA-Azo<sub>0.11</sub>)<sub>738</sub>RAFT for this particular concentration.

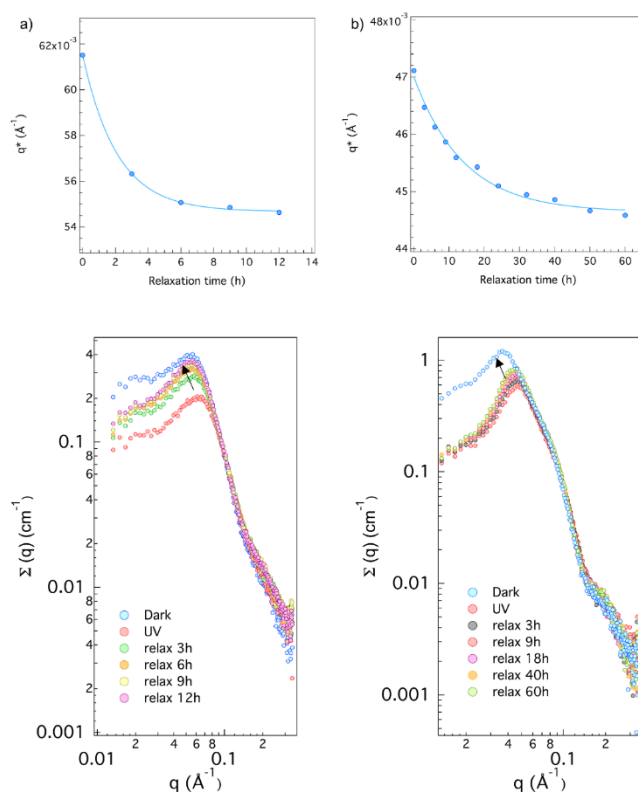


Figure 11 Thermal relaxation measured by SAXS. Position of the peak  $q^*$  as a function of time. a) 0.25 M (PAA-Azo<sub>0.15</sub>)<sub>54</sub>RAFT; b) 0.25 M (PAA-Azo<sub>0.11</sub>)<sub>738</sub>RAFT

### V.3.4 Structural organization in long chain PAA-Azo solutions ( $\tau_{\text{azo}} = 0.11$ )

The scattered intensity measured for (PAA-AZO<sub>0.11</sub>)<sub>738RAFT</sub> at different concentrations in dark and under UV radiation is presented in Figure 12 (a and b). A broad peak is present. Its position varies as a power law ( $q^* \propto c^\alpha$ ) but the exponent  $\alpha$  now equals 0.3 ( $\alpha \approx 1/3$ ) in the dark state and 0.26 under UV. This behaviour is very different from that of the parent unmodified NaPAA for which  $\alpha \approx 1/2$ . We are no longer in the classical semi-dilute regime generally found for hydrophilic PEs above  $c^*$ . The scattering profiles are also modified compared to the parent NaPAA. They are now characteristic of charged particles in solution. PEs therefore tend to collapse in water due to the presence of Azo groups along the backbone and form dense aggregates.

As already mentioned,  $q^*$  under radiation is systematically larger than  $q^*$  in dark. The difference is related to the variation of the number of chains embedded in the aggregate (aggregation number  $N_{\text{agg}}$ ).

A close inspection of the scattering intensity around  $0.2 \text{ \AA}^{-1}$  (especially for the highest concentrations) shows an unexpected  $q^{-2}$  decay that is not really compatible with homogeneous spherical particles.

Finally, no deep minimum is observed in the large  $q$  range (for which  $P(q)$  dominates). The particles are certainly polydisperse or not purely spherical.

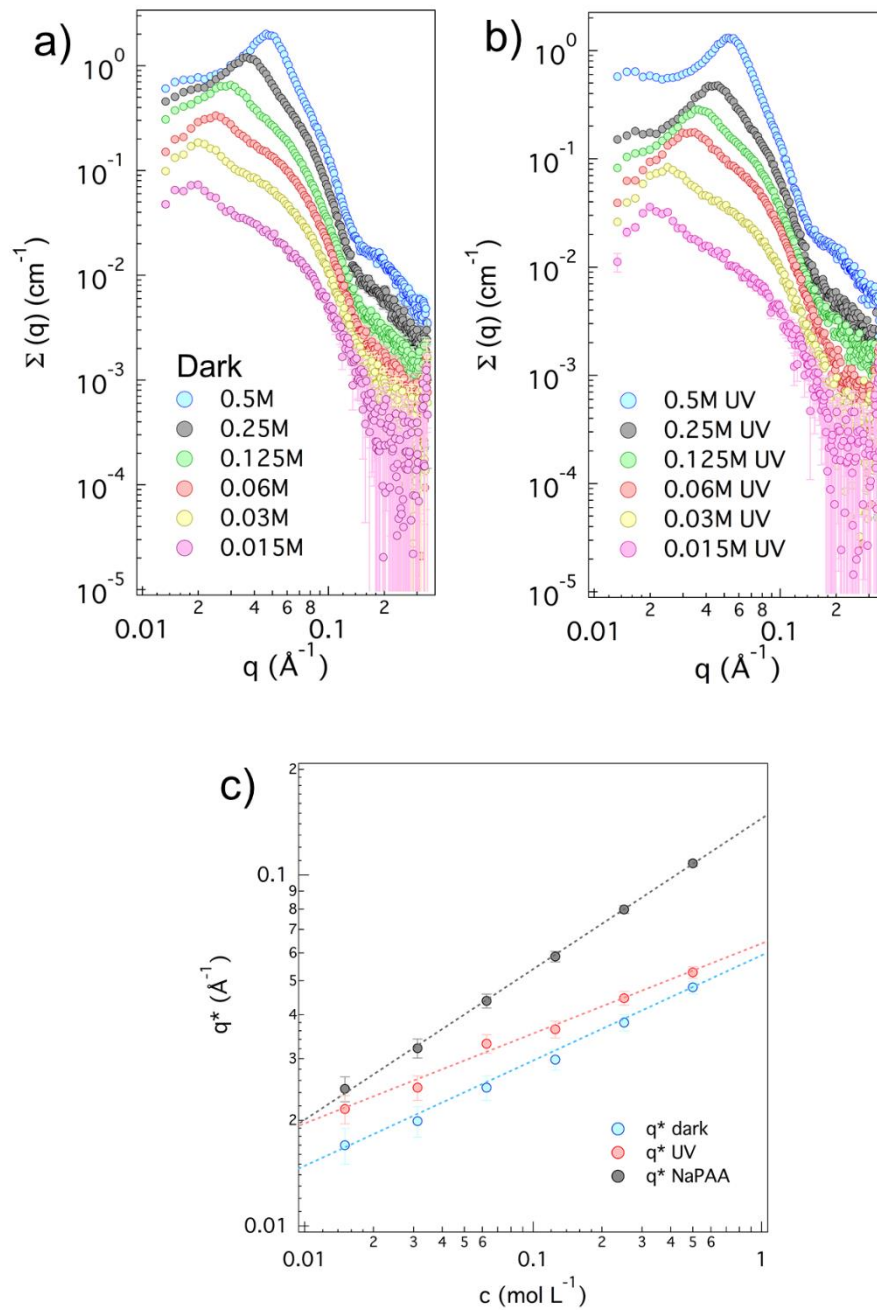


Figure 12 SAXS data of (PAA-AZO<sub>0.11</sub>)<sub>738</sub>RAFT. a) measurements in Dark b) measurements under UV c)  $q^*$  vs concentration.

Cryo-TEM measurements in dark have been performed to provide another view of these polymers in solution. This technique has a limited resolution ( $\approx 2$  nm) and cannot reveal small structural details in our systems (we are close to the detection limit). However, as long as the contrast is acceptable, it provides essential information (size, shape, location of the objects) that perfectly complements SAXS analysis.

Cryo-TEM experiments have been carried out at 0.03 mol L<sup>-1</sup>. An image is presented in Figure 13. We find distinct spherical objects evenly distributed in the sample. Small and big particles (average diameter 5 - 6 nm) coexist with a few rare elongated objects (long arrows). These results definitively validate our colloidal picture. According to these observations, we have considered a model based on well separated spherical polydisperse charged particles for the analysis of SAXS measurements.

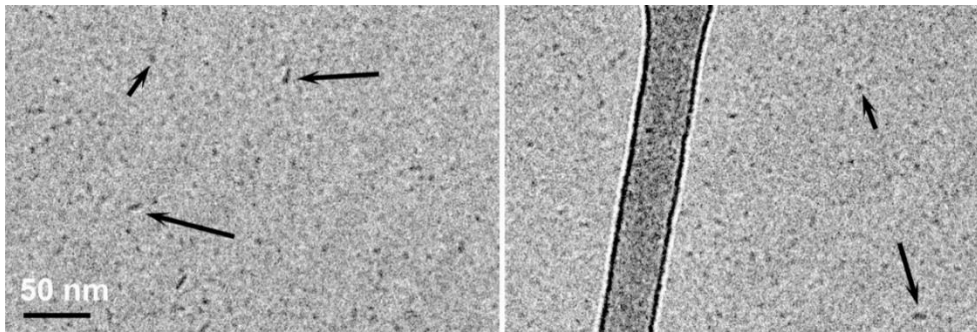


Figure 13 CryoTEM images of (PAA-Azo<sub>0.11</sub>)<sub>738</sub>RAFT at 0.03 mol L<sup>-1</sup>. Small arrows: typical small spherical objects. Long arrows: elongated objects. The particles are homogeneously distributed in the film.

As previously mentioned, an unexpected  $q^{-2}$  decay of the intensity is observed around 0.2 Å<sup>-1</sup>. This is close to the scattering signature of pure NaPAA in solution (this behaviour can be seen in Figure 6). That clearly indicates the presence of PAA segments in solution in our modified PAA-Azo system. In other words, we do not have a dense particle incorporating all PAA monomers. This scattering behaviour is often found with polymer-decorated particles or star branched polymers, in which chains are attached to the core and form a polymer network around it. This phenomenon is conceivable in our systems since our PEs are highly amphiphilic. Part of the chains may be embedded in a dense core while the other remains in solution (end of chains, loops...). A semi-dilute PE solution is then forming a shell around the core.

From a scattering point of view, this system can be treated as a homogeneous core-shell particle as long as the concentration fluctuations of the polymer network (forming the shell) are negligible (which is usually not the case at high  $q$ ). As a first approximation, this “non-homogeneous shell” can be accounted for by adding another contribution to the classical core-shell scattered intensity of the form<sup>6</sup>:

$$I_{fluc}(q) = \frac{I_{fluc}(0)}{1 + q^2 \xi^2} \quad (6)$$

where  $\xi$  is the correlation length of the PEs solution in the shell.  $I_{fluc}(0)$  and

$\xi$  are usually treated as adjustable parameters during the fitting procedure. In the present case, we prefer not to fit these values and rather subtract a common «background»  $I_{fluc}(q)$  to the data.  $I_{fluc,ref}(0)$  and  $\xi_{ref}$  have been estimated from the scattering curve at  $c_{ref} = 0.5 \text{ mol L}^{-1}$  in dark. For the correction of other data at concentration  $c$ ,  $\xi$  is considered constant ( $=\xi_{ref}$ ) while  $I_{fluc}(0,c) = (c/c_{ref})I_{fluc,ref}(0,c_{ref})$ . Examples showing the scattered intensities and  $I_{fluc}(q)$  are given in Figure 14. All the data have been corrected for the polymer network concentration fluctuations contribution before being analysed.

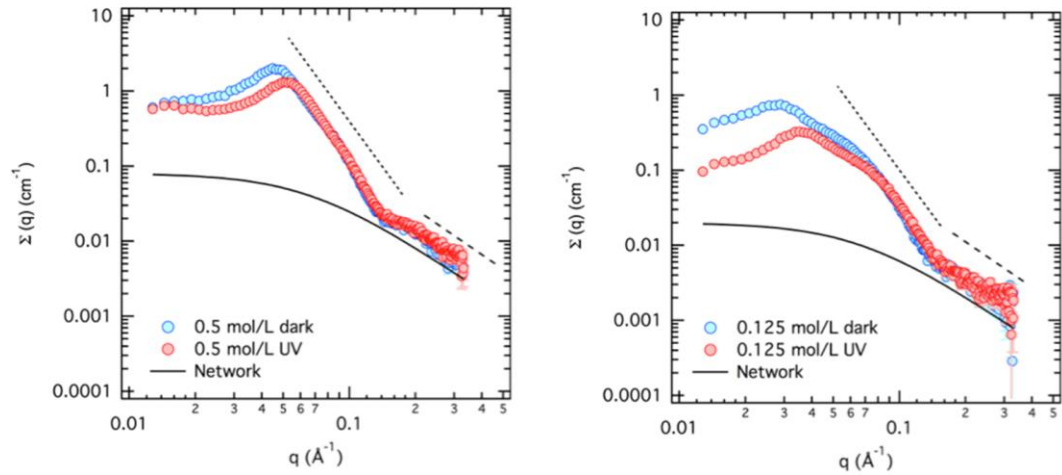


Figure 14 SAXS data measured at  $0.5 \text{ mol L}^{-1}$  (left) and  $0.125 \text{ mol L}^{-1}$  (right). The line corresponds to the contribution of the concentration fluctuations of the polymer network around the particles. ( $\xi_{ref} = 15 \text{ \AA}$ ,  $I_{fluc,ref}(0,c_{ref}) = 0.08 \text{ cm}^{-1}$ . Long dash line:  $q^2$  decay, short dash line:  $q^4$  decay.

The data have been fitted with a classical homogeneous core-shell model combined to a structure factor  $S(q)$  developed for charged colloids in a repulsive screened Coulomb potential<sup>7,8</sup>. We do not any longer consider concentration fluctuations in the shell. We estimate that the data have been corrected for these effects. We can anticipate that the average SLD of the shell will be close to that of the solvent since the layer is approximated to a semi-dilute PE solution. The fit parameters are the volume fraction, the average radius of the core, the average thickness of the shell, the radius polydispersity (standard deviation/average value) as well as the SLDs of the core and the shell. In order to correctly reproduce the structure factor  $S(q)$ , the effective charge of the particles and the salt concentration are also considered as adjustable parameters. The fits are presented in Figure 15 and Figure 16 for dark and UV experiments.

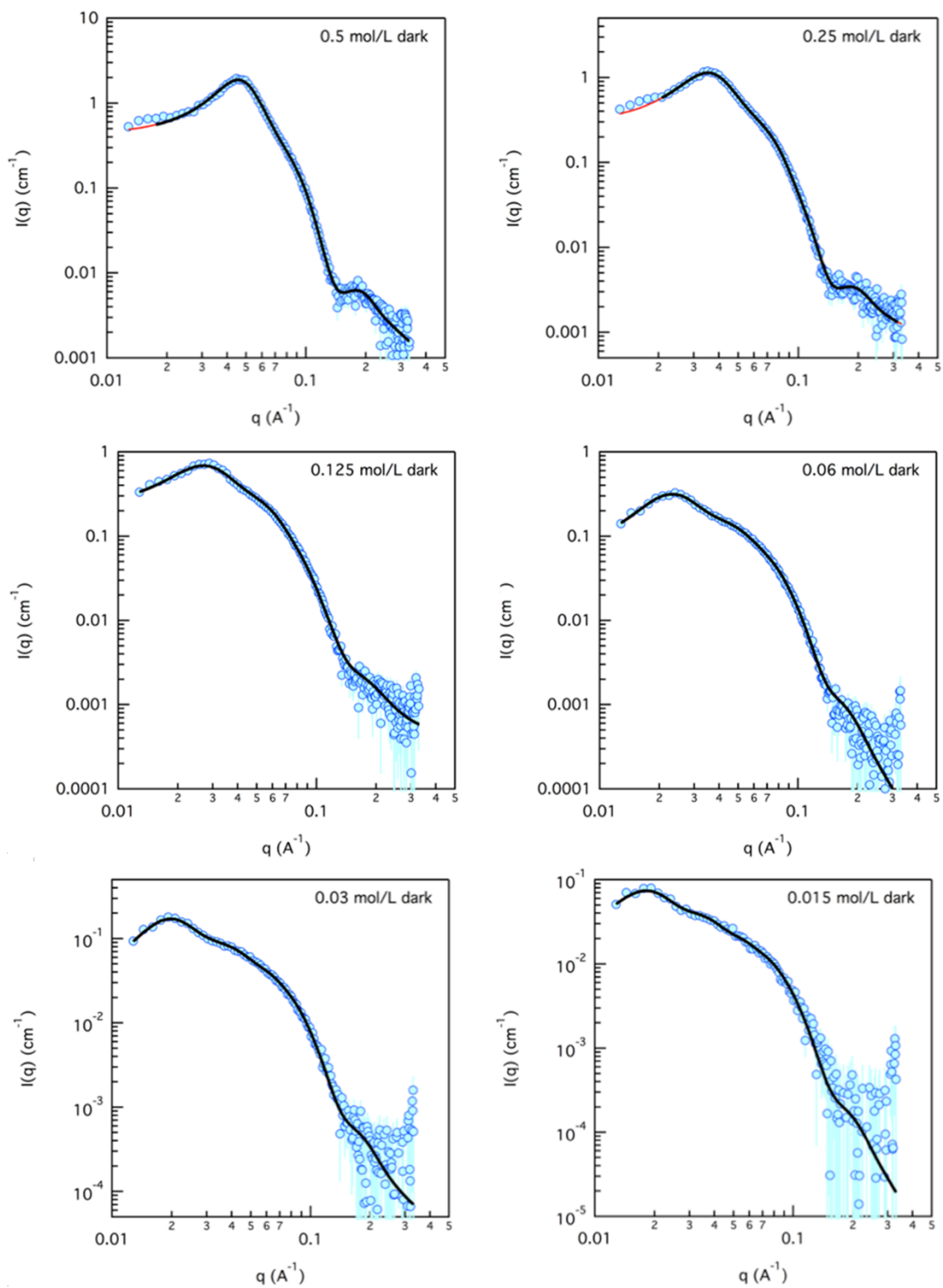


Figure 15 SAXS data and fits (lines) for measurements in dark.

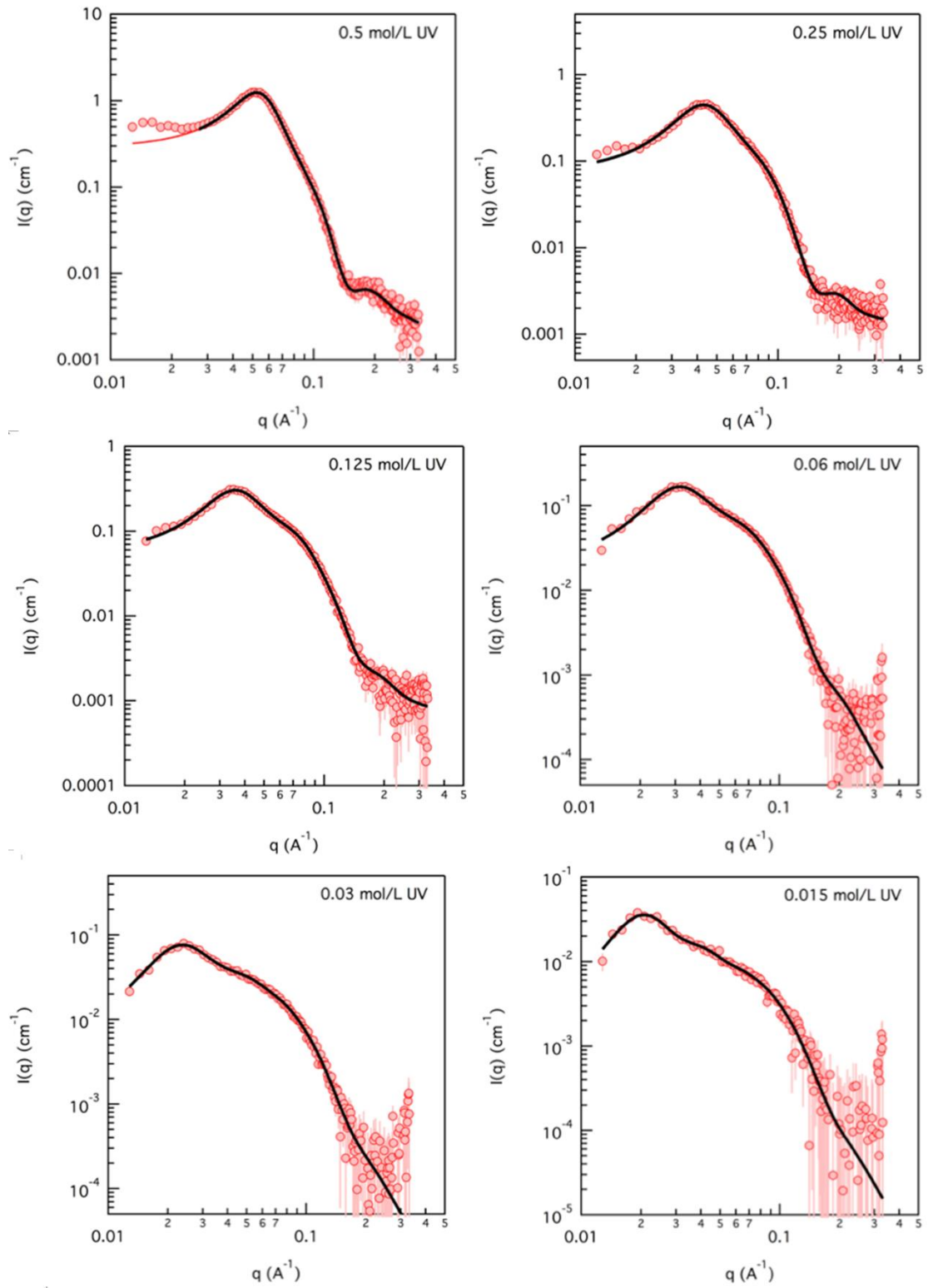


Figure 16 SAXS data and fits (lines) for measurements under UV irradiation.

The theoretical curves fit well the experimental data. The geometrical parameters and the SLD are summarized in Table 2.

Concentration (mol L <sup>-1</sup> )	0.5	0.25	0.125	0.06	0.03	0.015
Dark						
Average core radius (Å)	29.3	28.2	28.00	29.8	28.7	26.3
Average shell thickness (Å)	22.7	23.5	23.6	54.4	61.5	62.5
Polydispersity	0.16	0.17	0.23	0.20	0.20	0.20
SLD core (10 <sup>10</sup> cm <sup>-2</sup> )	11.40	11.7	12.1	11.5	11.3	11.2
SLD shell (10 <sup>10</sup> cm <sup>-2</sup> )	9.61	9.63	9.57	9.42	9.42	9.42
UV						
Average core radius (Å)	28.1	27.5	26.9	25.1	22.7	20.9
Average shell thickness (Å)	21.0	19.8	28.7	47.3	54.8	56.1
Polydispersity	0.16	0.15	0.19	0.23	0.26	0.26
SLD core (10 <sup>10</sup> cm <sup>-2</sup> )	11.02	10.82	11.00	10.88	11.05	10.88
SLD shell (10 <sup>10</sup> cm <sup>-2</sup> )	9.55	9.46	9.42	9.41	9.41	9.41

Table 2 Fits parameters for measurements in dark and under UV irradiation.

We can now give a schematic description of the structure of the particles. In the dark state, we have a dense core of typical radius around 29 Å and a shell of ionized charged PAA segments. The size of the core does not change with the concentration (except maybe for the lowest one 0.015 mol L<sup>-1</sup> where the statistics is very poor). This is consistent with Cryo-TEM measurements which have shown particles with a diameter of the order of 6 nm (the shell is not visible here due to a very low contrast). This is an important result in agreement with the variation of  $q^*$  as a function of the concentration (Figure 12 c). Indeed, a power law exponent of 1/3 has been determined that is characteristic of a simple dilution law *i.e.*, without variation of the aggregation number (the volume of the particle is therefore constant).

Under UV,  $q^*$  is higher and the exponent is reduced ( $\alpha = 0.26$ ). For a given concentration, this indicates the formation of new particles and thus, a decrease of the average aggregation number. This is compatible with the observed reduction of the core size with the concentration (from 28 to 21 Å when  $c$  varies from 0.5 to 0.015 mol L<sup>-1</sup>, which means a reduction in volume by a factor 2).

If we fix the concentration  $c$ , we can roughly estimate the ratio of the aggregation numbers in dark and under UV ( $N_{agg\ dark}/N_{agg\ UV}$ ) from the variation of  $q^*$  (Equation 5). For  $c = 0.03\ \text{mol L}^{-1}$ , we get

$$N_{agg\ dark}/N_{agg\ UV} = (q_{UV}^*/q_{dark}^*)^3 = 1.72 \quad (7)$$

If we assume that the core is a good indicator to extract the aggregation number (*i.e.*, each chain occupies the same volume in the core, and in absence of penetrating water), we can compare this value to that obtained from the fit by considering the ratio between the volumes of the core in dark and under UV:

$$N_{agg\ dark}/N_{agg\ UV} = V_{core\ dark}/V_{core\ UV} = (R_{core\ dark}/R_{core\ UV})^3 \approx 2 \quad (8)$$

The aggregation number is divided by a factor 2 under UV.

These values (eq7, eq8) are nearly identical. The variation of  $q^*$  is definitively related to the variation of the aggregation number in the particles. The PAA-Azo chains leaving the particles under UV radiation then reform smaller aggregates in solution.

Since the Azo group is highly hydrophobic, the majority should be confined in the core. The typical radius of the core is actually close to (but larger than) the size of one Azo modified monomer, *i.e.*, around 20 Å (in its extended form). Some PAA monomers are therefore certainly inserted (or the shape of the particle is not perfectly spherical and closer to an ellipsoid). The exact proportion is quite difficult to determine. If we consider the SLD of the core, it varies in between  $11.5 \cdot 10^{10}\ \text{cm}^{-2}$  (average value in dark) to  $10.94 \cdot 10^{10}\ \text{cm}^{-2}$  (average value under UV radiation). It is much lower than that of PAA<sup>-</sup> ( $22.18 \cdot 10^{10}\ \text{cm}^{-2}$ ) and close (but always below) that of the grafted Azo group ( $12.95 \cdot 10^{10}\ \text{cm}^{-2}$ ). It means that water penetrate in the core and decrease its average SLD. If we neglect the presence of PAA, the water volume fraction is given by

$$\phi_{H_2O} = \frac{\rho_{core} - \rho_{Azo\ group}}{\rho_{H_2O} - \rho_{Azo\ group}} \quad (9)$$

leading to water content in between 40% (dark) to 56%. These values are surprisingly high for hydrophobic components. However, similar values have already been reported in certain Azobenzene micellar systems<sup>9</sup>.

To fix the ideas, we can give an order of magnitude of the aggregation number  $N_{agg}$  (*i.e.*, the number of polymer chains in the aggregate) in dark and under UV. If we consider that all the Azo groups are present in the core, and that water can penetrate in the aggregate,  $N_{agg}$  is simply

$$N_{agg} = \frac{V_{core} (1 - \phi_{H_2O})}{N \tau_{Azo} V_{Azo\ group}} \quad (10)$$

where  $N$  is the degree of polymerization of the PE ( $N = 738$ ),  $\tau_{azo}$  is the molar fraction in Azo-groups ( $\tau_{azo} = 0.11$ ) and  $V_{azo\ group}$  is the volume of the Azo group ( $V_{azo\ group} = 293 \text{ \AA}^3$ ). The numerator corresponds to the total volume associated to the Azo groups in the core while the denominator is the total volume of Azo in a PE chain. If we consider the concentration  $c = 0.03 \text{ mol L}^{-1}$  (or any concentrations in the dark state), we find  $N_{agg} = 2.5$  in dark, and 0.9 under UV (we should have a single chain in the aggregate). Whatever the accuracy of the calculation, the number of chains in the pearls is very limited. Inter, but also intra-chain interactions are therefore very important for the stability of the particles.

Around the core, we have a shell in which we find polyions that form loops on the surface, as well as chain ends. It is clear that the structure of the shell is more complex than the classical homogeneous semidilute polymer solution we have considered (and subtracted) here. It might have been better to envisage a PE solution instead of neutral polymers. The main difference is the shape of the contribution  $I_{fluc}(q)$  that shows a maximum for charged systems.

According to the Azo fraction of the modified polymer ( $\tau_{azo} = 0.11$ ), we have in average  $\approx 9$  PAA monomers between two Azo groups. The typical distance is of the order of 22  $\text{\AA}$ . This seems to be too short to create a loop compatible with our shell thickness (around 20  $\text{\AA}$  at least). However, it must keep in mind that this number is only an average value and hides many disparities in terms of grafting homogeneities along the chains. Some chains also may have less Azo groups than other and therefore more facilities to do form loops, but also, to leave the aggregate.

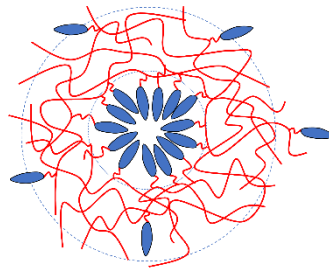


Figure 17 schematic representation of  $(\text{PAA-Azo}_{0.11})_{738\text{RAFT}}$  aggregates.

### V.3.5 Structural organisation in short chain PAA-Azo solutions ( $\tau_{\text{azo}} = 0.11$ )

In the previous paragraph, we have shown that long chains ( $\tau_{\text{azo}} = 0.11$ ) self-assemble and form spherical core-shell particles. Intra and intermolecular interactions play a key role in the process. The situation becomes very interesting if we reduce the size of the polymer while keeping the Azo fraction constant.

We focus here on a short polymer with a degree of polymerisation  $N = 42$ , an Azo fraction  $\tau_{\text{azo}} = 0.11$  (identical to that of the long chains) and a high polydispersity ( $I_p = 1.33$ ). Each chain has in average  $\approx 5$  Azo groups which is rather few compared to the long chains ( $\approx 74$ ). Since the polydispersity is large, the disparity in number of Azo groups per chain can be very important.

SAXS measurements at  $0.25 \text{ mol L}^{-1}$  in (dark and UV) are presented in Figure 18 and compared to unmodified NaPAA. As already mentioned in Figure 8, the maximum in dark is at a lower  $q$  value compared to NaPAA solution. Under UV irradiation, the peak shifts to higher  $q$  (and approaches very close to that of pure NaPAA) reflecting a large structural reorganization triggered by UV stimulus.

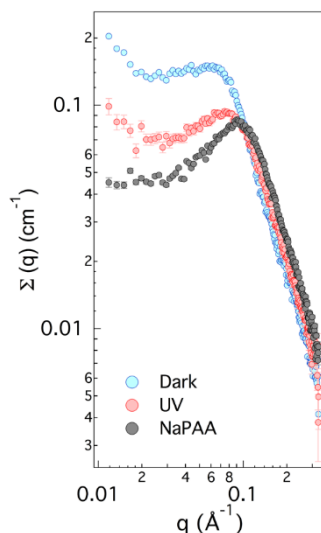


Figure 18 SAXS data of  $(\text{PAA-AZO}_{0.11})_{42\text{Sigma}}$  and NaPAA solutions at  $0.25 \text{ molL}^{-1}$ .

A series of solutions at different concentrations have been measured in dark and under UV (Figure 19a and b). The variation of  $q^*$  as a function of the concentration is plotted in Figure 19c ( $q^*$  values for pure NaPAA are indicated for comparison). Contrary to the long chains, for which a single power law  $q^* \propto c^\alpha$  is observed ( $\alpha \approx 0.3$  in dark and  $0.26$  under UV), different regimes in concentration with different exponents are now clearly visible. Since the unmodified parent NaPAA is in dilute regime in the whole concentration range, we can reasonably

assume the same situation for PAA-Azo. Departure from a classical  $c^{1/3}$  dilution law may therefore reflect an association (or an aggregation) process between polymers as roughly described by equation 5.

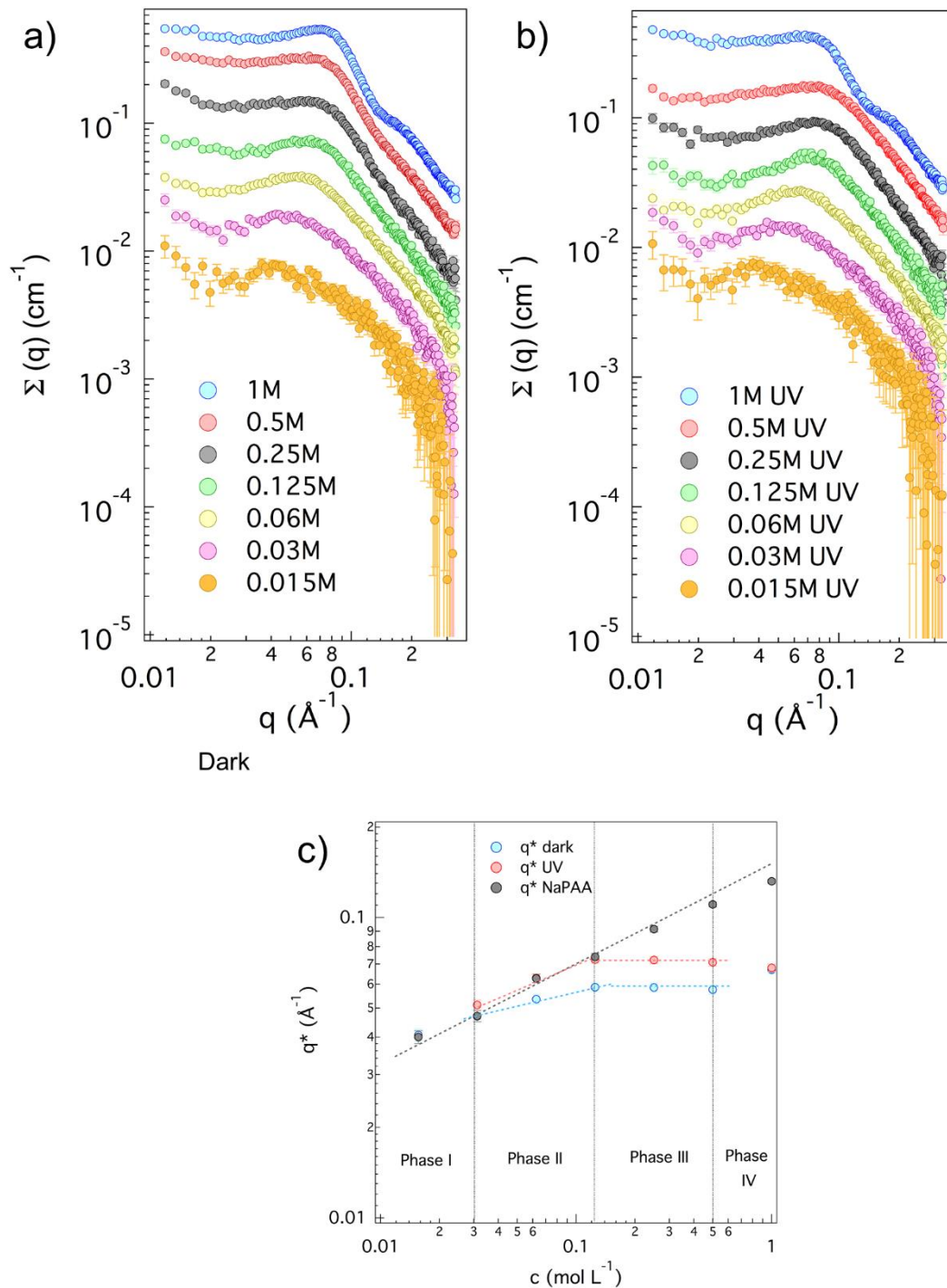


Figure 19 SAXS study of (PAA-Azo<sub>0.11</sub>)<sub>42Sigma</sub>. a) SAXS measurements in dark; b) SAXS measurements under UV irradiation; c) log-log plot of  $q^*$  vs concentration.

The structural organization therefore varies gradually with the concentration in dark and under UV. Based on  $q^*$  variations, four distinct regimes (Regimes I, II, III and IV) can be identified in dark, while three only are observed under UV (I, III and IV, regime II is absent). A close inspection of the scattering profiles in the different regimes shows subtle differences. These differences will help us to identify the structural organization and the origin of the different regimes. This can be summarized as follow.

**Regime 1** ( $c \leq 0.03 \text{ mol L}^{-1}$ )

In this regime,  $q^*$  values are identical for both dark and UV measurements but also for pure NaPAA. Since  $q^*$  varies as  $c^{1/3}$ , we just experience a dilution process of individual molecules, PEs are solubilised at the molecular level. For these very low concentrations, polyions are far apart (average distances between objects:  $d_{\text{NaPAA}}$ ,  $d_{\text{Dark}}$ ,  $d_{\text{UV}}$ ), and do not associate with others. The possible intramolecular collapse (due the hydrophobicity of the azo) and the eventual conformational transition under UV (induced by the photoisomerization) do not change the average distance between the objects ( $d \approx 2\pi/q^*$ ) and the power law exponent. Only the shape of the scattering curve may reveal these aspects, but no differences are observed (this is anyway difficult to evidence since we do not only observe the form factor of the chains at low  $q$ ). A schematic picture of the structural organisation is given in Figure 20.

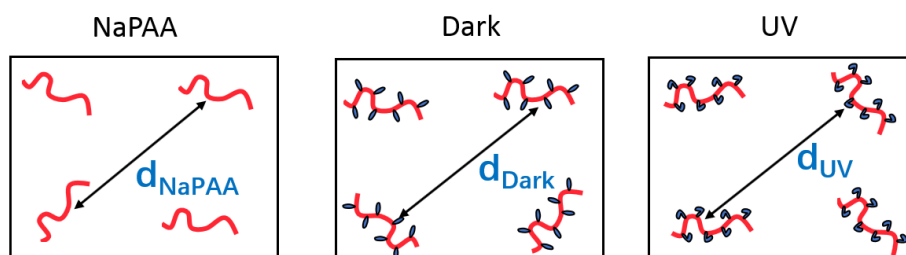


Figure 20 Schematic representation of the structural organization in regime I.

**Regime II** ( $0.03 \text{ mol L}^{-1} \leq c \leq 0.125 \text{ mol L}^{-1}$ )

When we increase the concentration, we are more sensitive to the intermolecular interactions.

$q^*$  values in dark are now lower than those under UV (or NaPAA): the average distance between the objects is larger ( $d_{\text{Dark}} > d_{\text{UV}} = d_{\text{NaPAA}}$ ). This implies the association (or the aggregation) of polyions. In this regime  $\alpha \approx 0.2$  (which corresponds to a clear departure from the classical dilution behaviour  $\alpha \approx 0.33$ ),

the average number of chains implicated in the association ( $N_{\text{agg}}$ ) is larger than unity and increases with  $c$ .

This association is induced by the large hydrophobicity of the *trans*-azo units and/or the interaction between inter-chain aromatic cycles ( $\pi$ - $\pi$  stacking). Under UV irradiation, the azo units undergo the photoisomerization from the *trans* form (hydrophobic form) to the *cis* form (hydrophilic form). Since PEs are more hydrophilic and the ring interconversion disturbs the  $\pi$ - $\pi$  stacking, we observe the disassociation of the aggregates (Figure 21) and we recover the classical  $q^* \propto c^{1/3}$  behaviour under UV values as with pure NaPAA. Since irradiated PAA-Azo are now solubilized at the molecular level, regime II is not present under UV.

The exact nature of the aggregate in dark is quite difficult to determine since the scattering pattern is very close to that a classical PE (only the maximum is shifted). The number of polyions implicated in the association is certainly very limited. No signature for a dense hydrophobic core (as for long chains) is visible. We believe that the interaction between polyions only gives very loose aggregates.

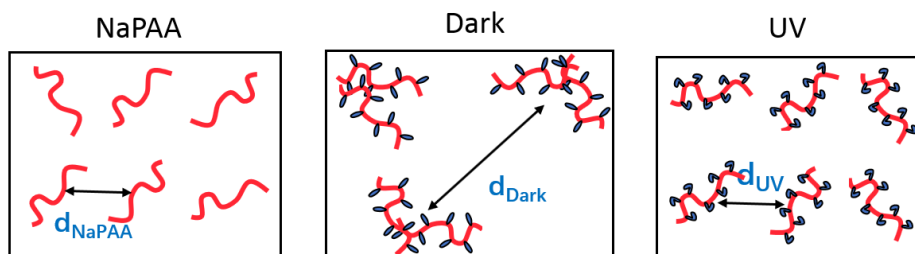


Figure 21 Schematic representation of the structural organization in regime II.

The regime II is very interesting since we can form, and completely disassemble small aggregates on demand by simple light stimulus.

This behaviour persists until  $0.125 \text{ mol L}^{-1}$  where the shape of scattering curves starts to change (yellow and green curve in Figure 22).

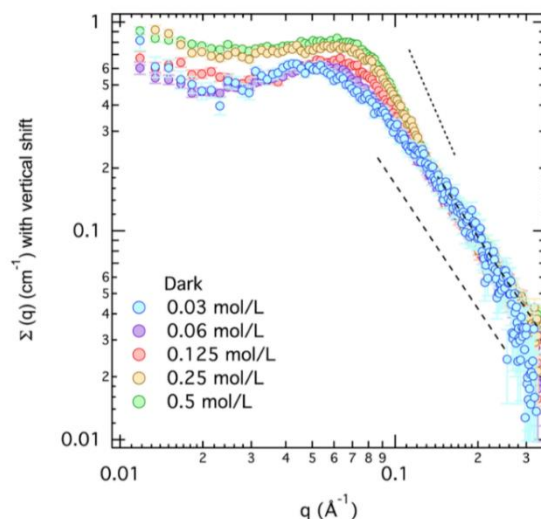


Figure 22 Scattering curves in dark close to regimes II and III. Data have been shifted vertically to better evidence the modifications around the maximum. Long dash line:  $q^{-2}$  decay, short dash line:  $q^{-3}$  decay.

### Regime III ( $0.125 \text{ mol L}^{-1} \leq c \leq 0.5 \text{ mol L}^{-1}$ )

In this concentration range,  $q^*$  values are constant in the dark state. From a geometrical point of view, as the chain concentration increases, the distance between the aggregate doesn't change ( $d_{\text{Dark}}$ ). The aggregates concentration in the solution is therefore constant, and their aggregation number  $N_{\text{agg}}$  is increased. This regime corresponds to a simple growth of the particles.

Under UV irradiation, contrary to what is observed in regime II,  $q^*$  values do not match that of pure PAA. UV stimulus therefore break the aggregates and form smaller ones. Since  $N_{\text{agg}}$  is reduced,  $q^*$  is higher. Curiously,  $q^*$  does not vary with the concentration meaning that the same fraction of chains is dissociated when the light stimulus is applied (eq7).

The shape of the scattered intensity in dark (Figure 22) starts to deviate below  $0.013 \text{ \AA}^{-1}$ . An extra contribution appears (with a scaling behavior close to  $q^{-3}$  as indicated in Figure 22) that looks very similar to stars shape molecules<sup>10</sup>. The origin for such an exponent comes from the particular radial density profile in the stars. The term star-like is certainly excessive in our case but we can say that a core is certainly forming in dark, with some arms around. The fact that our system behaves as a star-like assembly in this regime also indicates that the center of the particles does not form a large and dense core (as for long chains of PAA-Azo).

The growth of the particles in regime III in dark then leads to a star-like arrangement: a core is gradually forming due to the assembling of the Azo groups with a shell of PAA segments around (Figure 23). This correspond to the first step

of the formation of a core-shell particle.

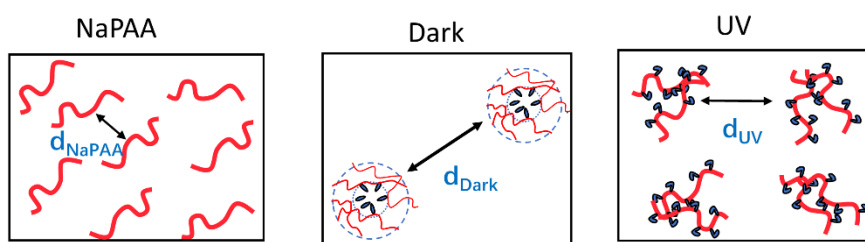


Figure 23 Schematic representation of the structural organization in regime III.

Upon UV irradiation, the scattering curves look different. We do no longer have the signature of star-like assembly. UV light stimulus is therefore able to disassemble the azo cores leading to the formation of loose aggregates.

#### Regime IV ( $c \geq 0.5 \text{ mol L}^{-1}$ )

For the largest concentration ( $1 \text{ mol L}^{-1}$ ),  $q^*$  is slightly increasing in the dark state. The average distance between aggregate is reduced. It is quite difficult to extract a power law tendency to judge the global variation of  $N_{\text{agg}}$  with the concentration. Under UV,  $q^*$  is decreased and matches the value found in dark: we have now very similar aggregation numbers. Compared to lower concentrations under UV, the aggregation is larger.

The scattering curves in dark and under UV (displayed in Figure 24) are very close to the “star-like” assembly observed in the dark state of regime III. The maximum is however more pronounced and sharper. In the meantime, a large shoulder is found around  $0.2 \text{ \AA}^{-1}$ . We believe the aggregates are simply better organized, which a small and denser core of hydrophobic azobenzene and a corona of PAA loops and chain ends. The description is now close to that of long chain except that the core is certainly smaller (Figure 25).

The local concentration of PAA in the shell may be very large leading to a smaller correlation length and the shoulder formation in the high  $q$  range.

Photo-induced effect are less important since the core is better defined with a better compactness.

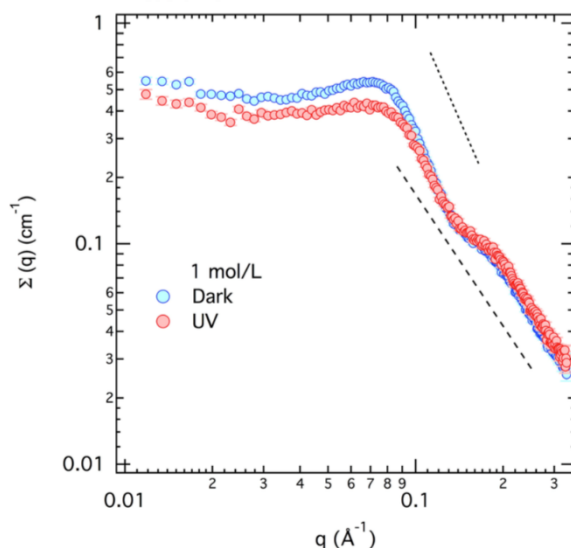


Figure 24 Scattering curves in dark and under UV irradiation in regime IV. Long dash line:  $q^{-2}$  decay, short dash line:  $q^{-3}$  decay.

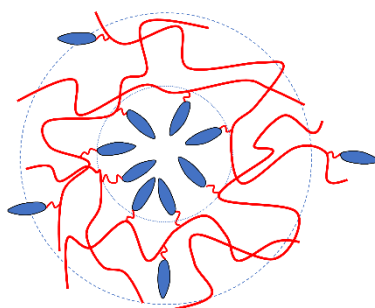


Figure 25 Schematic representation of the structural organization in regime IV.

The validation of this structural description would require the refinement of the data with a specific model especially in the high concentration regime. Cryo-TEM measurements are not possible since the size of the particles is too small, but also, the interesting concentration is too large (dilutions cannot be done as they modify the structural organization).

UV-Vis measurements estimated the *trans/cis* fraction under UV for this sample at different concentrations (Figure 3). The structural study shows that for  $c = 0.03, 0.06$  and  $0.125 \text{ mol L}^{-1}$  (regimes I and II), we have loose aggregates in dark that are completely disassembled under UV irradiation. In the meantime, UV-Vis measurements have determined a very low *trans* fraction under UV-irradiation (10% *trans*, 90% *cis*) for these concentrations. The high efficiency of the UV light stimulus is a consequence of the structural organization in loose aggregates observed in the dark state. The *trans*  $\rightarrow$  *cis* photoisomerization is facilitated.

On the other hand, at 0.25, 0.5 and 1 mol L<sup>-1</sup> for which a gradual structural evolution and the formation of a core is presumed, the final *trans* ratio under UV is very high (40% *trans*, 60% *cis*). The photoisomerization process and the photostationary state in the solution clearly depends on the structural organization that can impose geometric constraints that hinder the *trans* → *cis* isomerization.

### V.3.6 Structural organization in short chain PAA-Azo solutions ( $\tau_{\text{azo}} = 0.15$ )

We have shown previously that short chains with a moderate azo content (11%) exhibit different structural organizations, from isolated polyions in solution to a core-shell assembly. In order to evaluate the role of the Azo groups in the association, we have increased the Azo grafting ratio close to the limit of solubility in water.

We have considered two distinct PEs: (PAA-Azo<sub>0.15</sub>)<sub>39Sigma</sub> and (PAA-Azo<sub>0.15</sub>)<sub>54RAFT</sub>. Both have an Azo content of 15%. The main difference lies in the polydispersity. (PAA-Azo<sub>0.15</sub>)<sub>39Sigma</sub> ( $I_p = 1.26$ ) has been obtained from a commercial PAA ( $I_p = 1.40$ ) while the parent PAA of (PAA-Azo<sub>0.15</sub>)<sub>54RAFT</sub> has been synthesized in the laboratory by RAFT ( $I_p = 1.12$ ).

SAXS measurements and  $q^*$  variation in dark state and under UV irradiation are given in Figure 26 and Figure 27 for both PAA-Azo. The general trends are very similar. If we focus on  $q^*$  variations, and according to the previous section, only regime I (UV) and II (dark, UV) are observed.

For PEs in dark,  $q^*$  variation can be described a single exponent law on the whole concentration range ( $\alpha = 0.25$  and 0.23 for (PAA-Azo<sub>0.15</sub>)<sub>39Sigma</sub> and (PAA-Azo<sub>0.15</sub>)<sub>54RAFT</sub> respectively), this behaviour corresponds to regime II.

Under UV radiation, two regimes are observed. Below 0.03 mol L<sup>-1</sup> (as for (PAA-Azo<sub>0.11</sub>)<sub>42Sigma</sub>, Figure 19),  $q^*$  reaches the values of pure NaPAA (regime I). Above 0.03 mol L<sup>-1</sup>,  $q^*$  follow a power law variation with exponents 0.25 ((PAA-Azo<sub>0.15</sub>)<sub>39Sigma</sub>) and 0.23 (regime II, (PAA-Azo<sub>0.15</sub>)<sub>54RAFT</sub>).

At 1 mol L<sup>-1</sup>,  $q^*$  are almost identical in dark and under UV: the aggregation number does no longer vary with the UV light stimulus.

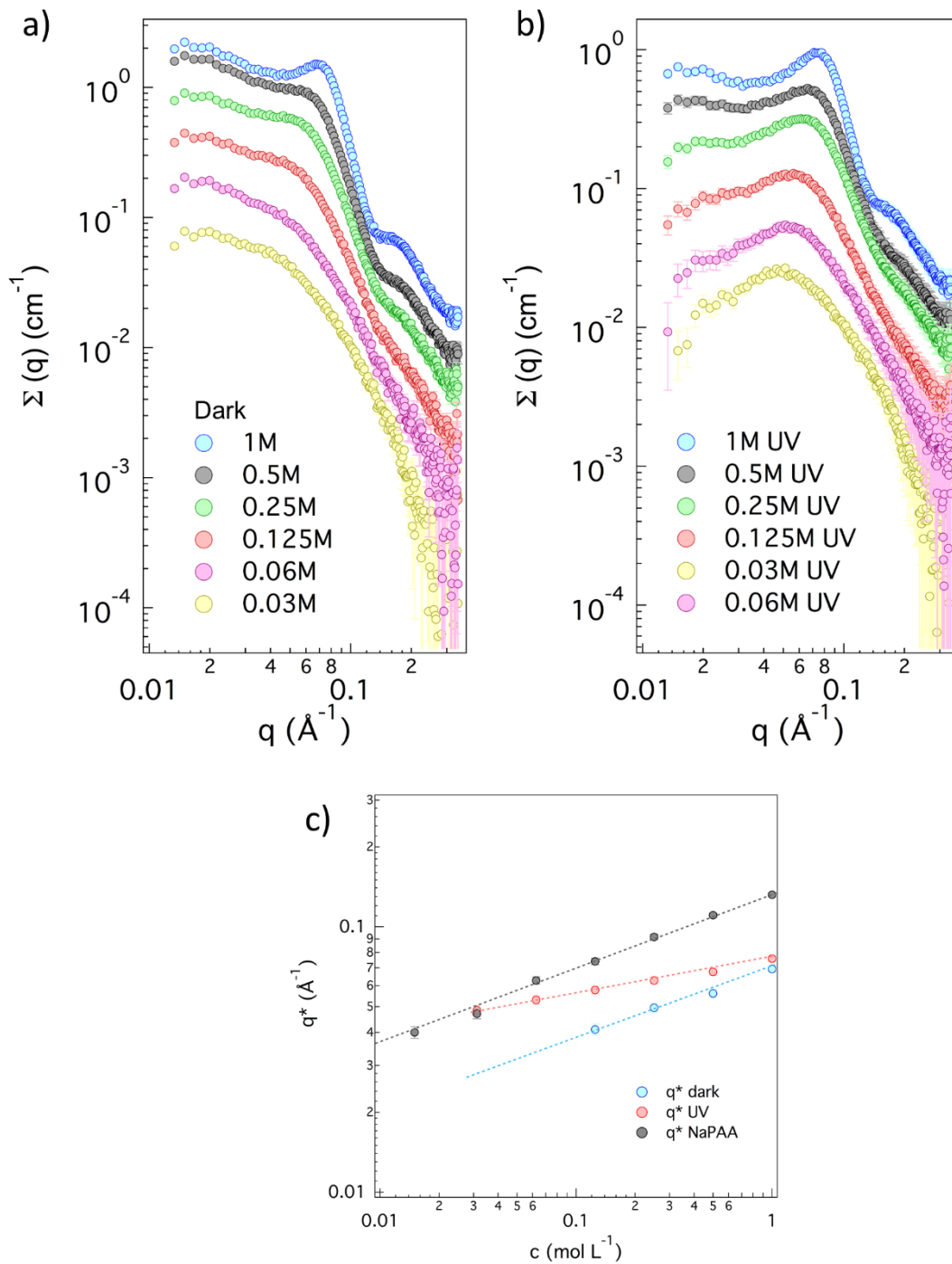


Figure 26 SAXS study of (PAA-Azo<sub>0.15</sub>)<sub>39</sub>Sigma. a) SAXS measurements in Dark b) SAXS measurements under UV c) log-log plot of  $q^*$  vs concentration.

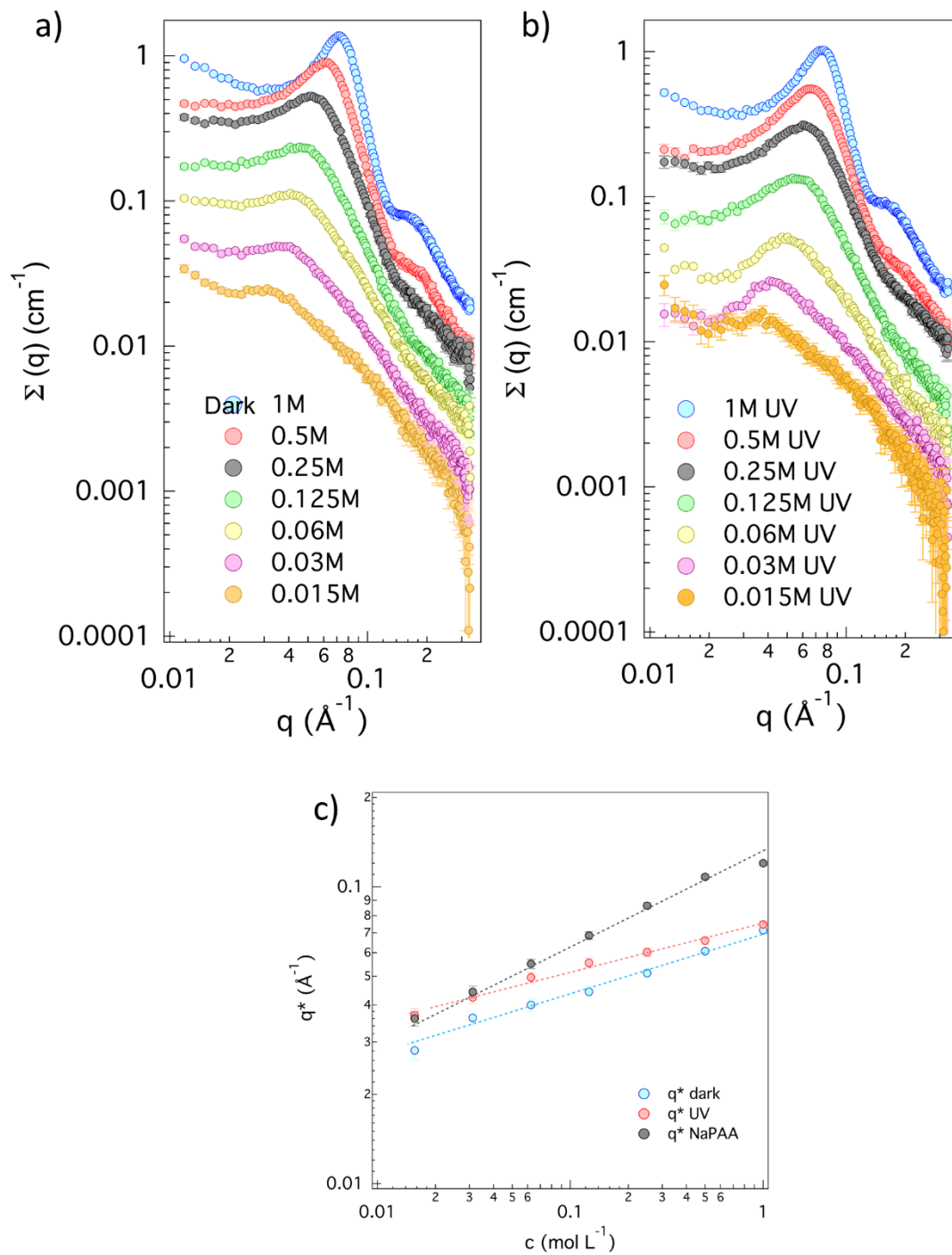


Figure 27 SAXS results of (PAA-AZO<sub>0.15</sub>)<sub>54</sub>RAFT. a) SAXS measurements in Dark b) SAXS measurements under UV c) log-log plot of  $q^*$  vs concentration.

More information can be gained from a rapid inspection of the shape of the scattered intensities. For simplicity we just discuss the case of (PAA-Azo<sub>0.15</sub>)<sub>54RAFT</sub> which behaves similarly to (PAA-Azo<sub>0.15</sub>)<sub>39Sigma</sub>.

For the lowest concentrations in dark ( $c \leq 0.03 \text{ mol L}^{-1}$ ), we identify the signature of loose aggregates that can be disassembled by UV stimulus. This is very similar to (PAA-Azo<sub>0.11</sub>)<sub>42Sigma</sub>, but the concentration limit is significantly lower than for (PAA-Azo<sub>0.11</sub>)<sub>42Sigma</sub>. This is a direct consequence of the larger Azo content. At large  $q$ , we find a  $q^{-2}$  intensity variation characteristic of PAA scattering in solution.

For  $c \geq 0.06 \text{ mol L}^{-1}$  in dark, we first find the signature of star-like particles that rapidly evolve with concentration. The maximum sharpens while a well-defined shoulder clearly appears around  $0.15 \text{ \AA}^{-1}$  (Figure 27). The shoulder is more pronounced than with (PAA-Azo<sub>0.11</sub>)<sub>42Sigma</sub> and still originates from the scattering of PAA segments in solution. The correlation length associated to the PAA lattice is therefore smaller. Finally, the power law exponent around the correlation peak is larger than the previous characteristic  $q^{-3}$  variation observed for “star-like” (PAA-Azo<sub>0.11</sub>)<sub>42Sigma</sub> systems. This announces a well-defined structure factor and a more compact core. In conclusion, we still have objects with a core made of Azo moiety and a shell made of semidilute PE segments.

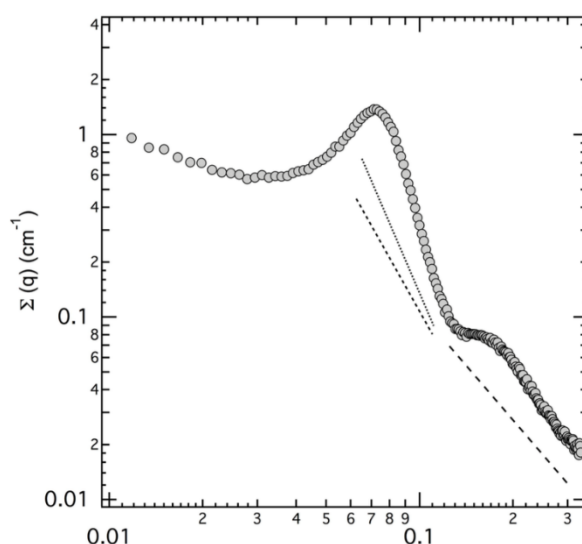


Figure 28 Scattering curves of (PAA-Azo<sub>0.15</sub>)<sub>54RAFT</sub> in dark at  $1 \text{ mol L}^{-1}$ . Long dash line:  $q^{-2}$  decay, intermediate dash line:  $q^{-3}$  decay, short dash line:  $q^{-4}$  decay.

This description is also valid for (PAA-Azo<sub>0.15</sub>)<sub>39Sigma</sub>, with a larger polydispersity (Figure 26). The only difference is the presence of a large upturn at low  $q$  value in the dark state that almost completely hides the scattering peak. This

upturn indicates the formation of very large clusters in solution that disappears upon UV radiation. This effect is reversible and is therefore related to the presence of azobenzene groups. The origin is still unknown and the link with the polydispersity needs to be clarified. This is however a very interesting effect since UV stimulus allows here to modulate the structural organization at a larger length scale.

### V.3.7 Conclusion

Four Azo-polymers with different lengths and different Azo fractions have been investigated. These systems show an important and reversible response upon light stimulus. The photoisomerization at the molecular level is responsible for a large structural reversible reorganization.

For all these systems, the addition of hydrophobic Azo groups to the hydrophilic NaPAA leads to the formation of spherical aggregates.

For long chains (PAA-AZO<sub>0.11</sub>)<sub>738</sub>RAFT, we find a compact core-shell structure in which the core is composed of Azo groups and the shell mainly contains PAA segments. Only a few chains are implicated in the assembly.

Under UV irradiation, the size of aggregates decreases, chains are released and form new aggregates. This behaviour is very similar to that of classical Azo-surfactants in which UV irradiation leads to the formation of smaller micelles. Our system behaves similarly. It is therefore not “frozen” and can be partly assembled and disassembled on demand by simple light stimulus (UV, Blue).

The situation is more complex for small chains (PAA-AZO<sub>0.11</sub>)<sub>42</sub>Sigma, (PAA-AZO<sub>0.15</sub>)<sub>39</sub>Sigma, (PAA-AZO<sub>0.15</sub>)<sub>54</sub>RAFT. If we still have small aggregates in which Azo groups are located, we observe different regimes in concentration.

In particular, we have identified a small concentration range in which it is possible to completely disassemble small aggregates under UV radiation. This situation is still comparable to that of pure micellar solutions of Azo-surfactants. In these systems, the change of hydrophobicity (and critical packing parameter) induced by the photoisomerization shifts the CMC to higher values under UV. For concentrations in between CMC<sub>dark</sub> and CMC<sub>UV</sub>, UV irradiation simply breaks the micellar aggregates. We therefore have a concentration range in which micelles can be disassembled under radiation. In our system, the situation looks more complicated since the Azo groups are chemically linked to the polymer, but the underlying process is probably identical. Within this crude description, the

transition between regimes I and II observed in the dark state and under UV ( $CMC^*_{\text{dark}}$  and  $CMC^*_{\text{UV}}$ ) corresponds to the equivalent  $CMC^*_{\text{dark}}$  and  $CMC^*_{\text{UV}}$  for Azo-surfactants.

If we go further in the analogy, above a CMC of Azo-surfactants, we have the formation of small pre-micellar aggregates that then grow in size with the concentration. UV irradiation only changes the size and shape of the micelles (and therefore the number of surfactants in the aggregates). This seems again very similar to what we observed. The variation under UV therefore just reflects the partial rearrangement of the micellar core. By the way, under UV, certain polyions are expelled from the pre-existing aggregates and re-assemble elsewhere.

The physics of the system sounds very similar to that of small surfactants. To go further, it would be necessary to find a model able to fit the data in order to determine important parameters such as the aggregation number and its modification under UV.

For long chains, no  $CMC^*_{\text{dark}}$  or  $CMC^*_{\text{UV}}$  are observed in the investigated concentration range. We always have well defined core-shell particles. The aggregates therefore form at concentration much lower than for short chains. This difference may be related to simple entropic effect.

During this work, we did not find any evidence for a pearl-necklace conformation as it could be expected for hydrophobic PEs. Indeed, the hydrophobicity of the polyions leads to the formation of inter-chains complexes that are out of the scope of the theory. To prevent this aggregation, one possibility would be to work in mixtures of water and organic solvent to slightly improve the quality of the solvent, and work at lower concentrations<sup>11</sup>.

## References:

- (1) Chevallier, E. Cascade d'effets Induits Par La Lumière Aux Interfaces Liquides : Du Photo-Surfactant à La Mousse. Thesis, Université Paris VI, 2012.
- (2) Chevallier, E.; Monteux, C.; Lequeux, F.; Tribet, C. Photofoams: Remote Control of Foam Destabilization by Exposure to Light Using an Azobenzene Surfactant. *Langmuir* **2012**, *28* (5), 2308–2312.
- (3) Akamatsu, M.; FitzGerald, P. A.; Shiina, M.; Misono, T.; Tsuchiya, K.; Sakai, K.; Abe, M.; Warr, G. G.; Sakai, H. Micelle Structure in a Photoresponsive Surfactant with and without Solubilized Ethylbenzene from Small-Angle Neutron Scattering. *J. Phys. Chem. B* **2015**, *119* (18), 5904–5910.
- (4) Zakrevskyy, Y.; Cywinski, P.; Cywinska, M.; Paasche, J.; Lomadze, N.; Reich, O.; Löhmannsröben, H.-G.; Santer, S. Interaction of Photosensitive Surfactant with DNA and Poly Acrylic Acid. *J. Chem. Phys.* **2014**, *140* (4), 044907.
- (5) Chen, S. H.; Sheu, E. Y.; Kalus, J.; Hoffman, H. Small-Angle Neutron Scattering Investigation of Correlations in Charged Macromolecular and Supramolecular Solutions. *J. Appl. Crystallogr.* **1988**, *21* (6), 751–769.
- (6) Dingenouts, N.; Seelenmeyer, S.; Deike, I.; Rosenfeldt, S.; Ballauff, M.; Lindner, P.; Narayanan, T. Analysis of Thermosensitive Core-Shell Colloids by Small-Angle Neutron Scattering Including Contrast Variation. *Phys. Chem. Chem. Phys. - PHYS CHEM CHEM PHYS* **2001**, *3*, 1169–1174.
- (7) Hayter, J. B.; Penfold, J. Self-Consistent Structural and Dynamic Study of Concentrated Micelle Solutions. *J. Chem. Soc. Faraday Trans. 1* **1981**, *77* (8), 1851–1863.
- (8) Hansen, J.-P.; Hayter, J. B. A Rescaled MSA Structure Factor for Dilute Charged Colloidal Dispersions. *Mol. Phys.* **1982**, *46* (3), 651–656.
- (9) Blayo, C.; Houston, J. E.; King, S. M.; Evans, R. C. Unlocking Structure–Self-Assembly Relationships in Cationic Azobenzene Photosurfactants. *Langmuir* **2018**, *34* (34), 10123–10134.
- (10) Pozza, G. M.-E.; Crotty, S.; Rawiso, M.; Schubert, U. S.; Lutz, P. J. Molecular and Structural Characterization of Hybrid Poly(Ethylene Oxide)–Polyhedral Oligomeric Silesquioxanes Star-Shaped Macromolecules. *J. Phys. Chem. B* **2015**, *119* (4), 1669–1680.
- (11) Mahmoud, S.; Wafa, E.; Brûlet, A.; Boué, F. How Necklace Pearls Evolve in Hydrophobic Polyelectrolyte Chains under Good Solvent Addition: A SANS Study of the Conformation. *Macromolecules* **2018**, *51*.



## Chapter VI. Complexes of polyelectrolytes and oppositely charged Azo-surfactants

Surfactant/PE complexes have been widely investigated in vast applications areas such as for delivery systems, paints, food preservation, rheological control...

The large variety of PEs and surfactants offers various combinations and many structural organizations exhibiting unique properties in the bulk, at the interface and in the solid state.

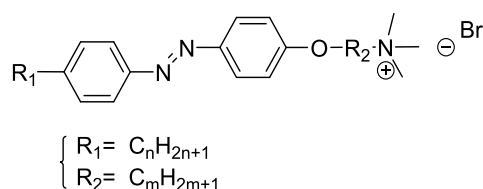
Azo-surfactants show interesting structural modifications triggered by UV light stimuli<sup>1-3</sup>. The combination of PEs and Azo-surfactants offers new possibilities through the photo-control of the complex under irradiation. Some Azo-surfactant/PE systems have already been reported as discussed in Chap II.2.3. Nevertheless, little work has explored their structural organization in aqueous solution.

This chapter contains two parts. The first part concerns the investigation of pure Azo-surfactants solutions and more specifically, the determination of the CMC, the photoconversion behaviours and the structural description of their micellar aggregates. The objective is to understand the organization of pure Azo-surfactant micelles in dark state and the variation upon light irradiation.

The second part of this chapter reports the study of PE/Azo-surfactant complexes. The photoisomerization behaviours (by NMR and UV-Vis spectroscopy) and the structural organization (SAXS and SANS) will be presented. A pearl-necklace model will be proposed to describe the structure of Azo-surfactant/PE complexes.

## VI.1 Azo-surfactants

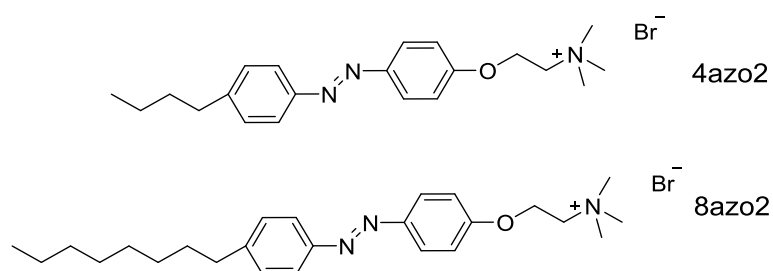
Azo-surfactants are composed of a polar head, an alkoxy spacer  $OR_2$ , a light-responsive Azo group and a hydrophobic alkyl tail  $R_1$ . To simplify the notation, cationic Azo-surfactants are denoted **xAzoyTAB**, where  $x$  is the carbon number of the alkyl tail  $R_1$  and  $y$  is the carbon number of the spacer  $R_2$ . The position of Azo unit along the surfactant architecture varies with the combination of  $R_1$  and  $R_2$ .



Scheme 1 Structure of cationic Azo-surfactant, where  $R_1$  is the alkyl tail and  $R_2$  is the spacer chain.

According to the studies of Hayashita<sup>4</sup> and Blayo<sup>1</sup> groups, the micellar morphology and the extent of structural modification under light irradiation depend on the total length of hydrophobic segment and the position of Azo moiety. It also appears that the combination of short spacers and long alkyl chains has more influence on the hydrophobicity of Azo-surfactants.<sup>1,4</sup>

In the present work, we chose a short two-carbon spacer for  $R_2$  ( $m = 2$ ). For the alkyl  $R_1$ , two chain lengths were considered: a butyl chain (moderate length,  $n = 4$ ) frequently used as hydrophobic tail of Azo-surfactant<sup>2,3,5-7</sup> and a longer octyl chain ( $n = 8$ ) which is supposed to form more elongated micellar aggregates<sup>1</sup>. Hence, 4Azo2TAB and 8Azo2TAB Azo-surfactants (Scheme 2) have been synthesized as described in Chap III.2.



Scheme 2 Structure of Azo-surfactants used in Azo-surfactant/PE systems.

## VI.2 Characterization of micelles

### VI.2.1 Surface tension and critical micellar concentration (CMC)

The critical micellar concentration (CMC) is an important characteristic for surfactants in solution. It is defined as the surfactant concentration, above which micelles start to form. The CMCs of Azo-surfactants for both *trans* and *cis* isomers have been determined on a Kibron tensiometer by measuring the surface tension of a concentration series at 21 °C (in dark and under UV irradiation). The surface tension varies linearly with the logarithm of the concentration just below the CMC. Above the CMC, it reaches a plateau. The CMC is located at the intersection of these two concentration regimes.

As shown in Figure 1 and Figure 2, the Azo-surfactants follow this general behaviour. The CMC is estimated at 2.6 mM for *trans*-4Azo2TAB and 8.2 mM for *cis*-4Azo2TAB. 8Azo2TAB is more hydrophobic, the CMC is found at 0.29 mM for the *trans* form and 0.82 mM for the *cis* form. All the determined CMCs agree with previously reported values<sup>1,4</sup>.

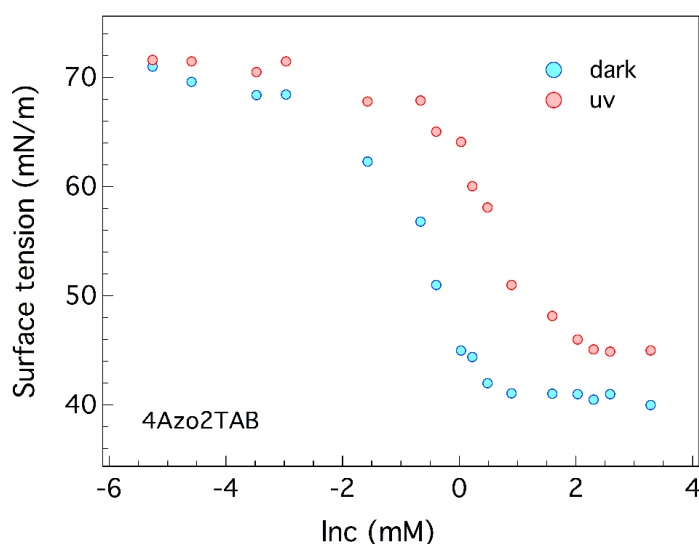


Figure 1 Surface tension as a function of Inc for 4Azo2TAB.

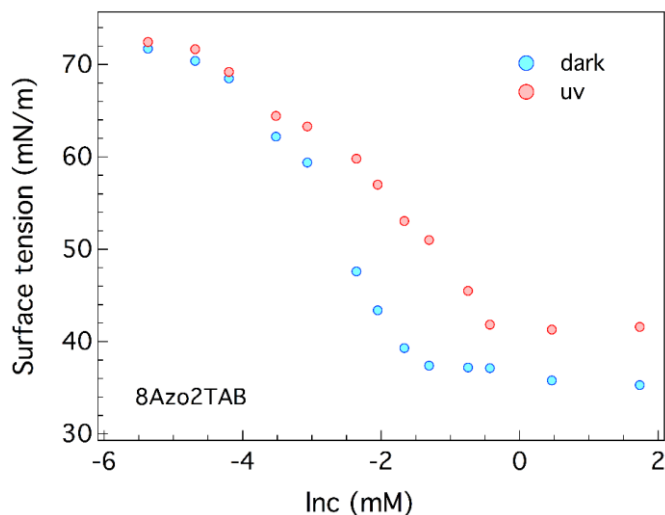


Figure 2 Surface tension as a function of Inc for 8Azo2TAB.

The amount of surfactant molecules adsorbed per unit area at aqueous/air interface, also known as the surface excess concentration  $\Gamma$  can be evaluated from the plots and the equation:

$$\Gamma = -\frac{1}{kT} \left( \frac{\partial \gamma}{\partial \ln C} \right)_{T,P} \quad (1)$$

where  $k$  is the Boltzmann constant ( $1.38 \cdot 10^{-23} \text{ J K}^{-1}$ ),  $T$  is the absolute temperature ( $K$ ). The area per molecule  $A$  at surface is defined as  $1/\Gamma$ . As shown in Table 1, the *cis* form of both 4Azo2TAB and 8Azo2TAB has a larger area per molecule value than the *trans* form. This is consistent with a bent conformation for the *cis* form. The area per molecule  $A$  of 8Azo2TAB is expected to be smaller than that of 4Azo2TAB, since the van der Waals interaction increases with increasing the chain length<sup>8</sup>. However, considering the accuracy of the measurements, we cannot conclude here.

Only the area per molecule of a similar Azo-surfactant 2Azo4TAB (with an ethyl tail  $R_1 = 2$  and a butyl spacer  $R_2 = 4$ ) can be found in the literature<sup>9</sup>, with  $A_{\text{trans}}$  equals to  $40 \text{ \AA}^2$  while  $A_{\text{cis}}$  is  $102 \text{ \AA}^2$ . Another similar Azo-surfactant 4-octylazobenzene-40-(oxy-2-hydroxypropyl) trimethylammonium methylsulfate, with an additionally OH group near the trimethylammonium polar head, shows an area per molecule of  $60 \text{ \AA}^2$  and  $74 \text{ \AA}^2$  for the *trans* and *cis* isomers respectively<sup>10</sup>.

	CMC <sub>trans</sub> (mM)	A <sub>trans</sub> (Å <sup>2</sup> )	CMC <sub>cis</sub> (mM)	A <sub>cis</sub> (Å <sup>2</sup> )
4Azo2TAB	2.6	34.5	8.2	50.0
8Azo2TAB	0.29	33.0	0.82	48.9

Table 1 CMC and area per molecule  $A$  values for Azo-surfactants (dark, UV).

## VI.2.2 Photoisomerization study

### VI.2.2.1 By UV-Vis spectroscopy

The photoinduced behaviour was probed by UV-Vis spectroscopy for both 4Azo2TAB and 8Azo2TAB solutions at a very low concentration ( $c = 0.08 \text{ mM} < \text{CMC}$ ). Absorption spectra are presented in Figure 3 and Figure 4 for different irradiation durations (UV and blue light).

The *trans* isomers present a maximum adsorption band at 350 nm, while the *cis* isomers are characterized by two adsorption bands at 312 nm and 435 nm (Figure 3a and Figure 4a). When exposed to UV light, the *trans* isomers progressively convert to the *cis* forms leading to a decrease of the band at 350 nm and the appearance of the bands at 312 nm and at 435 nm. For any irradiation time, the absorption spectrum is a linear combination of the pure *trans* and pure *cis* absorption spectra weighted by the *trans/cis* ratio. Two isosbestic points are present at 302 nm and 426 nm and simply reflect the superposition of the absorption spectra of the pure isomers. Reversibly, *cis* isomers convert to *trans* isomers quickly under blue light irradiation as shown in Figure 3b and Figure 4b.

We have extracted the *trans/cis* ratios during light irradiation by using the method described in Chap V.2.1. The *trans* molar fraction  $x_{trans}$  as a function of the irradiation time is presented in Figure 3c and Figure 4c (during UV and blue exposure). The isomerization rates of 4Azo2TAB and 8Azo2TAB are very similar.

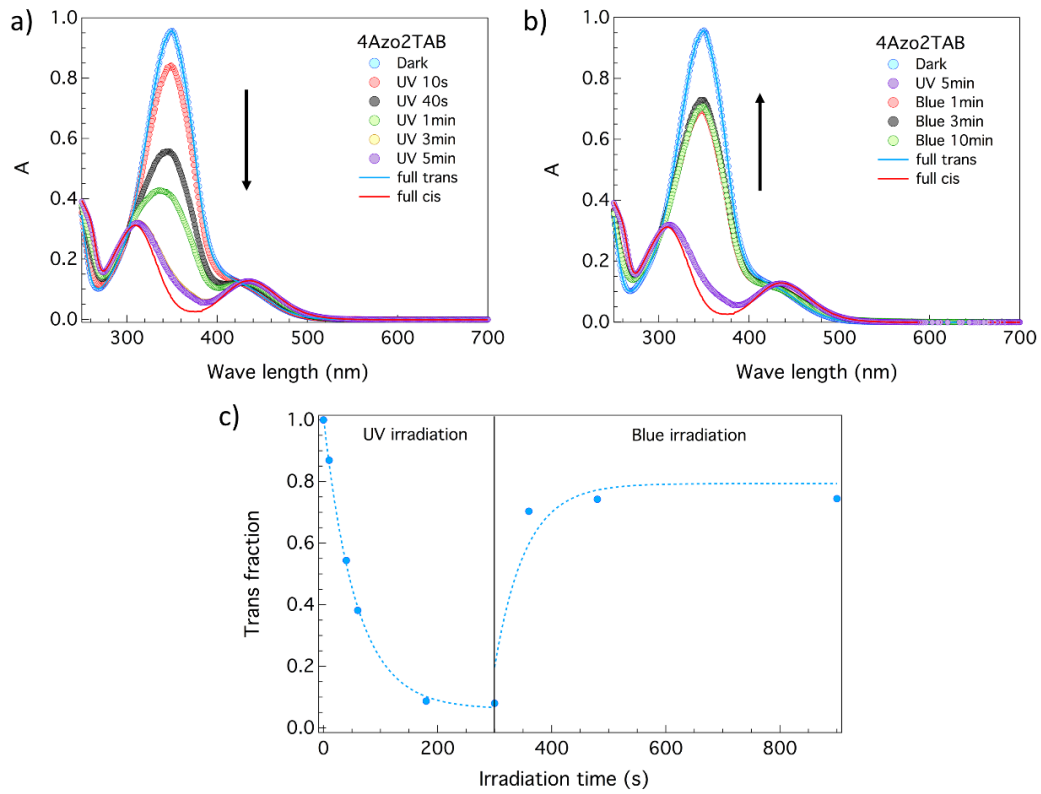


Figure 3 UV-Vis absorption spectra of a 0.08 mM 4Azo2TAB solution a) under UV light, b) under blue light; c) variation of  $x_{trans}$  upon UV and blue light stimulus.

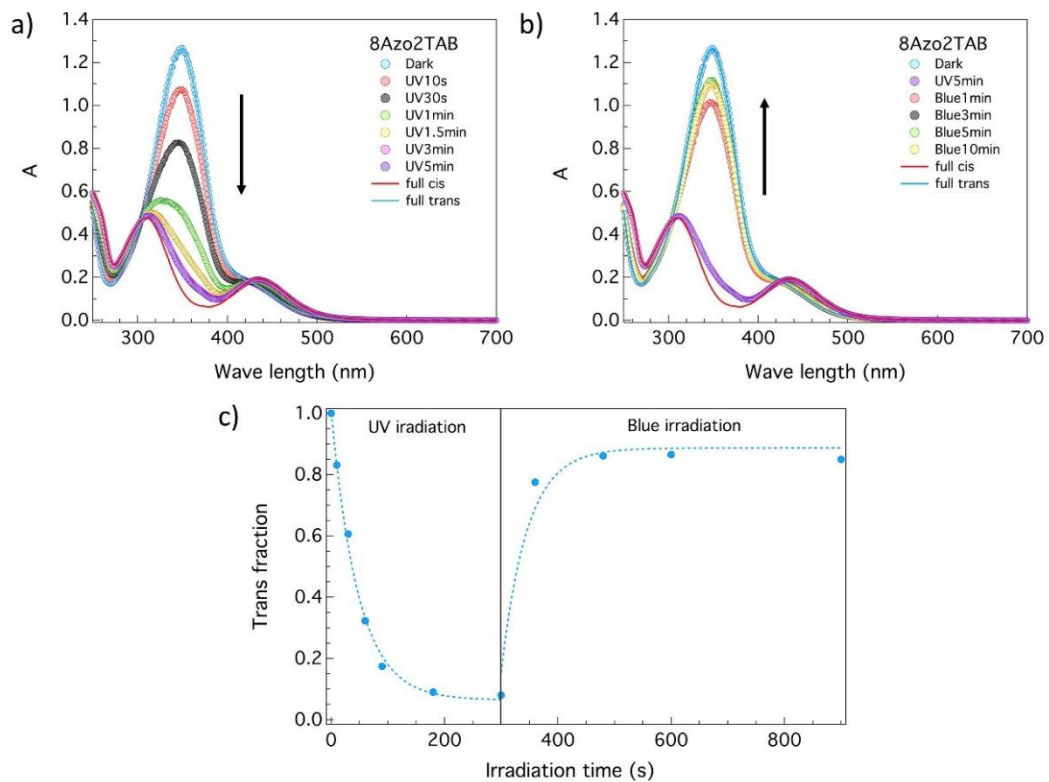


Figure 4 UV-Vis absorption spectra of a 0.08 mM 8Azo2TAB solution a) under UV light, b) under blue light; c) variation of  $x_{trans}$  upon UV and blue light stimulus.

## Reversibility

To characterize the switching efficiency and the reversibility of the process, Azo-surfactant solutions were irradiated alternatively by UV and blue light until they reach their equilibrium state. The *trans* fraction determined from UV-Vis absorption spectroscopy as a function of the irradiation cycles is presented in Figure 5. We find a good reversibility after 3 cycles.

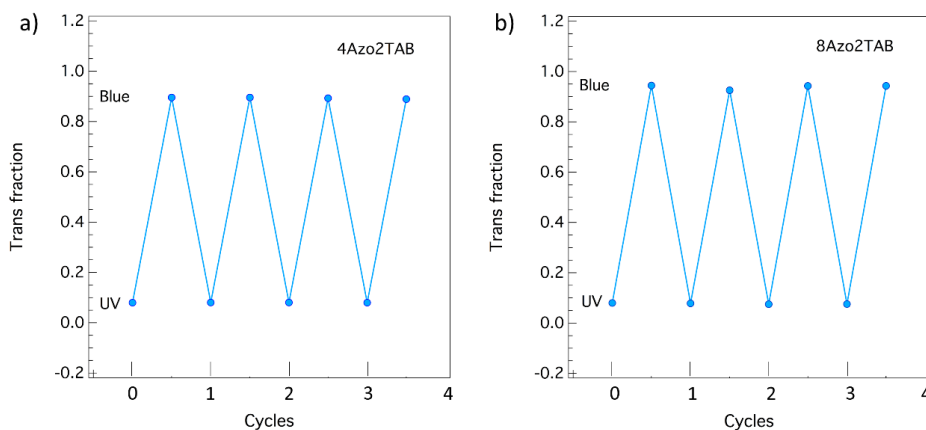


Figure 5 Isomerization reversibility measured with UV-Vis absorption spectroscopy: a) 4Azo2TAB; b) 8Azo2TAB.

## Thermal relaxation

The thermal relaxation has been studied by UV-Vis spectroscopy. The cuvette has been irradiated (UV light) until the photostationary state is reached, and then introduced and left in the spectrometer. UV-Vis spectra have been recorded *in situ* every three hours. Figure 6 shows the trans fraction  $x_{trans}$  as a function of the relaxation time. A characteristic time  $\tau = 85$  h for 4Azo2TAB and 195 h for 8Azo2TAB have been determined.

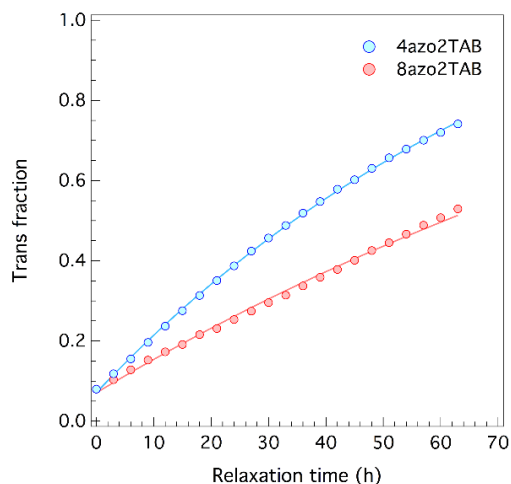


Figure 6 Thermal relaxation of Azo-surfactants by UV-Vis.

### VI.2.2.2 By NMR

The isomerization behaviour of Azo-surfactants has been investigated by  $^1\text{H}$  NMR.

Figure 1 shows the  $^1\text{H}$  NMR spectra of 4Azo2TAB ( $c = 50 \text{ mM} > \text{CMC}$ ) in  $\text{D}_2\text{O}$  (steady state) before and after light stimulus (UV and blue). Pure *trans* isomers (dark state, red curve in Figure 1) show two peaks at 7.62 ppm and at 7.03 ppm corresponding to aromatic protons. The two protons of the  $\text{CH}_2$  group adjacent to the oxygen ( $\text{H}_3$ ) are detected at 4.23 ppm while the signal of the  $\text{CH}_2$  group adjacent to the ammonium head ( $\text{H}_2$ ) is detected at 3.64 ppm. The sharp intense peak located at 3.08 ppm is attributed to the 9 protons of the ammonium head group ( $\text{H}_1$ ). Other peaks at 0.5 – 2.5 ppm correspond to protons of the hydrophobic chain.

After UV irradiation, isomers are mostly in their *cis* form (UV, green curve in Figure 1). Main peaks are slightly shifted with regard to the *trans* form. Furthermore, they appear to be split because of the presence of small fraction of *trans* isomers. For example,  $\text{H}_2$  observed at 3.64 ppm in dark is now divided into two peaks at 3.84 ppm (*trans* form) and 3.73 ppm (*cis* form). When the solution is irradiated with a blue light, most of the *cis* isomers return to the *trans* state. We recover the main intense peaks of the pure *trans* isomer (blue curve in Figure 7). A small fraction of *cis* isomers is however still present (small shifted peaks).

The mole fraction of *trans* isomers at the stationary state can be estimated using the following equation:

$$x_{trans} = \frac{I_{trans}}{I_{trans} + I_{cis}} \quad (2)$$

where  $I_{trans}$  is the integral of the peak  $\text{H}_2$  of the *trans* form and  $I_{cis}$  is the integral of the corresponding *cis* peak.

$x_{trans}$  is close to 15% at the stationary state after UV irradiation and returns to 82% after blue light irradiation. A less concentrated solution of 4Azo2TAB ( $c = 8.6 \text{ mM}$ ) has also been measured. We cannot reach a state of 100% *cis* isomers by UV irradiation even for very low concentration. There are still 8% *trans* isomers left at the stationary state, which is in agreement with the values reported in literature<sup>10,22</sup>. Under blue irradiation, we find the  $x_{trans}$  value (82%). These values are very close to that found in UV-Vis measurements on a very dilute sample.

8Azo2TAB at 50 mM shows very similar variation: 15 % of *trans* isomers are left at the equilibrium state under UV and the ratio of *trans* isomers increases to

82% under blue irradiation.

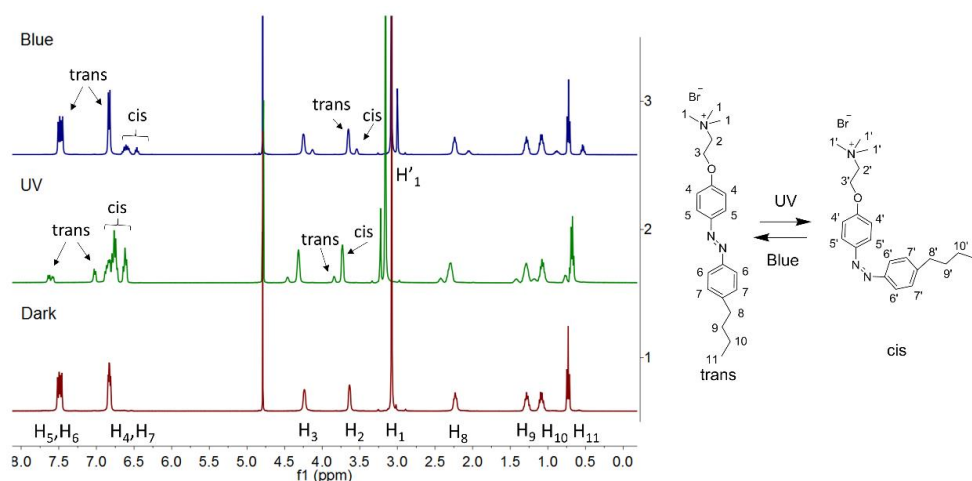


Figure 7  $^1\text{H}$  NMR spectra of 4Azo2TAB 50mM in  $\text{D}_2\text{O}$  before (dark) and after light irradiation (UV, blue).

### VI.2.3 Structural organization study

The structural organization has been carried out by SAXS and SANS for both 4Azo2TAB and 8Azo2TAB.

#### VI.2.3.1 Neutron scattering length density (SLD)

SLD calculation for molecules in solution (such as surfactant in water) needs the determination of their partial molar values. They have been evaluated “theoretically” by the incremental volume method (Table 2).

The SLD can also be obtained by scattering experiments using contrast variation at small enough concentration.

The scattered intensity  $I(q)$  writes  $\Delta\rho^2\phi VP(q)S(q)$ . For very dilute systems, there is no correlation between the particle,  $S(q) = 1$ . For  $q \rightarrow 0, P(q \rightarrow 0) = 1$ ,  $I(q \rightarrow 0) = \Delta\rho^2\phi V = (\rho - \rho_s)^2\phi V$ . The intensity is directly related to the square of the difference in scattering length densities. If we do different experiments at constant  $\phi$  for different  $\text{H}_2\text{O}/\text{D}_2\text{O}$  mixtures, *i.e.*, different SLDs for the solvent, then the plot of  $\sqrt{I(q \rightarrow 0)}$  versus  $\rho_s$  allows to extrapolate the scattering length of the solute  $\rho$ .

By theoretical calculation, the SLD of 4Azo2TA<sup>+</sup> (without Br) is  $1.3 \cdot 10^{10} \text{ cm}^{-2}$  and the SLD of 8Azo2TA<sup>+</sup> is  $1.0 \cdot 10^{10} \text{ cm}^{-2}$ . We have tried to estimate this quantity directly by SANS and contrast variation. Measurements are presented in Figure 8a for different  $\rho_s$  values. Our experimental conditions are not optimized since a correlation peak is observed ( $\approx 0.023 \text{ \AA}^{-1}$ ). We nevertheless selected the intensity

at the peak position. This leads to similar conclusions ( $I \propto (\rho - \rho_s)^2$ ) provided that the form factor and the structure factor are not modified when changing the contrast.

The root of the scattering intensity as a function of SLD solvent (different H<sub>2</sub>O/D<sub>2</sub>O mixtures) is presented in Figure 8b. The red and blue curves correspond to the fit with the theoretical model by considering all the measurements (blue) or only the three highest intensities (red). The SLD of 8Azo2TAB is estimated in between 0.87 and 1.00 10<sup>10</sup> cm<sup>-2</sup>, which is very close to the theoretical expectation (1.00 10<sup>10</sup> cm<sup>-2</sup>). Theoretical values are therefore fairly reliable and will be used in the data analysis. The theoretical molar volume will also be taken for SAXS SLD calculation.

Attention should be paid about the physical meaning of the scattering length density. The estimated SLD for each surfactant is an average value (valid for  $q \rightarrow 0$  where the molecule can be considered as point like). In fact, large difference in SLD can be found when considering different parts of the molecule (Figure 10 a and b). The Azo group has a SLD far from that of alkyl chains. When the surfactants form micellar aggregates, the micelles may have a heterogeneous organization from a SLD point of view: the surfactants may contribute to the scattered intensity at large  $q$  even if the contrast factor  $(\rho - \rho_s)^2$  is equal to 0.

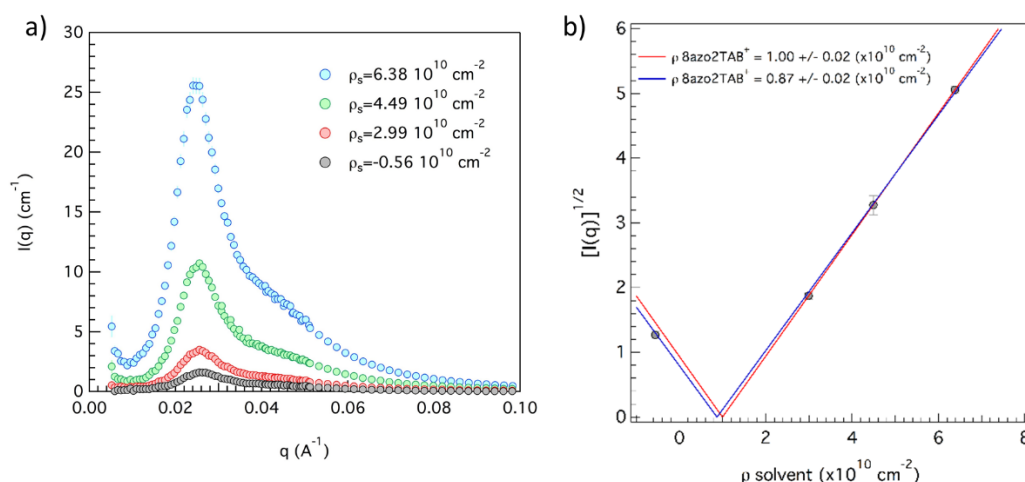


Figure 8 Contrast variation with 8Azo2TAB a) Neutron scattering curves of 8Azo2TAB (50 mM) measured in different H<sub>2</sub>O/D<sub>2</sub>O mixtures; b) Plot of  $\sqrt{I(q \rightarrow 0)}$  versus  $\rho_s$  for 8Azo2TAB.

### VI.2.3.2 Spherical and ellipsoidal models

A schematic representation of a spherical micellar aggregate in water is given in Figure 9. Hydrophobic tails are trapped in the center of the micelle while polar

head-groups are gathered outside. It is usually convenient to model this disordered organization as a mean core-shell structure with a hydrophobic core (of radius  $R_{\text{core}}$ ) made of surfactant tails and a hydrophilic shell (of thickness  $t_{\text{shell}}$ ) composed of polar-heads, hydration water and counterions.

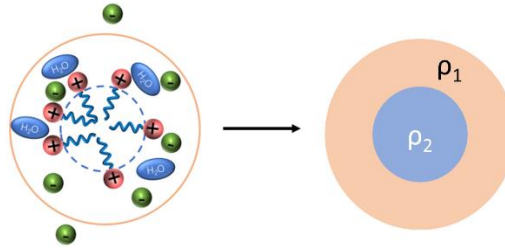


Figure 9 Schematic representation of a micellar aggregate. Left: molecular organization. Right: equivalent core shell structure from a scattering length point of view.

From a small-angle scattering point of view, this system is equivalent to a core-shell organization with two distinct scattering length densities  $\rho_{\text{core}}$  and  $\rho_{\text{shell}}$  in a solvent  $\rho_{\text{solvent}}$ . Since water may penetrate in the aggregate and part of the counterions are released in the solution, but also, due to the presence of non-assembled surfactants in the solution, the volume fraction of the core-shell particles of the model may be slightly different than the real volume fraction of the solute.

$\rho_{\text{core}}$  and  $\rho_{\text{shell}}$  depend on the composition of the micelles and are sensitive to the aggregation number, the counterions condensation (and therefore, the effective charge of the micelle) as well as the hydration process. In absence of water penetration in the hydrophobic core, the aggregation number  $N_{\text{agg}}$  can be estimated from the ratio between the volume of the core  $V_{\text{core}}$  and the volume of the tail  $V_{\text{tail}}$  ( $N_{\text{agg}} = V_{\text{core}}/V_{\text{tail}}$ ).

When increasing the surfactant concentration, the micelles grow and change their shape from spherical (just above the CMC) to ellipsoidal. However, their dimension is constrained in one direction by the size of the surfactant (in its fully extended conformation) to avoid the formation of a “hole” in the middle of the aggregate.

Behind its apparent simplicity, the intensity predicted by a core-shell organization can be very diverse and complex. It mainly depends on the radial SLD profile or more precisely, on the differences  $\rho_{\text{core}} - \rho_{\text{solvent}}$  and  $\rho_{\text{shell}} - \rho_{\text{solvent}}$ . This particularity is at the origin of the differences usually observed in SAXS and SANS experiments on micellar solutions. As an example, if  $\rho_{\text{core}} - \rho_{\text{solvent}} < 0$  and

$\rho_{\text{shell}} = \rho_{\text{solvent}}$  (a common situation in SANS), only the core is visible (the intensity is similar to that of a 'one-shell' model, *i.e.*, a single core). If  $\rho_{\text{core}} - \rho_{\text{solvent}} < 0$  and  $\rho_{\text{shell}} - \rho_{\text{solvent}} > 0$  (a common situation in SAXS), the first oscillation of the form factor can be largely amplified. If  $\rho_{\text{core}}$  tends to  $\rho_{\text{solvent}}$ , only the shell is visible. A very particular situation also occurs when the average scattering length density of the particle matches that of the solvent. The intensity tends to zero for  $q \rightarrow 0$  while the scattering at large  $q$  values is retained (zero average contrast situation).

For conventional cationic surfactants such as CTAB (cetyltrimethylammonium bromide) and DTAB (dodecyltrimethylammonium bromide) in SANS experiments, the excess scattering length density  $\Delta\rho$  between C<sub>12</sub> alkyl chain and D<sub>2</sub>O is  $-6.77 \cdot 10^{10} \text{ cm}^{-2}$ . The TMA<sup>+</sup> head have a similar  $\Delta\rho$  ( $-6.82 \cdot 10^{10} \text{ cm}^{-2}$ ). Counterions close to the micelle surface are diluted with water. Their SLDs are not large enough to contribute to the intensity. As a result, the one-shell model (ellipsoid, homogeneous particle) is appropriate to analyze the data<sup>11</sup>. The one-shell ellipsoid model has also been applied to different Azo-surfactants<sup>1,2,12</sup>.

Nevertheless, in contrast to CTAB and DTAB, the Azo-surfactants contain an azobenzene group, whose SLD is quite different from that of alkyl chains (Table 2).

	$\rho_x$ ( $10^{+10} \text{ cm}^{-2}$ )	$\rho_N$ ( $10^{+10} \text{ cm}^{-2}$ )
H <sub>2</sub> O	9.4	-0.56
D <sub>2</sub> O	9.4	6.38
C <sub>4</sub> H <sub>9</sub>	6.89	-0.52
C <sub>8</sub> H <sub>17</sub>	7.56	-0.43
Azo	15.06	3.90
oxygen	24.79	6.38
TMA <sup>+</sup>	9.40	-0.44
C <sub>2</sub> H <sub>4</sub> spacer	8.33	-0.31
4Azo2TA <sup>+</sup>	10.97	1.29
8Azo2TA <sup>+</sup>	10.49	1.00

Table 2 SLD for SAXS and for SANS for solvents, surfactants and molecular constituents.



complex due to the large variation of the SLD along the molecule, and therefore, along the radial direction in the aggregates (Figure 10 c and d). The core-shell structure is certainly a crude approximation, but it allows to get the main geometrical features of the assemblies and to catch the morphological transition under UV irradiation.

#### VI.2.3.3 SANS results

SANS profiles for Azo-surfactants in D<sub>2</sub>O are displayed in Figure 11. They have been measured at 50 mM, *i.e.*, at a much higher concentration than the CMC of the surfactants (in between 0.29 to 8.2 mM). The scattered intensity is characteristic of micellar solutions. In between 0.03 and 0.05 Å<sup>-1</sup>, we find a broad peak reflecting the correlations between charged particles. Its position  $q^*$  is directly related to the average distance between the micelles ( $d = 2\pi/q^*$ ).

At higher  $q$  values (above 0.2 Å<sup>-1</sup>), a shoulder is roughly visible. It is the signature of the form factor  $P(q)$  of the particles. The absence of well-defined characteristic oscillations may result from a polydisperse population but also, from well-defined anisotropic objects (such as ellipsoidal particles).

Under UV exposure, the position of the maximum is displaced to higher  $q$  values while the global intensity is reduced. The differences reflect large structural modifications under irradiation. If we omit the variation of the CMC (that also changes the particle concentration in the solution), the average distance between particles under UV is reduced: they are more abundant and therefore, smaller (their number of aggregations is reduced).

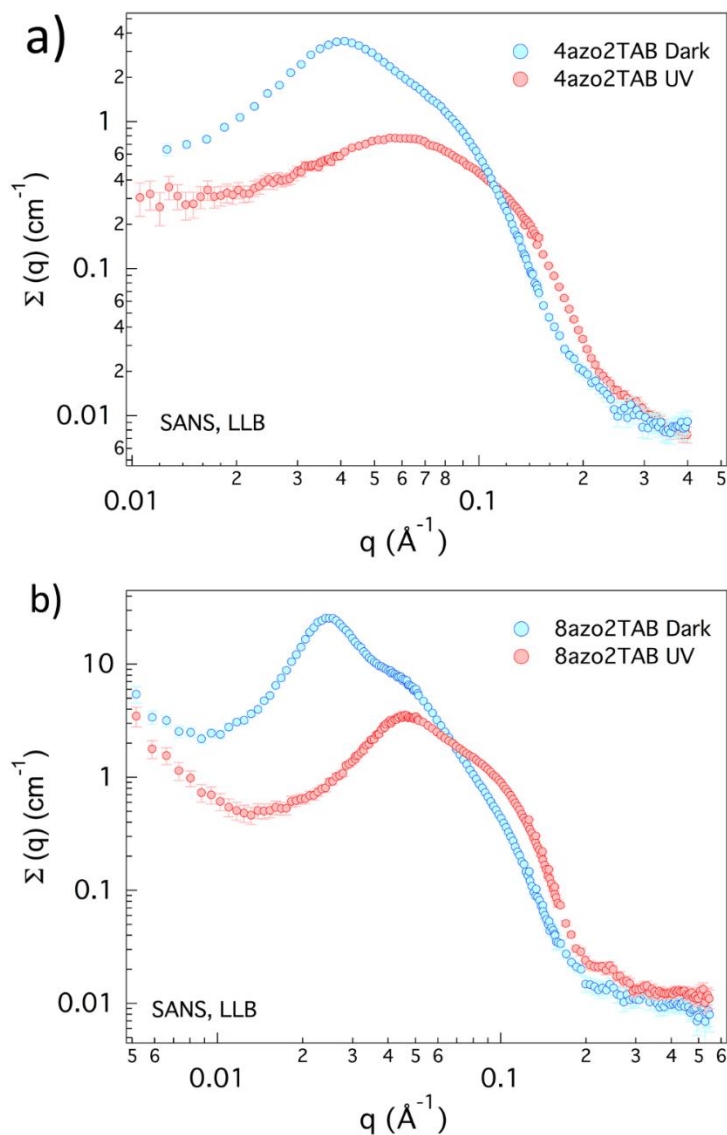


Figure 11 SANS profiles of 50 mM 4Azo2TAB and 50 mM 8Azo2TAB solutions.

We analyzed the data with different geometrical models, from spherical to ellipsoidal. All the form factors  $P(q)$  were combined to a structure factor  $S(q)$  developed for charged colloids in a repulsive screened Coulomb potential<sup>13,14</sup>. This structure factor has been widely utilized with charged micelles and accurately reproduces the interference function between particles. No general “scale factor” was introduced in the model to account for error in the absolute scale determination. Thus, the absolute intensities in SANS and SAXS experiments are supposed to be accurate.

The shape of the correlation peak depends on the electrostatic repulsions and varies with the effective charge of the objects (strength of the repulsive

interactions) and the ionic strength of the solution (screening effect). Its position is related to the particle concentration or to their volume fraction  $\phi$ . Due to the water penetration in the micelles or the counterion release, but also, to the presence of free surfactants above the CMC, the volume fraction of the model is close - but different - than the real volume fraction of the solute in the solution. In order to properly reproduce the correlation peak, the volume fraction  $\phi$  was therefore fitted during the analysis (and compared to the experimental one).

For similar reasons, the salt concentration in the solution and the charge of the micelles were also fitted. The first should be close to the CMC. The second should lead to a dissociation rate of the bromide ions of the order of 15 - 30% as found for similar polar heads (dissociation rate = charge/ $N_{agg}$ ). In any case, the final values of these parameters do not change the size and shape of the particles and are of little relevance in the present work.

For homogenous systems (one-shell model), the SLD of the particle directly impacts the global intensity ( $I(q) \sim \Delta\rho^2$ ). The SLD value was first set to that of the surfactant (in its ionic form) and kept fixed during the refinement. This parameter was then relaxed and fitted in a second time. The difference between the fitted SLD and that of the surfactants may have a physical origin (indicating for instance a water penetration in the micelle), but could also come from experimental problems such as a wrong estimation of the theoretical molar volumes (leading to an erroneous surfactant SLD) or difficulties with the absolute scale determination procedure.

In many micellar systems, the shape of the aggregates is changing with the concentration, from spherical just above the CMC, to anisotropic (such as ellipsoidal particles). We therefore analyzed the data with different simple globular models.

The simplest spherical model associated to a large polydispersity lead to unphysical results and was definitively discarded (large standard deviation and very small SLD). Other models for monodispersed ellipsoids (oblate/prolate) with a single shell or a core-shell scattering length density profiles were tested and were quite successful. Only the best results obtained with one-shell and core-shell monodisperse oblate ellipsoids will be presented in this section.

Fits are shown in Figure 12 and Figure 13 for 4Azo2TAB and 8Azo2TAB using the one-shell and the core-shell models. Fits are rather satisfying.

Below  $0.15 \text{ \AA}^{-1}$ , almost no difference can be observed in the fit quality with

these two models.

For 4Azo2TAB micelles, a slight difference appears in the high  $q$  region around  $0.15 - 0.4 \text{ \AA}^{-1}$  (Figure 12 a). The deviations are even more pronounced for 8Azo2TAB micelles (Figure 13 a).

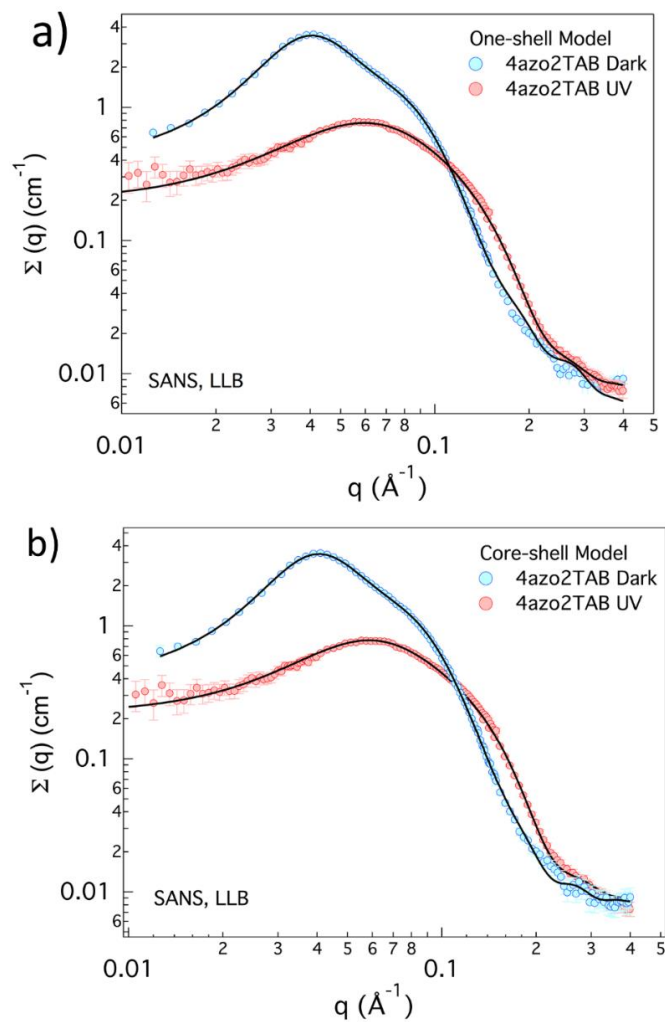


Figure 12 SANS data of 50 mM 4Azo2TAB solution and fit with: a) one-shell model; b) core-shell model.

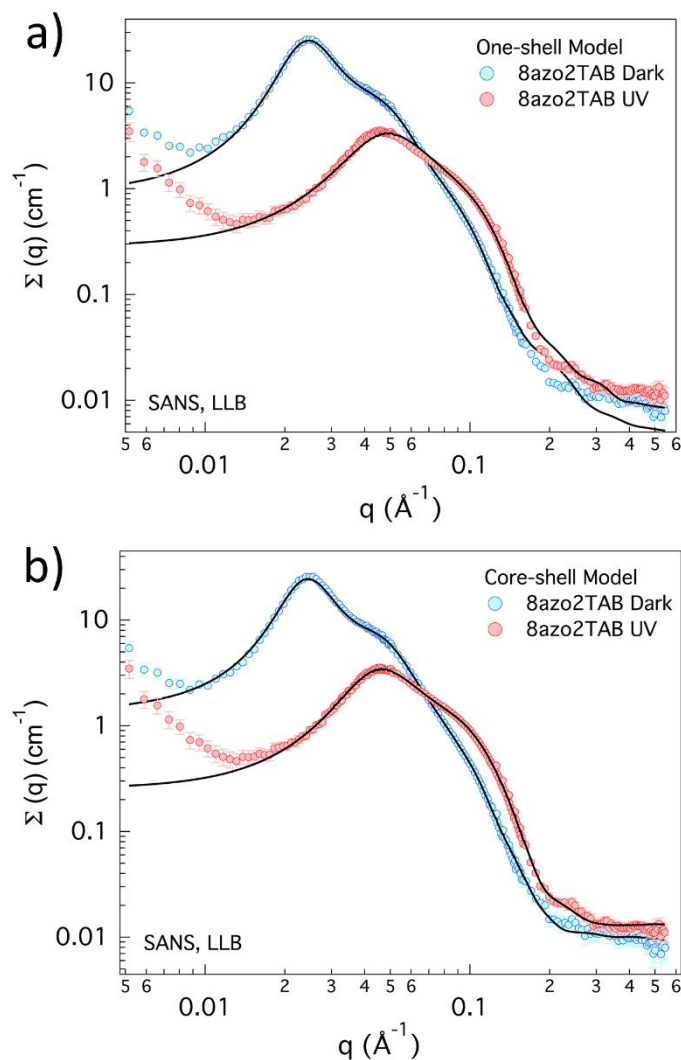


Figure 13 SANS data of 50 mM 8Azo2TAB solutions and fit with: a) one-shell model; b) core-shell model.

In order to improve the fit quality at high  $q$ , data were also fitted with a core-shell. (Figure 12 b and Figure 13 b). It is not common to use a core-shell model for classical micelles with neutron scattering. Most of the time, the different chemical groups of the surfactants have very similar SLD (without specific labelling). At the same time, counterions are often 'diluted' by the solvent and are not visible.

One-shell and core-shell models inevitably lead to the same results. In the present situation, we believe that the core of the micelle is preferably composed of alkyl group, while the rest of volume (shell) mixes all the other chemical groups. Due to the large difference between the SLD of the azo (and the oxygen) in the shell and the alkyl chain (in the core), we expect an average non uniform radius

SLD profile that can be better modeled by a core-shell description. In any case, these effects are certainly not very large since the volume of the core is probably much smaller than that of the shell. During the fitting procedure, we imposed the SLD of the core to that of the C<sub>4</sub>H<sub>9</sub> or C<sub>8</sub>H<sub>17</sub>. This model improves the quality of the fit in the large  $q$  range specially for 8Azo2TAB.

The fit parameters are summarized in Table 3 (one-shell model) and Table 4 (core-shell model).

One-shell Model	4Azo2TAB		8Azo2TAB	
	Dark	UV	Dark	UV
Minor shell radius (Å)	19	14	24	18
Major shell radius (Å)	35	23	66	31
$\phi$	0.017	0.020	0.025	0.025
$\rho$ ( $10^{10}$ cm <sup>-2</sup> )	1.45	2.24	1.54	1.53
Charge number	27	8	54	18
Monovalent sel (mol L <sup>-1</sup> )	0.0021	0.0021	0.00013	2.1 $10^{-6}$
$N_{agg}$	202	54	682	113

Table 3 SANS fit parameters with a one-shell ellipsoid model.

Core-shell Model (oblate)	4Azo2TAB		8Azo2TAB	
	Dark	UV	Dark	UV
Minor shell radius (Å)	20	17	28	22
Major shell radius (Å)	35	23	66	31
Minor core radius (Å)	5	5	11	13
Major core radius (Å)	19	18	57	22
$\phi$	0.019	0.020	0.025	0.025
$\rho_{shell}$ ( $10^{10}$ cm <sup>-2</sup> )	1.93	3.41	3.02	3.42
$\rho_{core}$ ( $10^{10}$ cm <sup>-2</sup> )	-0.55	-0.55	-0.43	-0.43
Charge	27	10	110	23
Monovalent sel (mol L <sup>-1</sup> )	0.0020	0.0043	0.0018	0.00037
$N_{agg}$	212	66	796	138

Table 4 SANS fit parameters with a core-shell ellipsoid model.

*Trans*-4Azo2TAB forms oblate ellipsoidal aggregates with a long radius ( $R_a$ ) of 35 Å and a short radius ( $R_b$ ) of 19 - 20 Å. *Trans*-8Azo2TAB with a longer alkyl tail, self-assembles in larger aggregates ( $R_a = 66$  Å,  $R_b = 24 - 28$  Å). The modification of the model (from a one-shell to a core-shell description) improves the quality of the fit at large  $q$  values without changing the external size of the

micelle (major shell and minor shell). The minor core radius is close to the length of the alkyl chain, which seems to validate our core-shell approach. The minor shells (19 - 20 Å for 4Azo2TAB and 24 - 28 Å for 8Azo2TAB) are shorter than the fully extended surfactant lengths if we consider the molecules as a whole (24.7 Å and 29.2 Å) and close to their lengths if we remove the polar head (20.7 Å and 25.2 Å) as presented in Figure 14.

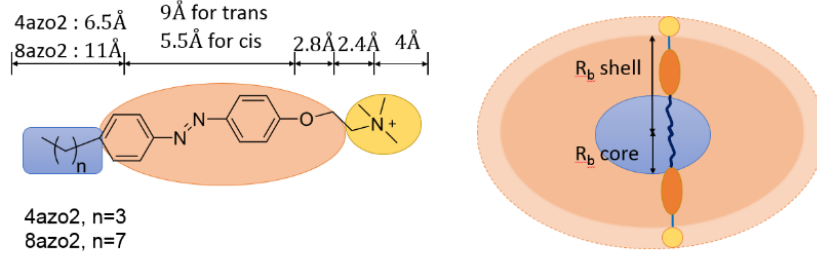


Figure 14 Azo-surfactants structure and model of their micelles (fully extended chain).

It is not evident to decide whether the polar head is visible or not with neutron. Very often it is supposed that the ionic heads are mixed with solvent molecules reducing their contrast and making them 'invisible'. For trimethyl ammonium head groups, their hydrophobicity prevents water penetration. Since their contrast in D<sub>2</sub>O is important, they certainly contribute to the scattered intensity.<sup>15</sup> Other studies report high penetration of water inside Azo-surfactant aggregates. This argument is motivated by the variation of scattering length density of the fitted particle.<sup>1</sup> In the present work, we will consider that the ammonium contributes to the scattering and that water may penetrate in the micelles. The aggregation number can be determined from the volume of the dry aggregate (*i.e.*, without water) and the surfactant (in its ionic form).

$$N_{agg} = \frac{V_{dry\ micelle}}{V_{surf}} = \frac{V_{micelle}(1 - \phi_{water})}{V_{surf}} \quad (3)$$

$\phi_{water}$  is the water content that can be extracted from the fitted SLD of the particle and the theoretical SLD of the surfactant :

$$\rho_{particle} = \phi_{water}\rho_{water} + (1 - \phi_{water})\rho_{surf} \quad (4)$$

$$\Rightarrow \phi_{water} = \frac{\rho_{particle} - \rho_{surf}}{\rho_{water} - \rho_{surf}} \quad (5)$$

Under UV irradiation, an oblate ellipsoid model is still adapted. The effective length of Azo-surfactants decreases due to the *trans* to *cis* isomerization. The

major radius of the shell and the core decrease significantly as well. The minor radius of the core, which is related to the length of alkyl tail remain unchanged. Consequently, the volume of the micelle as well as the aggregation number  $N_{agg}$  falls by 69% for 4Azo2TAB micelles and 83% for 8Azo2TAB micelles.

Structural analysis of 4Azo2TAB and 8Azo2TAB have already been studied in the literature in dark and under UV irradiation. The experimental conditions such as the concentration and the light source are however not always the same. Our SANS study was carried out in a larger  $q$  range, thus leading to a better spatial resolution. The geometrical description of *trans*-4Azo2TAB in the works of Akamatsu *et al.*<sup>2</sup> cannot be directly compared to our work since they used a prolate model which is definitively not adapted to explain our data in large  $q$  range. If we use their model in a limited  $q$  range ( $q < 0.15 \text{ \AA}^{-1}$ ), their values are close to our measurements. Under UV irradiation, they found that the long radius of micelles decreased from 38 Å to 32 Å (based on a prolate model). We observed a more significant change under UV irradiation, which is probably due to the different illumination setup. 8Azo2TAB in 5 mM was modeled by a prolate ellipsoid micelles by Blayo *et al.*<sup>1</sup> with  $R_a = 52 \text{ \AA}$  and  $R_b = 20 \text{ \AA}$  in the dark state and as spherical micelles with a radius of 24 Å under UV irradiation; for 8Azo2TAB in 20 mM the micellar size becomes a little larger with  $R_a = 53 \text{ \AA}$  and  $R_b = 24 \text{ \AA}$  in the dark state and  $R = 26 \text{ \AA}$  under UV irradiation.

We found a larger micellar size and a distinct oblate shape. The difference in size may be related to our higher concentration. Indeed, in conventional cationic surfactant systems (*i.e.*, CTAB and DTAB), the equatorial radius of micellar aggregates increases with increasing surfactants concentrations<sup>11</sup>.

#### VI.2.3.4 SAXS results

The structure of micellar aggregates has been investigated by SAXS (Figure 15). Fit results are given in Table 5. SAXS curves are almost similar to SANS data. They present a clear oscillation at high  $q$ , which is characteristic of micellar aggregates, and a broad maximum at low  $q$  related to the electrostatic repulsion between aggregates. The main difference is certainly the high intensity of the maximum around  $0.2 \text{ \AA}^{-1}$ . This is the direct consequence of a very particular radial SLD profile. Upon UV light exposure, the curves decrease significantly in intensity and both the correlation peak and the oscillation of the form factor are shifted to the higher  $q$  region suggesting a decrease of the particle size and therefore of

their aggregation number.

To reveal the structure of the micelles, SAXS curves were fitted with the same oblate ellipsoid core-shell model (except the *trans*-8Azo2TAB curve as explained later). It must be noted that the one-shell model doesn't work and can't reproduce the large intensity observed around  $0.2 \text{ \AA}^{-1}$ . Only a core-shell structure in which the core contains alkyl chains ( $\rho_{water} > \rho_{core} \approx \rho_{alkyl}$ , fixed parameter) and a shell with  $\rho_{shell} > \rho_{water}$  (fitted parameter) can reproduce the data. In this approach, the shell contains the rest of the surfactant molecule, but also a layer of condensed counterions (that certainly explains slight differences in the shell radius). The aggregation number  $N_{agg}$  is calculated in the same way as for SANS data. But it is only an estimated value due to the presence of an additional layer of condensed counterions. The geometrical parameters of *trans*-4Azo2TAB micelles are consistent with that found by SANS.

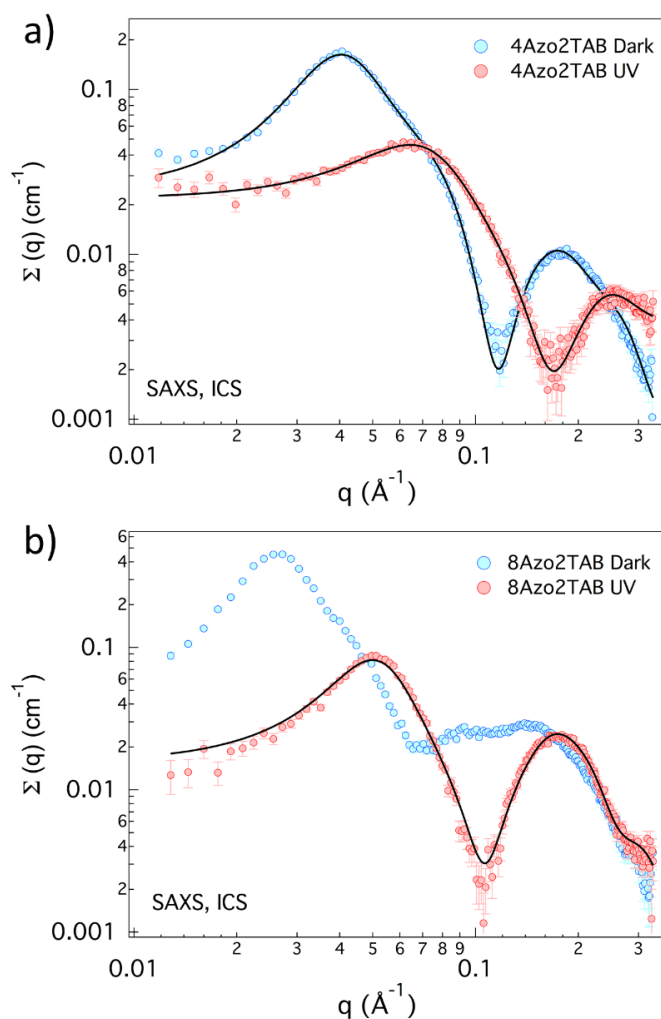


Figure 15 SAXS curves and fits. a) 4Azo2TAB 50 mM; b) 8Azo2TAB 50 mM. Solution in dark could not be fitted due a scattering pollution around  $0.1 \text{ \AA}^{-1}$ .

Parameters	4Azo2TAB		8Azo2TAB
	Dark	UV	UV
Minor shell radius (Å)	24	12	19
Major shell radius (Å)	35	22	30
Minor core radius (Å)	5	7	13
Major core radius (Å)	24	12	20
$\phi$	0.020	0.015	0.025
$\rho_{shell}$ ( $10^{10}$ cm <sup>-2</sup> )	10.64	11.56	11.38
$\rho_{core}$ ( $10^{10}$ cm <sup>-2</sup> )	6.89	6.89	7.56
Charge number	47	17	258
Monovalent sel (mol L <sup>-1</sup> )	0.0045	0.015	0.0078
$N_{agg}$	262	52	124

Table 5 SAXS fit parameters.

The differences in the radius between SANS and SAXS under UV can be explained by the different irradiation setup used in two techniques. In SAXS experiments, the sample is irradiated directly by two UV LEDs fixed above and below the capillary (2 mm apart) and measured in absence of external light (in the sample chamber). SANS used a multi-LED setup (ten LEDs arranged circularly, 1 cm apart on one side of the sample). Besides, SANS experiments were performed in ambient luminosity. Consequently, the photostationary state in SAXS experiments contains more *cis* isomers, leading to larger structural modifications.

The *trans*-8Azo2TAB curve could not be fitted with the core-shell model due to the presence of heterogeneous aggregates in the solution (at the origin of a “strange” scattering contribution around  $0.1 \text{ \AA}^{-1}$ ). SAXS measurement have been performed at a temperature very close to the Krafft temperature of 8Azo2TAB (the “equivalent” CTAB has a Krafft temperature around  $20 - 25 \text{ }^\circ\text{C}^{16}$ ).

#### VI.2.4 Conclusion

As a conclusion, 4Azo2TAB and 8azo2TAB self-assemble in oblate ellipsoidal aggregates above the CMC. SAXS and SANS data could be fitted with a core-shell model in which the core is composed of hydrophobic alkyl tail, and the shell, which is partially hydrophobic, contains the rest of the molecule. With a longer alkyl tail, the volume of *trans*-8azo2TAB aggregates is 4.5 times larger than that of *trans*-4azo2TAB aggregates. Under UV irradiation, 8Azo2TAB and 4Azo2TAB micelles undergo an important structural transition. Their shapes are still ellipsoidal, but their volumes are reduced by a fraction from 3 to 6.

## VI.3 Azo-surfactant/Polyelectrolyte complexes

Mixtures of Azo-surfactants and oppositely charged PEs have been investigated. Poly(styrene sulfonate) (PSS), a well-known polymer has been chosen as a model PE for this study. Deuterated and hydrogenated PSS (chemical charge fraction  $f = 1$ ) have been kindly synthesized by Jean-Philippe Lamps at ICS. The synthesis of PSS is presented in Appendix c).

### VI.3.1 Azo-Surfactant/Polyelectrolyte ratios and concentrations

#### VI.3.1.1 Phase diagram and reference system

The choice of the reference Azo-surfactant/PSS system has been guided by SAXS measurements on a series of different samples (with different molar ratios, concentrations) in dark and under UV irradiation. The equilibrium state is not reached instantaneously and requires the diffusion of 'complexes' (containing the azo) in solution. The scattered intensity was then measured at different times until it does no longer vary. This final state defines the structural 'equilibrium' state.

The phase diagram of Azo-surfactant/PE mixtures in aqueous solutions depends on several parameters, such as the Azo-surfactant/PE ratio, their concentrations, but also intrinsic properties of the PE (molecular weight, stiffness, charge) and of the surfactant (packing parameters).

Different molar ratios  $r$  of Azo-surfactant/PSS from 0.15 to 1.0 have been tested. Mixtures of 4Azo2TAB and PSS are soluble for ratios smaller than 0.5 (Table 6). 8Azo2TAB and PSS gives homogeneous solution until  $r = 0.6$  (Table 7). Both mixtures precipitate when approaching the charge stoichiometry (charge neutralization  $r = 1$ ).

4Azo2TAB (mM)	PSS (mM)	$r$	solubility
15	100	0.15	yes
30	100	0.3	yes
25	50	0.5	yes
50	100	0.5	yes
150	300	0.5	yes
60	100	0.6	turbid
80	80	0.8	precipitate
100	100	1.0	precipitate

Table 6 Phase diagram of 4Azo2TAB/PSS mixtures,  $r = [4Azo2TAB]/[PSS]$ , [PSS] is the monomer concentration of PSS.

8Azo2TAB (mM)	PSS (mM)	$r$	solubility
15	100	0.15	yes
30	100	0.3	yes
50	100	0.5	yes
60	100	0.6	yes
80	80	0.8	turbid
100	100	1.0	precipitate

Table 7 Phase diagram of 8Azo2TAB/PSS mixtures,  $r = [8\text{Azo2TAB}]/[\text{PSS}]$ ,  $[\text{PSS}]$  is the monomer concentration of PSS.

Figure 16 shows the SAXS profiles for solutions of different composition (constant PSS concentration 100 mM,  $0 < r < 0.8$ ). When the surfactant content is increased, we note the gradual appearance of a characteristic oscillation at around  $0.2 \text{ \AA}^{-1}$ . It is related to the presence of micellar aggregates on the system.

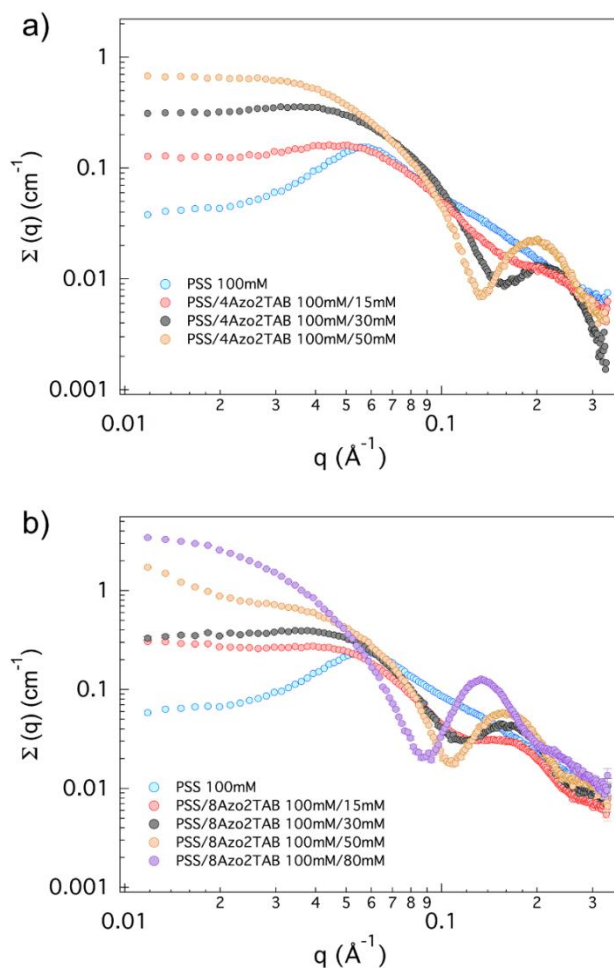


Figure 16 SAXS plots of a) 4Azo2TAB/PSS mixtures for molar ratios  $r = 0.15 - 0.5$  (dark state); b) 8Azo2TAB/PSS mixtures for molar ratios  $r = 0.15 - 0.8$  (dark state). The PSS concentration is constant  $[\text{PSS}] = 100 \text{ mM}$ .

Figure 17 shows SAXS measurements of 4Azo2TAB/PSS in dark and under UV for  $r = 0.3$  and  $0.5$ . The displacement of the oscillation ( $0.2 \text{ \AA}^{-1}$ ) to highest  $q$  values is the key effect observed under UV. It indicates a modification of the form factor of the aggregates under irradiation. The large oscillation around  $0.2 \text{ \AA}^{-1}$  is more intense for  $r = 0.5$  and shows large modifications with UV. This composition was therefore chosen as the reference ratio for this study.

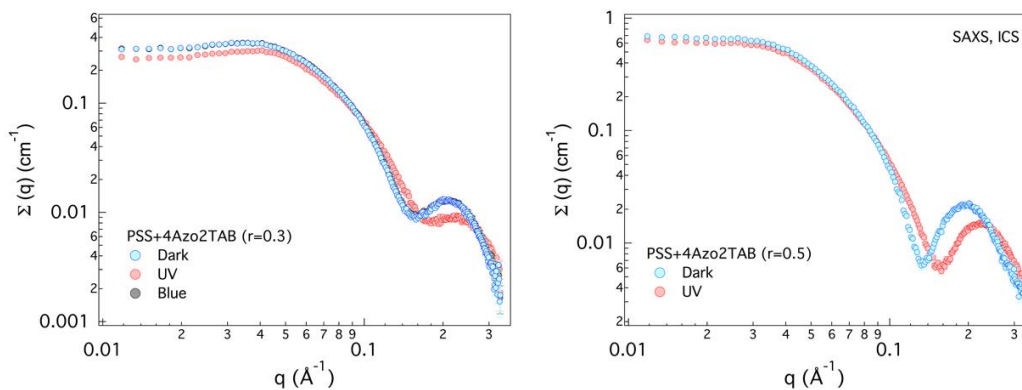


Figure 17 SAXS plots of 4Azo2TAB/PSS mixtures: a)  $r = 0.3$ ; b)  $r = 0.5$  in dark and under UV irradiation. The PSS concentration is constant  $[\text{PSS}] = 100 \text{ mM}$ .

A very important point concerns the nature of the regime (dilute/semi-dilute) of the solution. In absence of surfactant, PSS is always in the semi-dilute regime (long chains). As soon as the complexation with surfactants occurs, the regime can change rapidly since the effective size of the polyions can be dramatically reduced.

### VI.3.1.2 Influence of the concentration

Different concentrations of the mixtures at a constant ratio  $r = 0.5$  have been investigated by SAXS in the dark state and under UV exposure for 4Azo2TAB/PSS. The scattering curves are presented in Figure 18 after normalization to the concentration.

Without going into the details of the structural organization, we recall that the scattered intensity contains both intramolecular (or intra-particle) and intermolecular (inter-particle) contributions. In the colloidal approach,  $I(q)$  is written as the product of the form factor  $P(q)$  by the structure factor  $S(q)$ .

Curves in dark (Figure 18 a) are superposed above  $0.05 \text{ \AA}^{-1}$ , which means that the local structure doesn't vary with the concentration. Only the form factor is observed in this  $q$  range. This definitively validates our assumption that the

oscillation around  $0.2 \text{ \AA}^{-1}$  is a characteristic of the form factor of the aggregates.

On the contrary, curves measured under UV (Figure 18 b) do not completely overlap. For the mixtures denoted C (4Azo2TAB/PSS 50 mM/100 mM) and C/2 (25 mM/50 mM) measurements are superposed: the final states at the local level are identical. This is no longer the case for 3C (150 mM/300 mM). The oscillation is less shifted to higher  $q$ , indicating a larger *trans* molar fraction at the stationary state. This effect is probably a consequence of the higher viscosity of the system that slows down the diffusion of the particles and the homogenization of the solution.

In conclusion, the mixture of **Azo-surfactant/PSS 50 mM/100 mM ( $r = 0.5$ )** is the best compromise (larger scattering, larger modifications under UV, acceptable absorption) and will be considered as our **reference system**.

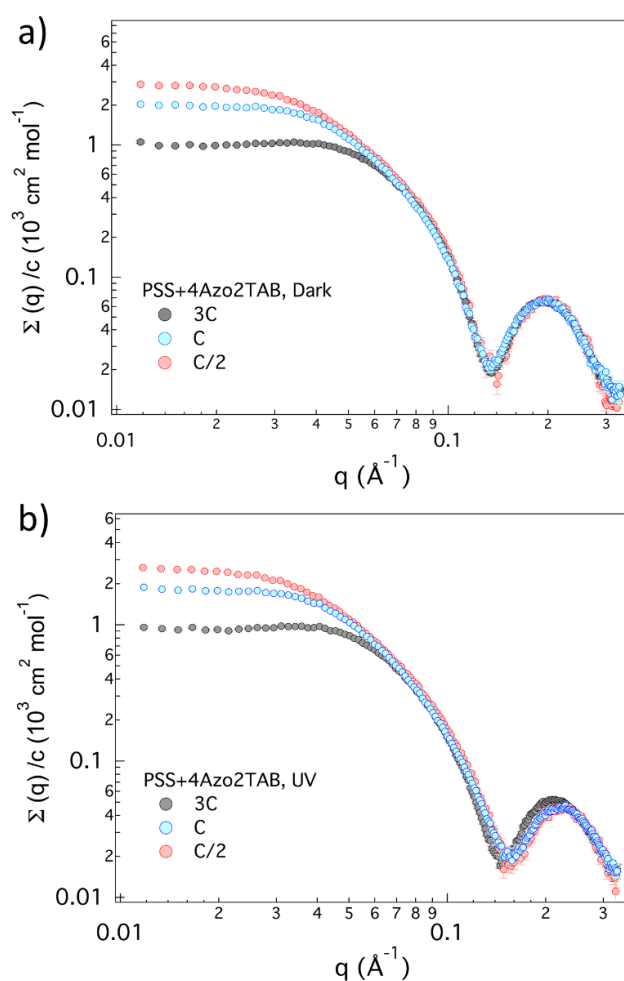


Figure 18 SAXS plots of 4Azo2TAB/PSS mixtures,  $r = 0.5$  : a) curves normalized to concentration in the dark state; b) curves normalized to concentration under UV irradiation. C corresponds to the global concentration PSS 100 mM and 4Azo2TAB 50mM.

### VI.3.1.3 Diameter of the capillary

Due to the strong UV absorption of azobenzene, the diameter of the capillary affects the photoconversion. 1 mm and 1.5 mm capillaries were tested under identical UV irradiation conditions (Figure 19). In the dark state, the experimental curves overlap indicating that the diameter of the capillary does not influence the scattering measurements. Under UV, the position of the oscillation for the 1.5 mm capillary is less shifted to higher  $q$ . This indicates that the *trans/cis* transformation is not optimal even after a long equilibrium time. It is therefore better to use a 1 mm diameter capillary for SAXS measurements.

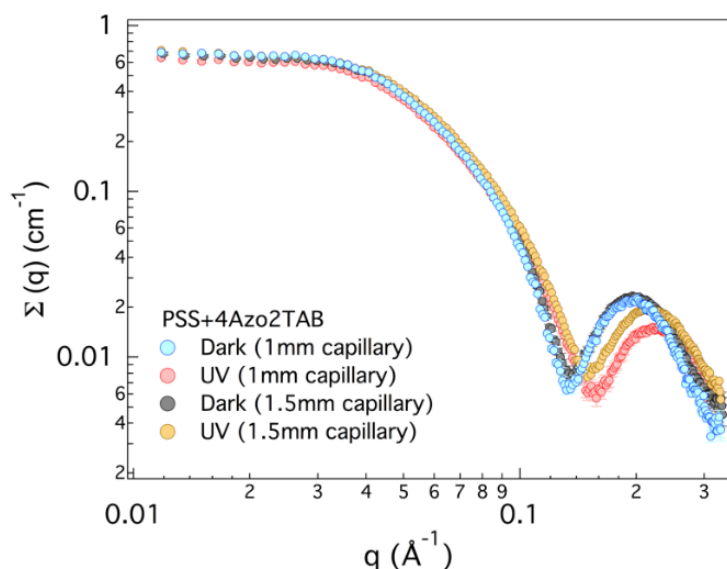


Figure 19 SAXS plots of 4Azo2TAB/PSS mixtures measured in 1mm and 1.5 mm capillaries.

## VI.3.2 Photoisomerization study

### VI.3.2.1 Determination of *trans/cis* ratio

We have done UV-Vis absorption measurements to characterize the *trans/cis* photoisomerization in 4Azo2TAB/PSS solutions. That concerns the determination of the *trans* fraction in the steady state, but also the kinetic of isomerization and the relaxation process. Two types of samples were investigated: very dilute solutions C/1000 (0.05 mM/0.1 mM), and our reference system of concentration C (4Azo2TAB/PSS, 50 mM/100 mM).

The very dilute solution (C/1000) is introduced in a quartz cell of 10 mm thickness, irradiated under UV and stirred several times during the irradiation. We do not really know the structural organization for such small concentration: the critical aggregation concentration (CAC) has not been measured. We can only note that complexes are probably present due to the usual very low CAC found

with PSS. As shown in Figure 20 b, the spectrum is similar to that of pure Azo-surfactant, a maximum peak is present at 347 nm. The photo-stationary state was achieved after about 5 min under UV irradiation.

For the “concentrated” reference system, a mother solution of concentration C was irradiated by UV LED in a 1 mm thickness quartz cuvette. This situation is close to the irradiation setup used for SAXS and SANS measurements. During the irradiation period, a small aliquot of the solution was regularly collected, diluted 1000 times and analyzed immediately. The variation of UV-Vis absorption is presented in Figure 20 a.

The procedure for the evaluation of the *trans* fraction is identical to that described in Chap V.2.1.

Each spectrum was fit on the whole wavelength range assuming a linear combination of pure *trans* and *cis* spectrum. The variation of the *trans* fraction as a function of the relaxation time is presented in Figure 21. For our reference concentration C, the final equilibrium state contains 39% *trans* isomers and is reached after more than 2 h irradiation. For the dilute solution, the final state is attained after only 3 mn and has only 10 % *trans* isomers.

The difference between Figure 20 a and Figure 20 b demonstrates that the concentration is an important factor which directly impacts the efficiency of irradiation and the kinetic of isomerization of the solutions.

Under blue light irradiation, the reverse *cis* to *trans* isomerization occurred leading to a steady state composed of 89 % *trans* and 11 % *cis* isomers for the mixture of concentration C.

Samples of 8Azo2TAB/PSS at very low concentrations (C/1000) behaves in the same way as 4Azo2TAB/PSS. Only 4Azo2TAB/PSS mixture has been measured at concentration C (50 mM/100 mM). We assume that 8Azo2TAB/PSS solutions (C) reaches a similar *trans/cis* ratio at the stationary state.

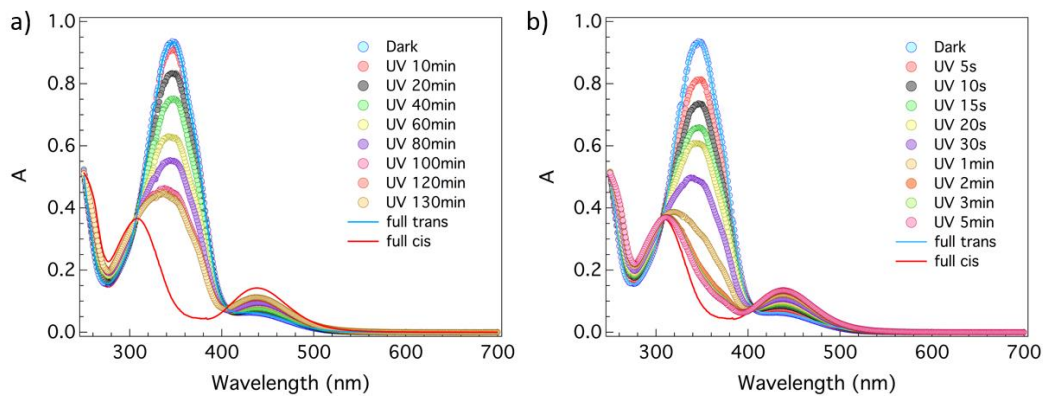


Figure 20 Variation of the UV-Vis absorbance of 4Azo2TAB/PSS mixtures for different UV irradiation times for a) the concentrated solution 50 mM/100 mM and b) the dilute solution 0.05 mM/0.1 mM.

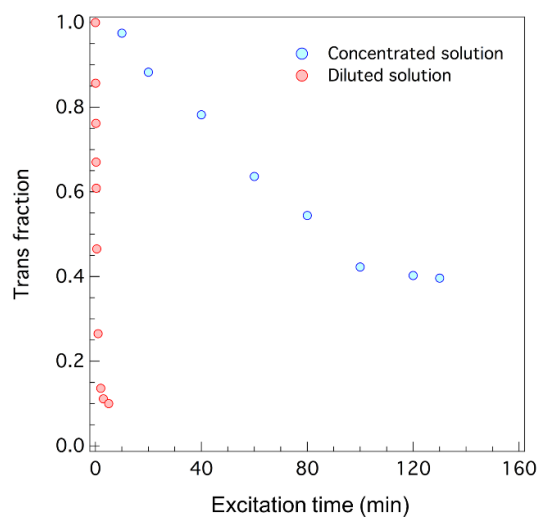


Figure 21 Variation of *trans* fraction for the concentrated (4Azo2TAB/PSS 50 mM/100 mM, blue curve) and diluted solutions (4Azo2TAB/PSS 0.05 mM/0.1 mM, red curve) as a function of the irradiation time.

### VI.3.2.2 Reversibility

Several UV  $\leftrightarrow$  blue irradiation cycles have been carried out for Azo-surfactant/PSS at very low concentration. Both the 4Azo2TAB/PSS and 8Azo2TAB/PSS mixtures show a good reversibility (Figure 22).

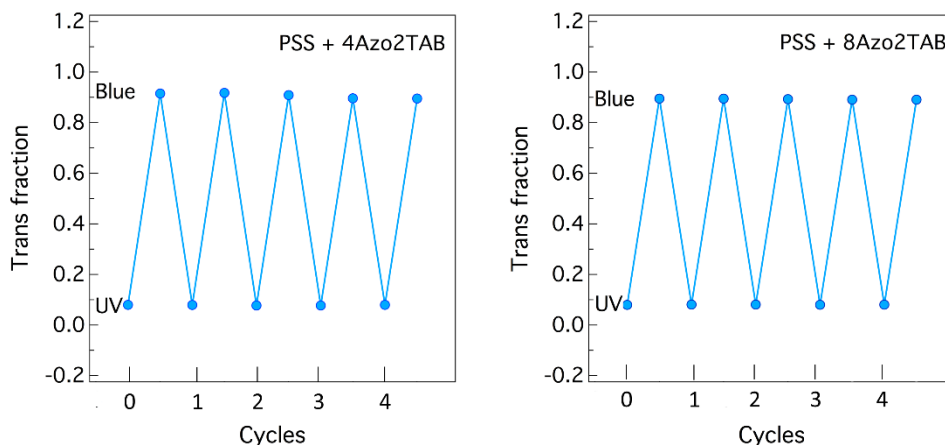


Figure 22 Reversibility of Azo-surfactant/PSS complexes measured by UV-Vis spectroscopy. 4Azo2TAB/PSS 0.05 mM/ 0.1 mM (left) and 8Azo2TAB/PSS 0.05 mM/ 0.1 mM (right).

### VI.3.2.3 Thermal relaxation

The thermal relaxation of 4Azo2TAB/PSS and 8Azo2TAB/PSS mixtures (C/1000) have been measured by UV-Vis spectroscopy. The two systems show similar behaviour (Figure 23) and characteristic times  $\tau$  of 20.8 h and of 24.2 h respectively. These measurements have been performed on dilute solutions only. The characteristic times of pure Azo-surfactants are  $\tau_{4Azo2TAB} = 85$  h and  $\tau_{8Azo2TAB} = 195$  h, which means the addition of PSS affects strongly the relaxation process.

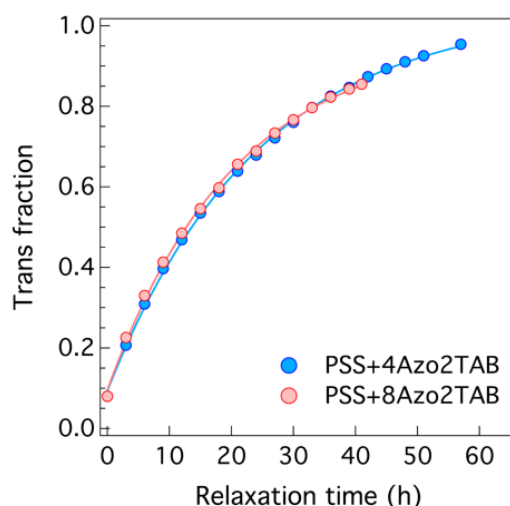


Figure 23 Thermal relaxation of Azo-surfactant/PSS (0.05 mM/ 0.1 mM) by UV-Vis measurements.

### VI.3.3 Structural study by NMR

NMR was used to confirm the association between Azo-surfactants and PSS

chains. As shown in Figure 24, hydrogenated PSS (PSS-H) has two broad peaks at 6.5 ppm – 7.5 ppm corresponding to the aromatic hydrogens ( $H_c$ ,  $H_d$ ) and a broad peak at 1.74 ppm corresponding to hydrogens on the polymer backbone ( $H_a$ ,  $H_b$ ). 4Azo2TAB presents two peaks at 7.6 ppm and 6.8 ppm associated to azobenzene protons ( $H_4$ -  $H_7$ ), and two peaks at 4.2 ppm and 3.6 ppm related to the hydrogens of the spacer ( $H_2$ ,  $H_3$ ). The intense sharp peak at 3.1 ppm corresponds to the quaternary ammonium head ( $H_1$ ). The alkyl tail of 4Azo2TAB has four peaks between 0.9 ppm and 2.7 ppm ( $H_8$ - $H_{11}$ ).

For the mixture of PSS-H and 4Azo2TAB, all the peaks of aliphatic protons are broader and slightly shifted. The peaks in the aromatic zone (6-8 ppm) are overlapped and difficult to distinguish. To resolve this problem and reveal only the contribution of 4Azo2TAB, we used deuterated PSS (PSS-D). As shown in Figure 25, the spectrum looks almost identical except that the broad peaks at 7.41 ppm and 6.10 ppm disappear. Hence, these two broad peaks belong to PSS. They are broader and shifted meaning that PSS chains in the mixture are not as mobile as in the pure PSS solution. The four broad peaks between 6 ppm and 8 ppm correspond mainly to the aromatic protons of 4Azo2TAB and are quite different from that of pure 4Azo2TAB (Figure 24, green curve) indicating that 4Azo2TAB interacts with PSS in mixture.

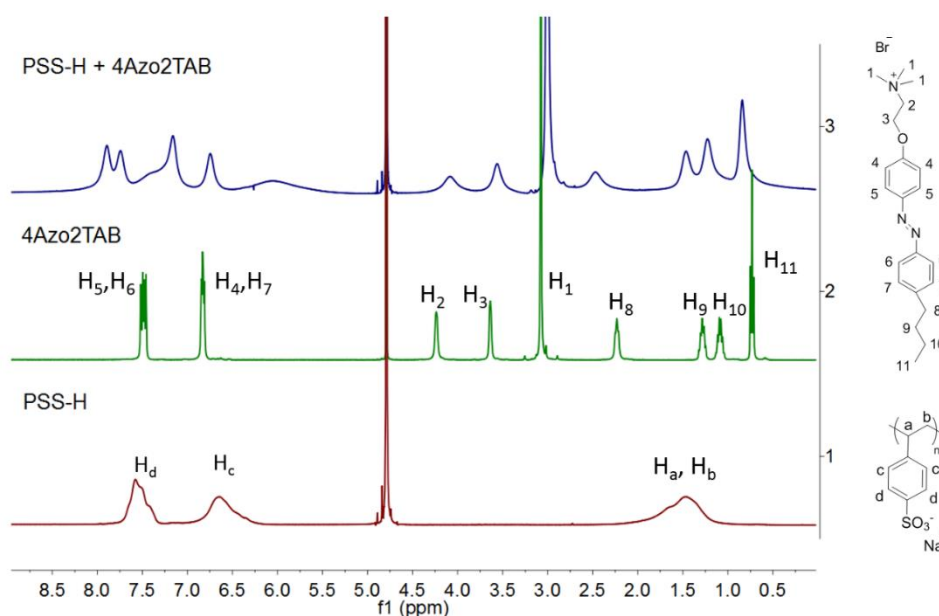


Figure 24  $^1\text{H}$  NMR in  $\text{D}_2\text{O}$  of 4Azo2TAB/PSS-H mixture (blue, 100 mM/50 mM), 4Azo2TAB (green, 50 mM) and PSS-H (red, 100 mM).

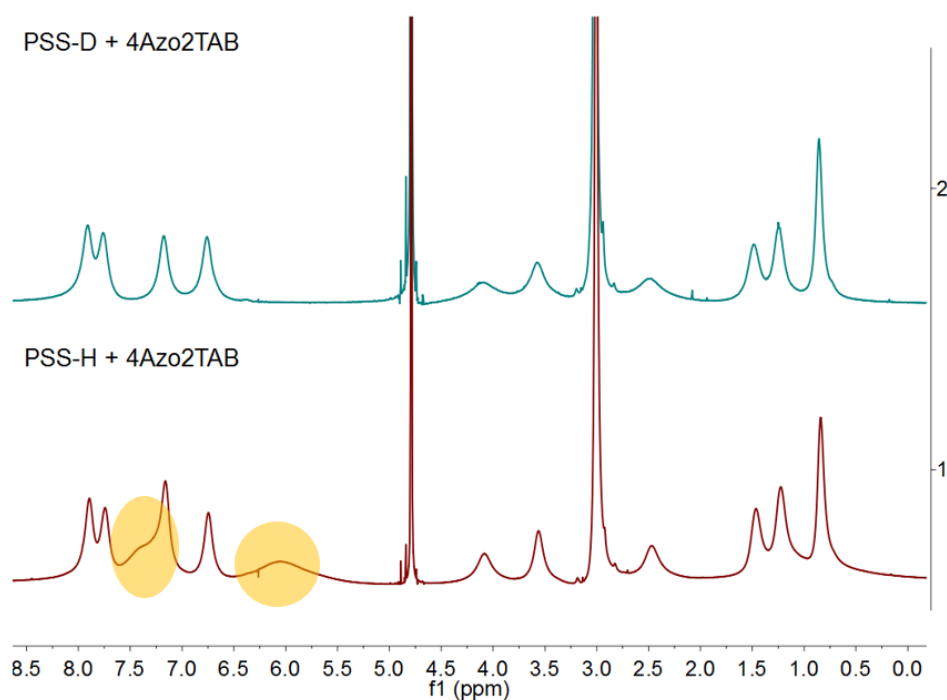


Figure 25  $^1\text{H}$  NMR spectra in  $\text{D}_2\text{O}$  of 4Azo2TAB/PSS-D mixture (green, 100 mM/50 mM) and 4Azo2TAB/PSS-H mixture (red, 100 mM/50 mM) in dark. The yellow areas correspond to signal of PSS-H chains, which is 'invisible' in the case of PSS-D.

We compare in Figure 26 the NMR spectra realized in dark, as well as under UV and blue light using PSS-D (only the peaks of the Azo-surfactants are visible). Under UV, the peaks are split due to the presence of the *trans/cis* isomers in the mixture. Since most of the peaks are broad and overlapped, it is quite difficult to estimate their respective contributions. An interesting peak is the singlet at 3.01 ppm corresponding to the ammonium head. Under UV, it splits in two identifiable contributions at 3.10 ppm and 3.01 ppm (corresponding to the *trans* and *cis* isomers respectively). These peaks are partially superposed, but we can roughly estimate the proportion of *trans/cis* isomers. At the stationary state, the proportion for *trans* isomers is approximately 28% (72% for *cis* isomers). The variation is less important than that observed for pure Azo-surfactant. This transformation is reversible by simple blue light irradiation (20 % *cis* and 80 % *trans*).

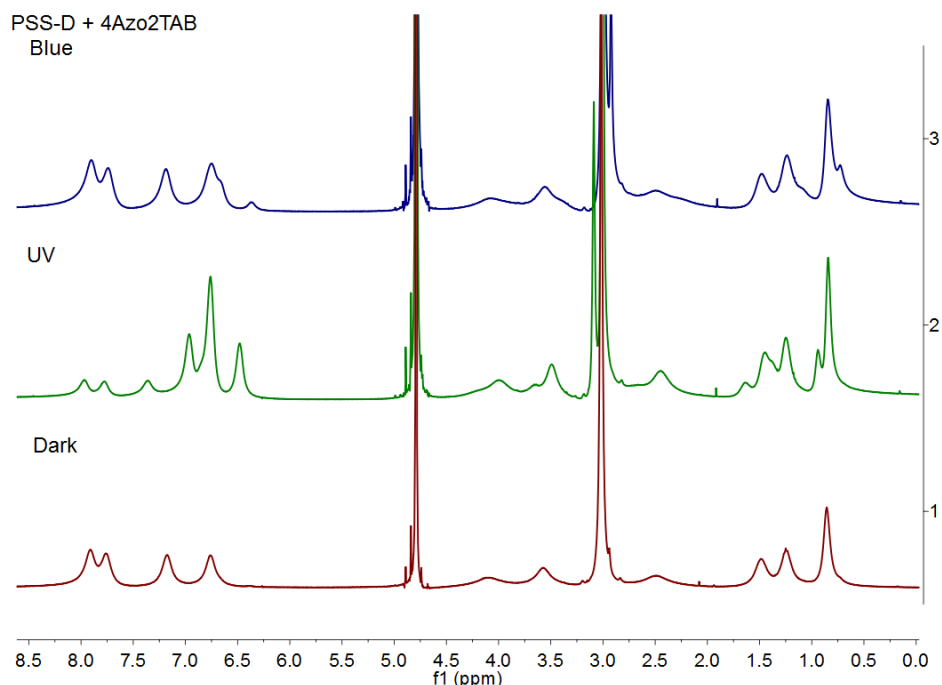


Figure 26  $^1\text{H}$  NMR spectra of 4Azo2TAB/PSS-D (100 mM/50 mM) mixtures in  $\text{D}_2\text{O}$ , in dark and under UV and blue irradiation.

The potential location of PSS in the aggregates can be proposed by comparing the spectra of pure 4Azo2TAB and that of 4Azo2TAB/PSS-D complexes (Figure 27). The chemical shift displacement  $\Delta\delta$  ( $\Delta\delta = \delta_{\text{complexes}} - \delta_{\text{pure}}$ ) depends on the local environment of the proton in the complexes, and therefore, on the organization of the micellar aggregate.

The experimental chemical shift displacement  $\Delta\delta$  of the different peaks vary with their location along the surfactant (Table 8). The protons of hydrophobic tail  $\text{H}_8 - \text{H}_{11}$  show downfield shifts (positive  $\Delta\delta$ ), while the protons of polar head  $\text{H}_1$  and of spacer  $\text{H}_2, \text{H}_3$  are slightly shifted upfield (negative  $\Delta\delta$ ). It is more complicated for aromatic protons (for which the correspondence is difficult to establish). We can speculate that these protons are partially shielded ( $\text{H}_4$ ) and the others deshielded ( $\text{H}_5, \text{H}_6, \text{H}_7$ ). The non-monotonic variation of the chemical shifts indicates that the nuclear environment varies along the surfactant molecule within the aggregate.

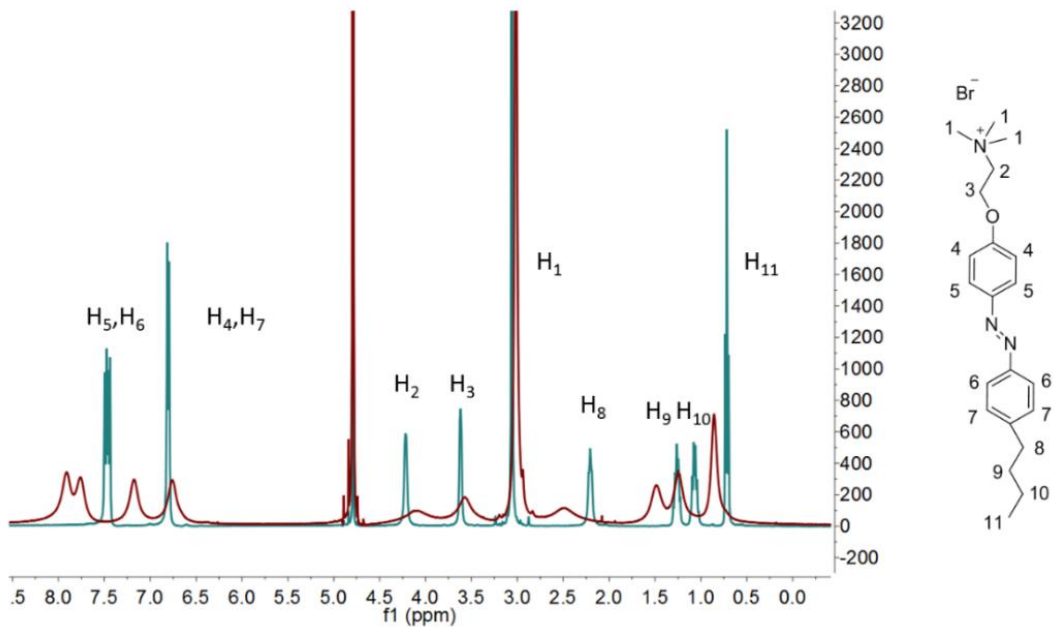


Figure 27  $^1\text{H}$  NMR spectra in  $\text{D}_2\text{O}$ : green line pure 4Azo2TAB 50 mM and red line 4Azo2TAB in 4Azo2TAB/PSS-D (100 mM/50 mM) mixtures.

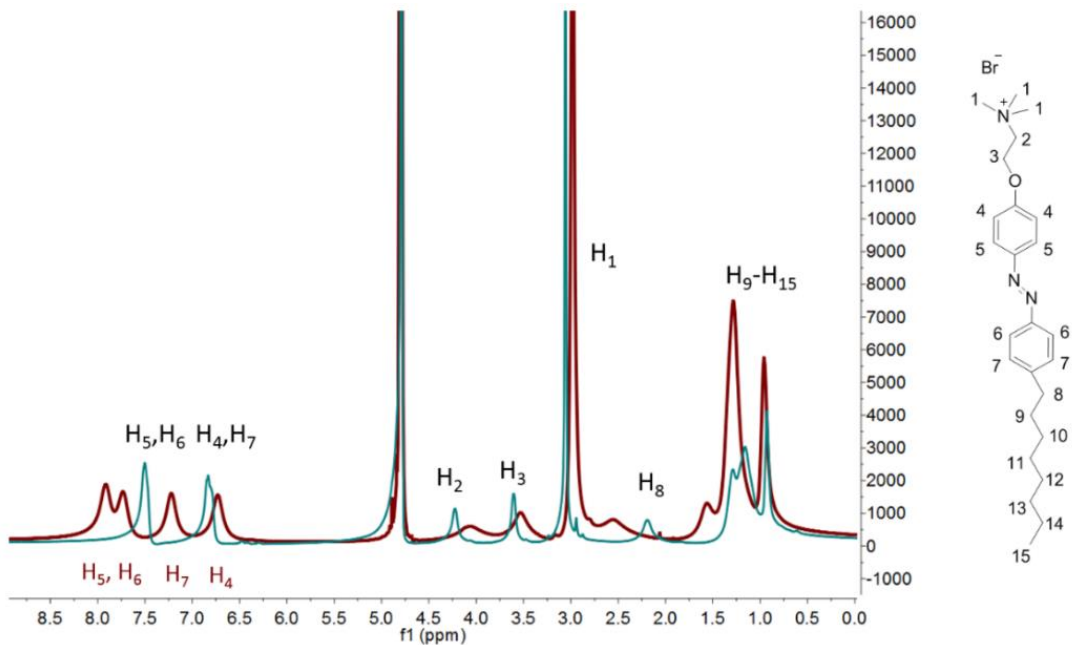
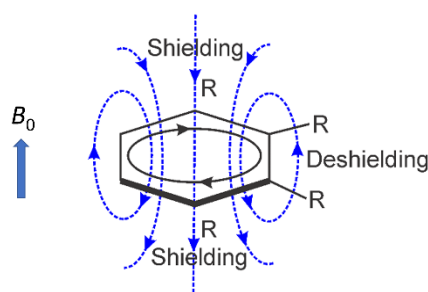


Figure 28  $^1\text{H}$  NMR spectra in  $\text{D}_2\text{O}$ : green line pure 8Azo2TAB 50 mM and red line 8Azo2TAB in 8Azo2TAB/PSS-D (100mM/50 mM) mixtures.

H	$\Delta\delta$	$\Delta\delta$
	PSSd/4Azo2TAB (ppm)	PSS-d/8Azo2TAB (ppm)
1	-0.06	-0.08
2	-0.13	-0.16
3	-0.06	-0.07
4	-0.06	-0.10
5	0.29	0.26
6	0.45	0.43
7	0.36	0.39
8	0.26	0.37
9	0.2	/
10	0.16	/
11	0.12	/

Table 8 Experimental chemical shift displacements  $\Delta\delta$  for Azo-surfactant/PSS complexes ( $\Delta\delta = \delta_{\text{complexes}} - \delta_{\text{pure}}$ ).

The sign and the magnitude of  $\Delta\delta$  can be explained by a ring current effect due to the presence of the aromatic rings of PSS chains. In the presence of an external magnetic field, the delocalized  $\pi$  electrons of the aromatic ring generates a ring current, which creates its own magnetic field (Scheme 4). The induced field above and below the plane of the ring is in the opposite direction to the external field, thus protons located above and below the ring shift upfield (negative  $\Delta\delta$ ). At the edge of the ring, the induced field is in the same direction as the external magnetic field, and protons are shifted downfield (positive  $\Delta\delta$ ).



Scheme 4 Schematic illustration of ring current effect.

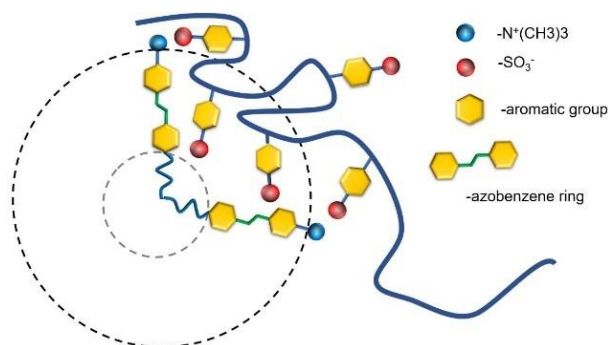
In mixtures, PSS strongly interacts with the micellar surfactants, and form complexes. The insertion of polyions in the aggregates is at the origin of the ring current effect observed in the chemical displacements. The aromatic rings of the

PSS lead to a negative chemical shift displacement of the surfactant peaks in the polar head region, and thus to the upfield shift of H<sub>1</sub>-H<sub>3</sub> protons. This is consistent with previous works on classical surfactants/PE systems (without azobenzene)<sup>17-20</sup>. PSS is therefore embedded between surfactant molecules, interact with the phenyl groups of azobenzene and further influence the chemical environment of the alkyl tail.

The largest magnitude of  $\Delta\delta$  is observed in the aromatic region. We can assume that aromatic rings or probably part of the aromatic rings of PSS are in the vicinity of azobenzene moiety. The sign of  $\Delta\delta$  depends on the relative orientation of aromatic rings, which may be parallel or perpendicular due to the steric constraint and the stiffness of PSS backbone. This may probably explain why the aromatic protons of Azo unit have different sign of  $\Delta\delta$  (negative for H<sub>4</sub> and positive for H<sub>5</sub> - H<sub>7</sub>).

Based on <sup>1</sup>H NMR studies, we can therefore conclude that Azo-surfactant/PSS complexes adopt a core-shell organization (Scheme 5). The aromatic rings of PSS penetrate deeply in the shell of aggregates. And that the PSS polyions participate to the micellization (co-micellization).

The 8Azo2TAB/PSS shows very similar NMR spectra, which are not presented here. We found in particular that the *trans/cis* ratio at the photostationary state was 30%. When blue light is applied, the *cis* peak of H<sub>1</sub> is merged with the *trans* peak. The estimation of the *trans* fraction is impossible.



Scheme 5 Schematic representation of Azo-surfactant/PSS complexes.

## VI.3.4 Structural study by SAXS and SANS

### VI.3.4.1 Scattering curves: general feature and modelling

#### SAXS measurements

SAXS measurements have been carried out on the two model systems 4Azo2TAB/PSS and 8Azo2TAB/PSS ( $r = 0.5$ ) at different concentrations ( $C$ ,  $C/2$ ,  $C/4$ ) in dark and under UV radiation. Scattered intensities normalized to the concentration are presented in Figure 29 (4Azo2TAB/PSS) and Figure 30 (8Azo2TAB/PSS).

For the two systems, the intensity increases at low  $q$  as the concentration decreases. This is a clear manifestation of a structure factor that varies with the concentration. Curiously, there is no peak in this region. This is certainly due to the release of the counterions (of the surfactants and the polyions) during the complexation process that screens the electrostatic interactions.

At higher  $q$ , all the curves are superposed (except maybe for 4Azo2TAB/PSS at  $C/4$  which shows slight variations) and a large oscillation is observed around  $0.2 \text{ \AA}^{-1}$ . This domain is dominated by the form factor of the aggregates. This maximum is very similar to that found in pure micelle solutions and certainly indicates to the formation of globular particles. We do not observe a classical  $q^{-4}$  variation of the intensity as for spherical uniform objects. The aggregates are probably heterogeneous on a local scale.

Under UV irradiation, the large oscillation is displaced to higher  $q$  indicating the size reduction of the aggregates.

From these observations, we can roughly estimate the  $q$  value from which the scattered intensity is mainly due to the form factor. This limit depends on the concentration. For the reference concentration  $C$ , it is close to  $0.05 \text{ \AA}^{-1}$  for 4AzoTAB/PSS, and close to  $0.04 \text{ \AA}^{-1}$  for 8AzoTAB/PSS. Since it is very complicated to find an analytical expression for the intermolecular correlations in our system ( $S(q)$ ), only a form factor can be fitted to the data in this restricted  $q$  range.

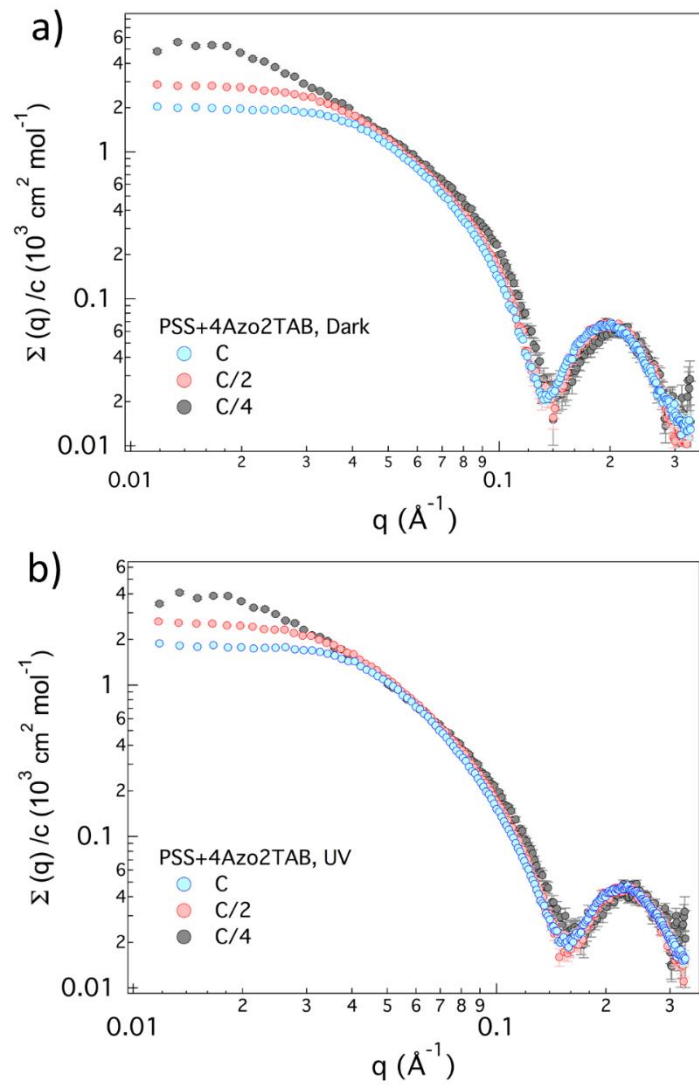


Figure 29 SAXS profiles of 4Azo2TAB/PSS normalized to the concentration a) in dark state b) under UV irradiation. The reference concentration is noted as C for 4Azo2TAB/PSS 50 mM/100 mM.

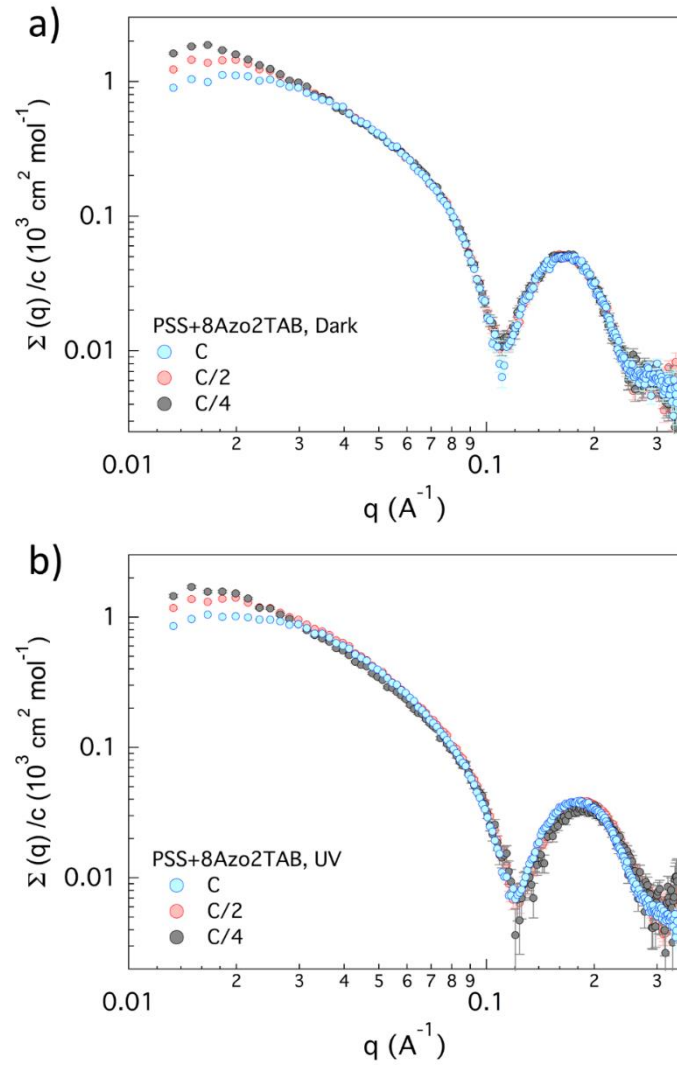


Figure 30 SAXS profiles of 8Azo2TAB/PSS normalized to the concentration a) in dark state b) under UV irradiation. The reference concentration is noted as C for 8Azo2TAB/PSS 50 mM/100 mM.

### SANS measurements

SANS measurements (dark, UV) have been done at a single concentration C and different contrast conditions. These experiments aim to determine the organization of the different species (polyions and surfactants).

We used deuterated PSS (PSS-D) and hydrogenated surfactants for these experiments. They have very different SLD (8Azo2TA<sup>+</sup>:  $1.00 \cdot 10^{10} \text{ cm}^{-2}$ , 4Azo2TA<sup>+</sup>:  $1.30 \cdot 10^{10} \text{ cm}^{-2}$ , PSS<sub>D</sub><sup>-</sup>:  $6.35 \cdot 10^{10} \text{ cm}^{-2}$ ). It is possible to find a H<sub>2</sub>O/D<sub>2</sub>O mixture that matches the SLD of the surfactant ( $\rho_{\text{solvent}} = \rho_{\text{azosurf}}$ ) in order to reveal the partial structure function of the polyions or, to mask the contribution of the polyions ( $\rho_{\text{solvent}} = \rho_{\text{PSS}}$ ) to highlight the structure function of the surfactants.

The scattered intensities (in dark) observed in different water compositions ( $\phi_{D_2O}$ ) are presented in Figure 31. In pure  $D_2O$  ( $\phi_{D_2O} = 1$ ,  $\rho_{\text{solvent}} = 6.38 \cdot 10^{10} \text{ cm}^{-2}$ ), only the surfactants are visible. In  $H_2O/D_2O$  mixture with  $\phi_{D_2O} = 0.267$  ( $\rho_{\text{solvent}} = 1.30 \cdot 10^{10} \text{ cm}^{-2}$ ), only the polyions are visible. This  $H_2O/D_2O$  solvent mixture does not perfectly match the SLD of  $8Azo2TA^-$ ,  $\rho_{8Azo2TA^-} = 1.00 \cdot 10^{10} \text{ cm}^{-2}$ , however, there will be no effect on the fitting procedure. An intermediate contrast condition with  $\phi_{D_2O} = 0.475$  ( $\rho_{\text{solvent}} = 2.74 \cdot 10^{10} \text{ cm}^{-2}$ ) was also used with  $4Azo2TAB/PSS$ . In this situation, every partial structure functions contribute to the scattered intensity.

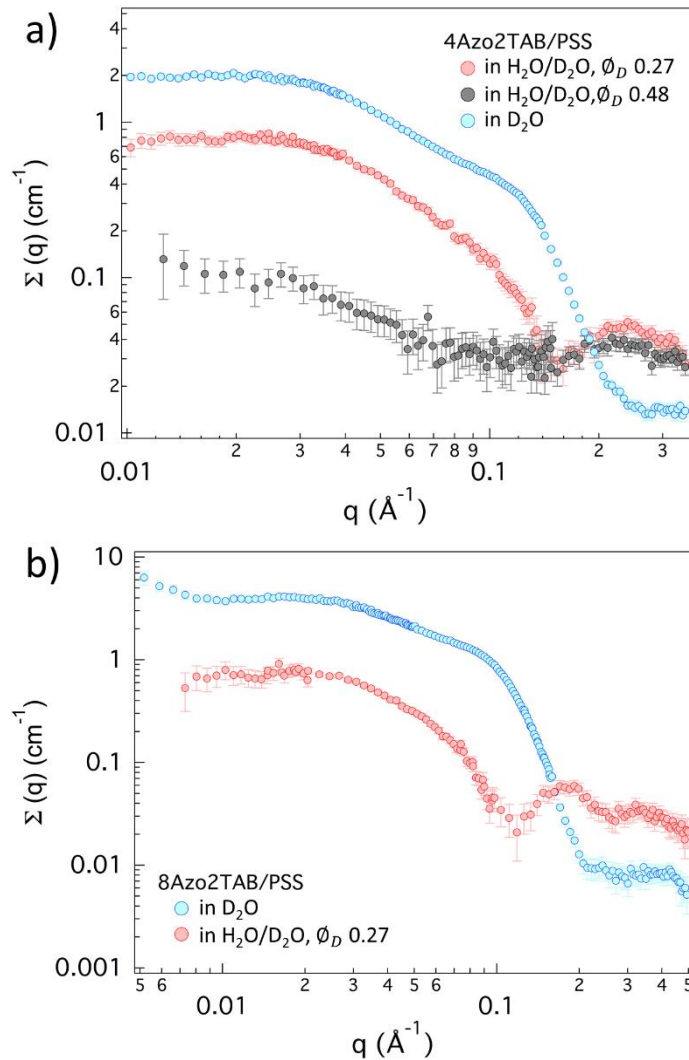


Figure 31 SANS plots: a)  $4Azo2TAB/PSS$  (50 mM/100 mM) in dark state (in  $D_2O$  and in  $H_2O/D_2O$ ); a)  $8Azo2TAB/PSS$  (50 mM/100 mM) in dark state (in  $D_2O$  and in  $H_2O/D_2O$ )

At low  $q$  values and up to  $0.03 \text{ \AA}^{-1}$ , each curve shows a similar plateau (as for X-rays). In this  $q$  range, we are dependent on the long-range intermolecular correlations. Above  $0.03 \text{ \AA}^{-1}$ , the intensity profiles vary with the contrast: the partial

structure functions of the polyions and the surfactants are therefore not identical. In other words, we have a heterogeneous structural organization at the local scale.

The presence of a well-defined oscillation in the polyion partial structure function around  $0.25 \text{ \AA}^{-1}$  (measured in  $\text{H}_2\text{O}/\text{D}_2\text{O}$ ,  $\phi_{\text{D}_2\text{O}} = 0.267$ ) indicates a global reorganization of the polyions and the formation of nanometric objects. Pure solutions of NaPSS (even in presence of salt) never show this behaviour.

The partial structure function of the surfactant (measured in  $\text{D}_2\text{O}$ ,  $\phi_{\text{D}_2\text{O}} = 1$ ) shows similarities with the scattering of pure surfactants in the high  $q$  range that indicates the presence of globular particles. Another important feature is the presence of a large shoulder in between  $0.03$  and  $0.1 \text{ \AA}^{-1}$ . This characteristic signature is related to the short-range correlations between the particles. They are therefore not uniformly distributed in the solution (like simple micelles) and tend to assemble to form larger objects (aggregate of aggregates).

All these remarks suggest a picture where polyions wraps around globular aggregates and link them together. More specifically, polyions and surfactants form the small globular objects. The surfactants are in the core of the aggregate while the polyions are rather found at the surface. According to NMR measurements, part of the chain can be mixed with the surfactant in the aggregate.

For long enough PE, these globules are linked by polyion segments and form a pearl-necklace organization. This kind of structure is often claimed in the literature to describe the surfactant/PE complexes in solution. However, there is very little structural experimental evidence of its existence and even less of the mutual organization of the different components.

From a practical point view, a pearl can be modelled by a simple core-shell assembly. This is of course a very simplified description, but it captures the main characteristics of the structure. In our pearl necklace model (Figure 32), these pearls are supposed to form ellipsoidal core-shell aggregates and they are arranged on a freely jointed chain of adjustable segment size  $d$ . The form factor for such a system has been derived by Schweins et al.<sup>21</sup> for hydrophobic polymers and spherical uniform pearls. In the present situation we use a simplified version and neglect the link between the pearls (extended polyions segments). For the fits, we assume that the scattered intensity is dominated by the form factor of the pearl necklace  $P(q)$  ( $S(q)=1$ ). Since experimental measurements always contain long-range intermolecular correlations in the low  $q$  region, the intensity is only fitted on a restricted  $q$  range ( $q_{\text{min}} = 0.05 \text{ \AA}^{-1}$  for 4Azo2TAB/PSS and  $0.04 \text{ \AA}^{-1}$  for

8Azo2TAB/PSS).

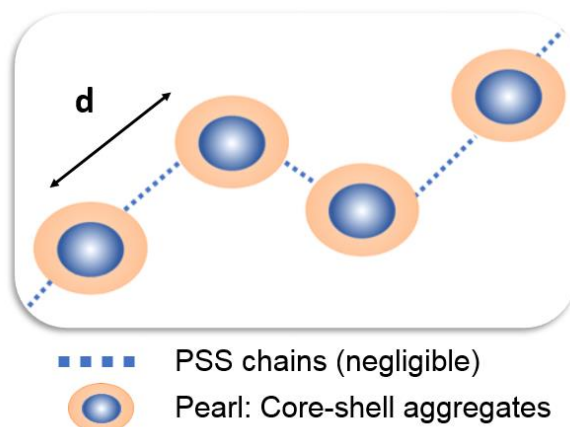


Figure 32 Schematic representation of pearl necklace model.

#### VI.3.4.2 SANS results

SANS data have been analyzed with the pearl necklace model using core-shell elliptical pearls. The fit parameters are the internal and external major and minor shells radius of the pearls, the SLDs of the core and the shell, the numbers of pearls along the necklace and the average distance between them. Since the core of the aggregate probably contains alkyl tails (as for simple micelles), the corresponding SLD is fixed to that of  $C_4H_9$  or  $C_8H_{17}$ . Fits have been done independently for the different contrast conditions. The volume fraction is set at its theoretical value.

The fits are presented in Figure 33 and Figure 34 for 4Azo2TAB/PSS and 8Azo2TAB/PSS in  $D_2O$  ( $\phi_{D_2O} = 1$ , surfactants are visible) and in  $H_2O/D_2O$  ( $\phi_{D_2O} = 0.267$ , polyions are visible), in dark and under UV. The fit parameters are summarized in Table 9 and Table 10. The intermediate contrast  $\phi_{D_2O} = 0.475$  ( $\rho_{\text{solvent}} = 2.74 \cdot 10^{10} \text{ cm}^{-2}$ ) measured with 4Azo2TAB/PSS was not fitted here due to the low signal and the bad statistics.

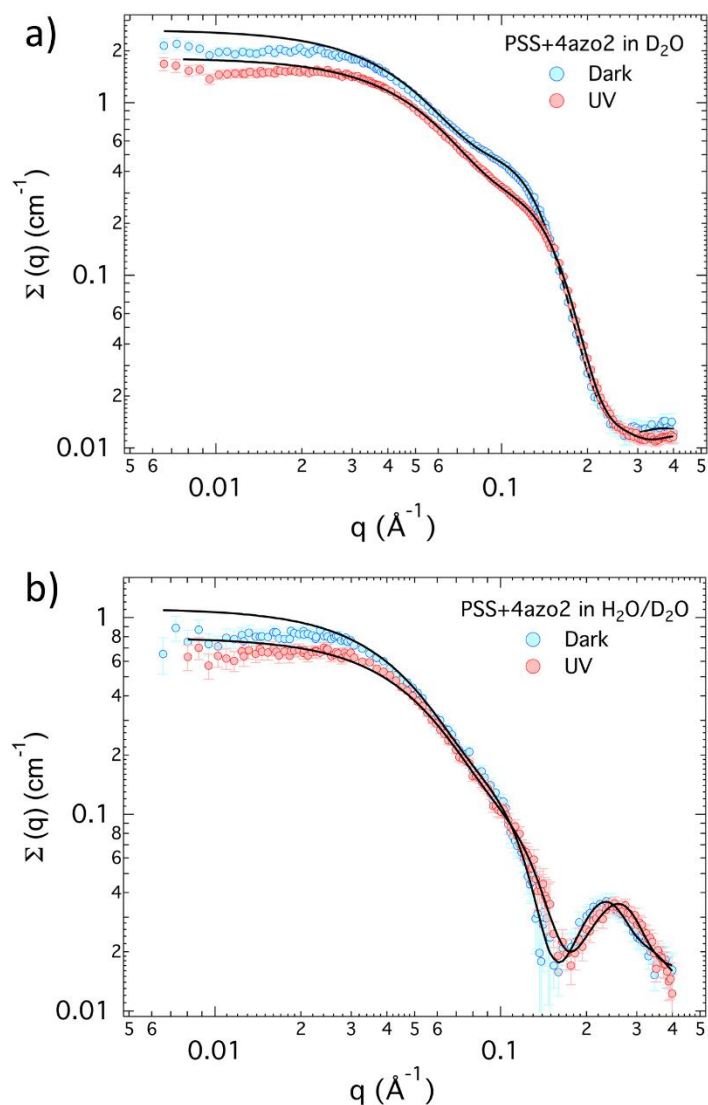


Figure 33 SANS profiles and fits for 4Azo2TAB/PSS (50 mM/100 mM): a) in D<sub>2</sub>O b) in H<sub>2</sub>O/D<sub>2</sub>O. Data are only fitted in between 0.05 Å<sup>-1</sup> to 0.4 Å<sup>-1</sup>.

Parameters	4Azo2TAB		Polyions	
	Dark	UV	Dark	UV
Major shell radius (Å)	26	23	26	23
Minor shell radius (Å)	18	16	18	17
Major core radius (Å)	13	12	18	13
Minor core radius (Å)	8	4	7	9
Distance between pearls (Å)	57	49	56	51
Pearls number	2	2	2	2
SLD core (10 <sup>10</sup> cm <sup>-2</sup> )	-0.5	-0.5	-0.5	-0.5
SLD shell (10 <sup>10</sup> cm <sup>-2</sup> )	3.9	3.8	4.1	3.8
∅	0.03	0.03	0.03	0.03

Table 9 SANS fitting parameters for 4Azo2TAB/PSS.

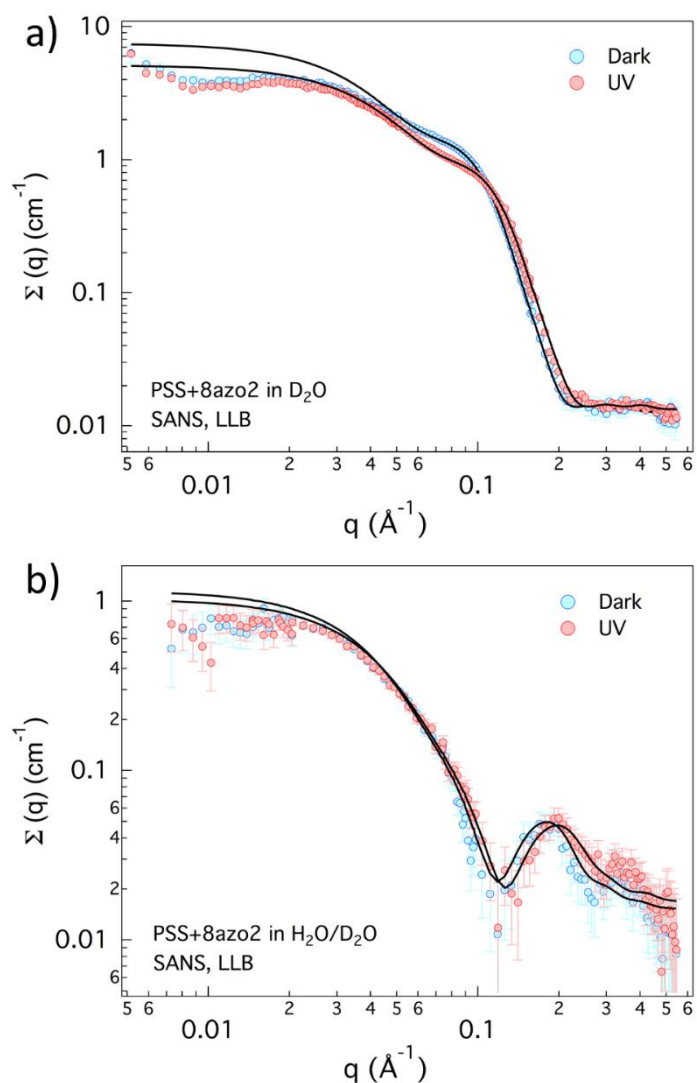


Figure 34 SANS profiles and fits for 8Azo2TAB/PSS (50 mM/100 mM): a) in D<sub>2</sub>O b) in H<sub>2</sub>O/D<sub>2</sub>O. Data are only fitted in between 0.04 Å<sup>-1</sup> to 0.4 Å<sup>-1</sup>.

Parameters	Surfactant		Polyions	
	Dark	UV	Dark	UV
Major shell radius (Å)	34	31	32	30
Minor shell radius (Å)	20	18	23	21
Major core radius (Å)	19	16	22	23
Minor core radius (Å)	15	14	12	11
Distance between pearls (Å)	75	65	65	61
Pearls number	2	2	2	2
SLD core (10 <sup>10</sup> cm <sup>-2</sup> )	-0.43	-0.43	-0.43	-0.43
SLD shell (10 <sup>10</sup> cm <sup>-2</sup> )	3.3	3.7	4.2	4.9
∅	0.025	0.029	0.022	0.022

Table 10 SANS fitting parameters for 8Azo2TAB/PSS.

The fits properly reproduce the data in both contrast conditions, in dark and under UV. The model seems appropriate to describe the structure of the complexes.

In particular, the shoulder observed in the surfactant structure function (below  $0.1 \text{ \AA}^{-1}$ , measurements in  $\text{D}_2\text{O}$ , Figure 33a and Figure 34a) and related to the pearl-pearl correlations is perfectly reproduced and gives accurate value of the average inter-pearl distance. For the 4Azo2TAB/PSS complexes, the radius of the shell (major, minor) are 26 and 18  $\text{\AA}$ . The inter-pearl distance is 57  $\text{\AA}$ , which is nearly twice the major shell radius. For the 8Azo2TAB/PSS complexes, the inter-pearl distance is also twice the major shell radius. The pearls are therefore very close to each other.

When we probe the polyions organization (Figure 33b and Figure 34b), we are also able to reproduce the large oscillation around  $0.2 - 0.3 \text{ \AA}^{-1}$ . This maximum finally comes from a shell type arrangement of the PE around the micellar core.

The geometrical parameters determined for the two contrast conditions are very similar. The PSS does not only decorate pre-existing micelles but is also mixed with the Azo-surfactants in the shell (co-micellization). The minor core and shell radii are very close to the radii observed for pure surfactant micelles. The major core and shell radius are shorter than that for pure surfactant. The global size of the aggregate is therefore smaller than for pure surfactant micelles at the same concentration even with the incorporation of the polyions in the aggregates.

Since the geometrical parameters only slightly vary with the contrast conditions, it is possible to use a single set of parameters to fit the different measurements simultaneously. Since the number of parameters in the model is important, a global fit leads to a more robust description.

We present in Figure 35 the results of the global fits for 4Azo2TAB/PSS. A single set of geometrical parameters for the core radius (minor and major), the shell radius (minor and major) and the inter-pearl distance has been used for the three contrast conditions. We imposed a constant shell thickness as well in the aggregate. Since water may penetrate in the shell, the shell SLD cannot be treated as a general parameter and needs to be fitted independently. This procedure was applied both in the dark state (blue curves) and under UV radiation (red curves). Fit results are given in Table 11.

A single geometrical description for the three contrast conditions allows to fit correctly the data (the fit can be slightly improved if we relax the constraint on the

constant shell thickness). This really proves that the location of both surfactant and PSS are intricately with each other, especially in the shell of the aggregate.

The global fit for 8Azo2TAB/PSS was also tested (without intermediate contrast conditions). The main results are identical, but the fit quality is not as good.

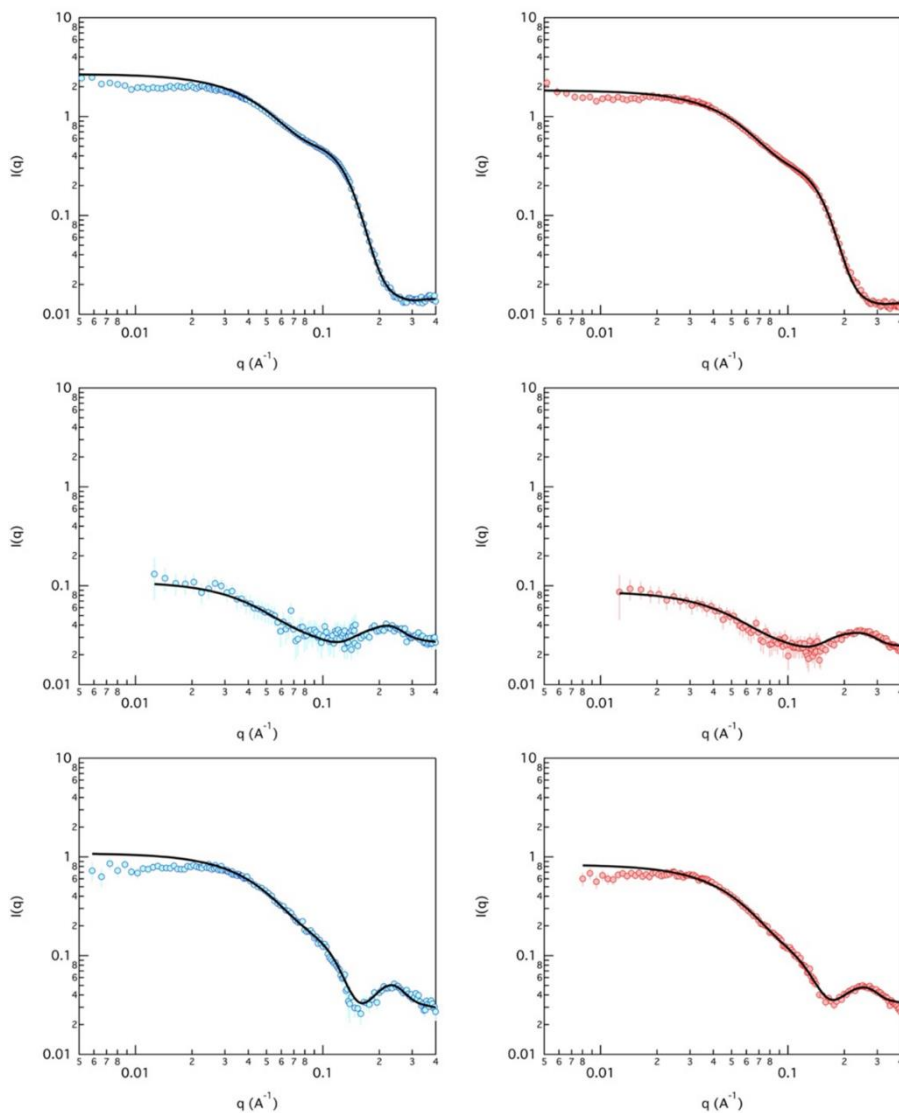


Figure 35 Global fits (in a restricted  $q$  range from 0.05 to 0.4  $\text{\AA}^{-1}$ ). Blue curve: dark state. Red curves: under UV radiation. Top curves:  $\phi_{D2O} = 1$  ( $\rho_{\text{solvent}} = 6.38 \cdot 10^{10} \text{ cm}^{-2}$ ); Middle curves  $\phi_{D2O} = 0.475$  ( $\rho_{\text{solvent}} = 2.74 \cdot 10^{10} \text{ cm}^{-2}$ ); Bottom curves  $\phi_{D2O} = 0.267$  ( $\rho_{\text{solvent}} = 1.30 \cdot 10^{10} \text{ cm}^{-2}$ ). The three contrasts conditions have been fitted simultaneously. The volume fraction is fixed and set to its theoretical value. The SLD of the core is fixed to that of the alkyl chain ( $-0.5 \cdot 10^{10} \text{ cm}^{-2}$ ). The number on pearls is fixed at two. SLDs of the solvents are set and fixed to their theoretical values. Global geometrical fitted parameters are the core radius (minor and major), the shell radius (minor and major) and the inter-pearl distance. We imposed a constant shell thickness in the aggregate. The SLD of the shell are fitted individually.

	Dark	UV
Major shell radius (Å)	25.80	24.0
Minor shell radius (Å)	18.9	17.5
Major core radius (Å)	14.9	13.8
Minor core radius (Å)	8.0	7.3
Distance between pearls (Å)	58.6	50.1
SLD core ( $10^{10} \text{ cm}^{-2}$ )	-0.5	-0.5
SLD shell ( $10^{10} \text{ cm}^{-2}$ ) $\phi_{\text{D}_2\text{O}}=1$ , $\rho_{\text{solvent}}=6.38 \cdot 10^{10} \text{ cm}^{-2}$	3.71	3.75
SLD shell ( $10^{10} \text{ cm}^{-2}$ ) $\phi_{\text{D}_2\text{O}}=0.475$ , $\rho_{\text{solvent}}=2.74 \cdot 10^{10} \text{ cm}^{-2}$	3.94	3.97
SLD shell ( $10^{10} \text{ cm}^{-2}$ ) $\phi_{\text{D}_2\text{O}}=0.267$ , $\rho_{\text{solvent}}=1.30 \cdot 10^{10} \text{ cm}^{-2}$	3.97	4.00

Table 11 Results of the global fits for 4azo2TAB/PSS

To figure-out the location of PSS and the surfactant in the pearls, the SLD of the core and the shell can be compared to that of the molecules or to different constituting molecular groups. The SLD of the core has been fixed to the theoretical value for alkyl groups. The minor core radius is on the order of the alkyl chain length in its fully extended conformation. This validates, the location of the hydrophobic tail in the center of the aggregate. The SLD of the shell lies in between the SLD of PSS and the surfactants (see Figure 10 a). For 4Azo2TAB/PSS, it varies very little with the nature of the solvent ( $\text{H}_2\text{O}/\text{D}_2\text{O}$  mixture) indicating that there is almost no water penetration. The pearls can therefore be described by a dense and compact entity formed by Azo-surfactant and polyions. This intermediate SLD value then reflects the mixing of PSS and surfactants in the shell (co-micellization).

The number of pearls appear very limited ( $N = 2$ ). Curiously, they tend to be almost in contact along the chain. We believe that our restricted  $q$  range potentially affect these results and cannot exclude a signature of larger assemblies ( $N > 2$ ) at smaller  $q$  values. Cryo-TEM measurements should be suited to explore larger lengths scales.

Under UV irradiation, we observe a displacement of the typical oscillation in the polyion structure function ( $\text{H}_2\text{O}/\text{D}_2\text{O}$ ) to larger  $q$  values: the size of the aggregate is reduced. This is also visible on the surfactant structure function ( $\text{D}_2\text{O}$ ) and more specifically on the shoulder associated to the pearl-pearl correlations. It shifts to higher  $q$  under UV indicates that the distance between pearls decreases.

The experimental curves were fitted with the same model. The conclusions are identical as in the dark situation. Globular aggregates composed of surfactant

and polyions still form a necklace like structure. The volume of the pearls is now reduced by 29% compared to the dark situation. The variation is smaller than that observed for pure micelles (69% for 4Azo2TAB micelles and 83% for 8Azo2TAB micelles).

#### VI.3.4.3 SAXS results

The SAXS analysis is similar to the SANS study (same model). As for neutrons scattering the SLD of the core is fixed to that of the alkyl chain. The volume fraction is also set at its theoretical value. Fits for 4Azo2TAB/PSS and 8Azo2TAB/PSS are presented in Figure 36.

Fit parameters are given in Table 12. The model reproduces well the data. The shell radii are however larger than those determined by SANS (by a few Å). This effect could be due to the presence of a condensed counterions layer that is always more visible with X-rays than with neutrons.

Under UV, large modifications are observed at high  $q$  indicating a structural rearrangement (pearl size reduction). We observe a variation of the pearl's size (24% for 4Azo2TAB/PSS and 26 % for 8Azo2TAB/PSS) and a decrease of the inter-pearls distance under UV irradiation. This change is reversible by blue light irradiation. Except for the "counterion size effect", all these observations are consistent with SANS results.

SAXS Parameters	PSS + 4Azo2TAB		PSS + 8Azo2TAB	
	Dark	UV	Dark	UV
Major shell radius (Å)	31	26	35	32
Minor shell radius (Å)	22	21	24	20
Major core radius (Å)	16	13	22	22
Minor core radius (Å)	8	8	15	13
Distance between pearls (Å)	52	48	68	64

Table 12 Fit parameters for 4Azo2TAB/PSS and 8Azo2TAB/PSS.

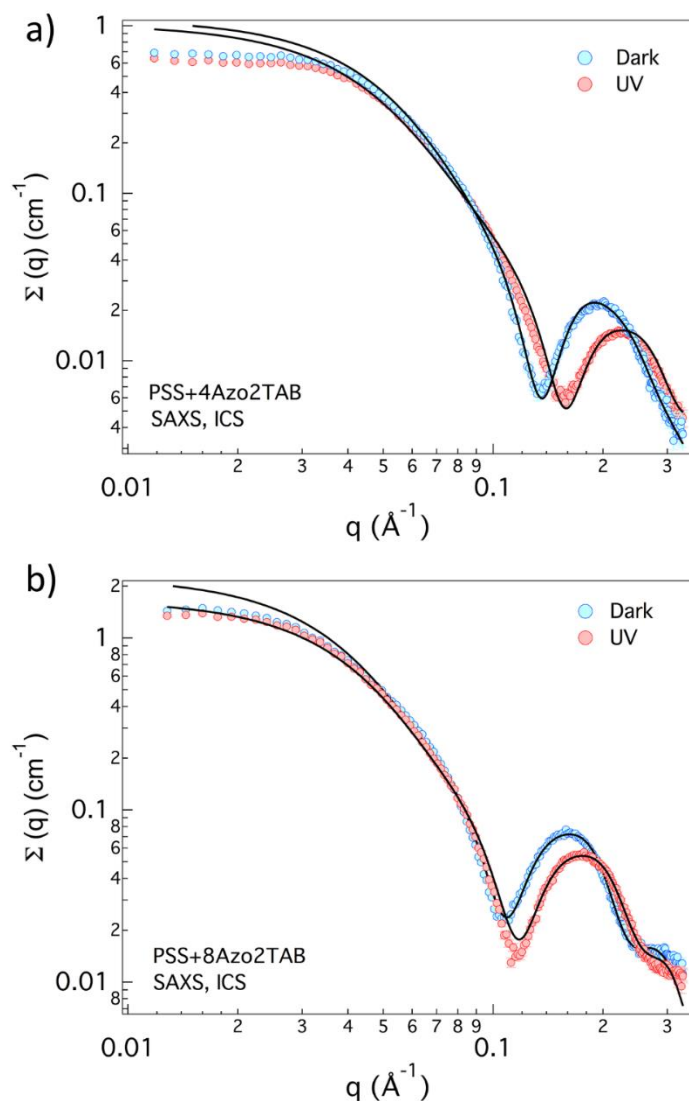


Figure 36 SAXS profiles for a) 4Azo2TAB/PSS (50 mM/100 mM) and b) 8Azo2TAB/PSS (50 mM/100 mM) in dark and under UV.

### Reversibility

The reversibility of the photoinduced structural modifications was tested by SAXS on 4Azo2TAB/PSS and 8Azo2TAB/PSS at the concentration C (Figure 37). We followed the position of the oscillation around  $0.2 \text{ \AA}^{-1}$  in the steady state under UV and blue irradiation (during several UV  $\leftrightarrow$  blue cycles). Both systems show a perfect reversibility.

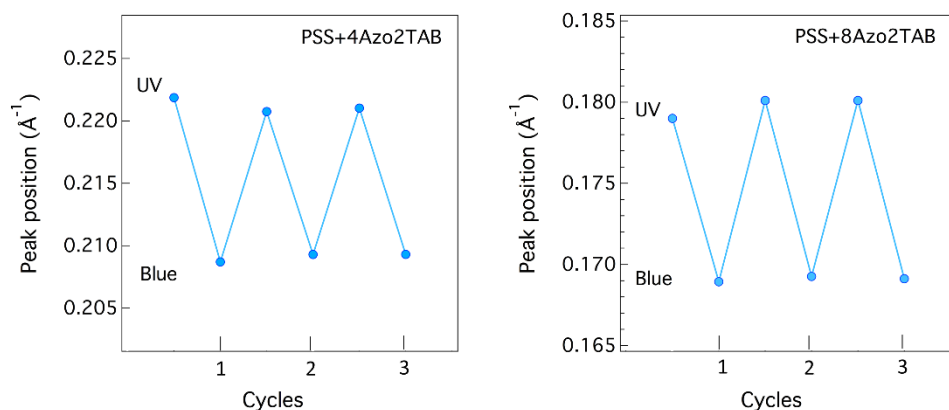


Figure 37 Reversibility of Azo-surfactant/PSS complexes (50 mM/100 mM) measured by SAXS.

### Thermal relaxation

For the thermal relaxation study, the capillary was pre-irradiated by UV light and then left to relax with time. We trace the position of the maximum as a function of time in Figure 38. 4Azo2TAB/PSS solution ( $\tau = 4.5$  h) relaxes faster than the 8Azo2TAB/PSS ( $\tau = 8.6$  h).

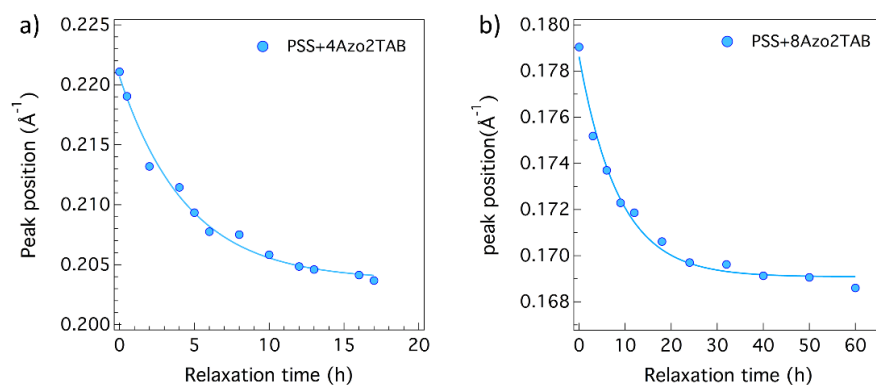


Figure 38 Thermal relaxation measured by SAXS. Position of the peak  $q^*$  as a function of time for a) 4Azo2TAB/PSS; b) 8Azo2TAB/PSS.

#### VI.3.4.4 Cryo-TEM results

Cryo-TEM measurements were carried out for Azo-surfactant/PSS complexes in dark state at a concentration  $C/10$ .

For 4Azo2TAB/PSS, small objects are present but difficult to observe. At the most, we can notice that these small aggregates are not homogeneously distributed in the film and tend to assemble with others (circle in Figure 39).

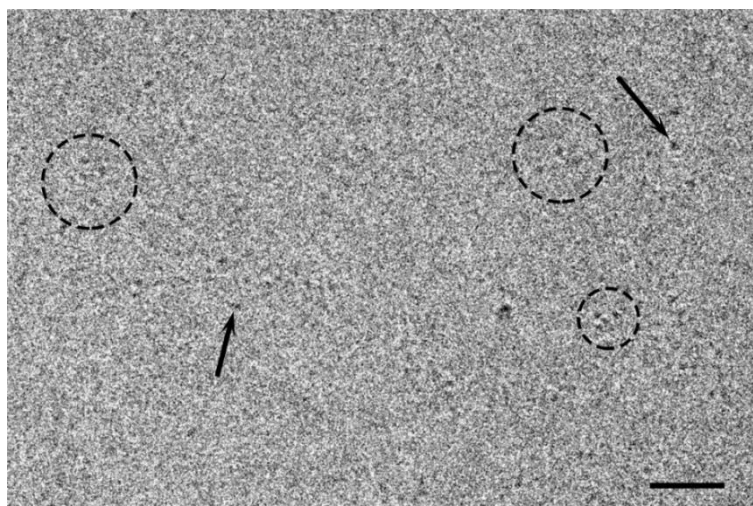


Figure 39 CryoTEM image of 4Azo2TAB/PSS (5 mM/10 mM). Arrow: apparent isolated particle. Circles: small aggregate of particles (aggregate of aggregates). The particles are not homogeneously distributed in the film.

For 8Azo2TAB/PSS, small particles are easily visible (Figure 40 and Figure 41). They are not homogeneously distributed and clearly form pearl necklace assemblies. This definitively validate the necklace organization. The size of the pearls ( $\approx 7$  nm) also coincide with small angle measurements. From these images, it is clear that the number of pearls per necklace can be larger than 2. The exact number of pearls is complex to determine and may also vary from one necklace to another. This example highlights the complementarity between electronic microscopy and scattering technics to reveal the structural organization in soft matter systems.



Figure 40 Cryo-TEM images for 8Azo2TAB/PSS (5 mM/10 mM) in dark. Particles are not homogeneously distributed in the film. Small arrow: region without micellar aggregate. Long arrow: region where the density in aggregates is higher. Pearl-necklace organisation is clearly visible.

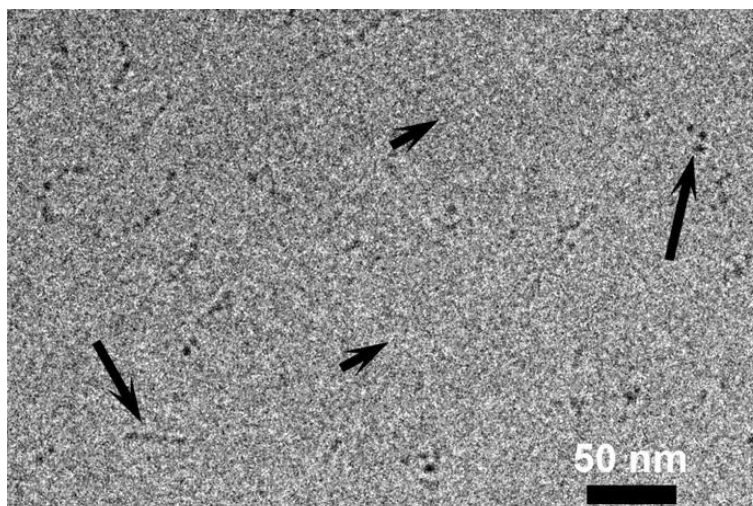


Figure 41 Cryo-TEM image of 8Azo2TAB/PSS (5 mM/10 mM). Particles are not homogeneously distributed in the film. Small arrow: region without micellar aggregate. Long arrow: region where the density in aggregates is higher. Pearl-necklace organisation is clearly visible.

### VI.3.5 Conclusion

We have investigated the structural organization of Azo-surfactant/PSS complexes and their photoisomerization behaviour. Both NMR and SANS studies indicate that polyions interact with oppositely charged Azo-surfactants due to the electrostatic interaction but also, participate to the micellization (co-micellization). The *cis* fraction at the photostationary state determined by NMR is around % (28% *trans* isomers, 72% *cis* isomers) under UV radiation. The system recovers 80% *trans* isomers (80% *trans* isomers, 20% *cis* isomers) under blue irradiation.

We have studied the structural organization by SAXS and SANS. We demonstrated the presence of micellar aggregates forming a necklace organization. Pearls are made of surfactants and polyions. The internal organization is however heterogenous and can be described as a core-shell structure. The core contains the hydrophobic tail of the surfactants, while the shell is an intimate mixture of polyions, Azo groups, C<sub>2</sub>H<sub>4</sub> spacers and polar heads. The complexation can rather be described by a co-micellization.

The aggregates formed by Azo-surfactant and PSS are smaller than micelles of pure Azo-surfactants. The distance between aggregates (pearls) is almost twice larger than the major shell radius. It seems like that 'pearls' are close to each other. This is further confirmed by the Cryo-TEM images. For 4Azo2TAB/PSS, the major and minor shell radius are 31 - 26 Å and 22 - 18 Å respectively. Larger major and minor shell radius are found for 8Azo2TAB/PSS: 35 - 32 Å and 24 - 20 Å.

Upon UV irradiation, aggregates still present but become smaller. The major and minor shell radius are 26 - 23 Å and 21 - 16 Å for 4Azo2TAB/PSS and 35-32 Å and 24-20 Å for 8Azo2TAB/PSS. The micellar size decreases by around 30%. This modest variation is certainly due to the large constraints in the aggregates imposed by the presence of polyion segments.

## References:

- (1) Blayo, C.; Houston, J. E.; King, S. M.; Evans, R. C. Unlocking Structure–Self-Assembly Relationships in Cationic Azobenzene Photosurfactants. *Langmuir* **2018**, *34* (34), 10123–10134.
- (2) Akamatsu, M.; FitzGerald, P. A.; Shiina, M.; Misono, T.; Tsuchiya, K.; Sakai, K.; Abe, M.; Warr, G. G.; Sakai, H. Micelle Structure in a Photoresponsive Surfactant with and without Solubilized Ethylbenzene from Small-Angle Neutron Scattering. *J. Phys. Chem. B* **2015**, *119* (18), 5904–5910.
- (3) Peng, S.; Guo, Q.; Hartley, P. G.; Hughes, T. C. Azobenzene Moiety Variation Directing Self-Assembly and Photoresponsive Behavior of Azo-Surfactants. *J Mater Chem C* **2014**, *2* (39), 8303–8312.
- (4) Hayashita, T.; Kurosawa, T.; Miyata, T.; Tanaka, K.; Igawa, M. Effect of Structural Variation within Cationic Azo-Surfactant upon Photoresponsive Function in Aqueous Solution. *Colloid Polym. Sci.* **1994**, *272* (12), 1611–1619.
- (5) Lund, R.; Brun, G.; Chevallier, E.; Narayanan, T.; Tribet, C. Kinetics of Photocontrollable Micelles: Light-Induced Self-Assembly and Disassembly of Azobenzene-Based Surfactants Revealed by TR-SAXS. *Langmuir* **2016**, *32* (11), 2539–2548.
- (6) McCoy, T. M.; Liu, A. C. Y.; Tabor, R. F. Light-Controllable Dispersion and Recovery of Graphenes and Carbon Nanotubes Using a Photo-Switchable Surfactant. *Nanoscale* **2016**, *8* (13), 6969–6974.
- (7) Zakrevskyy, Y.; Roxlau, J.; Brezesinski, G.; Lomadze, N.; Santer, S. Photosensitive Surfactants: Micellization and Interaction with DNA. *J. Chem. Phys.* **2014**, *140* (4), 044906.
- (8) Koźlecki, T.; Sokołowski, A.; Wilk, K. A. Surface Activity and Micelle Formation of Anionic Azobenzene-Linked Surfactants. *Langmuir* **1997**, *13* (26), 6889–6895.
- (9) Donaldson, S. H.; Lee, C. T.; Chmelka, B. F.; Israelachvili, J. N. General Hydrophobic Interaction Potential for Surfactant/Lipid Bilayers from Direct Force Measurements between Light-Modulated Bilayers. *Proc. Natl. Acad. Sci.* **2011**, *108* (38), 15699–15704.
- (10) Kang, H.-C.; Lee, B. M.; Yoon, J.; Yoon, M. Synthesis and Surface-Active Properties of New Photosensitive Surfactants Containing the Azobenzene Group. *J. Colloid Interface Sci.* **2000**, *231* (2), 255–264.
- (11) Bergström, M.; Skov Pedersen, J. Structure of Pure SDS and DTAB Micelles in Brine Determined by Small-Angle Neutron Scattering (SANS). *Phys. Chem. Chem. Phys.* **1999**, *1* (18), 4437–4446.
- (12) Tabor, R. F.; Pottage, M. J.; Garvey, C. J.; Wilkinson, B. L. Light-Induced Structural Evolution of Photoswitchable Carbohydrate-Based Surfactant Micelles. *Chem. Commun.* **2015**, *51* (25), 5509–5512.
- (13) Hayter, J. B.; Penfold, J. Self-Consistent Structural and Dynamic Study of Concentrated Micelle Solutions. *J. Chem. Soc. Faraday Trans. 1 Phys. Chem. Condens. Phases* **1981**, *77* (8), 1851–1863.

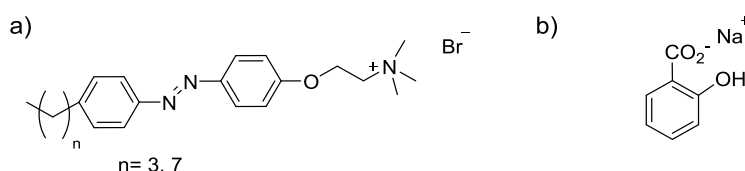
- (14) Hansen, J.-P.; Hayter, J. B. A Rescaled MSA Structure Factor for Dilute Charged Colloidal Dispersions. *Mol. Phys.* **1982**, *46* (3), 651–656.
- (15) Lee, C. T.; Smith, K. A.; Hatton, T. A. Small-Angle Neutron Scattering Study of the Micellization of Photosensitive Surfactants in Solution and in the Presence of a Hydrophobically Modified Polyelectrolyte<sup>†</sup>. *Langmuir* **2009**, *25* (24), 13784–13794.
- (16) Roy, J. C.; Islam, Md. N.; Aktaruzzaman, G. The Effect of NaCl on the Krafft Temperature and Related Behavior of Cetyltrimethylammonium Bromide in Aqueous Solution. *J. Surfactants Deterg.* **2014**, *17* (2), 231–242.
- (17) Gao, Z.; Kwak, J. C. T.; Wasylishen, R. E. An NMR Study of the Binding between Polyelectrolytes and Surfactants in Aqueous Solution. *J. Colloid Interface Sci.* **1988**, *126* (1), 371–376.
- (18) Macdonald, P. M.; Tang, A. <sup>1</sup>H and <sup>2</sup>H NMR Studies of Poly(Acrylate) and Poly(Sodium Styrenesulfonate) Interactions with Cationic Surfactant Micelles. *Langmuir* **1997**, *13* (8), 2259–2265.
- (19) Effing, J. J.; McLennan, I. J.; van Os, N. M.; Kwak, J. C. T. <sup>1</sup>H NMR Investigations of the Interactions between Anionic Surfactants and Hydrophobically Modified Poly(Acrylamide)s. *J. Phys. Chem.* **1994**, *98* (47), 12397–12402.
- (20) Wasylishen, R. E.; Kwak, J. C. T.; Gao, Z.; Verpoorte, E.; MacDonald, J. B.; Dickson, R. M. NMR Studies of Hydrocarbons Solubilized in Aqueous Micellar Solutions. *Can. J. Chem.* **1991**, *69* (5), 822–833.
- (21) Schweins, R.; Huber, K. Particle Scattering Factor of Pearl Necklace Chains. *Macromol. Symp.* **2004**, *211* (1), 25–42.
- (22) Chevallier, E. Cascade d'effets Induits Par La Lumière Aux Interfaces Liquides : Du Photo-Surfactant à La Mousse. Thesis, Université Paris VI, 2012.

# Chapter VII. Self-assembly of azo surfactants with co-surfactants

During the study on Azo-surfactant/PE complexes, we tested many different formulations. We found accidentally that 8Azo2TAB and sodium salicylate (NaSal) can form gel-like solutions. This gel-like property can be switched 'on' or 'off' by simple UV or blue light irradiation. The aggregation of azo-surfactants and two aromatic salts (sodium salicylate and sodium benzenesulfonate) and their response to light stimulus are investigated in this chapter. In particular, we aim to give a brief overview on the structural modifications induced by the irradiation.

## VII.1 Self-assembly of 8Azo2/sodium salicylate (NaSal)

### VII.1.1 Azo-surfactant/NaSal: molar ratio and concentration



Scheme 1 Chemical structures of a) Azo-surfactants (4Azo2TAB and 8Azo2TAB) and b) NaSal

In the absence of additives, pure 8Azo2TAB molecules self-assemble and form oblate ellipsoidal aggregates with a short radius of 28 Å and a long radius of 66 Å at a concentration of 50 mM. Pure 4Azo2TAB molecules form smaller ellipsoidal aggregates with a short and long radius of 20 Å and 35 Å respectively at the same concentration.

Different Azo-surfactant/NaSal mixtures have been prepared with molar ratios  $r$  in between 0.5 and 1.2 ( $r = [\text{Azo-surfactant}]/[\text{NaSal}]$ ) and a concentration of Azo-surfactant from 40 mM to 75 mM. None of the 4Azo2TAB/NaSal mixtures exhibit gel property (Table 1).

On the other hand, the addition of NaSal to 8Azo2TAB solutions leads to a significant increase of viscosity and a gel behavior (Table 2). The gel texture of 8Azo2TAB/NaSal assembly is more pronounced when increasing the concentration. 8Azo2TAB/NaSal at 75 mM/62.5 mM ( $r=1.2$ ) mixture can even

support its own weight. It becomes fluid when the UV light is applied (Figure 1). This composition and concentration define our reference sample. The corresponding concentration is noted C hereafter.

4Azo2TAB (mM)	NaSal (mM)	$r$	texture
50	100	0.5	precipitate
50	62.5	0.8	fluid
50	50	1	fluid
60	50	1.2	fluid
75	62.5	1.2	fluid

Table 1 Tests on 4Azo2TAB/NaSal mixtures,  $r = [4\text{Azo2TAB}]/[\text{NaSal}]$ .

8Azo2TAB (mM)	NaSal (mM)	$r$	texture
50	100	0.5	fluid
50	62.5	0.8	viscous
50	50	1	viscous
60	100	0.6	viscous
60	50	1.2	gel
75	62.5	1.2	gel

Table 2 Tests on 8Azo2TAB/NaSal mixtures,  $r = [8\text{Azo2TAB}]/[\text{NaSal}]$

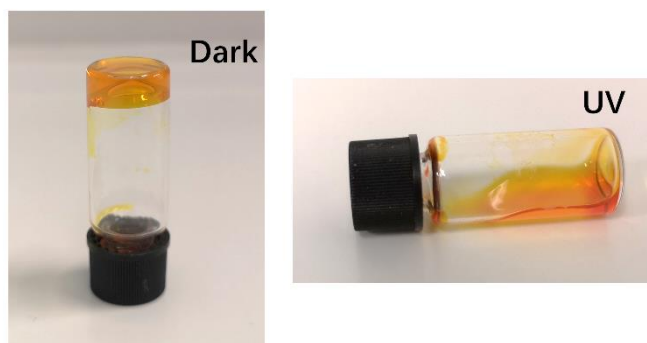


Figure 1 Photos of 8Azo2TAB/NaSal mixture (75 mM/62.5 mM) in dark state (gel) and under UV irradiation (fluid).

## VII.1.2 Photoconversion study

### VII.1.2.1 UV-Vis absorption spectroscopy

The photoisomerization was studied by UV-Vis absorption spectroscopy. 8Azo2TAB/NaSal mixture (concentration C/2000) in the dark state (*trans* isomers) exhibits an absorption band at 351 nm and a weak band at around 438 nm associated to the 8Azo2TAB molecule. The shoulder at 305 nm corresponds to

the absorption band of NaSal. Under UV irradiation, due to the *trans* to *cis* conversion, the absorption band at 438 nm for *cis*-8Azo2TAB increases; the maximum absorption band at 351 nm is shifted to lower wavelength and is overlapped with the band of NaSal (around 300 nm). The photoconversion is totally reversible under UV/blue light irradiation cycles.

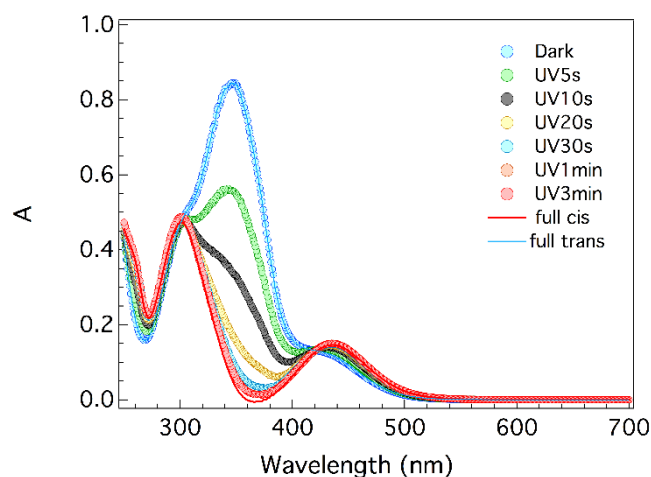


Figure 2 UV-vis spectra of 8Azo2TAB/NaSal aqueous solution (0.0375 mM/0.0312 mM, C/2000) for different irradiation times.

#### VII.1.2.2 NMR

NMR measurements on the reference sample 8Azo2TAB/NaSal (C) have been carried out in D<sub>2</sub>O. Pure NaSal (62.5 mM) and pure 8Azo2TAB (75 mM) solutions have been studied for comparisons.

As shown in Figure 3, pure NaSal solution presents well-defined narrow peaks. 8Azo2TAB solution whose concentration is above the CMC, has broader peaks due to the formation of micelles. Surfactant in the micelles and individual surfactants in solution are in thermal equilibrium: we always have dynamical exchanges between the two populations. The resulting peak is an average of all the peak positions corresponding to the free and self-assembled surfactants. Since the concentration of 8Azo2TAB is much higher than its CMC ( $CMC_{trans} = 0.29$  mM), the detected signals almost correspond to the hydrogens of micelle-forming molecule.

The resonance peaks of 8Azo2TAB/NaSal mixture (C) are much broader (blue curve in Figure 3) and the peaks of 8Azo2TAB at 4.23 ppm and 3.60 ppm corresponding to the spacer C<sub>2</sub>H<sub>4</sub> even disappear (H<sub>2</sub>, H<sub>3</sub>) indicating the formation of larger aggregates. Generally, aromatic rings generate a negative contribution to the local magnetic field, resulting in upfield shifts for the adjacent molecules<sup>1-3</sup>.

The intense peak of ammonium head at 3.1 ppm is shifted to 2.9 ppm (upfield), which indicates that NaSal molecules approach the polar head of 8Azo2TAB surfactant. The overlapping peaks associated to the hydrophobic tail (around 0.8-1.5 ppm) are unaltered, which means their environment is not influenced upon the addition of NaSal. All these modifications suggest that NaSal molecules are packed in the hydrophilic region of 8Azo2TAB aggregates.

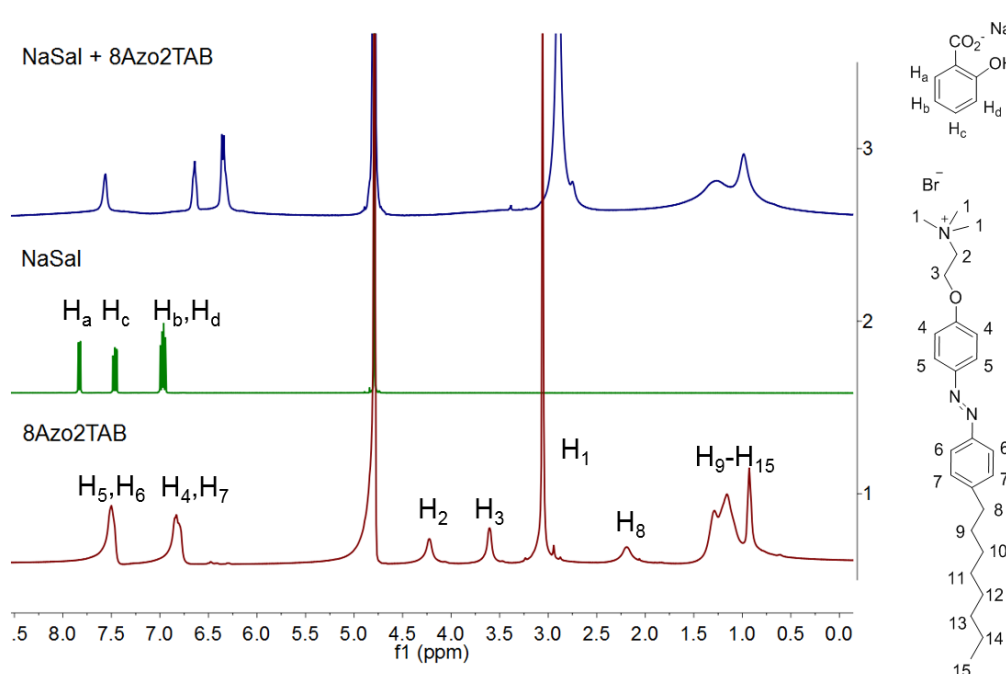


Figure 3  $^1\text{H}$  NMR spectra in  $\text{D}_2\text{O}$  of 8Azo2TAB (75 mM, red curve) NaSal (62.5 mM, green curve), and the 8Azo2TAB/NaSal (75 mM/62.5 mM, blue curve) mixture.

The previous description only applies for the dark state. Since large photo-induced structural modification appears under UV, we expect to see a clear signature of the new arrangement by NMR. However, the spectra under UV light does not show much difference from that in the dark state even after 20 h of UV irradiation (Figure 4, green curve). We barely observe the splitting of peaks due to the coexistence of *trans* and *cis* isomers, but we cannot extract useful information.

A less concentrated sample, C/4 mixture was thus investigated (Figure 5). A similar spectrum for the dark state was observed. But the photostationary state was reached faster (after 8 h under UV irradiation). The UV curve shows the splitting of certain peaks which is typical for the coexistence of *trans* and *cis* isomers. The two peaks attributed to the spacer of 8Azo2TAB ( $\text{H}_2$ ,  $\text{H}_3$ ) reappear (Figure 5, green curve). The sharp intense peak ( $\text{H}_1$ ) located at 2.82 ppm is split

into two peaks, at 3.01 ppm for *trans* isomers and 2.93 ppm for *cis* isomers. It allows to determine the *trans/cis* ratio in the solution. At the equilibrium, the *trans/cis* ratio can be estimated to 26:74.

Under blue light irradiation, the reverse photoisomerization occurs (*cis* to *trans*). The spectrum (blue curve in Figure 5) is quite similar to the one in dark state (red curve in Figure 5), while the small peak at 2.72 ppm indicates that there are still *cis* isomers left. The *trans/cis* ratio is determined as 81:19.

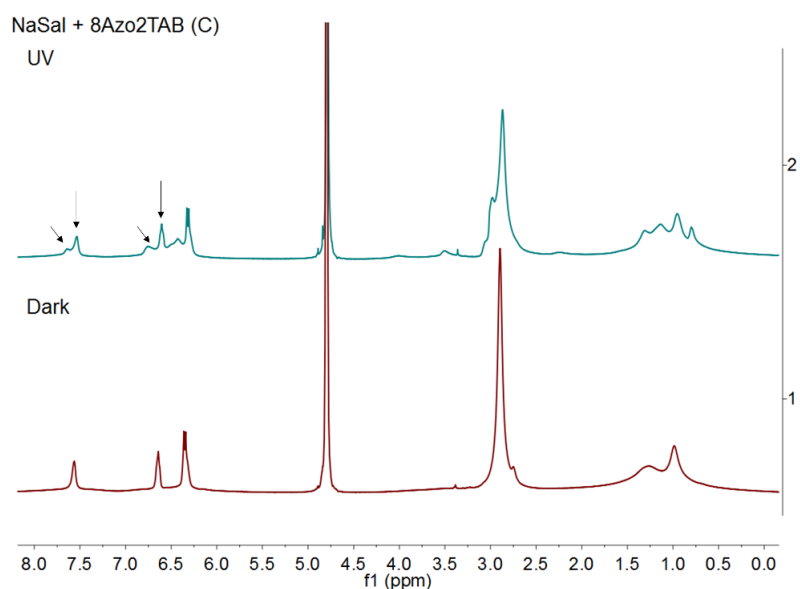


Figure 4  $^1\text{H}$  NMR spectra in  $\text{D}_2\text{O}$  for 8Azo2TAB/NaSal (75 mM/62.5 mM) in dark and under UV.

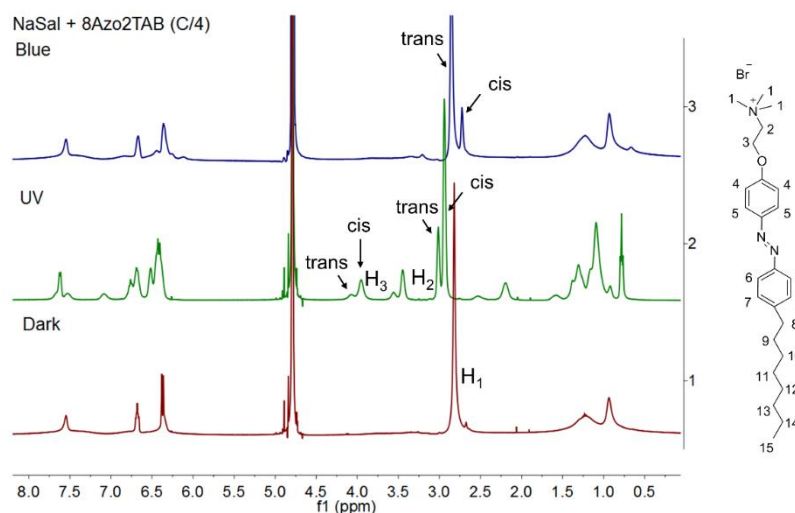


Figure 5  $^1\text{H}$  NMR spectra in  $\text{D}_2\text{O}$  for 8Azo2TAB/NaSal (18.75 mM/15.62 mM, C/4).

### VII.1.3 Structural study

The macroscopic rheological properties are governed by the microstructure of the system. Scattering methods as well as electronic microscopy are complementary techniques that allow to probe different length scales and give an accurate description of the structural organization.

#### VII.1.3.1 Cryo-TEM measurements

Cryo-TEM measurements have been performed on 8Azo2TAB/NaSal C/4 in dark and after UV irradiation. After 4 hours the sample was completely fluid and considered to be in its photostationary state. The images are presented in Figure 6.

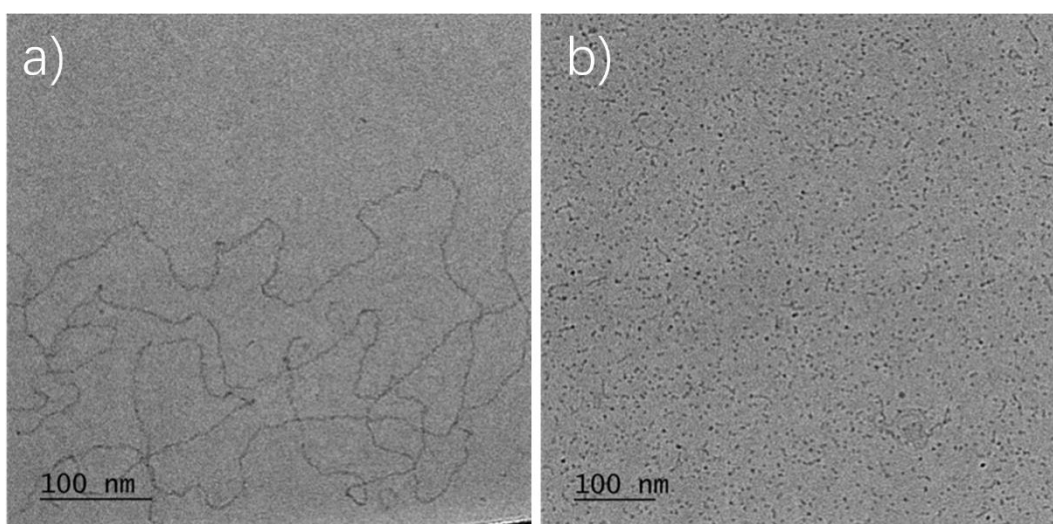


Figure 6 Cryo-TEM measurements of 8Azo2TAB/NaSal C/4 (18.75 mM/15.62 mM) (a) in dark and (b) after 4 h under UV irradiation.

The images clearly show two distinct organizations. In the dark state, we find wormlike particles with a diameter between 5 to 7 nm and length of several micrometers. After 4 hours of UV irradiation, we find mainly spherical objects with a diameter around 4 nm but also small wormlike particles with the same diameter but with lengths in between 10 to 29 nm. This morphological transition under irradiation explains the variation of the rheological properties. In order to get a better picture of the local organization, these observations need to be combined with small angle scattering experiments.

### VII.1.3.2 Small angle neutron scattering

The irradiation procedure has been optimized to ensure the most efficient use of the beam time at the LLB. Three concentrations  $C$ ,  $C/2$  and  $C/4$  have been measured in dark and under UV. The samples were pre-illuminated by UV tubes (during 24 h) and then installed in the automatic sample changer on the instrument. Sample irradiation was performed *in situ* during the measurement using a multi-LED setup developed at the LLB. Additional LEDs were installed at other positions of the sample changer (illuminating both sides of the sample) to keep the solutions under UV irradiation before the measurements (to prevent the thermal relaxation process). Each measurement under UV were repeated several times and compared to ensure that the equilibrium state is reached. The presence of external light sources in the close environment might slightly influence the *trans/cis* ratio at the equilibrium state.

Two distinct experiments (*i.e.*, beam time allocation) have been performed at the LLB on these systems. In the second experiment, we re-measured the  $C/4$  sample under more rigorous conditions to reduce the surrounding light influence. Only this sample will be fitted below.

The scattering curves normalized to the concentration (of 8Azo2TAB) are presented in Figure 7.

In the dark state (Figure 7 a), the three curves are superposed for  $q \geq 0.03 \text{ \AA}^{-1}$ . The scattering in this region only reflects the form factor of the particles. Since we have long objects in solution, the large decrease in intensity above  $0.03 \text{ \AA}^{-1}$  is related to the cross section of particles (and therefore to their radius).

For  $q \leq 0.03 \text{ \AA}^{-1}$ , the intensity does not vary as  $q^{-1}$  (as it should do for a rod-like systems) except for the lowest concentration  $C/4$ . We have a clear contribution of a structure factor in this  $q$ -range. In the following, only the sample at  $C/4$  will be considered for the fit.

Under UV radiation (Figure 7 b), the curves are close, but not superposed at large  $q$ . Two effects may explain these differences. First, the size of the globular micelles varies with the concentration (classical behaviour). Second, the photostationary states are not identical, for physical reasons or due to our irradiation procedure. During the fit, we will only focus on the sample at  $C/4$  for which the difference with the dark state is larger.

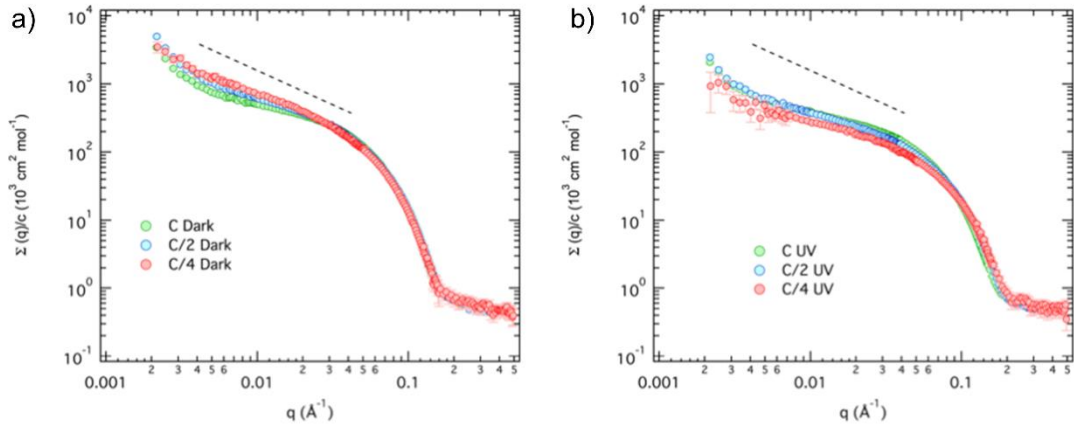


Figure 7 SANS patterns of 8Azo2TAB/NaSal normalized to the concentration. a) in dark, b) under UV radiation. Dash line indicates a  $q^{-1}$  decay.

In Figure 8, we present the variation of the intensity between the dark and the photostationary states (under UV) for two concentrations: C (Figure 8 a) and C/4 (Figure 8 b).

The variation found for the highest concentration C is very modest. Intensity is lowered at low  $q$ , while it is shifted to largest  $q$  around  $0.1 \text{ \AA}^{-1}$ .

The lowest concentration is more interesting. As already mentioned, the intensity in dark almost follow the classical  $q^{-1}$  variation characteristic of rod-like particles. This is in accordance with Cryo-TEM measurements. However, a small contribution of the structure factor is still present. We could expect the signature of wormlike micelle at very low  $q$ , and the appearance of a Gaussian behaviour below  $ql_p = 1.9$  (where  $l_p$  is the persistence length of the micelles)<sup>4</sup>. However, no significant upturn is present. In the high  $q$  regime (above  $0.03 \text{ \AA}^{-1}$ ), we are sensitive to the cross section of the particles. Since no oscillation (or minimum) is observed for the highest  $q$  values, we may have polydisperse radius and an elliptic cross section. Data in the dark state have been fitted with a cylindrical model of elliptic section that seems consistent with these observations.

Under UV irradiation, we note a large decrease at low  $q$ . The power law exponent (in the intermediate regime) is changing indicating a modification of the shape of the particles. In the meantime, the intensity around  $0.1 \text{ \AA}^{-1}$  is clearly shifted indicating a reduction of the typical size of the object. Curiously, we do not find the Guinier regime and a plateau at low  $q$ . This is a consequence of the high polydispersity of the objects as demonstrated by Cryo-TEM. Hence the modelling is more complicated. Since small objects are more abundant, we have used a

model of uniaxial ellipsoids particles.

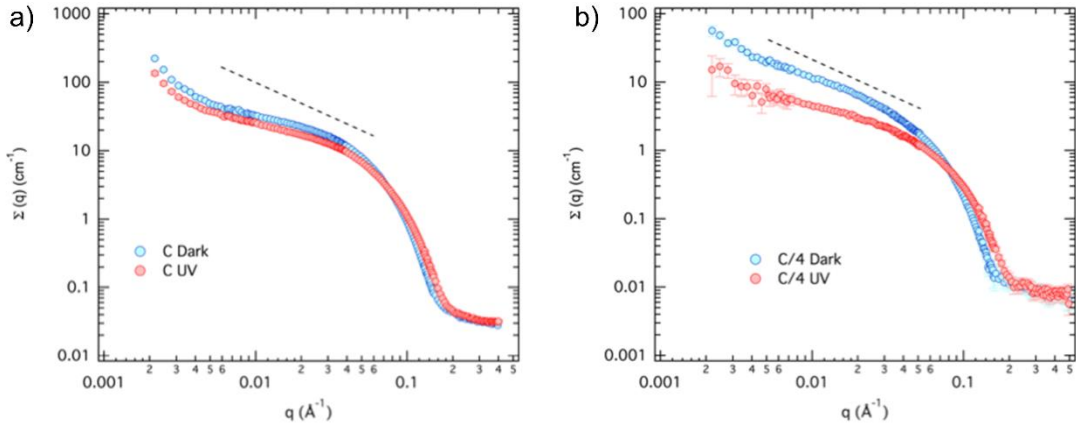


Figure 8 SANS patterns of 8Azo2TAB/NaSal in dark and under UV irradiation. a) concentration C (75 mM/62.5 mM); b) concentration C/4 (18.75 mM/15.62 mM). Dash line indicates a  $q^{-1}$  decay.

The fits in the dark state and under UV radiation are presented in Figure 9 a) and b). For the dark state, we used a model of long elliptical cylinder. Since we do not observe the Guinier range, we fixed its length to an arbitrary value of 1000 Å (this value does not affect the quality of the fit). Other fitted parameters are the minor radius and the ellipticity (major radius/minor radius), the SLD of the cylinder and a constant background. Due to the contribution of the structure factor, the fit was limited to  $q_{\min} = 0.015 \text{ \AA}^{-1}$ .

For the photostationary state (UV), we used the form factor of a prolate ellipsoid. According to Cryo-TEM, globular shapes and elongated systems are present in the solution. It is therefore very hard to find a simple suitable model. In this context, we just tried to reproduce the large  $q$  behaviour which certainly contains information about the cross section of the objects (either cylindrical or globular). Since this procedure is not very accurate, we impose the lowest  $q$  limit to  $0.04 \text{ \AA}^{-1}$ . Changing the length of the prolate ellipsoid does not modify the high  $q$  behaviour and the final radius. We arbitrary fixed this value to 100 Å. The fitted parameters are the radius of the ellipsoid, the SLD of the particle and the background.

For both models, we fixed the volume fraction to its theoretical value ( $\phi = 0.0086$ ) and the SLD of the deuterated water ( $\rho_{N D20} = 6.38 \cdot 10^{10} \text{ cm}^{-2}$ ).

The fits reproduce well the experimental measurements without introducing polydispersity in the model. Final parameters are summarized in Table 3.

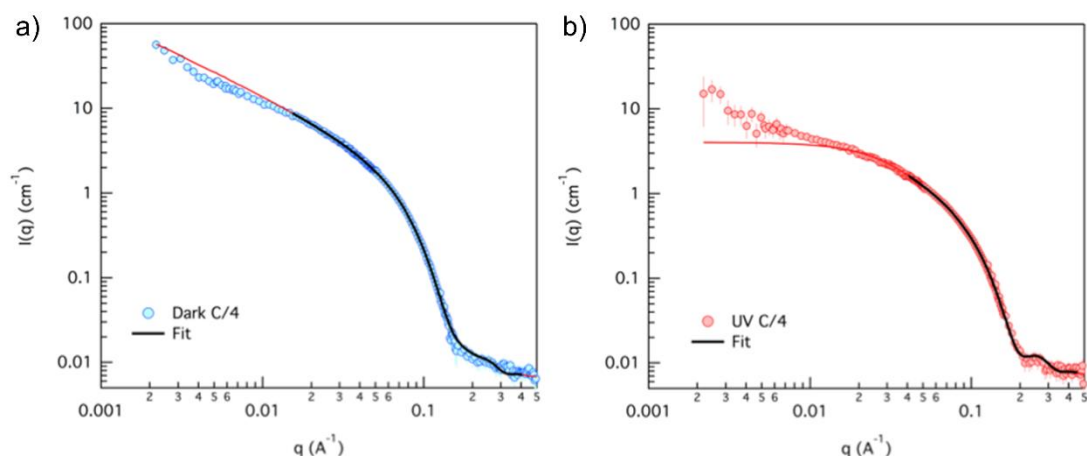


Figure 9 Fit of the SANS patterns at C/4 (18.75 mM/15.62 mM). a) In the dark state using an infinite elliptical cylinder. b) Under UV irradiation using a prolate ellipsoid.

8Azo2TAB/NaSal C/4	Dark (elliptic cylinder)	UV (prolate ellipsoid)
Volume fraction	0.0086*	0.0086*
Length (Å)	1000*	-
Minor radius (Å)	20.1	20.9
Major radius (Å)	32.8	100*
Ellipticity (major/minor)	1.63	-
SLD cylinder ( $10^{10} \text{ cm}^{-2}$ )	1.34	1.32

Table 3 SANS fit parameters. In the elliptic cylinder model, the section has two radii: the major and the minor. The ratio between the major and the minor radius gives the ellipticity. In the prolate ellipsoid, the major axis corresponds to the rotation axis. The cross-section perpendicular to the axis of symmetry is circular. Asterisks correspond to fixed parameters. The parameters for the aggregate under UV irradiation should be taken with care (the system is polydisperse and the fit is restricted on a very particular  $q$  range).

To get the meaning of the fitted SLD values, it is necessary to recall the SLD of the different components in the system. They are presented in Table 4.

	$\rho_x (10^{+10}\text{cm}^{-2})$	$\rho_N (10^{+10}\text{cm}^{-2})$
8Azo2TAB	10.54	1.003
8Azo2TA <sup>+</sup>	11.32	1.031
NaSal	14.86	3.141
Sal <sup>-</sup>	12.19	2.715
NaBenSulf	15.24	2.647
BenSulf	12.76	2.286
NaSal/8Azo2TAB *	11.88	1.39
Sal <sup>-</sup> /8Azo2TA <sup>+</sup> *	10.82	1.33
NaBenSulf/8Azo2TAB *	12.00	1.32
BenSulf /8Azo2TA <sup>+</sup> *	10.96	1.26
Tail C <sub>8</sub> H <sub>17</sub>	7.56	-0.43

Table 4 Scattering length densities of the different components. The asterisk \* means that the value has been calculated according to the volume fraction of each component (taking into account their molar composition in the mixture).

The SLD of the particles are nearly identical to the expected one (Table 4). Since the volume fraction has been fixed to the theoretical value, we conclude that the two components are fully integrated in the micelles. Water penetration is negligible. The smallest dimension of the aggregate (20 - 21 Å) is much smaller than the fully extended size of 8Azo2TAB (around 30 Å) and smaller than what we found in pure 8Azo2TAB micelle (50 mM). Curiously, no difference is observed on the minor radius between dark and UV. The presence of the salicylate in the particle deeply changes the local organization of the surfactant with regard to the classical micelle.

### VII.1.3.3 Small angle X-ray scattering

SANS measurements have been completed by SAXS analyses. The main difference between the two techniques is that the SLD of the particles cannot be considered as uniform with X-rays. As we have done in the previous chapters, we need to introduce a core-shell description. The second difference lies in the illumination setup which is more efficient with the SAXS diffractometer and allows a better control of the UV irradiation.

The scattering curves normalized to the concentration are presented in Figure 10 for C, C/2 and C/4 in the dark state and under UV irradiation. For both measurements, we find a large maximum around  $0.2 \text{ \AA}^{-1}$ , that is characteristic of micellar aggregates.

In the dark state, as for neutrons experiments, the highest concentration is not superposed to the others due to the contribution of the structure factor. C/2 and C/4 are superposed: the structure factor is negligible; we are only sensitive to the form factor.

Under UV, and for same reason, the concentration C is not superposed on the others. Furthermore, the minimum found around  $0.1 \text{ \AA}^{-1}$  for C/4 is not as deep as the one found for C/2. This could reflect a variation of the ellipticity of the ellipsoid with the concentration or a small polydispersity. Additionally, as for neutron experiments, we never see the Guinier regime. Despite a more efficient irradiation setup, we cannot avoid the coexistence of globular and elongated particles in the system.

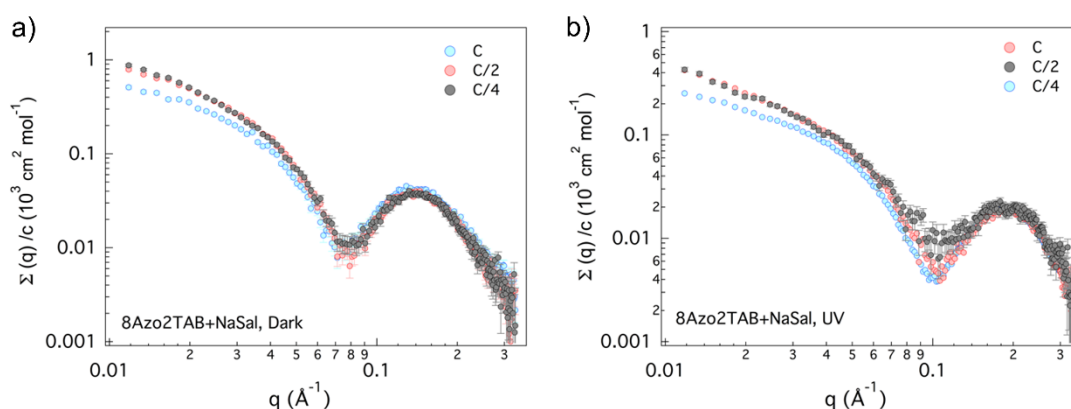


Figure 10 SAXS patterns of 8Azo2TAB/NaSal normalized to the concentration. a) in dark, b) under UV radiation.

The variation under UV for C and C/4 are shown in Figure 11. The maximum at  $0.2 \text{ \AA}^{-2}$  is shifted to higher  $q$  values in a reversible way. Contrary to SANS measurements, this effect is also important for the largest concentration C.

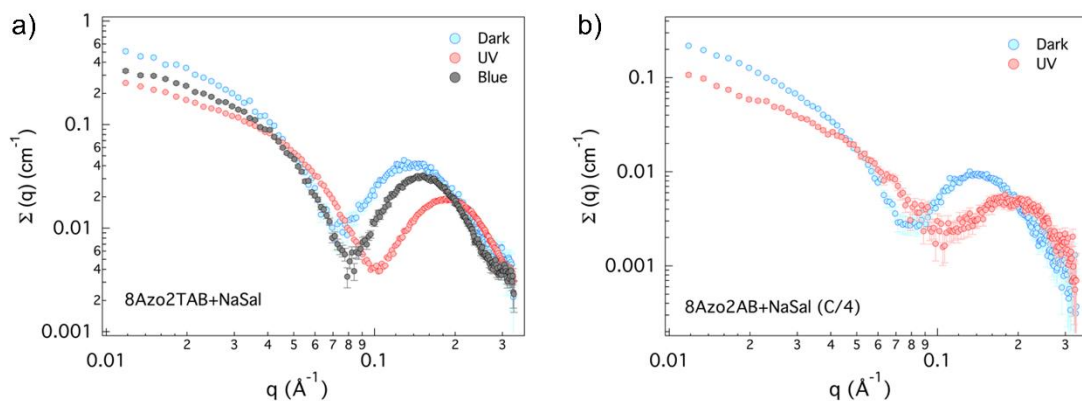


Figure 11 SAXS patterns of 8Azo2TAB/NaSal in dark and under UV and blue irradiation. a) concentration C (75 mM/62.5 mM) b) concentration C/4 (18.75 mM/15.62 mM).

We have fitted the scattered intensity with the same shapes (elliptic cylinder and prolate ellipsoid) as for SANS measurements. The only difference is the introduction of core-shell organization. With the exception of the shell thickness and its own SLD, everything is similar to the neutron analysis. In order to minimize the number of adjustable parameters, we have considered a constant shell thickness for the prolate ellipsoid and a constant ellipticity for the elliptic core-shell cylinder.

The fits are presented in Figure 8. Data are well reproduced in the selected  $q$  range. Final parameters are summarized in Table 5.

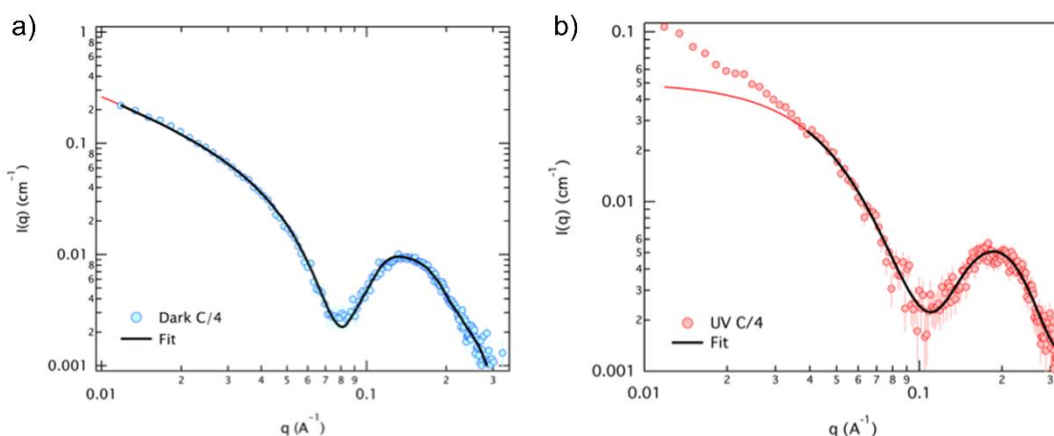


Figure 12 Fit of the SAXS patterns at C/4 (18.75 mM/15.62 mM). a) In the dark state using an infinite core-shell elliptical cylinder. b) Under UV irradiation using a prolate core-shell ellipsoid.

8Azo2TAB/NaSal C/4	Dark (elliptic core-shell cylinder)	UV (prolate core-shell ellipsoid)
Volume fraction	0.0086*	0.0086*
Length (Å)	1000*	-
Minor core radius (Å)	14.0	10.4
Major core radius (Å)	22.7	46.1
Minor shell radius (Å)	20.4	24.8
Major shell radius (Å)	33.0	60.5
Minor shell thickness (Å)	6.40	14.4
Major shell thickness (Å)	10.3	14.4
Ellipticity (major/minor)	1.62	-
SLD core ( $10^{10} \text{ cm}^{-2}$ )	8.35	7.13
SLD shell ( $10^{10} \text{ cm}^{-2}$ )	11.67	10.5

Table 5 SAXS fit parameters. In the elliptic core shell cylinder model, the section has four radii: the major and the minor shells and the major and the minor core. The ellipticity is identical for the core and the shell. In the prolate core shell ellipsoid, the major axis corresponds to the rotation axis. The cross section perpendicular to the axis of symmetry has a circular core-shell geometry. The thickness is held constant. Asterisks correspond to fixed parameters. The parameters for the aggregate under UV irradiation should be taken with care (the system is polydisperse and the fit is restricted on a very particular  $q$  range).

First of all, in the dark state SAXS and SANS give exactly the same result for the cross section of the micelle (major and minor shell radius of the core-shell elliptic cylinder: 33.0 and 20.4 Å; major and minor radius of the elliptic cylinder: 32.8 and 20.1 Å).

Second, the SLD profile determined from the SAXS analysis is very particular. The SLD of the core ( $8.35 \cdot 10^{10} \text{ cm}^{-2}$ ) is lower to that of the water ( $9.40 \cdot 10^{10} \text{ cm}^{-2}$ ) and close to that of the alkyl tail ( $\text{C}_8\text{H}_{17}$ ,  $7.56 \cdot 10^{10} \text{ cm}^{-2}$ ). The SLD of the shell ( $11.67 \cdot 10^{10} \text{ cm}^{-2}$ ) is larger to that of water and close the average 8Azo2TAB/NaSal value ( $11.88 \cdot 10^{10} \text{ cm}^{-2}$ ). In other words everything happens as is the core was mainly composed of the  $\text{C}_8\text{H}_{17}$  tails of the surfactant while the shell is made of azo and hydrophilic groups but also, salicylate molecules. This is in accordance with NMR results. The same trend is observed under UV (these results are however less relevant due to the absence of a well-defined form factor and the very limited

$q$  range for the fit).

Finally, we monitored the thermal relaxation by SAXS (C/4). The variation of the position of the maximum around  $0.2 \text{ \AA}^{-1}$  (characteristic of the surfactant assembly) is given the Figure 13. A characteristic time of 22.2 h was obtained using an exponent decay relaxation.

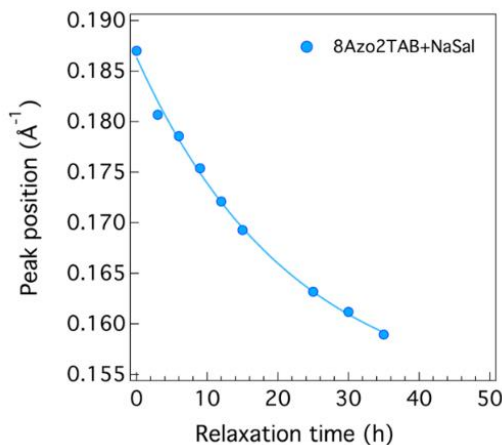


Figure 13 Thermal relaxation by SAXS for 8Azo2TAB/NaSal (18.75 mM/15.62 mM). Position of the maximum as a function of the relaxation time.

## VII.2 Self-assembly of 8Azo2TAB/sodium benzenesulfonate

The chemical structure of NaBenSulf is very close to that PSS monomer (Figure 14). But they show different phase behaviours when mixed with Azo-surfactants.

Using the same concentrations as for Azo-surfactant/PSS complexes, the mixture (8Azo2TAB/NaBenSulf 50 mM/100 mM,  $r=0.5$ ) precipitates. However, similarly to NaSal, for 8Azo2TAB/NaBenSulf 75 mM/62.5 mM,  $r = 1.2$ , reference concentration C), the mixture shows gel property (Figure 15). We can speculate that similar threadlike micelles are formed. But the differences in the chemical structure between NaSal and NaBenSulf may result in different micellar morphology that we propose to investigate hereafter.

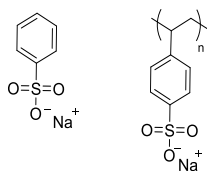


Figure 14 Chemical structures of sodium benzenesulfonate (NaBenSulf) (left) and poly(styrene sulfonate) (right).



Figure 15 Photos of 8Azo2TAB/NaBenSulf mixture (75 mM/62.5 mM) in dark state and under UV irradiation.

## VII.2.1 Study by NMR

The mixture 8Azo2TAB/NaBenSulf C/4 (18.75 mM/15.62 mM) has been analyzed by  $^1\text{H}$  NMR (Figure 16). The 8Azo2TAB/NaBenSulf mixture shows more broader peaks than their individual spectra. We clearly observe that the protons in the hydrophilic region of 8Azo2TAB ( $\text{H}_1$ ,  $\text{H}_2$ ,  $\text{H}_3$ ) are shifted upfield for the mixture. While, the protons of hydrophobic region ( $\text{H}_8 - \text{H}_{15}$ ) is not influenced by the addition of NaBenSulf. Hence, we can assume that NaBenSulf molecules are intercalated between hydrophilic ammonium head and participate to the micelle formation. This will further be proved by small-angle scattering study.

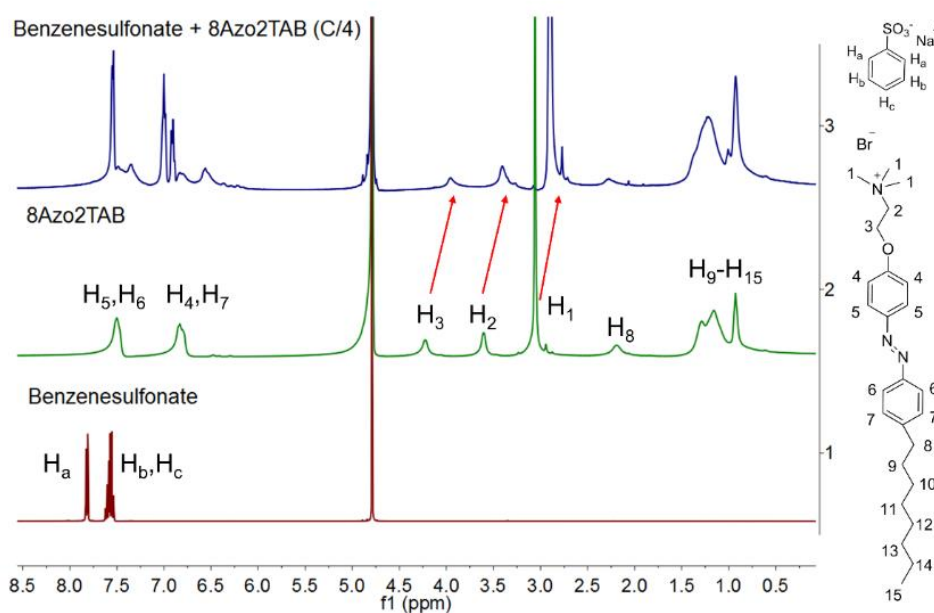


Figure 16  $^1\text{H}$  NMR spectra in  $\text{D}_2\text{O}$  of pure NaBenSulf 15.62 mM, pure 8Azo2TAB 18.75 mM and NaBenSulf/8Azo2TAB mixture (15.62 mM/18.75 mM).

### Photoconversion: determination of *trans/cis* ratio

The  $^1\text{H}$  spectra of the 8Azo2TAB/NaBenSulf mixture at the reference concentration C (75 mM/62.6 mM) are presented in Figure 17.

Under UV irradiation, two peaks at 3.05 ppm and 2.97 ppm are detected for protons of the ammonium head, corresponding to *trans* and *cis* isomers respectively. The *trans/cis* ratio can be roughly determined from the integrated intensities of these peaks and is equal to 36:64 in the stationary state. When blue light is applied, the *cis*→*trans* transition occurs and the *trans/cis* ratio reaches 73:27.

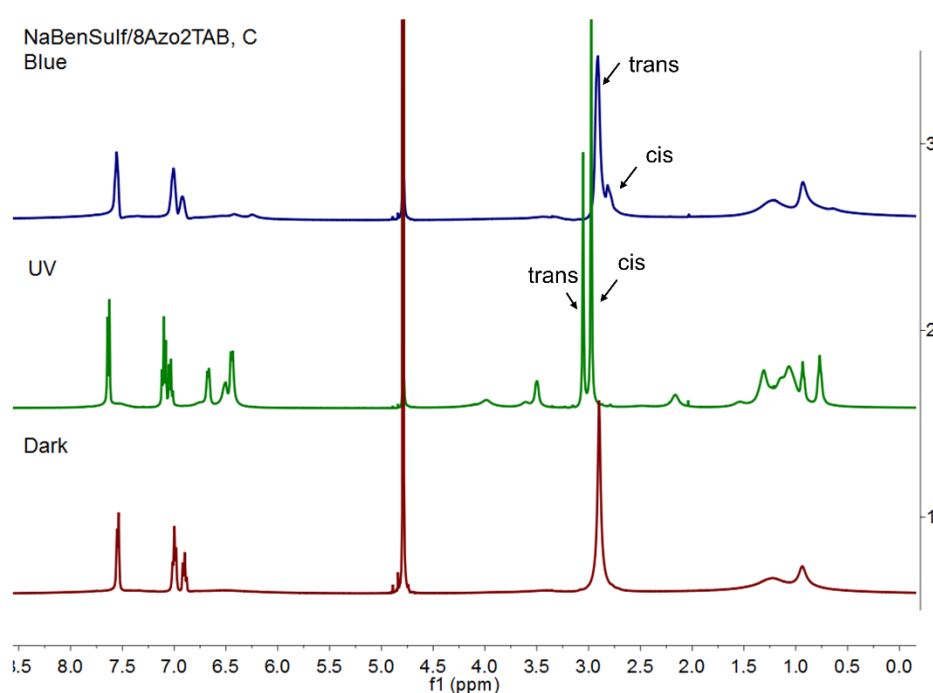


Figure 17  $^1\text{H}$  NMR spectra in  $\text{D}_2\text{O}$  for 8Azo2TAB/NaBenSulf C (75 mM/62.5 mM).

For the mixture C/4, the  $^1\text{H}$  NMR spectra are easier to analyze (Figure 18). The resonance peaks detected are narrower. Well-separated peaks are observed for the hydrophobic tail protons (Figure 18). The aromatic zone may be too chaotic to extract information, because the peaks for *trans* and *cis* isomers coexist with that of NaBenSulf. But for the  $\text{C}_2\text{H}_4$  spacer ( $\text{H}_2$ ,  $\text{H}_3$ ), well distinguished *trans* and *cis* peaks are detected. We found a *trans/cis* ratio of 13:87 at the equilibrium state. Inversely blue light triggers the *cis*→*trans* isomerization, the mixture recovers its initial viscosity. The resonance peaks are broader, but we can still distinguish the *trans*-peak at 2.93 ppm and the *cis*-peak at 2.82 ppm for the ammonium head ( $\text{H}_1$ ). The *trans/cis* ratio turns back to 84:16.

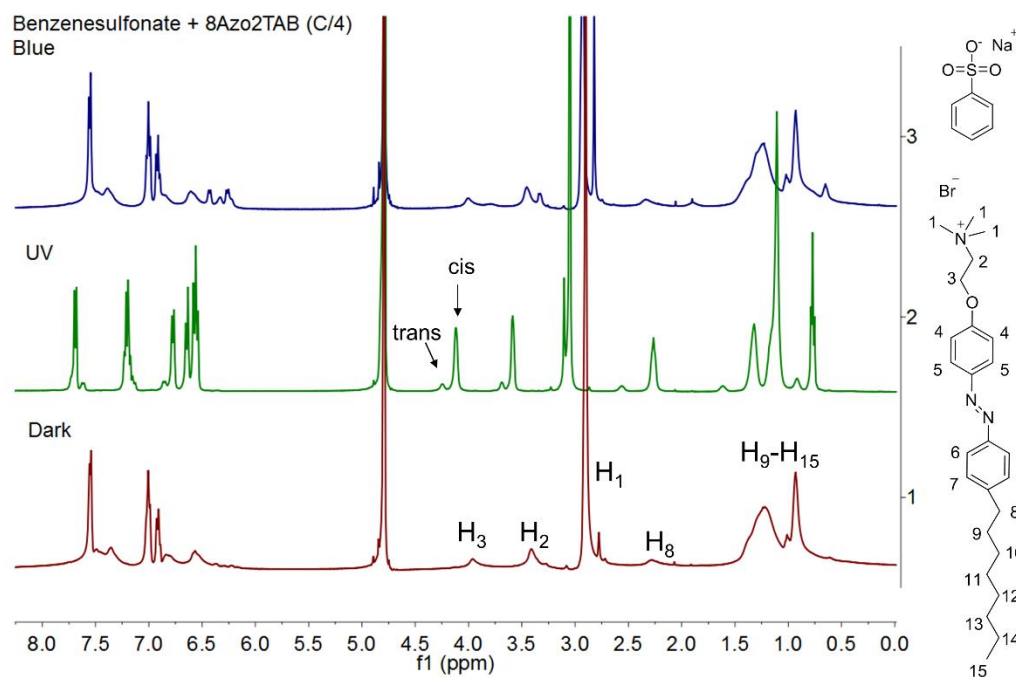


Figure 18  $^1\text{H}$  NMR spectra in  $\text{D}_2\text{O}$  for 8Azo2TAB/NaBenSulf C/4 (18.75 mM/15.62 mM).

## VII.2.2 Structural study

The strategy for the structural investigation of 8Azo2TAB/NaBenSulf systems is identical to that of 8Azo2TAB/NaSal. SAXS and SANS data are very similar with the exception that UV irradiation now leads to a well-defined systems. Hence, we have used the same models (dark state: elliptical cylinder for SANS and elliptical core-shell cylinder for SAXS; under UV radiation: prolate ellipsoid for SANS and core shell prolate ellipsoid for SAXS).

### VII.2.2.1 SANS measurements

A single concentration C/4 has been measured by SANS. The scattering curves are presented in Figure 19 (dark, UV). In the dark state, the intensity almost varies as  $q^{-1}$  for very low  $q$ . Under UV irradiation, we see the Guinier regime and almost find a plateau below  $0.05 \text{ \AA}^{-1}$ . The scattered intensity is close to that of a pure form factor, but the presence of a structure factor can still be detected below  $q \leq 0.03 \text{ \AA}^{-1}$ .

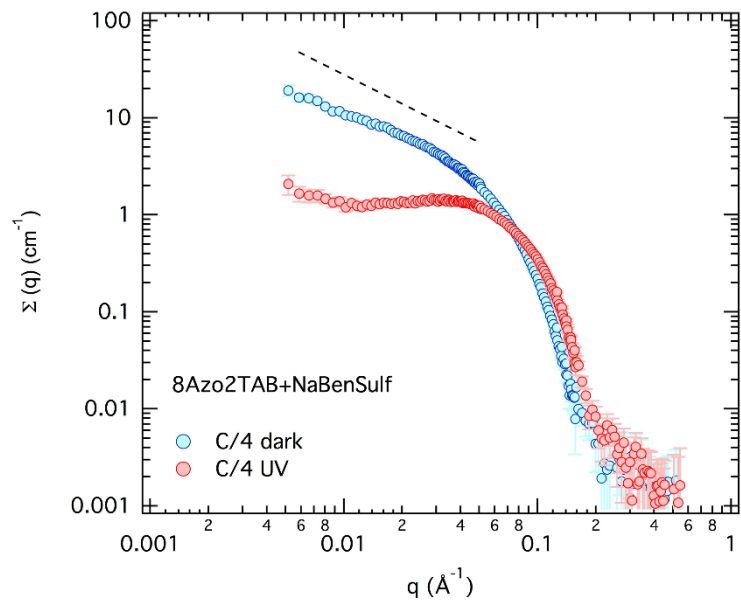


Figure 19 SANS patterns for 8Azo2TAB/NaBenSulf in dark and under UV irradiation at a concentration C/4 (18.75 mM/15.62 mM). Dash line indicates a  $q^{-1}$  decay.

We have fitted the data with an elliptical cylinder (dark state) and a prolate ellipsoid (UV) models. The volume fraction has been fixed to its theoretical value (0.0087) as well as the SLD of the deuterated water ( $\rho_{N D20}=6.38 \cdot 10^{10} \text{ cm}^{-2}$ ).

The fits are presented in Figure 20. They can reproduce well the experimental measurements. Final parameters are given in Table 6.

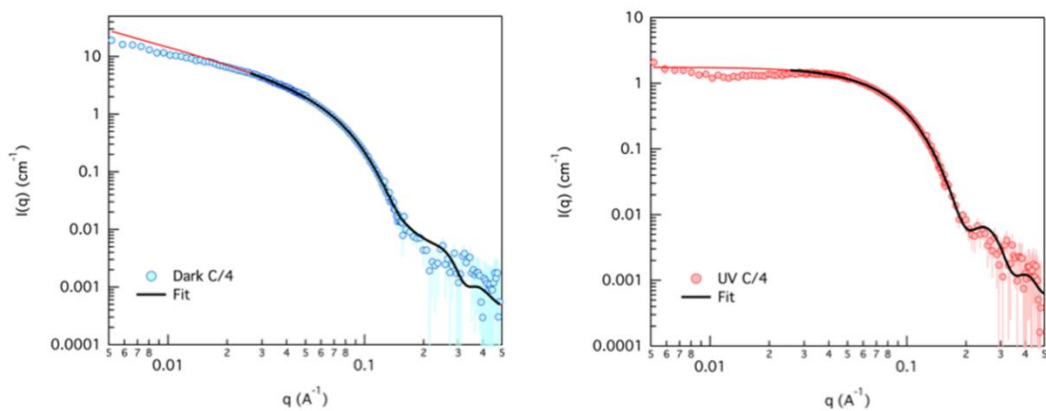


Figure 20 Fit of the SANS patterns at C/4. a) In the dark state using an infinite elliptical cylinder. b) Under UV irradiation using a prolate ellipsoid.

8Azo2TAB/NaBenSulf (C/4)	Dark (elliptic cylinder)	UV (prolate ellipsoid)
Volume fraction	0.0087*	0.0087*
Length (Å)	1000*	-
Minor radius (Å)	20.4	21.3
Major radius (Å)	33.1	39.7
Ellipticity (major/minor)	1.62	-
SLD cylinder ( $10^{10} \text{ cm}^{-2}$ )	1.18	1.19

Table 6 SANS Fit parameters. In the elliptic cylinder model, the section has two radii: the major and the minor. The ratio between the major and the minor radius gives the ellipticity. In the prolate ellipsoid, the major axis corresponds to the rotation axis. The cross-section perpendicular to the axis of symmetry is circular. Asterisks correspond to fixed parameters.

The structural parameters are very close to that of 8Azo2TAB/NaSal C/4. The description of the aggregate under UV radiation is however more accurate since the particles are now monodisperse. The shape of the aggregate is not dramatically modified by changing the aromatic salt. The SLD of the particle ( $1.18 \cdot 10^{10} \text{ cm}^{-2}$ ) is very close to that of the pure components ( $1.26 \cdot 10^{10} \text{ cm}^{-2}$ ).

#### VII.2.2.2 SAXS measurements

Typical SAXS measurements for different concentrations C and C/4 are presented in Figure 21 and Figure 22. The mixture C/2 is not studied here because it precipitates. 8Azo2TAB/NaBenSulf presents a maximum in between 0.1 and 0.2  $\text{\AA}^{-1}$  which is characteristic of micellar aggregates. This maximum is clearly modified under UV irradiation indicating a large modification of the micellar shape. Data normalized to the concentration are almost superposed at large  $q$ . The depth of the minimum is however higher under UV reflecting slight modification of the ellipticity or a smaller polydispersity.

From a general point of view, the local structure of the aggregates is preserved at different concentrations. At low  $q$ , we find small differences (below  $0.03 \text{ \AA}^{-1}$ ) due to the presence of a structure factor. The effects of structure factor almost disappear at C/4 but are still present. The fits have been only performed on the lowest concentrations using an adapted  $q$  range.

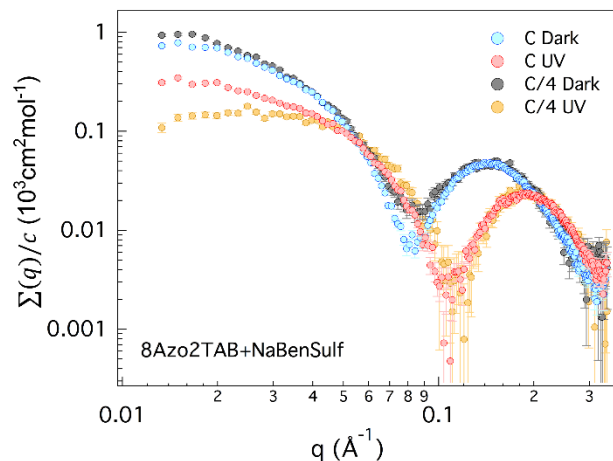


Figure 21 SAXS patterns normalized to the concentration, in dark and under UV radiation.

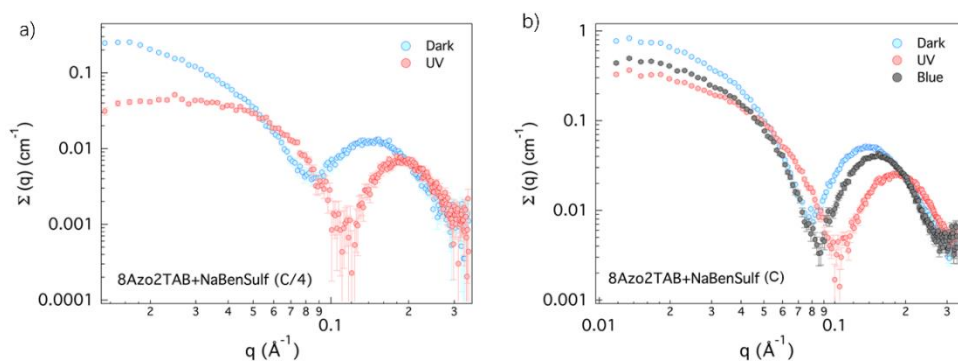


Figure 22 SAXS patterns of 8Azo2TAB/NaBenSulf in dark, under UV and blue irradiation. a) concentration C/4 (18.75 mM/15.62 mM); b) concentration C (75 mM/62.5 mM).

SAXS data have been fitted using an elliptic core-shell cylinder (dark state) and a prolate core-shell ellipsoid (under UV irradiation). The fits are given in Figure 23, the final parameters are in Table 7.

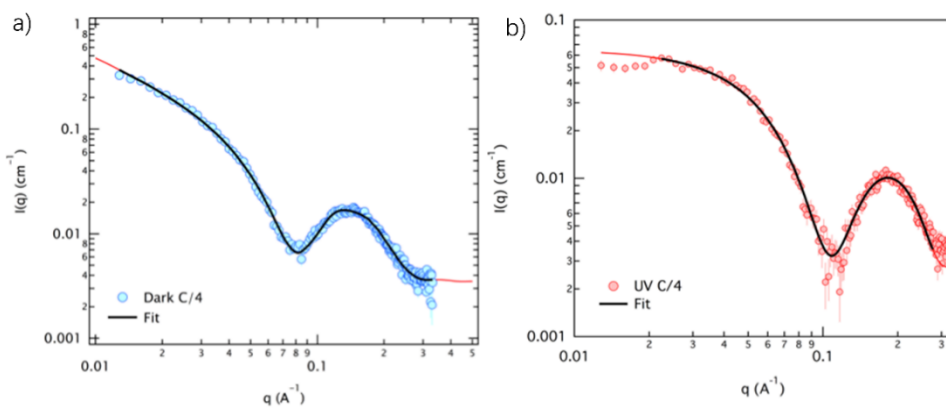


Figure 23 Fit of the SAXS patterns of 8Azo2TAB/NaBenSulf at C/4 (18.75 mM/15.62 mM). a) In the dark state using an infinite core-shell elliptical cylinder. b) Under UV irradiation using a prolate core-shell ellipsoid.

In the dark state (wormlike micelles), SANS and SAXS find very similar values for the cross section (major and minor radius of the elliptic cylinder: 33.1 and 20.4 Å; major and minor shell radius of the core-shell elliptic cylinder: 36.9 and 23.4 Å). The difference of 3-4 Å could reflect be the presence of a counterion layer.

Under UV (globular micelles), SANS and SAXS find identical values for the cross section (major and minor radius of the prolate ellipsoid: 39.7 and 21.3 Å, major and minor radius of the prolate ellipsoid: 38.8 and 23.6 Å). The difference is negligible.

8Azo2TAB/NaBenSulf (C/4)	Dark (elliptic core-shell cylinder)	UV (prolate core-shell ellipsoid)
Volume fraction	0.0086*	0.0086*
Length (Å)	1000*	-
Minor core radius (Å)	11.3	13.9
Major core radius (Å)	17.8	29.1
Minor shell radius (Å)	23.4	23.6
Major shell radius (Å)	36.9	38.8
Minor shell thickness (Å)	12.1	9.7
Major shell thickness (Å)	19.1	9.7
Ellipticity (major/minor)	1.58	-
SLD core ( $10^{10} \text{ cm}^{-2}$ )	7.60	7.52
SLD shell ( $10^{10} \text{ cm}^{-2}$ )	11.25	11.3

Table 7 SAXS fit parameters. In the elliptic core shell cylinder model, the section has four radii: the major and the minor shells and the major and the minor core. The ellipticity is identical for the core and the shell. In the prolate core shell ellipsoid, the major axis corresponds to the rotation axis. The cross section perpendicular to the axis of symmetry has a circular core-shell geometry. The thickness is held constant. Asterisks correspond to fixed parameters.

The SLD of the core (dark:  $7.60 \cdot 10^{10} \text{ cm}^{-2}$ , UV  $7.52 \cdot 10^{10} \text{ cm}^{-2}$ ) and the shell (dark:  $11.25 \cdot 10^{10} \text{ cm}^{-2}$ , UV  $11.3 \cdot 10^{10} \text{ cm}^{-2}$ ) coincide with that of the  $\text{C}_8\text{H}_{17}$  tail ( $7.56 \cdot 10^{10} \text{ cm}^{-2}$ ) and that of 8Azo2TAB/NaBenSulf ( $12.0 \cdot 10^{10} \text{ cm}^{-2}$ ).

Furthermore, the minor core radius (dark: 11.3 Å, UV: 13.9 Å) almost represents the size of the tail in its extended conformation ( $\approx 11.6$  Å). We definitely validate our previous description. The micellar aggregate has a core mainly composed of the  $\text{C}_8\text{H}_{17}$  tails of the surfactant and a shell made of azo and hydrophilic groups of the surfactant in which NaBenSulf is introduced. This is in

accordance with NMR results. Under UV irradiation, we note a large decrease of the shell thickness in which Azo groups are embedded.

We have also tested the structural reversibility of the system (concentration C) by using alternative UV and blue light irradiation. The variation of the position of the maximum (around  $0.2 \text{ \AA}^{-1}$ ) is shown in Figure 24. A good reversibility is observed.

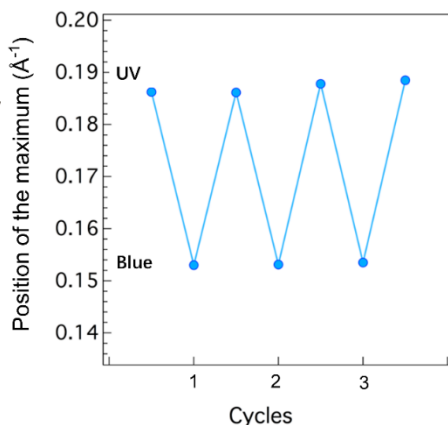


Figure 24 Structural Reversibility followed by SAXS in 8Azo2TAB/NaBenSulf mixture C (75 mM/62.5 mM)

We studied the thermal relaxation (concentration C/4) by measuring the variation of the position of the maximum with time (at  $t = 0$ , we are in the photosationary state and we stop the irradiation). Results are presented in Figure 25. A characteristic time  $\tau$  of 22.0 h was obtained. It is almost the same value as for 8Azo2TAB/NaSal mixture C/4 (22.2 h). For comparison, the characteristic time for 8Azo2TAB/PSS (50 mM/100 mM) is only 8.6 h.

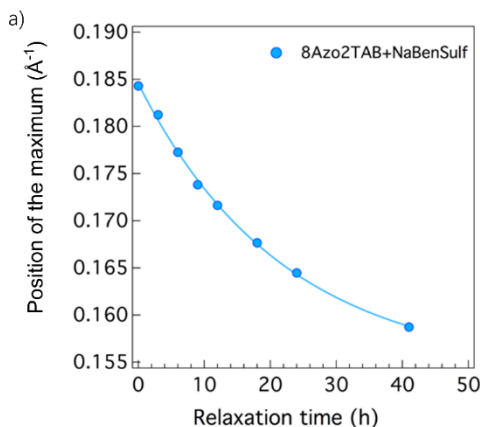


Figure 25 Thermal relaxation by SAXS. Position of the maximum as a function of the relaxation time. in 8Azo2TAB/NaBenSulf mixture C/4 (18.75 mM/15.62 mM)

### VII.3 Comparison of wormlike micelles systems

The growth of 8Azo2TAB micelles and the formation of wormlike structures (clearly demonstrated by cryo-TEM) is induced by the addition of both NaSal and NaBenSulf. This phenomenon results from the electrostatic interaction between the cationic headgroup of the surfactants and the anionic co-surfactants, but also, from the hydrophobic interaction and probably the  $\pi$ - $\pi$  interaction between aromatic groups. The addition of aromatic salts changes the “average” critical packing parameter of the surfactant (as presented in Chap II.2.2) and finally the shape of the micellar assembly. In the dark state, it favours the formation of wormlike micelles, while under UV it provokes the formation of globular particles. A reversible gel $\leftrightarrow$ fluid transition is observed under alternative UV/bleu irradiation.

According to NMR studies, protons of the hydrophilic region (H<sub>1</sub>-H<sub>3</sub>) are shifted upfield with addition of aromatic salts, while the hydrophobic tails were almost unchanged. Aromatic anions are therefore intercalated into the hydrophilic layer of the micelles due to the electrostatic interaction with cationic ammonium headgroups. The aromatic region is quite complicated to analyze due to the coexistence of protons of azobenzene and aromatic anions. But similar investigation on 8Azo2/PSS systems demonstrates that the external added aromatic rings of PSS interact with azobenzene moieties. We assume here that the aromatic salts (which is more mobile in the solution than the PSS monomer) may also penetrate in the aggregate even more deeply and interact with phenyl groups of azobenzene moiety due to the  $\pi$ - $\pi$  interaction

These arguments have been validated by SANS and SAXS experiments. Wormlike micelles observed in the dark state have been modelled by elliptic cylinders. Globular particles found under UV radiation were modelled by prolate ellipsoids. SAXS have evidenced the presence of a core-shell organization within the objects. The core is made of alkyl tail (C<sub>8</sub>H<sub>17</sub>) while the shell contains mainly the Azo groups, the spacer (C<sub>2</sub>H<sub>4</sub>) and the hydrophilic headgroup of the surfactant, but also, the aromatic anions.

In the dark state, both wormlike micelles have a minor radius of 20 – 23 Å and a major radius of 33 – 37 Å. Under UV irradiation, the wormlike micelles break and form smaller aggregates resulting in a significant decrease of viscosity (Figure 26). At the photostationary state, the 8Azo2TAB/NaSal mixture (C/4) contains 74% of cis isomer (*trans/cis* ratio 26:74) resulting in a situation where globular shapes

and elongated aggregates coexist. In average, we found a prolate ellipsoid with radii of 25 Å and 61 Å. For 8Azo2TAB/NaBenSulf mixture (C/4), we have 87% of *cis* isomers (*trans/cis* ratio 13:87), the system is more homogeneous. The globular aggregates have a minor and major radius of 21 – 24 Å and 39 - 40 Å respectively. 8Azo2TAB/NaBenSulf is certainly the best candidate to elucidate the mechanism of the structural transition.

Since the majority of isomers are in their *cis* form, and since they are located in the shell of the micelle, one must find structural difference at the local scale in between dark and irradiated states. The thickness of the shell that varies between 12 and 19 Å in the dark state (since we choose a model with constant ellipticity, we have one thickness for minor axis and one for the major) is reduced to 9.7 Å under UV. The difference of about 5 Å (in average) is a direct consequence of the conformational transition between *trans* to *cis* conformers.

In the dark state, the fully extended size of the 8Azo2TAB is around 29.2 Å in its fully extended form, or 18.2 Å if we remove the contribution of the alkyl tail. We must therefore introduce the Azo group, the spacer (C<sub>2</sub>H<sub>4</sub>) and the hydrophilic headgroup (18.2 Å long) in a shell of thicknesses in between 12 and 19 Å, which appears clearly feasible. Under UV irradiation, the shell thickness is reduced to 10 Å. With additional condition that the polar head lies at the surface of the micelle (in contact with water) and that one benzene of the Azo group is in contact with the micellar core.

The Azo groups are literally sandwiched in the thin shell. The critical packing parameter is naturally increased leading to a morphologic transition.

Salicylate ions are more effective in promoting the micellar growth (leading to more viscous mixtures). This is probably due to the presence of -OH in NaSal molecules that may create hydrogen bonds with surrounding water and stabilize the micellar assembly<sup>5</sup>.

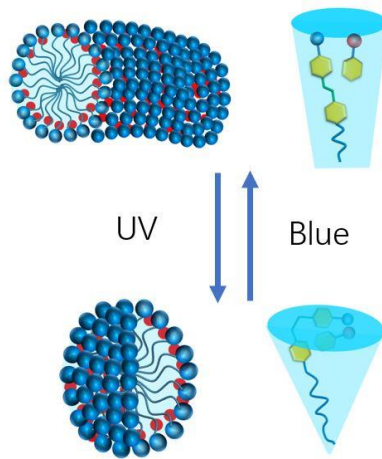


Figure 26 Schematic representation of gel-fluid transition

## References:

- (1) Kreke, P. J.; Magid, L. J.; Gee, J. C.  $^1\text{H}$  and  $^{13}\text{C}$  NMR Studies of Mixed Counterion, Cetyltrimethylammonium Bromide/Cetyltrimethylammonium Dichlorobenzoate, Surfactant Solutions: The Intercalation of Aromatic Counterions. *Langmuir* **1996**, *12* (3), 699–705.
- (2) Eriksson, J. C.; Gillberg, G. NMR Studies of the Solubilisation of Aromatic Compounds in Cetyltrimethylammonium Bromide Solution. In *Surface Chemistry*; Ekwall, P., Groth, K., Eds.; Academic Press, 1965; pp 148–156.
- (3) Shikata, T.; Hirata, H.; Kotaka, T. Micelle Formation of Detergent Molecules in Aqueous Media. 2. Role of Free Salicylate Ions on Viscoelastic Properties of Aqueous Cetyltrimethylammonium Bromide-Sodium Salicylate Solutions. *Langmuir* **1988**, *4* (2), 354–359.
- (4) Combet, J.; Lorchat, P.; Rawiso, M. Salt-Free Aqueous Solutions of Polyelectrolytes: Small Angle X-Ray and Neutron Scattering Characterization. *Eur. Phys. J. Spec. Top.* **2012**, *213*, 243–265.
- (5) Bijma, K.; Rank, E.; Engberts, J. B. F. N. Effect of Counterion Structure on Micellar Growth of Alkylpyridinium Surfactants in Aqueous Solution. *J. Colloid Interface Sci.* **1998**, *205* (2), 245–256.



## General Conclusion and Perspectives

This thesis aims to study model photo-sensitive PEs systems in aqueous solutions. The photo-sensitivity arises from the presence of azobenzene groups. We are more specifically interested in the photoconversion behaviour, the structural organization and the structural variation observed under UV irradiation.

Three different light-responsive systems have been synthesized and studied, they are:

- Azo-modified sodium polyacrylates
- Azo-surfactant/PSS complexes
- Azo-surfactant/co-surfactant wormlike micelles

These three systems have been investigated by UV-Vis spectroscopy, NMR, small-angle scattering and cryo-TEM leading to the following conclusions.

### ➤ **Azo-modified sodium polyacrylates**

The grafting of Azo moiety on side group of sodium polyacrylates increases the hydrophobicity of PEs and leads to the formation of spherical photo-sensitive aggregates in aqueous solution. The structure of these aggregates depends on the polymer length and the Azo fraction as well as the concentration.

We find that compact core-shell aggregates are formed for the long chains ((PAA-AzO<sub>0.11</sub>)<sub>738</sub>RAFT). The dense core is made of the Azo groups while the shell is composed of polyion segments. Only a very limited number of chains are inserted in the aggregate. Upon UV irradiation, aggregates are partly disassembled and form smaller particles.

For short chains with 11% Azo, we still find macromolecular association, but the structural organization now varies with the concentration. Different regimes are observed. Short chains with 15% Azo show similar organization, but the core is more compact. In these systems, it is possible to find a concentration range in which loose aggregates can assemble and disassemble by simple light stimulus. This regime could be interesting for certain applications such as active compound carrier. The hydrophobic core may encapsulate the active compound and release it under UV irradiation. The aggregate size can be adjusted by varying the polymer length and the Azo molar fraction.

In these systems, Azo units are grafted randomly on polydisperse PE chains. The polydispersity can affect the structural organisation and increases the

difficulty in structural studies. The synthesis of monodisperse Azo-polymers with a regular distribution of Azo unit along the PE chain may be a solution. This might be realized by controlled copolymerization. It could also be interesting to decrease the Azo content along PE chains. By changing the electrostatic repulsion between the polyions segments we could imagine being able to completely break the hydrophobic core of long chains under UV.

➤ **Azo-surfactant/PSS complexes**

Pure 8Azo2TAB and 4Azo2TAB surfactants form photo-sensitive micelles in aqueous solutions. They can be described by oblate ellipsoidal core-shell particles in which the core contains the hydrophobic alkyl tails and the shell (still partly hydrophobic) contains the rest of the molecule. Under irradiation, the *trans* to *cis* photoconversion of the Azo group changes the critical packing parameter and the hydrophobicity of the surfactant: a significant decrease in micellar size is observed.

Azo-surfactant and oppositely charged PSS interact strongly due to the electrostatic interaction. The <sup>1</sup>H NMR measurements clearly confirm the formation of aggregates and the strong interaction between the aromatic ring of PSS and the shell of the micelles (polar head, Azo unit): polyions participate to the micellization process. The structural organization of Azo-surfactant and PSS in the complex have been studied separately by SANS using contrast variation. We find the existence of globular aggregates (pearls) composed of both surfactants and polyions. These aggregates have a core-shell organization: the core contains only the alkyl chains of surfactant while the shell is composed of Azo moiety, polar head and portions of polyions. The signature of pearl-pearl correlations is observed and is consistent with a pearl necklace organisation. This typical structure is confirmed by Cryo-TEM images. Under irradiation, the structural modification is very modest. The pearl size is only reduced (in a reversible way) by around 30%.

In this study we definitely demonstrate the existence of a pearl necklace organization in Azo-surfactant/PSS complexes. We also show a small structural photo-sensitivity under UV. This formulation may represent a model for photoresponsive systems. However, the photo-response needs to be improved.

➤ **Azo-surfactant/co-surfactant wormlike micelles**

Wormlike micelles are formed for 8Azo2TAB with addition of co-surfactant (NaSal or NaBenSulf). The wormlike micelles can be destabilized and turn into smaller ellipsoidal micelles under UV irradiation. SAXS and SANS studies validate

this scenario and give a precise picture of the structural modification at a very local scale. The *trans* ↔ *cis* transformation of the isomers at the molecular level is propagated at the nanometric scale (self-assembly level: wormlike micelles ellipsoidal micelles) and amplified at the macroscopic scale leading to a reversible gel ↔ fluid transition. We have a nice example of a macroscopic property that can be triggered by simple UV irradiation. Rheological studies on these systems could certainly reveal interesting effects especially in relation with the concentration and the nature of the co-surfactant.

The presence of multivalent counterions -in general- can modify the structural organization of PE solutions<sup>1,2</sup> and control the conformation and the compaction of polyions<sup>3</sup>. Thus, Azo-containing counterions can be a new strategy for the photo-control of polymeric systems (in a non-covalent way). This strategy avoids the synthesis of Azo-modified polymers while the Azo fraction can be adjusted easily.

There are few pioneering works about Azo-dications. Zinchenko et al.<sup>4</sup> reported an Azo-containing dication which can match or mismatch the distance of two DNA adjacent phosphates leading to a reversible DNA compaction under light stimulus. A light-induced shape modification has been reported for self-assemblies of poly(diallyldimethylammonium chloride) (PDADMAC) and oppositely charged Azo-dication (Ay38)<sup>5</sup>. PDADMAC/Ay38 forms long flexible cylinders with a large elliptical cross-section in the dark state that turns into a core-shell ellipsoid organization under UV.

We have synthesized an Azo-dication counterion and studied Azo-dication/PSS solutions by SAXS and SANS. The preliminary results are presented in appendix e). We find that Azo-divalent counterions interact with polyions and re-organize along the polyions in solution. A structural modification is observed under UV irradiation. Data analysis are going on in order to understand their structural organization (form factor and dispersion state), the nature of the interaction and the photoinduced effects.

## References:

- (1) Liu, X.; Luo, S.; Ye, J.; Wu, C. Effect of Ca<sup>2+</sup> Ion and Temperature on Association of Thermally Sensitive PAA-b-PNIPAM Diblock Chains in Aqueous Solutions. *Macromolecules* **2012**, *45* (11), 4830–4838.
- (2) Hansch, M.; Hämisch, B.; Schweins, R.; Prévost, S.; Huber, K. Liquid-Liquid Phase Separation in Dilute Solutions of Poly(Styrene Sulfonate) with Multivalent Cations: Phase Diagrams, Chain Morphology, and Impact of Temperature. *J. Chem. Phys.* **2018**, *148* (1), 014901.
- (3) Bloomfield, V. A. DNA Condensation by Multivalent Cations. *Biopolymers* **1997**, *44* (3), 269–282.
- (4) Zinchenko, A. A.; Tanahashi, M.; Murata, S. Photochemical Modulation of DNA Conformation by Organic Dications. *ChemBioChem* **2012**, *13* (1), 105–111.
- (5) Mariani, G.; Krieger, A.; Moldenhauer, D.; Schweins, R.; Gröhn, F. Light-Responsive Shape: From Micrometer-Long Nanocylinders to Compact Particles in Electrostatic Self-Assembly. *Macromol. Rapid Commun.* **2018**, *39* (17), 1700860.

---

## Appendix

### a) UV-Vis calibration curve of AzoC4Br for $\tau_{azo}$ determination and error calculation

A calibration curve of AzoC4Br was established. A mother solution (SM) was prepared. Other solutions were prepared by dilution. THF/H<sub>2</sub>O 1/1 was used as solvent to have a good solubility of both AzoC4Br and azo containing sodium polyacrylate. Each concentration was measured three times to have an average value.

#### Mother solution

$m=5.66$  mg,  $\Delta m = 0.02$  mg (error in mass measurement)

$V_0=250$  ml,  $\Delta V_0 = 0.15$  mL (error in volume)

$C_{SM}=6.79 \cdot 10^{-5}$  mol/L

#### Diluted solutions

$$C = C_{sm} \frac{v_{sm}}{V} = \frac{m}{V_0} \frac{v_{sm}}{V}$$

$m$  mass of AzoC4Br,  $V_0$  volume of mother solution,  $v_{sm}$  withdrawn volume by micropipette,  $V$  volume of diluted solution

$\Delta v_{sm}/v_{sm}$  was obtained from the accuracy of 500  $\mu$ L micropipette (2.4 %)

$\Delta V/V$  depends on the used volumetric flask

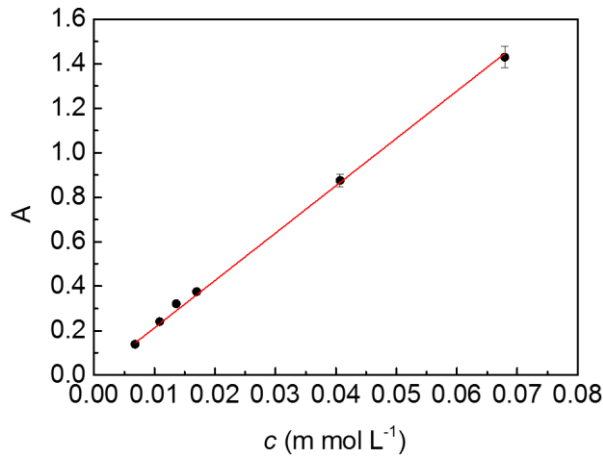
$$\frac{DC}{C} = \frac{Dm}{m} + \frac{DV_0}{V_0} + \frac{Dv_{sm}}{v_{sm}} + \frac{DV}{V}$$

$\Delta C/C$  was around 3.3 %

#### Calibration Curve

It is found that

$A = (21278 \pm 221) * C$  ,  $R^2 = 0.99935$



### Solution of azo containing sodium polyacrylate and $\tau_{azo}$ determination

A solution of PAA-Azo at an appropriate concentration was prepared for UV-Vis measurements. Three measurements were performed for each sample.

$m$  mass of polymer

$V$  volume of prepared solution

$A$  measured absorbance for a concentration  $C$

$$A = (21278 \pm 221) * C$$

From which we can determine the concentration of azo unit in solution:  $C = A/\epsilon$

Number of moles of monomer 2 (which contains AzoC4Br unit):

$$n_2 = C * V = A/\epsilon * V$$

Mass of monomer 2 in solution:

$$m_2 = C * V * M_2 = C * V * 324,38$$

Mass of monomer1 in solution (sodium acrylate):

$$m_1 = m - m_2$$

Number of moles of monomer1 (sodium acrylate):

$$n_1 = m_1/M_1 = m_1/94.04$$

Ratio of monomers 1 and 2 is  $R = n_1/n_2$

Molar fraction of azo unit  $\tau = \frac{1}{R+1}$

$$\tau = \frac{1}{1 + \frac{n_1}{n_2} \epsilon}$$

$$\tau = \frac{1}{1 + \frac{m - n_2 M_2}{M_1 n_2} \epsilon}$$

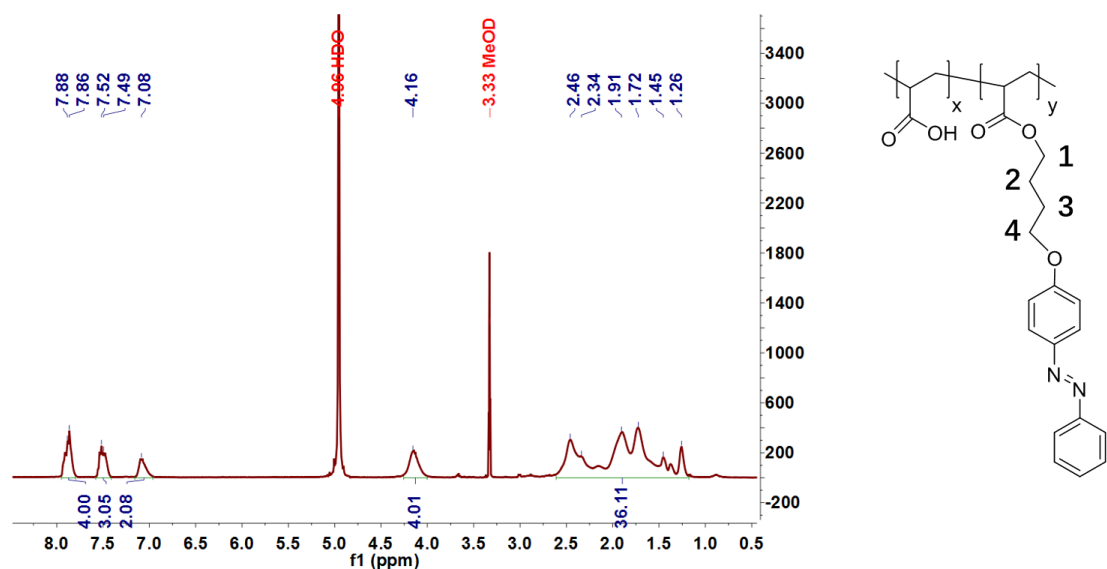
$$\tau = \frac{1}{1 + \frac{1}{M_1} \left( \frac{m \epsilon}{AV} - M_2 \right) \epsilon}$$

where  $m$  (mg) is the mass of azo containing polymer used for solution preparation;  $V$  (mL) is the total volume of the prepared solution;  $A$  is the measured absorbance;  $M_1$  (g.mol<sup>-1</sup>) is the molar mass of the non-functionalized monomers;  $M_2$  (g.mol<sup>-1</sup>) is the molar mass of the functionalized monomers.

$$Dt = \frac{t^2}{M_1} \frac{me}{AV} \left( \frac{Dm}{m} + \frac{DV}{V} + \frac{De}{e} + \frac{DA}{A} \right)$$

Synthesized polymer	$\tau_{azo}$ by UV-Vis
(PAA-AZO <sub>0.11</sub> ) <sub>42</sub> Sigma	10.7 ± 0.4 %
(PAA-AZO <sub>0.15</sub> ) <sub>39</sub> Sigma	15.1 ± 1.5 %
(PAA-AZO <sub>0.15</sub> ) <sub>54</sub> RAFT	15.0 ± 0.6 %
(PAA-AZO <sub>0.11</sub> ) <sub>738</sub> RAFT	11.4 ± 0.3 %

## b) NMR for determination of $\tau_{azo}$ and Calculation of error



$$\text{Azo molar fraction } y = \frac{3}{4} \times \frac{R}{1-R}$$

Error calculation

$$\frac{\Delta y}{y} = \frac{\Delta R}{R(1-R)}$$

For example, (PAA-AzO<sub>0.11</sub>)<sub>42Sigma</sub>

$R = 0.1108$ ,  $y = 9.3 \%$

Aromatic Peak at 7.88 pm: error about 10%

Integral for 4 protons at 4.16 ppm, error =  $(4.16-4)/4 = 4\%$

$$\frac{\Delta R}{R} = \frac{\Delta Area1}{Area1} + \frac{\Delta Area2}{Area2} = 0,14$$

$$\frac{\Delta y}{y} = \frac{\Delta R}{R(1-R)} = 0.157$$

$$y = 9.3 \% \pm 1.5 \%$$

Synthesized polymer	$\tau_{azo}$ by NMR
(PAA-AzO <sub>0.11</sub> ) <sub>42Sigma</sub>	9.0 % $\pm$ 1.9 %
(PAA-AzO <sub>0.15</sub> ) <sub>39Sigma</sub>	18.0 % $\pm$ 3.3 %
(PAA-AzO <sub>0.15</sub> ) <sub>54RAFT</sub>	13.7 % $\pm$ 2.6 %
(PAA-AzO <sub>0.11</sub> ) <sub>738RAFT</sub>	9.3 % $\pm$ 1.5 %

### c) Synthesis of poly(sodium styrene sulfonate) PSS

Hydrogenated and deuterated PSS (PSS-H and PSS-D) were synthesized by J.-P. Lamps at Institut Charles Sadron. The synthesis consists of three steps. The first step is the anionic polymerization to obtain polystyrene. The next step is the sulfonation of the polystyrene using a method developed by Makowski *et al.* PSS was then dialyzed at pH 12 and finally obtained by freeze-drying. The degree of sulfonation was determined by <sup>1</sup>H NMR for the hydrogenated PSS. The degree of sulfonation for deuterated PSS was calculated by elemental analysis. Both PSS-H and PSS-D were 100% sulfonated. PSS-H and PSS-D were characterized by SEC using a mixture of H<sub>2</sub>O/ACN (40% ACN and 0.1 M NaNO<sub>3</sub>+NaN<sub>3</sub>) as eluent.

	$M_w$ (g mol <sup>-1</sup> ) 10 <sup>5</sup>	$M_n$ (g mol <sup>-1</sup> ) 10 <sup>5</sup>	$I_p$	DP <sub>w</sub>	%H <sub>2</sub> O
NaPSS-h	2.20	2.08	1.06	1078	15.9%
NaPSS-d	2.11	1.95	1.08	990	16.5%

Table 1 SEC results: weight-average molecular weight ( $M_w$ ), number-average molecular weight ( $M_n$ ), polydispersity index ( $I_p=M_w/M_n$ ) and weight-average degree of polymerization ( $DP_w$ ).



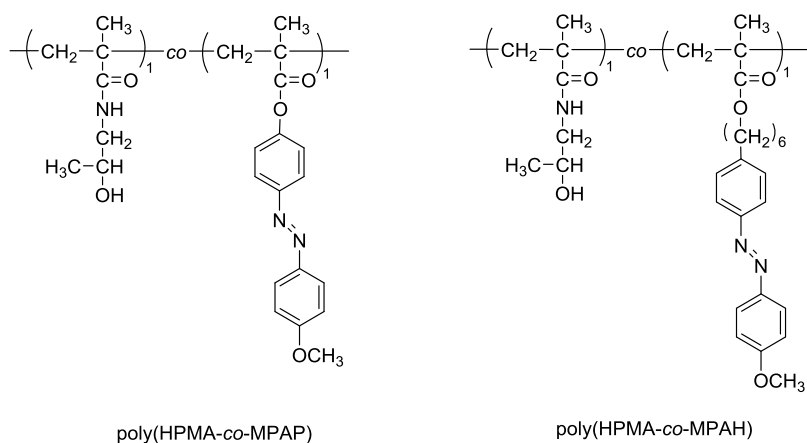


Figure 1 Structure of copolymers poly(HPMA-co-MPAP) and poly(HPMA-co-MPAH).

As shown in Figure 2, copolymers containing push-pull azo chromophores were obtained by radical polymerization between Azo-pendent methacrylate and methacrylic acid<sup>2</sup>. The reaction was carried out in DMF initiated by AIBN at 60°C for 24h. The Azo-monomer content was ranged from 15 to 37 mol.%. Colloidal particles were formed by slow addition of various concentrations of aqueous NaOH to the copolymer THF solutions. The colloid size varied with the molar ratio of the Azo-monomer and the quantity of added NaOH solution. Nevertheless, there was no further investigation under UV irradiation.

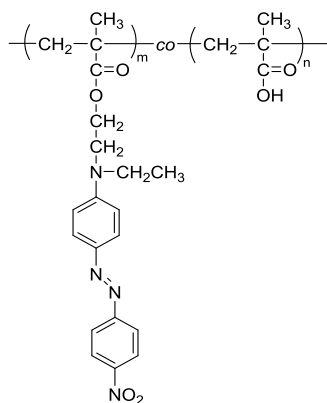


Figure 2 Structure of amphiphilic copolymer.

The synthesis of amphiphilic methacrylates containing hydrophilic oligo(oxyethylene) segments and Azo moieties has been attempted by radical homopolymerization. Methacrylates (MEn) were introduced in benzene at 60°C for 24h in the presence of AIBN (Figure 3). However, the homopolymerization of MEnME did not occur neither in the same condition of MEn nor in DMSO at 70°C for 24h. this is likely due to the formation of stable radicals that are unable to sustain the chain propagation<sup>3</sup>.

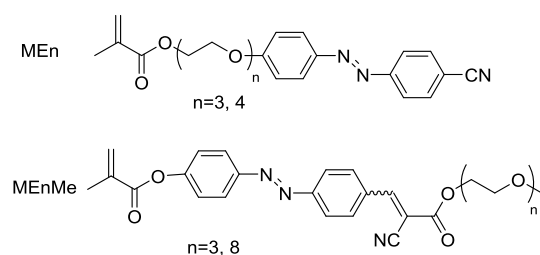


Figure 3 Structure of Azo-containing monomers MEn and MEnME.

The copolymerization of a functional monomer (containing the Azo) and a hydrophilic monomer may be the straightforward approach. Unfortunately, this method does not work for all the monomers such as the example of MEnMe shown in Figure 3. Azobenzene is known to have strong inhibition to the radical polymerization process. The solvent, temperature, type and amount of initiator must be chosen carefully.

The radical copolymerization is badly controlled, copolymers have usually a large polydispersity. An alternative method is the post-functionalization of hydrophilic well-defined polymers. Precursor polymers with reactive groups can be readily prepared by classical polymerization process.

A series of **random copolymers** (Figure 4) containing a minor fraction of octadecylamine and/or a primary Azo-amine were synthesized by Pouliquen et al.<sup>4</sup>. The grafting procedure was carried out in N-methyl-2-pyrrolidone through successive reactions of amines (octadecylamine and/or the azobenzene derivative) on poly(acrylic acid), in the presence of 1.2 eq of dicyclohexylcarbodiimide as activating agent.

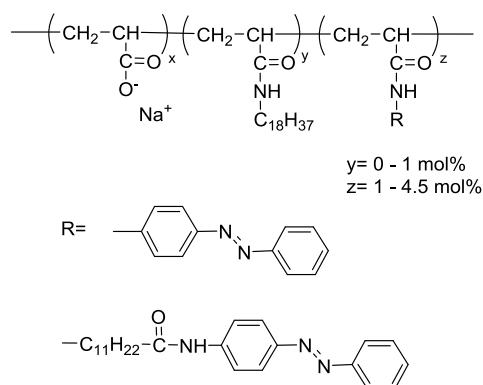


Figure 4 Structure of Azo-modified poly(acrylic acid).

Poly(acrylic acid) based Azo-polyelectrolyte was obtained by post-modification of an active precursor polymer poly(acryloyl chloride)<sup>5</sup>. Different azo compounds containing a hydroxyl group could be grafted on the polymer chains through esterification (Figure 5 a). The degree of functionalization was about 36%. The

corresponding Azo-polyelectrolytes were formed by the hydrolysis of unreacted acyl chloride groups. Another successful method was also proposed by the authors. An epoxy-based polymer could be post-functionalized by the azo-coupling reaction to form polymers with donor-accept type azo chromophores (Figure 5 b). The conversion of the side chain anilino moieties could reach near 100% by using diazonium salt in excess.

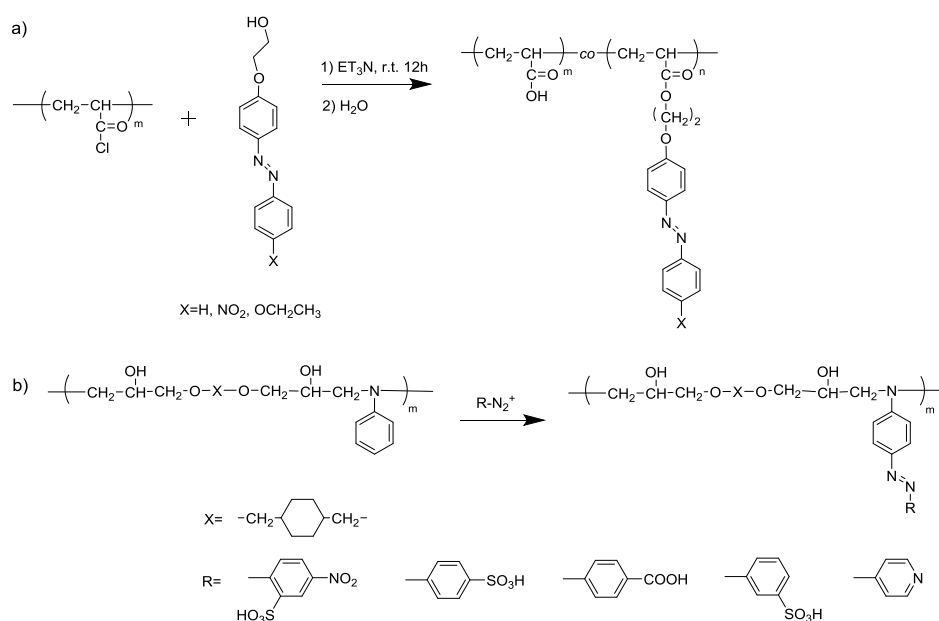


Figure 5 a). Scheme of the synthesis of poly(acrylic acid) based Azo-polyelectrolytes; b). Scheme of the synthesis of epoxy based Azo-polyelectrolytes.

Above-mentioned methods allow to synthesize a large variety of homo and random amphiphilic Azo-polymers. The conventional radical polymerization usually leads to polymers of high polydispersity. Another strategy is the 'living' radical polymerization. **Diblock** or **triblock Azo-polymers** with well defined structures can be prepared by atomic transfer radical polymerization (ATRP) or reversible addition-fragmentation transfer polymerisation (RAFT).

An example is given in Figure 6. A poly(ethylene glycol) block (PEGBr) as macroinitiator was first prepared by reaction between PEG monomethyl ether and 2-bromo-2-methylpropionyl chloride<sup>6</sup>. Then the ATRP polymerization of Azo-monomer was carried out at 80°C by using Cu(I)Cl complexed with HMTETA as the catalyst and PEGBr as the initiator. The polymerization degree of Azo-monomer was well controlled in a range from 24 to 92. Block Azo-polymers with narrow polydispersity ( $PI = 1.08 - 1.10$ ) from 13 200 to 47 500 g mol<sup>-1</sup> were obtained. Such block polymers were used to form thin films with liquid crystalline phases.

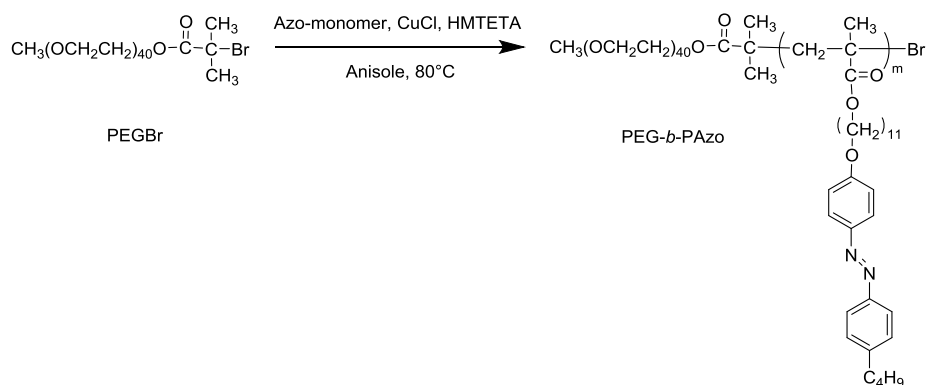


Figure 6 Synthesis route of block copolymer PEG-*b*-PAzo.

Diblock copolymers composed of Azo-containing polymethacrylate and poly(tert-butyl acrylate) (PAzoMA-*b*-PtBA) were synthesized via ATRP polymerization<sup>7</sup>. A subsequent selective hydrolysis of PtBA yielded poly(acrylic acid) (PAA). Thus, amphiphilic diblock copolymers of PAzoMA-*b*-PAA were obtained. After the hydrolysis, there remained 10-40% residual tBA units in the PAA block. Therefore, the PAA block was weakly hydrophilic. Reversible changes in micellar aggregates were achieved under UV and visible light illumination.

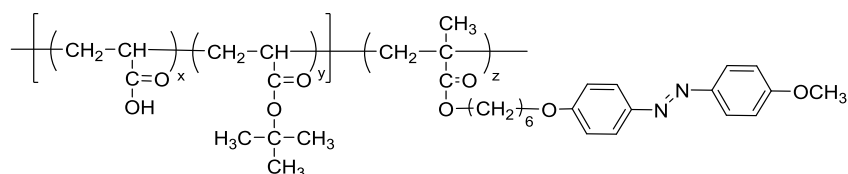


Figure 7 Synthesis route of diblock copolymer PAzoMA-*b*-PAA.

The macro-RAFT agent, poly(N-isopropylacrylamide) capped with dithiobenzoate (PNIPAM-SC(S)Ph) was firstly synthesized by RAFT polymerization in THF at 70°C using dithiobenzoate derivatives as the chain transfer agent<sup>8</sup>. Then this agent was used for the RAFT polymerization of Azo containing monomer to yield the diblock amphiphilic copolymer PNIPAM-*b*-PAzoM (PI= 1.2) (Figure 8).

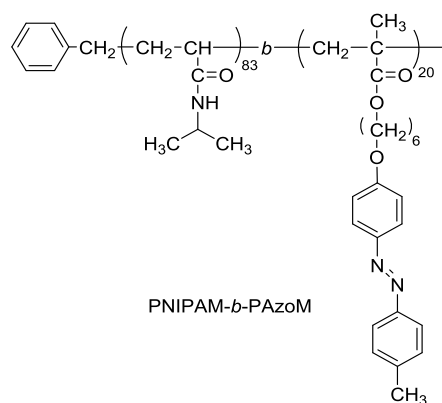


Figure 8 Structure of diblock copolymer PNIPAM-*b*-PAzoM.

A unique synthesis method was developed by Wang et al.<sup>9</sup>. The block copolymer was synthesized via the combination of a macromolecular azo coupling reaction and the RAFT polymerization method (Figure 9). The agent CTA-N-Ph was designed to have a suitable terminal group for the azo coupling. One polystyrene block with terminal anilino functionality (PS-N-Ph) was formed by RAFT polymerization in DMF at 60°C for 40 h using the designed agent (CTA-N-Ph). The other block, a diazonium salt mPEG-N<sub>2</sub><sup>+</sup> was prepared from aniline functionalized PEG chain (mPEG-NH<sub>2</sub>). The macromolecular azo coupling reaction between the above two polymer blocks in DMF gives an amphiphilic block Azo-polymer (PEG-*b*-PS).

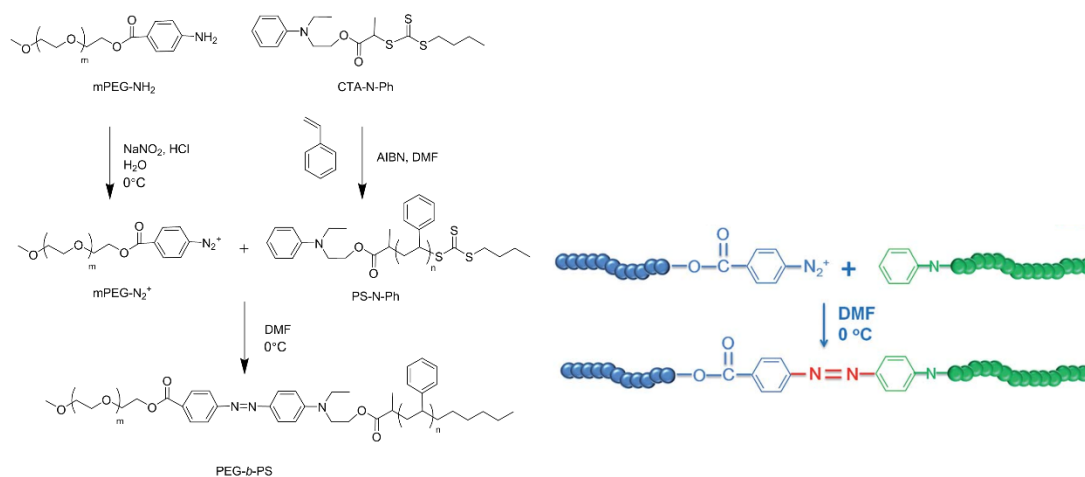
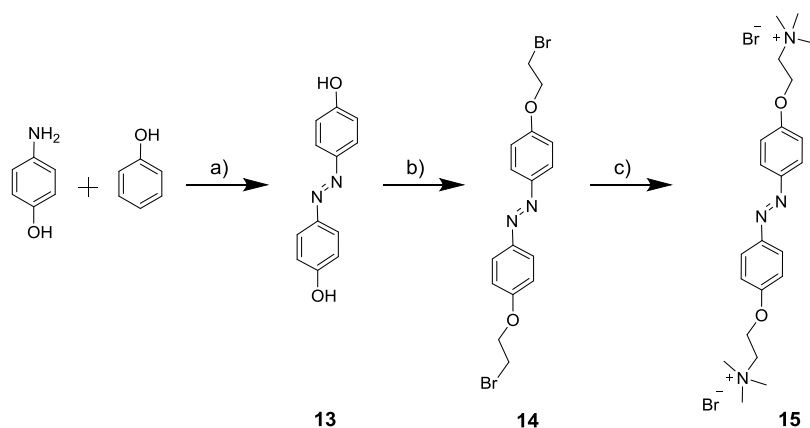


Figure 9 Schematic preparation of block copolymers *via* macromolecular azo-coupling reaction. Adapted from Ref<sup>9</sup>.

## e) Azo-divalent/PSS system

### e.1 Azo-divalent ions synthesis

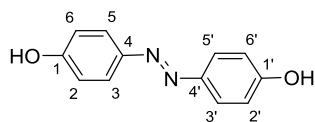
Azo-containing divalent counterions were synthesized in three steps. The symmetric 4,4'-dihydroxyazobenzene was formed by the azo-coupling reaction between 4-aminophenol and phenol<sup>1</sup>. The same reaction conditions for the synthesis of azo-surfactants were used to introduce the two short spacers and the quaternary ammonium heads.



Scheme 1 Synthesis of **15**. a) NaNO<sub>2</sub>, HCl, 0 °C; b) K<sub>2</sub>CO<sub>3</sub>, Bu<sub>4</sub>NBr, DMF, 50 °C; c) NEt<sub>3</sub>, THF, acetone, 75 °C under argon.

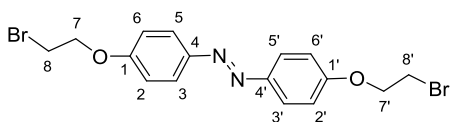
#### 4,4'-dihydroxyazobenzene (HO-Azo-OH) (**13**):

In a 250 ml flask, 4-aminophenol (5.0 g, 45.8 mmol) was dispersed in 100 ml HCl aqueous solution (1 mol L<sup>-1</sup>) at 0 °C. Sodium nitrite (3.2 g, 45.6 mmol) in 25 ml water was slowly added. The mixture was left to react for 15 min at 0 °C. Then phenol (4.3 g, 45.6 mmol) in 3 M NaOH was introduced dropwise in the reaction media. The solution was kept in the ice bath for 2 hrs before allowing to the room temperature. The crude product was recovered by filtration and evaporated under vacuum. The filtrate was purified by chromatography (SiO<sub>2</sub>, DCM/MeOH, 100/0 to 90/10) to afford **13** as an orange solid (1.8 g, 19% yield). <sup>1</sup>H NMR (400 MHz, Acetone-*d*<sub>6</sub>) δ 7.79 (dt, *J* = 8.9, 5.3 Hz, 4H, H<sub>3</sub>, H<sub>3'</sub>, H<sub>5</sub>, H<sub>5'</sub>), 6.98 (dt, *J* = 8.9, 5.3 Hz, 4H, H<sub>2</sub>, H<sub>2'</sub>, H<sub>6</sub>, H<sub>6'</sub>). <sup>13</sup>C NMR (100 MHz, Acetone-*d*<sub>6</sub>) δ 160.76 (C<sub>1</sub>, C<sub>1'</sub>), 147.17 (C<sub>4</sub>, C<sub>4'</sub>), 125 (C<sub>3</sub>, C<sub>3'</sub>, C<sub>5</sub>, C<sub>5'</sub>), 115, 116.54 (C<sub>2</sub>, C<sub>2'</sub>, C<sub>6</sub>, C<sub>6'</sub>). HRMS (ESI<sup>+</sup>) *m/z* 215.082330 (calcd for C<sub>12</sub>H<sub>10</sub>N<sub>2</sub>O<sub>2</sub>: 215.081504). Anal. Found: C, 67.16; H, 4.78; N, 12.81. (calcd for C<sub>12</sub>H<sub>10</sub>N<sub>2</sub>O<sub>2</sub>: C, 67.28; H, 4.71; N, 13.08).



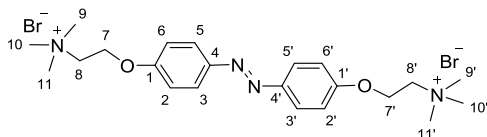
1,2-bis(4-(2-bromoethoxy)phenyl)diazene BrC<sub>2</sub>AzoC<sub>2</sub>Br (**14**):

Compound **13** (1.1 g, 5.3 mmol), 1,2-dibromoethane (9.2 ml, 106 mmol), K<sub>2</sub>CO<sub>3</sub> (10 g, 72.3 mmol) and Bu<sub>4</sub>NBr (10 mg) were introduced in 10 ml DMF. The mixture was heated at 50 °C under argon during 6 hrs. K<sub>2</sub>CO<sub>3</sub> solid was removed by filtration. Most of solvent were removed by extraction with DCM and water. Then the residue was precipitated into a mixture of 800 ml MeOH and 50 ml water and kept in refrigerator. After two days, the crude product was filtrated and evaporated under vacuum. Chromatology (SiO<sub>2</sub>, DCM) afforded (**14**) as a yellow solid (0.35 g, 15% yield). <sup>1</sup>H NMR (400 MHz, Acetone-*d*<sub>6</sub>) δ 7.90 (dt, *J* = 9.0, 5.3 Hz, 4H, H3, H3', H5, H5'), 7.15 (dt, *J* = 9.0, 5.2 Hz, 4H, H2, H2', H6, H6'), 4.49 (t, *J* = 5.6 Hz, 4H, H7, H7'), 3.87 – 3.80 (t, *J* = 5.8 Hz, 4H, H8, H8').



2,2'-((diazene-1,2-diylbis(4,1-phenylene))bis(oxy))bis(N,N,N-trimethylethan-1-aminium) bromide TABC<sub>2</sub>AzoC<sub>2</sub>TAB (**15**):

Compound **14** (0.2 g, 0.5 mmol) and a solution of trimethylamine in ethanol (1.0 ml, 3 mol L<sup>-1</sup>, 2.5 mmol) were dissolved in a mixture of 5 ml THF and 8 ml acetone. The mixture was stirred at 75 °C under argon for 26 hrs. After cooling to room temperature, the precipitate was filtrated and recrystallized from EtOAc/MeOH (3/1) at 90 °C to afford (**15**) as a yellow solid (0.24 g, 90% yield). <sup>1</sup>H NMR (400 MHz, D<sub>2</sub>O) δ 7.80 (dt, *J* = 9.3, 5.2 Hz, 4H, H3, H3', H5, H5'), 7.17 (dt, *J* = 9.2, 5.3 Hz, 4H, H2, H2', H6, H6'), 4.59 (s, 4H, H7, H7'), 3.85 (s, 4H, H8, H8'), 3.28 (s, 18H, N(CH<sub>3</sub>)<sub>3</sub>). <sup>13</sup>C NMR (100 MHz, D<sub>2</sub>O) δ 159.58 (C1, C1'), 146.84 (C4, C4'), 124.30 (C3, C3', C5, C5'), 115.31 (C2, C2', C6, C6'), 65.03 (C7, C7'), 62.12 (C8, C8'), 54.06 (N(CH<sub>3</sub>)<sub>3</sub>). HRMS (ESI<sup>+</sup>) *m/z* 193.134570 (calcd for C<sub>22</sub>H<sub>34</sub>N<sub>4</sub>O<sub>2</sub><sup>2+</sup>: 193.133540). Anal. Found: C, 47.84; H, 6.22; N, 10.14. (calcd for C<sub>22</sub>H<sub>34</sub>Br<sub>2</sub>N<sub>4</sub>O<sub>2</sub>: C, 48.32; H, 6.22; N, 10.25).



## e.2 Photoconversion of pure Azo-divalent ions

The photoconversion behaviour of Azo-divalent ions has been investigated by UV-Vis measurements. The maximum absorption at 361 nm is typical for *trans* isomers.

Upon UV irradiation, this band decreases progressively and two bands at 317 nm and 450 nm appear for *cis* isomers.

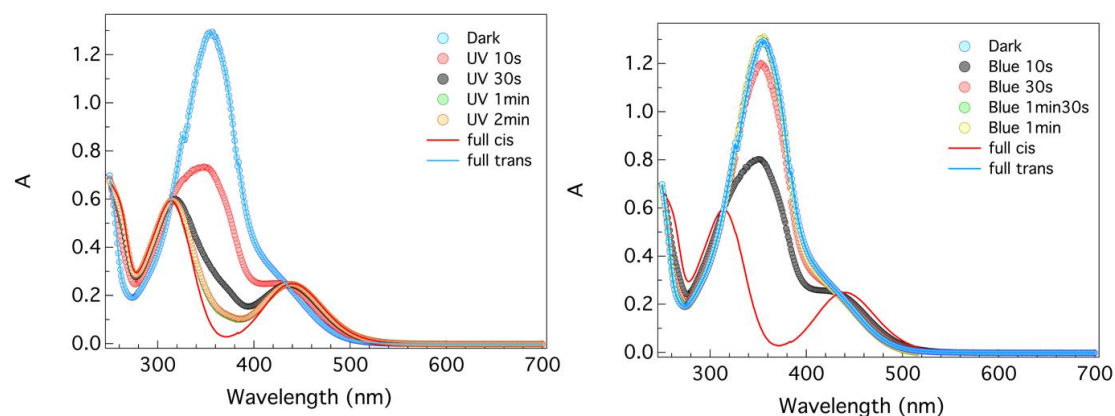


Figure 10 UV-Vis spectra of Azo-divalent (0.08 mM).

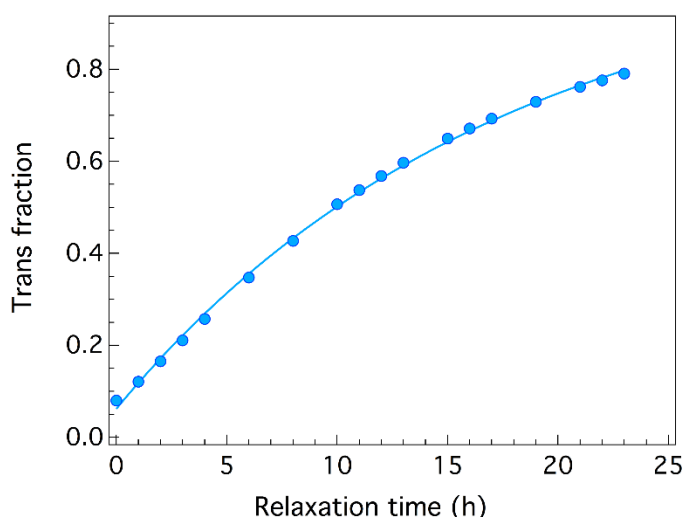


Figure 11 Thermal relaxation of pure Azo-divalent (0.08 mM).

The thermal relaxation from *cis* to *trans* state was monitored by UV-Vis. The characteristic time is 17.3 h. The relaxation process is faster than azo surfactants (4Azo2TAB  $\tau = 86$ h, 8Azo2TAB  $\tau = 195$ h). The approach of two charges in the bent *cis* form may favour the reversible conversion to the stretched *trans* form.

### e.3 Structural study of Azo-divalent/PSS mixture

#### e.3.1 PSS/divalent ratios and concentrations

PSS is also used at 100 mM like in the Azo-surfactant/PSS systems. The PSS/Azo-divalent molar ratio  $r$  is fixed at 0.25 (1:4). When more azo-divalent ions are added in the mixture, they precipitate. The molar charge ratio in the mixture (between divalent ions and PSS) is thus 0.5 (1:2), which is equal to that of Azo-surfactant/PSS.

### e.3.2 SAXS measurements

The characteristic scattering peak associated to electrostatic repulsion is absent in Azo-divalent/PSS solutions due to the presence of added salts (screening effect, Figure 12). A clear modification is observed under UV irradiation.

Flat curves are observed in pure divalent ions solution (Figure 13). This indicates that they are dispersed in solution and do not assemble into organized structures. No modification is observed for pure Azo-divalent under UV irradiation.

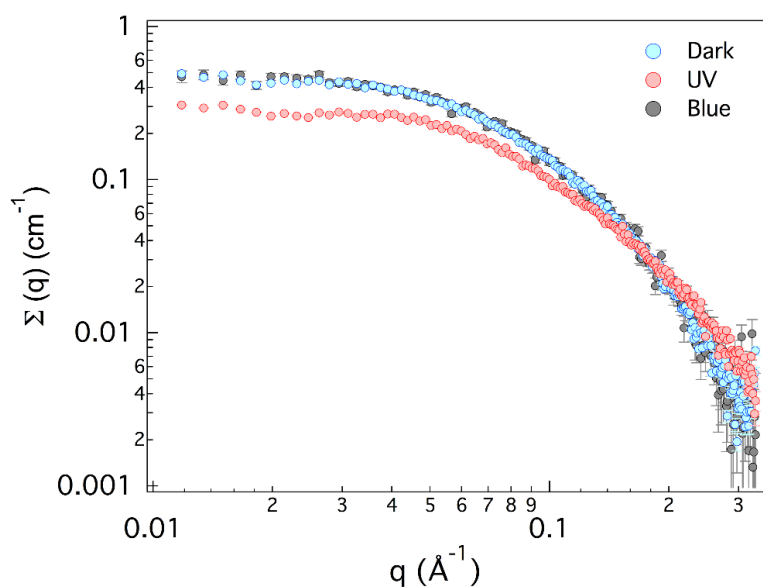


Figure 12 SAXS profiles of Azo-divalent/PSS (25 mM/100 mM).

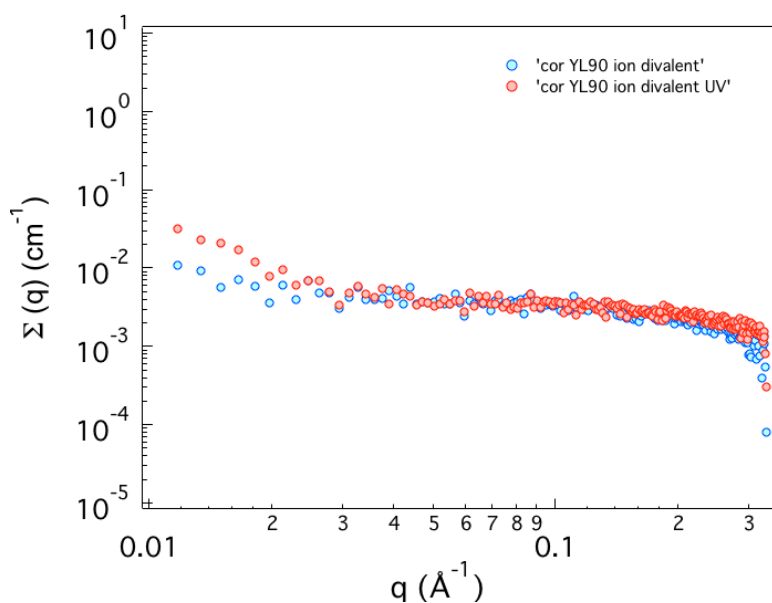


Figure 13 SAXS profiles of pure Azo-divalent at 25 mM.

### e.3.3 SANS measurements

We have used mixtures of H<sub>2</sub>O/D<sub>2</sub>O to probe the structural organization of PSS-D and Azo-divalent separately by SANS. Similarly to SANS measurements on Azo-surfactant/PSS complexes, in H<sub>2</sub>O/D<sub>2</sub>O solutions ( $\phi_{D2O}=0.267$ ), only PSS chains are detected by neutron scattering (Figure 14). In D<sub>2</sub>O, PSS-D are masked, only Azo-divalent counterions are visible (Figure 15).

Azo-divalent counterions interact strongly with polyions. Their structure function in dark reproduces that of the polyions. Under UV irradiation, the structural organization of both Azo-divalent and PSS changes. Works are going on to understand their structural organization and the modifications under UV radiation.

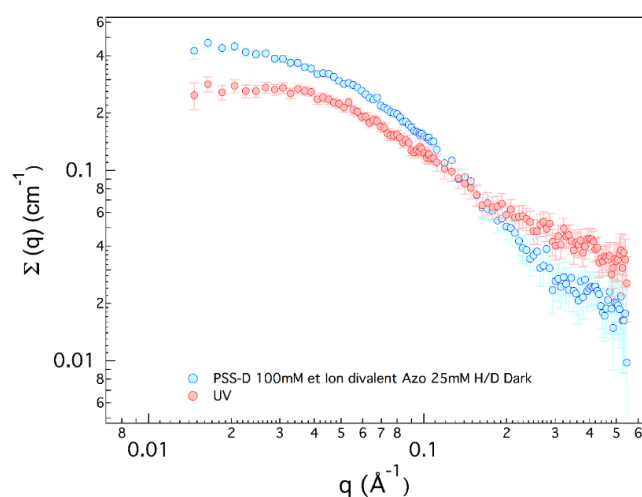


Figure 14 SANS profiles of Azo-divalent/PSS (25 mM/100 mM) in H<sub>2</sub>O/D<sub>2</sub>O ( $\phi_{D2O}=0.267$ ), only PSS chains are “visible”.

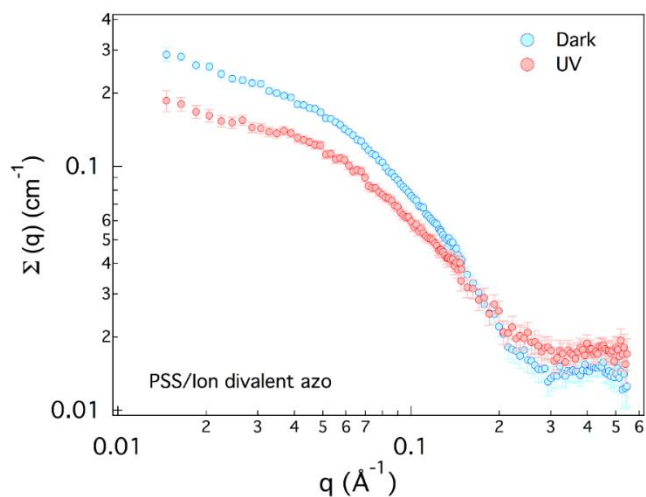


Figure 15 SANS profiles of Azo-divalent/PSS (25 mM/100 mM) in D<sub>2</sub>O, only Azo-divalent counterions are “visible”.





## Résumé

Cette thèse vise à concevoir, synthétiser et étudier des systèmes photo-stimulables modèles en solution aqueuse formés à partir de polyélectrolytes (PEs) et de tensioactifs. La photosensibilité est liée à la présence de chromophores azobenzène (Azo) qui subissent une isomérisation *trans* → *cis* sous irradiation UV.

Nous avons considéré dans un premier temps un PE hydrophile sur lequel nous avons greffé des groupements Azo. Ce système forme de agrégats globulaires en solution en raison du collapse des chaînes et des associations inter/intramoléculaires. La taille des agrégats varie sous irradiation UV. Elle dépend également de la masse molaire des PEs et du taux de greffage des groupements Azo.

Nous avons considéré dans un second temps des tensioactifs sur lesquels des groupements Azo ont été introduits (Azo-tensioactifs). Nous avons étudié leur complexation avec des PEs de charge opposée. Ces systèmes s'organisent en colliers de perles. Les polyions décorent les micelles et pénètrent à l'intérieur de celles-ci (co-micellisation). Sous irradiation UV, la taille des perles diminue sans vraiment modifier l'organisation des complexes.

Nous nous sommes enfin intéressés à l'auto-assemblage d'Azo-tensioactifs et de co-tensioactifs. Ce mélange conduit à la formation des micelles allongées et à la création d'un gel. Sous irradiation UV, on observe une transition gel → fluide. L'origine ce phénomène est lié à un changement morphologique des agrégats micellaires (micelles allongées → micelles globulaires).

Mots-clés : Polyélectrolytes (PEs) photosensibles, Azo-tensioactif/PE complexes, Auto-assemblage Azo-tensioactif/co-tensioactif, diffusion des rayons X et des neutrons aux petits angles

## Résumé en anglais

This thesis aims at designing, synthesizing and characterizing model photo-responsive systems in aqueous solution. These systems are based on polyelectrolytes (PEs) and surfactants. The photosensitivity arises from the presence of azobenzene (Azo) groups that undergo a photoisomerization from a *trans* to a *cis* isomer under UV irradiation.

We first considered a hydrophilic PE on which we grafted Azo groups. This system forms globular aggregates in solution due to chains collapse and inter/intramolecular associations. The size of the aggregates varies under UV irradiation. It also depends on the molar mass of the PEs and the Azo content.

We then considered surfactants in which Azo groups have been introduced (Azo-surfactants). We studied their complexation with oppositely charged PEs. These systems show a pearl necklace organization. The PEs decorate the micelles and penetrate inside (co-micellisation). Under UV irradiation, the size of the pearls decreases without really modifying the general organization of the complexes.

Finally, we were interested in the self-assembly of Azo-surfactants and co-surfactants. This mixture leads to the formation of wormlike micelles and the creation of a gel. Under UV irradiation, a gel → fluid transition is observed. The origin of this phenomenon is linked to a morphological transition of the micellar aggregates (wormlike micelles → globular micelles).

Keywords: Photoresponsive polyelectrolytes (PEs), Azo-surfactant/PE complexes, Azo-surfactant/co-surfactant self-assembly, small-angle X-ray and neutron scattering.